学位論文

Infrared Observation of PAH Emission in Galactic Planetary Nebulae

(系内惑星状星雲における PAH 放射の観測的研究)

平成 25 年 12 月 博士 (理学) 申請

東京大学大学院 理学系研究科
天文学専攻

大澤 亮

THESIS

Infrared Observation of PAH Emission in Galactic Planetary Nebulae

系内惑星状星雲における PAH 放射の観測的研究

A dissertation presented by

Ryou Ohsawa

to

Department of Astronomy
Graduate School of Science, University of Tokyo

in partial fulfillment of the requirements
for the degree of Doctor of Philosophy
in the subject of Astronomy

Submitted in December, 2013

Abstract

Polycyclic aromatic hydrocarbons (PAHs) are small dust grains composed of fused aromatic rings with hydrogen. When they absorb a single UV-photon, specific vibrational modes are excited, causing strong band emission in the infrared (e.g, at 3.3, 6.2, 7.7, 8.6, and 11.3 μm). The band emission is usually referred to as the unidentified infrared (UIR) bands or the PAH features. Since the PAH features are observed in a variety of objects such as evolved stars, reflection nebulae, and star-forming galaxies, PAHs are considered to be common grain species in the Universe.

Where PAHs are formed is an important topic. It is widely believed that PAHs are formed in the stellar-wind ejecta asymptotic giant branch (AGB) stars, and then injected into interstellar space. The PAH features are, however, rarely observed around AGB stars, since the effective temperature of these stars is too low to excite PAHs. PAH formation around AGB stars has not been observationally confirmed.

Another important topic is the origin of the variations in the spectral profile of the PAH features. Although the PAH features are expected to be almost identical around all objects because of a single-photon excitation process, the variations in the spectral profile of the PAH features have been reported. Interestingly, observations show that the PAH features in circumstellar environments are systematically different from those in interstellar environments. Evolution of the PAH features is expected to be observed from circumstellar environments, where PAHs are formed, to interstellar environments.

Planetary nebulae (PNe) are the terminal stage of low- and intermediate-mass stellar evolution. They are surrounded by abundant circumstellar medium, which is ejected in the AGB phase. The central star of PNe is one of the hottest objects in the Universe. There are abundant UV-photons to excite PAHs in PNe. PNe are one of the major PAH emitting objects showing the circumstellar PAH characteristics. After the PN phase, the circumstellar materials are injected into interstellar space. PNe are an important object to investigate the difference between the circumstellar and interstellar PAH features.

PAHs in PNe have been investigated with space and ground-based telescopes. The number of targets in previous studies have been, however, limited by insufficient sensitivity, especially in the 3 μm region. Properties of PAHs in a typical PN and evolution of the PAH features during the PN phase remain to be statistically investigated based on a

large number of samples.

In this paper, we introduce a 2.5–5.0 μm spectral catalog of Galactic PNe (hereafter, PNSPC catalog) based on observations by *AKARI*, the first Japanese astronomical infrared satellite. Thanks to the high sensitivity of *AKARI*, the PNSPC catalog contains more than 70 spectra of Galactic PNe, making it the largest spectral catalog in the near-infrared. The catalog enables us to statistically investigate the properties of PAHs and evolution of the PAH features in PNe.

Characteristics of the near-infrared PAH features are investigated based on the PNSPC catalog. The detection rate of the PAH emission in Galactic PNe is estimated to be about 65–80%. We find that the strength of the 3.3 μm PAH feature significantly varies with the evolution of PNe, and that the amount of the aliphatic components in PAHs increases as the PN evolves. The present results suggest that the PAH features evolve together with PNe.

The properties of PAHs are investigated based on the PNSPC catalog and mid-infrared spectra provided by the *Spitzer space telescope*. The ionization fraction of PAHs in a typical PN is estimated to be lower than other PAH emitting objects, as reported in previous studies. We suggest that small-sized PAHs in PNe are totally dehydrogenated and the degree of PAH dehydrogenation in PNe is as high as in a Galactic reflection nebula. The present result is quite consistent with theoretical predictions. We find that the peak position of the 6.2 μm PAH feature moves toward shorter wavelengths with PN evolution, indicating that the 6.2 μm feature in PNe changes into that usually seen in interstellar objects as the PN evolves. The amount of small-sized PAHs decreases with the PN evolution, while the amount of aliphatic components in PAHs increases at the same time.

The origin of the evolution of the PAH features is investigated. We conclude that the evolution is not caused by PAH processing such as photo-dissociation or ion-sputtering. To account for the observed variations, we propose a hypothesis: PAHs are formed in the AGB phase and the properties of PAHs change with the evolution of AGB and post-AGB stars. Circumstellar materials ejected in the AGB phase spread outside the envelope of PNe (AGB wind region). As the nebula expands, PAHs in the AGB wind region (far-side PAHs) are taken into the envelope. The amount of the far-side PAHs in the envelope increases with the expansion. The observed variations in the PAH features are consistently explained by the increasing amount of the far-side PAHs in the envelope. The evolution of the total intensity of the PAH features is also consistent with the proposed hypothesis.

The present results suggest that the dynamical evolution of PNe should be taken into account to understand the variations in the PAH features, which are not accounted for only by processing of PAHs. The results observationally support the idea that PAHs are formed in the AGB phase and suggest that the variations in the PAH features are attributed in part to the physical conditions during PAH formation.

Acknowledgments

First of all, I would like to express my greatest gratitude to Prof. Takashi Onaka for his continuous support of my research. He introduced me to infrared astronomy. When I have trouble in my research, he always offers me useful advice and a scientific way of thinking. I am always encouraged by his sense of humor. I could not finish my research without his support.

I fully appreciate the co-investigators for their helpful support. Prof. Christine Joblin and Dr. Olivier Berné helped me a lot when I visited Toulouse. They give me a lot of useful ideas on processing of PAHs. Dr. Jeronimo Bernard-Salas has made a large contribution to my research by giving me profound insights on planetary nebulae. Comments from Dr. Mikako Matsuura are always important and give me new perspective on my research. Prof. Issei Yamamura has helped me to understand the evolution of evolved stars. I have been inspired many times by important comments from Prof. Hidehiro Kaneda, who is a specialist in observational investigation of PAHs. Dr. Itsuki Sakon has taught me several methods of analyzing *AKARI* data. Ms. Tamami I. Mori has helped me to understand the variation in the PAH features by offering theoretical calculations. It is my great pleasure to be able to study with these co-investigators.

My research is also supported by many other people. I am grateful, especially, to Prof. Giard Martin, Prof. Hiroyuki Hirashita, Dr. Masaaki Otsuka, Prof. Koo Bon-Chul, Dr. Seok Ji-Yeon, Ms. Ruka Misawa, Dr. Takuya Fujiyoshi, Dr. Yoshifusa Ita, and Dr. Daisuke Ishihara for giving me a lot of helpful comments in conferences, e-mails, and daily conversations.

I have been supported by the members of Onaka's laboratory. I would like to show my gratitude to, especially, Dr. Itsuki Sakon, Dr. Tomohiko Nakamura, Dr. Chikako Yasui, Dr. Mark Hammonds, Ms. Tamami I. Mori, and Mr. Kazuki Sato, Mr. Aaron C. Bell, and Ms. Sayaka Shimamoto and the members who graduated from Onaka's laboratory, Dr. Daisuke Kato, Dr. Hideaki Fujiwara, Dr. Takafumi Kamizuka, Dr. Takashi Shimonishi, Mr. Ikki Takase, Ms. Ingrid Koch, Ms. Janette Suherli, and Dr. Lee Ho-Gyu. The warm atmosphere in the laboratory is really comfortable for me. I am grateful to them and glad to be a member of the laboratory.

I would also like to acknowledge the members of the TAO[*1] project. They have allowed me to visit Chile and join the project to start up the 1-m miniTAO telescope. They have brought me a chance to experience the observations in extreme conditions at 5640 m above sea level. I am grateful, especially, to Prof. Kentaro Motohara, Dr. Masahiro Konishi, Ms. Natsuko Kato, Dr. Takeo Minezaki, Dr. Shintaro Koshida, Prof. Takashi Miyata, Dr. Kentaro Asano, and Prof. Yuzuru Yoshii.

I am always encouraged by my friends so that I can survive though days in the University. I am especially thankful to Dr. Takashi J. Moriya, Dr. Kimihiko Nakajima, Dr. Takafumi Sonoi, Dr. Soh Ikarashi, Dr. Kohei Hattori, Dr. Yasuhiro $\mathcal{H}$. Takahashi, Dr. Takayuki Hayashi, Dr. Masaomi Tanaka, Dr. Yusei Koyama, Mr. Shingo Shinogi, Mr. Takuya Hashimoto, Mr. Ryosuke Goto, Mr. Ko Takahashi, Mr. Kazuhiro Maeda, and Mr. Kyle A. Mede. We have a lot of parties together in *Oishi-ya* (Koyama, 2011), which always give me enormous energy in my life and severe damage to my stomach.

I am grateful to Dr. Hinako Fukushi, Dr. Masaaki Hiramatu, Dr. Norita Kawanaka, Dr. Rieko Momose, and Ms. Miyoko Maruyama, who help me to make my life happy and wonderful. We went sightseeing together, enjoyed some festivals, and had good times in good restaurants. I also thank Mr. Toshiya Ohta, who is my best drinking buddy. Dr. Bosco Yung continuously encourages me. I would like to thank him and I am very glad to hear that he found a nice job at the University of Hong Kong. I would like to show my best gratitude to Ms. Jun Yabuki, who patiently supports me. Her smile always makes me happy and cheers me up.

Finally, I would like to express my gratitude to my parents, Mr. Hiroshi Ohsawa and Ms. Emiko Ohsawa, who allow me to go on to graduate school and continuously support me both mentally and financially. I also thank my brother, Mr. Jun Ohsawa, and hope that you will make good research in your doctoral course.

The thesis is reviewed by Prof. Takuya Yamashita, Prof. Hiromoto Shibahashi, Prof. Motohide Tamura, (the University of Tokyo), Prof. Toshiya Ueta (University of Denver), and Prof. Hideyuki Izumiura (National Observatory of Japan) and has their endorsement.

[*1] The University of Tokyo Atacama Observatory Project

The results are in part based on observations with AKARI, a JAXA project with the participation of ESA and on archival data obtained with the Spitzer Space Telescope, which is operated by the Jet Propulsion Laboratory, California Institute of Technology under a contract with NASA. We fully appreciate all the people who worked in the operation and maintenance of those instruments. This publication makes use of data products from the Wide-field Infrared Survey Explorer, which is a joint project of the University of California, Los Angeles, and the Jet Propulsion Laboratory/California Institute of Technology, funded by the National Aeronautics and Space Administration. This research has made use of the SIMBAD database, operated at CDS, Strasbourg, France.

Contents

List of Figures

List of Tables

Chapter 1
Introduction

Broad and strong emission bands are observed in a variety of objects in the Universe. They are referred to as unidentified infrared (UIR) bands. The most likely candidate for the UIR band carrier is polycyclic aromatic hydrocarbons (PAHs). PAHs are small carbonaceous dust particles and they are considered to be one of the most common dust species in the Universe. The emission from PAHs (PAH features) are frequently detected in planetary nebulae (PNe). PNe are in a late stage of low- and intermediate-mass stellar evolution. They are believed to be major PAH suppliers in galaxies. In the thesis, the evolution of the PAH features during the PN phase is investigated to understand the formation of PAHs and the variations in the PAH characteristics. In this chapter, the characteristics of the PAH features and PNe are reviewed, followed by the general outline of the thesis.

1.1 Polycyclic Aromatic Hydrocarbons

1.1.1 Unidentified Infrared Band

Diffuse interstellar and circumstellar emission in the infrared is dominated by emission from dust grains. The emission from dust grains is well explained by a combination of three dust components (Désert et al., 1990; Dwek et al., 1997; Puget & Leger, 1989). Figure 1.1 shows the emission from the diffuse high galactic latitude medium. The spectra in the mid-infrared is provided by the *ISO*/SWS*[1]; while that in the far-infrared is provided by the *COBE*/FIRAS*[2]. The square symbols show the measurements by the *COBE*/DIRBE*[3]. The observations are fitted using `DustEM` model (Compiègne et al., 2011). The dot-dashed line shows the emission from classical grains or big grains. They are typically larger than 20 Å and in radiative equilibrium with the ambient radiation field. The dotted line shows the emission from Very Small Grains (VSGs). They are quite small and

*[1] *Infrared Space Observatory*/Short Wavelength Spectrometer
*[2] *Cosmic Background Explorer*/Far Infrared Absolute Spectrophotometer
*[3] Diffuse Infrared Background Experiment

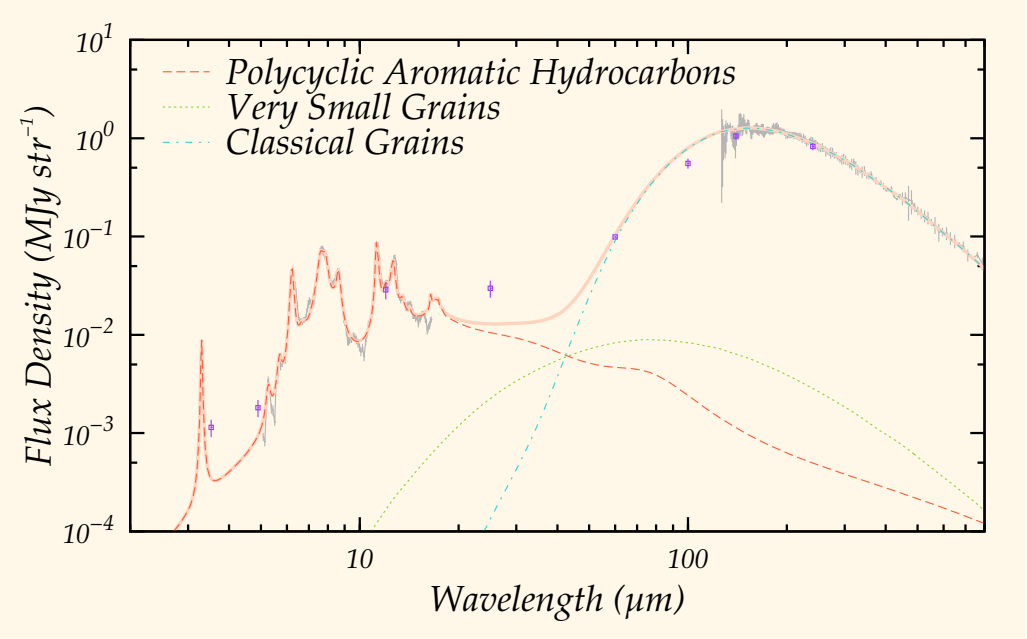

Figure 1.1 – Emission from the diffuse high galactic latitude medium (Compiègne et al., 2011) The mid- and far-infrared spectra are provided by the *ISO*/SWS and *COBE*/FIRAS, respectively. The square symbols are the *COBE*/DIRBE measurements. The dashed, dotted, and dash-dotted lines show the emission of PAHs, VSGs, and classical grains, respectively.

rarely absorb starlight photons. They can cool down to a very low temperature before the next photon absorption. When they absorb a photon, their temperature becomes very high because of their small heat capacity. The emission from VSGs is dominant in the mid-infrared. The dashed line shows the emission from Polycyclic Aromatic Hydrocarbons (PAHs). The carbonaceous grains which are smaller than VSGs absorb a single UV-photon, which then excites their vibrational modes (*single-photon excitation process*). The broad emission bands are emitted when the vibrational modes are deexcited. Each emission is attributed to a specific functional group on the surface of dust grains (Duley & Williams, 1981). These emission bands are widely referred to as the unidentified infrared (UIR) bands. PAHs, which are made of fused aromatic rings, are one of the most plausible candidates of the carriers of the UIR bands (hereafter, *PAH features*).

The major PAH features appear at about 3.3, 6.2, 7.7, 8.6, 11.2, and 12.7 μm. These features come from specific vibrational modes (Allamandola et al., 1989). Figure 1.2 shows the typical PAH features seen in the near- and mid-infrared. The 3.3 μm feature comes from C—H stretching modes (blue in Figure 1.2). The 3.4–3.5 μm features are attributed to C—H stretching modes of aliphatic components in PAHs (orange; Joblin et al., 1996; Sloan et al., 1997). The origins of the 5.2 and 5.7 μm features are not well understood, but they are tentatively attributed to a blend of combination, difference, and overtone vibrational modes of C—H bonds (yellow; Boersma et al., 2009). The 6.2 and 7.7 μm features are attributed to C—C stretching modes (green). The 8.6 μm feature is attributed to C—H in-plane bending modes (dark purple). The 11.2, 12.0, 12.7, and 13.4 μm features

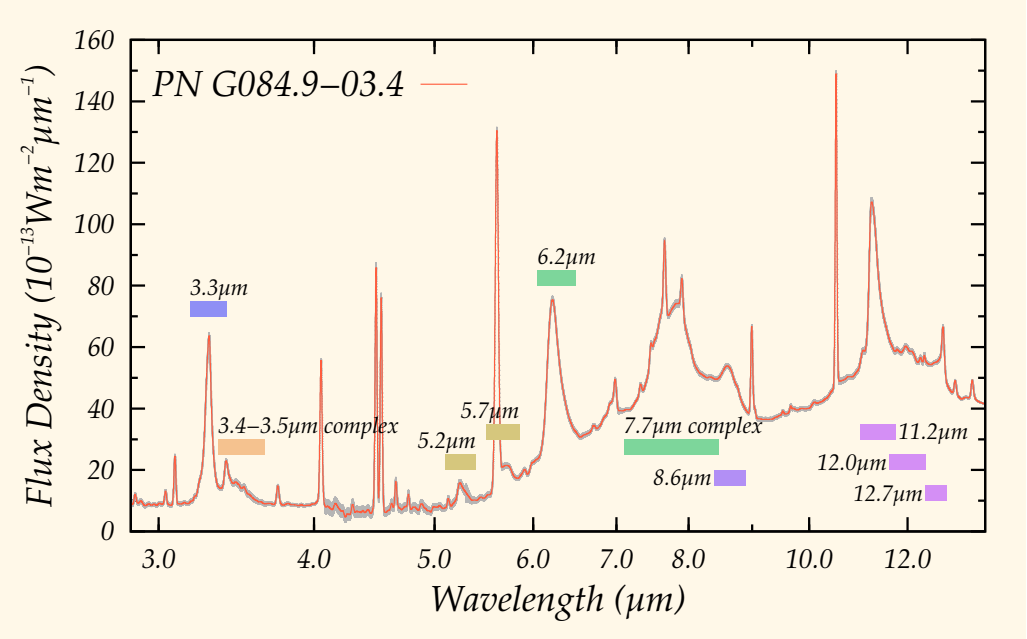

Figure 1.2 – Unidentified Infrared Bands in PN G084.9−03.4. The major UIR bands appear at about 3.3, 3.4–3.5, 6.2, 7.7, 8.6, 11.2, 12.7 μm and are attributed to specific vibrational modes (*see* text).

originate from C—H out-of-plane bending modes (light purple; Hony et al., 2001). The PAH features around 15–20 μm are attributed to C—C—C bending modes. At wavelengths longer than 20 μm, there are PAH features attributed to "Jumping-Jack", "Butterfly", and "Drumhead" modes (Boersma et al., 2011).

1.1.2 Diagnostics of PAHs

The relative strength of the PAH features can be used to diagnose the physical conditions of PAHs. DeFrees et al. (1993) theoretically suggest that the 6.2 and 7.7 μm features become strong when PAHs are ionized. Bregman & Temi (2005) and Galliano et al. (2008) observationally confirm that the intensity ratio of the 6.2 to 11.2 μm PAH features is well explained by the PAH ionization parameter $G_0/n_e\sqrt{T}$, where G_0 is the intensity of the ambient UV radiation field, T is the gas temperature, and n_e is the electron density. The intensity ratios of the 6.2 to 11.2 μm features and 7.7 to 11.2 μm features are widely recognized as estimators of the PAH ionization fraction. The 11.0 μm feature also becomes strong when PAHs are ionized (Sloan et al., 1999). The intensity ratio of the 11.0 to 11.2 μm features can also be an estimator of the PAH ionization, which is extinction free and obtainable from ground-based telescopes (Sakon et al., 2006). The intensity ratios of the 6.2 to 7.7 μm features and 3.3 to 11.2 μm features are less sensitive to the PAH ionization, while they are sensitive to the excitation or size of PAHs. Mori et al. (2012b) investigate the intensity ratio of the 3.3 to 11.2 μm features in the compact H II region with different star-formation activities. They confirm that the 3.3 to 11.2 μm ratio changes with the star-formation activity, and that the 3.3 to 11.2 μm ratio drops when the star-formation activity becomes intense, suggesting

processing of small-sized PAHs by strong UV radiation. The PAH features around 11–14 μm are sensitive to the molecular structure of PAHs. The 11.2μm feature is mainly attributed to a solo C—H bond: only one H-atom in an aromatic ring, while the 12.7 μm feature originates from a duo or trio C—H bond: two or three H-atom in an aromatic ring. The intensity ratio of the 12.7 to 11.2 μm features is useful to investigate the molecular structure (solo-to-duo ratio) of PAHs (Hony et al., 2001). The 3.4–3.5 μm features are attributed to aliphatic C—H bonds in PAHs. The intensity ratio of the 3.4 to 3.3 μm features is used to estimate the aliphatic-to-aromatic ratio of PAHs (Joblin et al., 1996; Sloan et al., 1997). While the PAH features are used to diagnose the physical conditions of PAHs, they are useful for the investigation of the intensity and hardness of the radiation field.

1.1.3 Formation of PAHs

PAHs are thought to be formed around evolved stars as classical grains, and PAH formation by shattering of carbonaceous dust grains has been proposed to account for the metalicity dependence of PAH abundance in galaxies (Seok et al., 2014). It is still unclear which formation process is dominant in the Universe.

Shattering of dust grains is considered to be an important process in determining the observed extinction curve and the size distribution of dust grains (Hirashita, 2010; Jones et al., 1996). When large carbonaceous grains are fragmented by shattering, a large amount of VSGs are supplied to interstellar space (e.g., Hirashita et al., 2010). These fragmented grains can be as small as PAHs, suggesting that PAHs may be formed by shattering. Whether of not such small grains, formed by shattering, could emit the PAH feature is however unconfirmed.

Carbon-rich AGB and post-AGB stars are proposed as a major PAH formation site (e.g., Buss et al., 1991). When the core mass exceeds $\sim 0.6\,M_{\odot}$, the third dredge-up occurs and the star becomes carbon-rich (Iben, 1982). Carbonaceous dust grains are formed in the stellar wind blown by the AGB star. Cau (2002) theoretically investigate the formation of PAHs in periodical shocks in the AGB wind. On the other hand, several studies propose that thermal or UV processing is important to form aromatic components in small carbonaceous grains (e.g., Goto et al., 2003, 2000). Cernicharo et al. (2001a,b) detect the absorption from benzene and long polyynes in the post-AGB star, CRL 618, and propose that PAHs are formed by photo-chemical process only after a late post-AGB phase. Based on the *Spitzer* observation of SMP LMC 11, Bernard-Salas et al. (2006), however, discuss that the dust envelope of post-AGB stars could be too thick to exclude the PAH formation during the AGB and post-AGB phases. By understanding when PAHs are formed, we can constrain the physical environments in PAH formation around evolved stars. The PAH features are however not expected to be observed around AGB stars. Even though PAHs are formed during the AGB phase, the effective temperature of AGB stars is too low to excite PAHs. Boersma et al. (2006) report the detection of the PAH features around the AGB star, TU Tauri, which is accompanied by an A-type star. PAHs in TU Tauri are thought to be excited by the radiation from the companion star. There is no other detection of the PAH features in AGB stars and we cannot exclude the possibility that the radiation from the companion contributes to the PAH formation in TU Tauri. The detection in

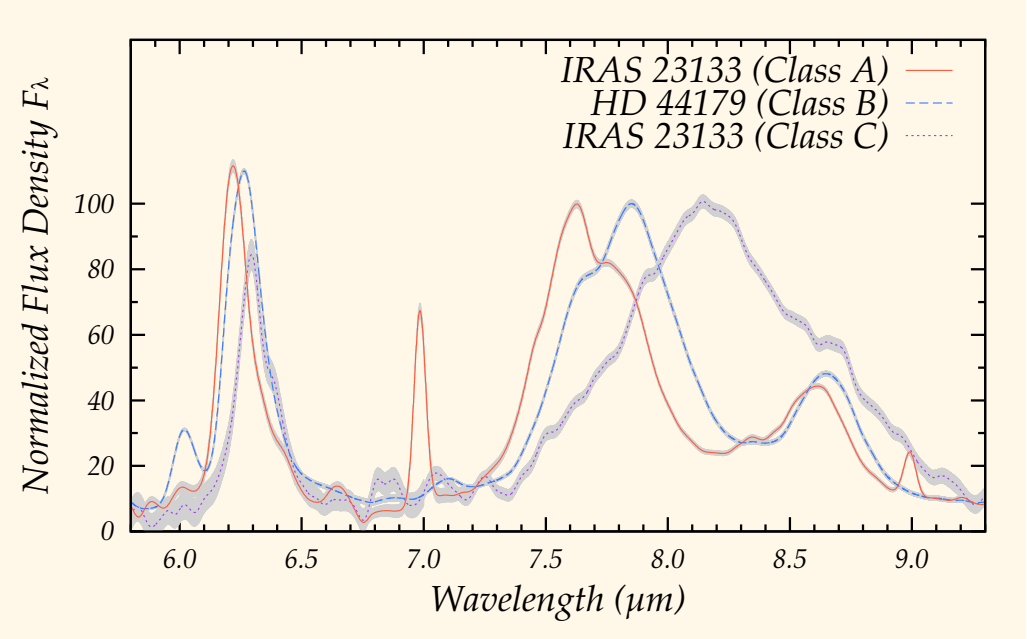

Figure 1.3 – Classification of the PAH emission in the 6–9 μm region. The solid, dashed, and dotted lines are the representative spectra of Class $\mathcal{A}$, $\mathcal{B}$, and $\mathcal{C}$ PAH emission, respectively (Peeters et al., 2002b).

TU Tauri does not necessarily lead to the conclusion that PAHs are commonly formed around AGB stars. Whether PAHs are formed during the AGB phase should be observationally investigated.

1.1.4 Classification of the PAH Emission

The PAH features are widely detected in a variety of types of objects (Acke & van den Ancker, 2004; Peeters et al., 2002b), suggesting that PAHs are common dust species in the Universe. The spectral profile of the PAH emission is expected to be almost identical because of the single-photon excitation process. However, the variations in the spectral profile of the PAH features have been reported. The 6–9 μm PAH features are intensively investigated by Peeters et al. (2002a). They point out that the PAH features in the 6–9 μm can be classified into three classes (hereafter Class $\mathcal{A}$, $\mathcal{B}$, and $\mathcal{C}$). The representative spectra are illustrated in Figure 1.3. Interestingly, the observed PAH emission class is strongly related to the type of objects as illustrated in Figure 1.4. The Class $\mathcal{A}$ emission is generally detected in H II regions, reflection nebulae, and non-isolated Herbig Ae/Be stars. The 6.2 μm feature has the peak around 6.22 μm and the 7.6 μm component is stronger in the 7.7 μm component. The Class $\mathcal{B}$ emission is detected in PNe, post-AGB stars, and isolated Herbig Ae/Be stars. The peak position of the 6.2 μm feature is around 6.24–6.28 μm. The 7.8 μm component is stronger in the 7.7 μm component. The Class $\mathcal{C}$ emission is quite rare and detected mainly in post-AGB stars. The 6.2 μm feature peaks at around 6.3 μm. The 7.7 and 8.6 μm features are blended peaking at around 8.2 μm. The 3.3 and 11.2 μm features are intensively investigated by van Diedenhoven et al. (2004). They find that a similar classification

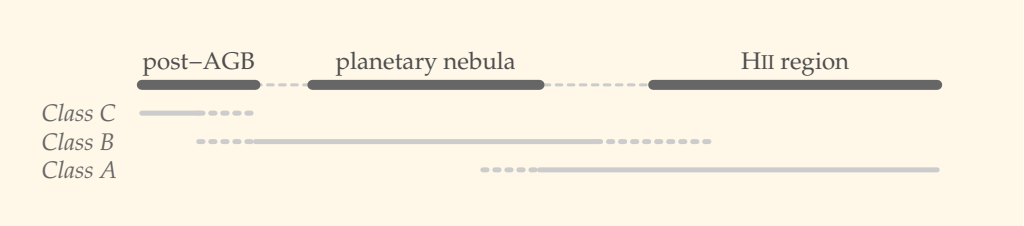

Figure 1.4 – Classification of the PAH emission and the type of PAH-emitting objects. The gray solid lines respectively indicate the typical objects which show the PAH features of the emission class (*see* text).

scheme can be applied to the 3.3 and 11.2 μm features.

The origin of the variations in the spectral features is not identified. Hudgins et al. (2005) suggest that the variation in the peak position of the 6.2 μm feature is related to N/C ratio in nitrogen-substituted PAHs (PANHs). Wada et al. (2003) investigate the 6.2 μm peak shift in terms of the C^{13}/C^{12} ratio. Pino et al. (2008) experimentally confirm that the 6.2 μm peak moves to shorter wavelengths with decreasing aliphatic-to-aromatic ratio. Bauschlicher et al. (2009) propose that the cation-to-anion ratio determines the 6.2 μm peak position. Bregman & Temi (2005) suggest that the Class $\mathcal{B}$ to $\mathcal{A}$ transition is explained by the cation-to-anion ratio. These explanations should be tested observationally.

1.1.5 Outstanding Issues of PAHs

Two unsolved issues of PAHs are featured above: whether PAHs are formed in the AGB phase and what is the origin of the PAH emission class. To investigate these topics, we focus on planetary nebulae (PNe). The PAH features are frequently observed in PNe. Since PNe are evolved from AGB and post-AGB stars, the properties of the PAH features in PNe may reflect the physical conditions in PAH formation around evolved stars. PAHs in PNe are injected to interstellar space. PAHs in PNe typically show the Class $\mathcal{B}$ features, while PAHs in interstellar space show the Class $\mathcal{A}$ features. It is important to investigate the PAH features of PNe to understand the origin of the Class $\mathcal{B}$ to $\mathcal{A}$ transition between circumstellar and interstellar environments. PNe may be suitable environments for investigating the origin of PAHs and the evolution of the PAH features.

1.2 Planetary Nebulae

1.2.1 Overview

PNe are a late stage of low- and intermediate-mass (~0.8–8 $M_\odot$) stellar evolution. The name was given by William Herschel based on their greenish disk-like appearance. The nature of PNe is the circumstellar nebula illuminated by the hot central star. The nebula is formed by an efficient mass loss during the asymptotic giant branch (AGB) phase. The temperature of the central star of PNe is high (~ 40 000–100 000 K; Kohoutek, 2001), so that emission lines of highly-ionized elements, such as O III and S IV, are detected. These emission lines are efficient in

cooling and account for almost 10% of the total luminosity of PNe. The bolometric luminosity is a few $\times 10^3$ $L_\odot$. The core mass is about $0.6 M_\odot$, corresponding to the progenitor of about 0.8–$8 M_\odot$ at the zero age main sequence. The duration of the PN phase is typically a few thousand years, although it depends heavily on the mass of the central star. After the PN phase, the central star evolves into the white dwarf phase. The circumstellar medium is finally injected into interstellar space. PNe and AGB stars are considered to be important gas and dust sources in galaxies (Matsuura et al., 2009). Investigating their circumstellar medium is important to understand the chemical evolution of galaxies.

1.2.2 Galactic Planetary Nebulae

In the Milky Way, more than 3000 PNe have been identified (e.g., Kohoutek, 2001; Parker et al., 2006, 2012; Parker & Frew, 2011; Sabin et al., 2010). The chemical abundance of PNe is different from that of the Solar neighborhood. Generally, carbon and nitrogen are rich in PNe (e.g., Aller & Czyzak, 1983; Khromov, 1989), although there is a large variation in the chemical abundance among PNe. Many Galactic PNe are large and diffuse objects, and their morphology has also been investigated. Manchado et al. (1996) compiled a catalog of Galactic PNe in the northern hemisphere. About 85% of Galactic PNe are elliptical or round, while the rest of them are bipolar or multi-polar (Stanghellini et al., 2002). The morphology is investigated in terms of the chemical abundance and the core mass. Bipolar PNe are believed to have higher nitrogen and helium abundance and evolve from more massive ($\gtrsim 3\, M_\odot$) progenitors (Stanghellini et al., 2006, 2002). Although the morphology of PNe is investigated intensively in the optical, the distribution of dust in PNe has been examined in the infrared (e.g., Bernard et al., 1994; Matsumoto et al., 2008; Ohsawa et al., 2012). PNe are expanding and it is important to understand their kinematics. The expansion velocity is measured by high-resolution spectroscopy (e.g., Gesicki et al., 2003; Robinson et al., 1982; Schönberner et al., 2005a). Several models have been investigated to account for the radial variation in the expansion velocity (Matsumoto et al., 2006; Sabbadin et al., 1984). High-resolution images by *Hubble Space Telescope (HST)* enables us to investigate the proper motion of the nebulosity (Sahai et al., 2007).

PNe are also an important tool for investigating chemical abundance variation in the Milky Way. Stanghellini et al. (2006) investigate the abundance of Galactic PNe in different positions and derive a global metalicity gradient. The chemical evolution of the Milky Way is discussed based on this gradient (Stanghellini & Haywood, 2010). PNe are also useful to investigate kinematics of the Milky Way. Durand et al. (1998) measure the velocity of 867 Galactic PNe and investigate the rotation of the Milky Way. The velocities of PNe are used to study the kinematics of the Galactic bulge (Beaulieu et al., 2000).

Distance determination is the most troublesome topic in the investigation of Galactic PNe. The expansion parallax method uses the ratio of the expansion velocity to the angular expansion velocity (e.g., Gomez et al., 1993). However, this method is only available for nearby PNe because of the difficulty in measuring the angular expansion. In the interstellar extinction method, the distance is estimated based on the reddening-distance relation using neighborhood stars

(Gathier et al., 1986a). This method can be applied only to PNe near the Galactic plane. The absorption of the 21 cm H I line is also employed to estimate the distance, $D = N(\mathrm{H\ I})/n_{\mathrm{H}}$, where D is the distance, $N(\mathrm{H\ I})$ is the column density of the neutral hydrogen to the PN, and n_{H} is the averaged number density of hydrogen (Gathier et al., 1986b). The main uncertainty in this method comes from n_{H}, which can vary with the direction. High-resolution spectral profiles of the absorption lines enable us to measure the surface gravity of the central star and accurately estimate the absolute luminosity (e.g., Mendez et al., 1992, 1988). This method is only applicable to PNe bright enough for high-resolution spectroscopy. Statistical (empirical) methods are widely used to estimate the distance. Shklovsky (1956) develop a method to estimate the distance by radio flux density and the angular size, assuming that the mass of the ionized gas is constant. Later, the Shklovsky method is generalized assuming a relationship between the ionized gas mass and the radius. In the revised Shklovsky method, the radio flux density is given by

$$F_\nu \propto \theta^{2\beta-3} D^{2\beta-5}, \tag{1.1}$$

where θ is the angular radius, D is the distance to the PN, and β is the parameter of the mass-radius relationship. The distance to Galactic PNe are calculated assuming different β values (e.g., Cahn et al., 1992; Daub, 1982; Maciel & Pottasch, 1980). Recently, (Stanghellini et al., 2008) calibrate the relationship using PNe in the Large Magellanic Cloud (LMC) and obtain reliable distances of Galactic PNe. However, the uncertainty in the distance is at least $\sim 30\,\%$ even with the latest methods. We still have great difficulty obtaining accurate distances to Galactic PNe as well as the absolute luminosity and the mass of the nebula.

1.2.3 Extragalactic Planetary Nebulae

Since PNe are bright ($\sim 10^4 L_\odot$) and their emission lines are narrow ($\sim$30 km s^{-1}), it is easy to identify PNe even in nearby galaxies. Sanduleak et al. (1978) compile a catalog of PNe in the Magellanic Clouds (MCs). PNe in the bulge of M 31 are collected by Ciardullo et al. (1989b). Recently, PNe in the MCs are observed by *Spitzer Space Telescope (Spitzer)* and the characteristics of the mid-infrared emission are investigated (Bernard-Salas et al., 2009, 2008; Stanghellini et al., 2007). Arnaboldi et al. (1998) investigate kinematics of the outer region of NGC 1316 based on the radial velocity of PNe. The metalicity gradient in M 33 is intensively investigated by Magrini et al. (2007, 2009). Unlike Galactic PNe, the distance to extragalactic PNe is measured as accurately as the distance to the host galaxy. Thus, the luminosity of extragalactic PNe is accurately measured. Ciardullo et al. (1989b) obtain the [O III]λ5007 luminosity function of PNe and find the steep decline at the bright end. Ciardullo et al. (1989a) confirm that the luminosity function is almost the same in the Leo I group – NGC 3379, NGC 3384 and NGC 3377. Ciardullo (2004) suggest that the luminosity function can be useful as a standard candle to estimate the distance to the galaxy at 1-10 Mpc.

1.2.4 Formation and Structure of Planetary Nebulae

The basic mechanism of PN formation, known as the interacting stellar wind (ISW) theory, is proposed by Kwok et al. (1978). The ISW theory has been improved by including radiation physics (e.g., Bedogni & Dercole, 1986; Marten & Schönberner, 1991; Schmidt-Voigt & Köppen, 1987). Recently, dynamical evolution of PNe has been investigated based on more advanced hydrodynamical calculations with radiation processes (e.g., Mellema, 1994; Villaver et al., 2002). Figure 1.5 shows the schematic view of the PN structure (Perinotto et al., 2004). At the end of the AGB phase, the central star is surrounded by the circumstellar medium ejected during the AGB phase (AGB wind) and the post-AGB phase (the super wind; Renzini, 1981). As the central star becomes hot, an ionization front (R_{IF}) penetrates into the circumstellar medium. The circumstellar medium is compressed by the ionized gas and a dense shell is formed (hereafter, *outer shell*). R_o shows the boundary between the outer shell and the AGB wind. The AGB wind remains intact outside of R_o (Region 1; hereafter, *AGB wind region*). The central star is extremely hot and produces a fast wind with $v \gtrsim 1000\,\mathrm{km\,s^{-1}}$ (*fast wind*). When the fast wind collides with the surrounding materials, the forward and reverse shocks run toward the AGB wind region and the central star, respectively. R_i is the boundary between the fast wind and the circumstellar medium. R_r shows the position of the reverse shock. The circumstellar medium is compressed and accumulated by the forward shock and a dense shell is formed just in front of R_i (*inner rim*). The region between R_o and R_i (Region 2) is referred to as the *envelope*. Region 3, between R_r and R_i, means the material shocked by the reverse shock (*hot bubble*). The temperature in the hot bubble is as high as $\sim 10^6$ K. Region 4 means the fast wind, which is not shocked yet.

A characteristic of PNe is their clearly outlined shape. The radiative cooling is efficient in the envelope because of its high density ($\sim 10^2$–$10^4\,\mathrm{cm^{-3}}$). Thus, the gas temperature in the envelope is considered to be at most about 10^4 K, a typical gas temperature in an H II region. The gas temperature in the hot bubble is as high as 10^6 K and the gas is too dilute to cool efficiently. The cooling function is expected to reach a maximum around the transitional region between the inner rim and hot bubble (Bedogni & Dercole, 1986). As a result, a large amount of the luminosity comes from the transitional region as emission lines, creating a clear shell-like morphology. Emission from dust grains becomes strong in the envelope, where the dust column density is high. Dust emission shows a similar but more extended shell-like structure (e.g., Matsumoto et al., 2008; Ohsawa et al., 2012).

Although the hydrodynamical model successfully reproduces the shell-like morphology of PNe, the structure highly depends on the evolution of the central star and the mass loss history during the AGB and post-AGB phases. Furthermore, PNe show various and complicated morphologies such as bipolar structure. The hydrodynamical model does not explain the origin of these morphologies. Figure 1.5 provides a very general view of the radial structure of a PN.

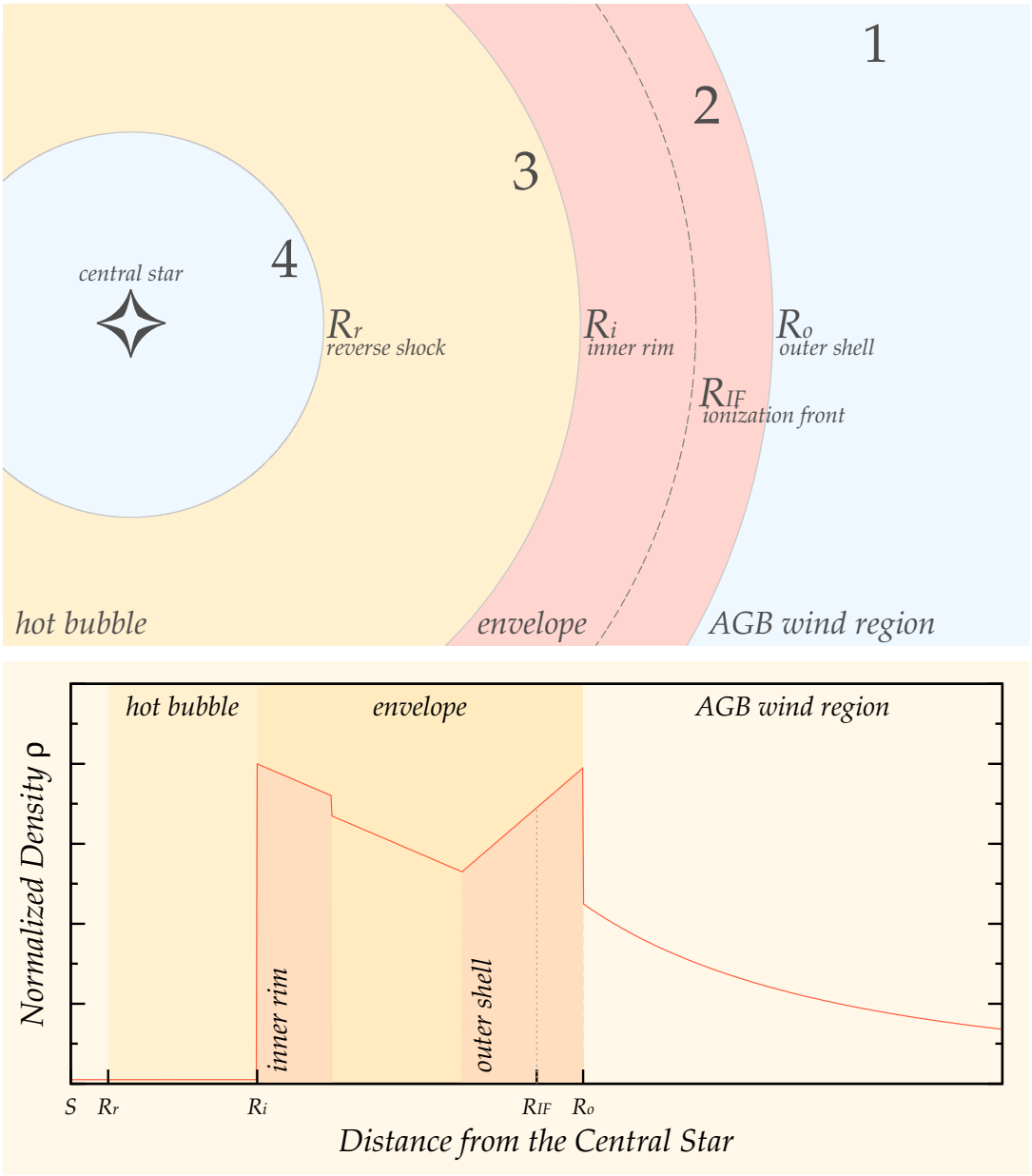

Figure 1.5 – *Top*: Schematic view of PNe. Region 1 is the unshocked AGB wind. Region 3 is the materials shocked by the reverse shock. The shock front is at R_r. Region 4 is the unshocked fast wind. R_{IF} is the position of the ionization front. R_i and R_o respectively show the inner and outer boundary of the envelope. *Bottom*: Schematic view of the density profile of PNe. The vertical and horizontal axes show the normalized gas density and the distance from the central star, respectively. The inner rim and outer shell are shown by the colored regions (*see* text).

1.2.5 Central Star Evolution of Planetary Nebulae

The basic understanding of the evolution of the PN central star is brought by Paczyński (1971). The central star of the PN is a degenerated carbon-oxygen core surrounded by a thin hydrogen envelope. The mass of the hydrogen envelope (M_e) should be small in order to reach a high temperature of ~30 000 K. Before hydrogen exhaustion, the hydrogen envelope shrinks and the effective temperature increases. Meanwhile, the luminosity of the central star is determined by the total mass of the core and hydrogen envelope. Since $M_{\rm core}+M_e \sim M_{\rm core}$, the luminosity remains almost constant during this stage. Thus, the central star evolves horizontally in the H-R diagram, eventually exhausting the hydrogen envelope. Then, the luminosity and temperature start to drop, and the central star evolves toward the white dwarf phase.

The Paczyński models are improved by several authors (e.g., Blöcker, 1995; Schönberner, 1981). Figure 1.6 shows the evolutionary tracks of PNe in the H-R diagram (Blöcker, 1995). The solid and dashed lines are the tracks of 0.605 and $0.625\,M_\odot$ core stars, respectively, which evolve from $3\,M_\odot$ stars on the main sequence. The dotted line shows the track of a $0.696\,M_\odot$ core star, which evolves from a $4\,M_\odot$ star on the main sequence. The numbers next to the cross symbols are the age of the PNe in units of 10^3 years. The figure suggests that the effective temperature is a good indicator of the evolutionary stages of a PN, although the actual timescale of the evolution heavily depends on the core mass.

1.2.6 Evolution of Dust Emission

As a PN evolves, the envelope expands and the central star becomes hotter. The physical conditions in the envelope, where the circumstellar dust resides, change with evolution of the PN. During the evolution from AGB stars to PNe, the systematic evolution of the dust emission is suggested (García-Lario & Perea Calderón, 2003). As the PN evolves, the envelope becomes more diffuse and distant from the central star. As the optical depth and temperature of dust grains decrease, evolution of dust emission could result (Ohsawa et al., 2012). Since the central star is extremely hot, dust grains in the envelope could be processed by hard UV radiation from the central star. The evolution of dust emission during the PN phase is an important topic.

Statistical characteristics of the mid-infrared dust emission are intensively investigated based on the spectra provided by the *Spizter*/Infrared Spectrograph (IRS). Stanghellini et al. (2007) find that the dust temperature decreases with increasing diameter and decreasing electron density for PNe in the MCs as well as PNe in the Milky Way (Stanghellini et al., 2012). Bernard-Salas et al. (2009) find a broad emission feature around 11–12 μm, tentatively attributed to SiC, which is detected more frequently in PNe in the MCs than in the Milky Way. They point out that the strength of the SiC feature systematically decreases with increasing excitation of the PN. Interestingly, Stanghellini et al. (2007) suggest that the overall appearance of the carbonaceous emission in the mid-infrared shows a systematic transition with increasing radius of the nebula. The origin of the transition in

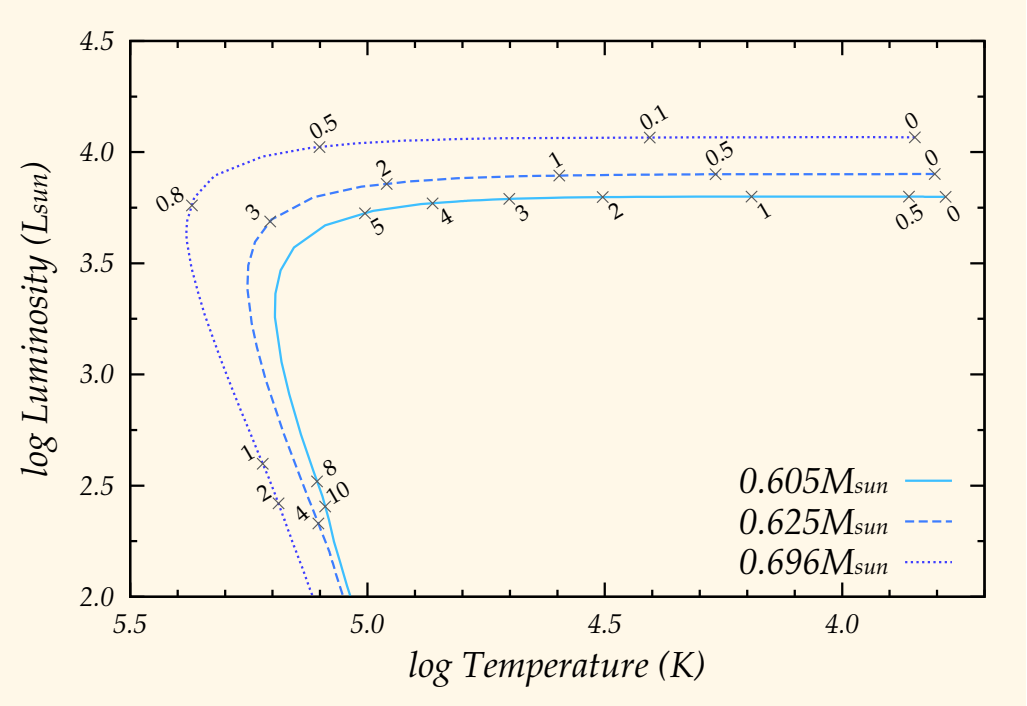

Figure 1.6 – Evolutionary tracks of 3 and 4 $M_\odot$ stars. Data are adopted from Blöcker (1995). The solid, dashed, and dotted lines shows the evolution of PNe with the core mass of 0.605, 0.625, and 0.696$M_\odot$, respectively. The numbers next to the cross denote the age of the PNe in 10^3 years.

the dust emission remains unclear. They may be attributed to the processing of dust grains, the evolution of the central star, or the dynamical evolution of the envelope. It is important to investigate what causes the apparent co-evolution of dust emission with PNe.

1.3 PAHs in Planetary Nebulae

1.3.1 Characteristics of PAHs in PNe

PNe are surrounded by circumstellar materials, which may contain PAHs if the nebula is carbon-rich (C-rich). The central star is hot enough to excite PAHs. They are a typical exhibit of PAH emission in the Universe.

As mentioned in Section 1.1.4, PNe generally show Class $\mathcal{B}$ emission. Although the radiation field in PNe is hard and intense, the ionization fraction of PAHs in PNe is relatively low among other PAH emitting objects (Galliano et al., 2008). The intensity ratio of the 12.7 to 11.3 μm features in PNe is lower than that in H II regions and galaxies, indicating that duo C—H bonds are scarce in PAHs: PAHs in PNe are generally large and compact (Hony et al., 2001).

1.3.2 Evolution of the PAH Feature in PNe

PAHs in PNe are believed to be formed in the AGB or post-AGB phases. They are finally ejected into interstellar space. PAHs are exposed to different physi-

cal conditions in the different phases. The PAH features are expected to show a systematic transition from post-AGB to PN phases.

Sloan et al. (2007) investigate the PAH features in Galactic post-AGB stars. They measure the peak wavelength of the 11.3 μm PAH feature and find that the Class $\mathcal{C}$ 11.3 μm feature evolves to the $\mathcal{A}$ or $\mathcal{B}$ feature along with evolution of the central star. They propose that the amount of aliphatic components in PAHs decreases due to UV processing, leading to a transition from Class $\mathcal{C}$ to $\mathcal{A}$ or $\mathcal{B}$. Geballe et al. (1992) find that the intensity ratio of the 3.4 to the 3.3 μm feature is quite large in some post-AGB stars compared to those generally seen in PNe. This result suggests that the amount of aliphatic components in PAHs changes along with the evolution from post-AGB stars to PNe. Recently, (Matsuura et al., 2014) investigate the PAH features of post-AGB stars in the LMC with *Spitzer*. Their results confirm that the peak wavelength of the 7–8 μm feature systematically changes along with the stellar effective temperature.

Although there are many studies on the evolution of the PAH features during the post-AGB phase or in the transition from the post-AGB to the PN phase (e.g., Matsuura et al., 2014; Sloan et al., 2007), the evolution of the PAH emission during the PN phase remains to be investigated. PAHs in PNe will be ejected into interstellar space. It is important to investigate the evolution of the PAH features during the PN phase for better understanding of the PAH transition between Class $\mathcal{A}$ and $\mathcal{B}$. The PAH features in PNe should be investigated in terms of the evolution of the PNe.

The PAH features around 3 μm are especially important. The PAH features around 3 μm are attributed to small-sized PAHs (Schutte et al., 1993). The carriers of the 3.3 μm features may be sensitive to processing of PAHs. The 3.4 μm feature is important for investigating the amount of aliphatic components in PAHs. By measuring PAH emission around 3 μm, we can observationally constrain the processing of PAHs during the PN phase.

1.4 This Thesis...

As mentioned in Section 1.1, the PAH features are observed in a variety of objects and PAHs are considered to be common dust grain species in the Universe. PAHs are believed to be formed around AGB and post-AGB stars. However, the PAH features are rarely observed in AGB stars. By investigating whether PAHs could be formed in the AGB phase, we can constrain the physical environments of PAH formation. PAH formation around AGB stars should be observationally confirmed. The spectral profile of the PAH features systematically changes from evolved stars to interstellar space, while the origin of the PAH emission classes is not identified. Investigating the physical conditions along with the transition of the PAH features from Class $\mathcal{B}$ to $\mathcal{A}$ is important.

The PAH features are frequently observed in PNe. Since PNe evolve from AGB stars, the PAH features in PNe may be helpful to investigate the sign of PAH formation in the AGB phase. PAHs in PNe are ejected into interstellar space after the PN phase. The transition of the PAH emission class from Class $\mathcal{B}$ to $\mathcal{A}$ can be observed during the PN phase. Investigation of the PAH features in PNe

along with PN evolution may be useful to identify the origin of the PAH emission classes. The effective temperature of the central star can be used as an indicator of the evolutionary phase of PNe. Although the evolutionary timescale depends on the core mass, PNe with the PAH features are expected to be carbon-rich and their core mass should be limited to a narrow range (e.g., Iben & Renzini, 1983). The limited core mass range of carbon-rich PNe is observationally confirmed by Stanghellini et al. (2012) based on *Spitzer* observations. PNe are suitable laboratories for addressing the two unsolved problems on PAHs: whether PAHs are formed in the AGB phase and what is the origin of the PAH emission class.

This research is intended to answer the questions above by investigating the variation of the PAH features in terms of the evolution of PNe. The near- to mid-infrared continuous spectrum of PNe is essential to achieve our scientific goals, while the near-infrared spectrum of PNe has not been provided with a sufficient signal-to-noise ratio. The Infrared Camera (IRC) onboard Infrared Astronomy Satellite *AKARI* enables us to obtain the 2–5 μm spectrum of Galactic PNe with a high sensitivity of ∼10 mJy. For the first time, the evolution of the PAH features during the PN phase is investigated based on the near- to mid-infrared continuous spectrum.

This paper is organized as follows: The instruments we used are described in Chapter 2. The 2–5 μm infrared spectral catalog is compiled for more than 70 Galactic PNe. Chapter 3 describes characteristics of the catalog. A statistical view of the near-infrared spectra of the PNe is discussed in Chapter 4. We combine the near-infrared spectra with the mid-infrared counterparts provided by *Spitzer* and investigate the evolution of the PAH features during the PNe phase in Chapter 5. Finally, the paper is summarized in Chapter 6.

Chapter 2
Instruments

This chapter introduces the instruments used in the paper, the Infrared Camera (IRC) onboard Infrared Astronomy Satellite *AKARI* and the Infrared Spectrograph (IRS) onboard the *Spitzer Space Telescope*. The 2.5–5.0 and 5.5–14.0 μm spectra of Galactic PNe were obtained with the *AKARI*/IRC and *Spitzer*/IRS, respectively. This chapter summarizes the characteristics of these instruments.

2.1 *AKARI*/Infrared Camera

2.1.1 Infrared Astronomy Satellite *AKARI*

AKARI was the first Japanese astronomical infrared satellite and the second Japanese space mission for infrared astronomy (Murakami et al., 2007). *AKARI* was developed by the JAXA/ISAS[*1] and collaborators. It was launched on February 21, 2006 (UT) by JAXA's M-V rocket. It orbited around the earth in a Sun-synchronous polar orbit. The altitude of the orbit was about 700 km and the period was about 100 minutes. *AKARI* was cooled by 170 liters of liquid helium and mechanical cryostat. This system enabled *AKARI* to observe in the mid- and far-infrared with high sensitivity. The liquid helium was exhausted on August 26, 2007. After that, only observations in the near-infrared were carried out (hereafter, *Phase 3*). Scientific observations with *AKARI* were finished in June, 2012 and *AKARI* was successfully turned off on November 24, 2012.

AKARI is equipped with a 68.5 cm mirror with Ritchey-Chretien reflection optics. Two scientific instruments were installed on-board *AKARI*, the Far-infrared Surveyor (FIS) and the Infrared Camera (IRC). The FIS has two 2-dimensional arrays and obtains images in four far-infrared bands at around 65, 90, 140, and 165 μm. A Fourier-transform spectrometer is also installed in the FIS. The IRC is a near- and mid-infrared camera and spectrometer. It covers 1.8–26 μm with three channels (NIR, MIR-S, and MIR-L). Nine broad band filters were installed in the IRC. The IRC was also capable of low-resolution ($R \sim 20$–100) spectroscopy.

[*1] Japan Aerospace Exploration Agency/Institute of Space and Astronautical Science

Only the NIR-channel (1.8–5.5 μm) was available for Phase 3 observations.

The *AKARI* mission was intended to obtain all-sky images in the mid- and far-infrared. AKARI all-sky survey data are superior in sensitivity, spectral coverage and spatial resolution to the previous all-sky infrared mission carried out by *IRAS*[*2]. The results were published as the AKARI FIS Bright Source Catalog (Yamamura et al., 2010) and AKARI IRC Point Source Catalog (Ishihara et al., 2010a,b). As well as the all-sky survey, *AKARI* carried out pointed observations. About 5 000 pointed observations were carried out before the liquid helium was exhausted.

2.1.2 Infrared Camera (IRC)

Data used in Section 3, 4, and 5 were obtained with the *AKARI*/IRC during Phase 3. Since the observations were carried out post-helium exhaustion, only the NIR-channel was used. In this section, the general characteristics of the *AKARI*/IRC are described, followed by details of the IRC NIR-channel.

The IRC is originally designed for deep imaging observations in the pointed observation mode. The field of view of the IRC is about $10' \times 10'$. The low-resolution slit and slit-less spectroscopy are available. The latter is suitable for multi-object spectroscopic observations. The three different channels, NIR, MIR-S, and MIR-L, cover the 1.8–5.5, 4.6–13.4, and 12.6–26.5 μm range, respectively. Each channel has three broad-band imaging filters and the capability of low-resolution spectroscopy. The NIR and MIR-S channels have two dispersion elements, while the MIR-L channel has one.

Figure 2.1 shows the field of view of the NIR channel. The pixel scale is $1\farcs46 \times 1\farcs46$. There are four regions (N/Nc, Ns, Np, and Nh). The N/Nc region is used for imaging and multi-object slit-less spectroscopy. The Ns and Nh are used for slit spectroscopy. The Np is a $1' \times 1'$ region prepared for slit-less spectroscopy of point sources. Spectroscopy in the Np-window has a great advantage in that it is not affected by slit efficiency. Three broad-band filters (N2, N3, and N4) and two dispersion elements (NP and NG) are incorporated into the NIR channel. Their specifications are summarized in Table 2.1. The relative response functions of the imaging filters and the NG grism are shown in Figure 2.2 together with those of the *WISE*[*3] W1 and W2 filters (Wright et al., 2010)[*4].

Table 2.1 – IRC Filters and Dispersion Elements

Name	Type	Wavelength (μm)	Dispersion (μm/pix)
N2	filter	1.9–2.8	···
N3	filter	2.7–3.8	···
N4	filter	3.6–5.3	···
NP	prism	1.8–5.5	0.06 at 3.5 μm
NG	grism	2.5–5.0	0.0097

[*2] *Infrared Astronomical Satellite*

[*3] *Wide-field Infrared Survey Explorer*

[*4] available at `http://wise2.ipac.caltech.edu/docs/release/allsky/expsup/`

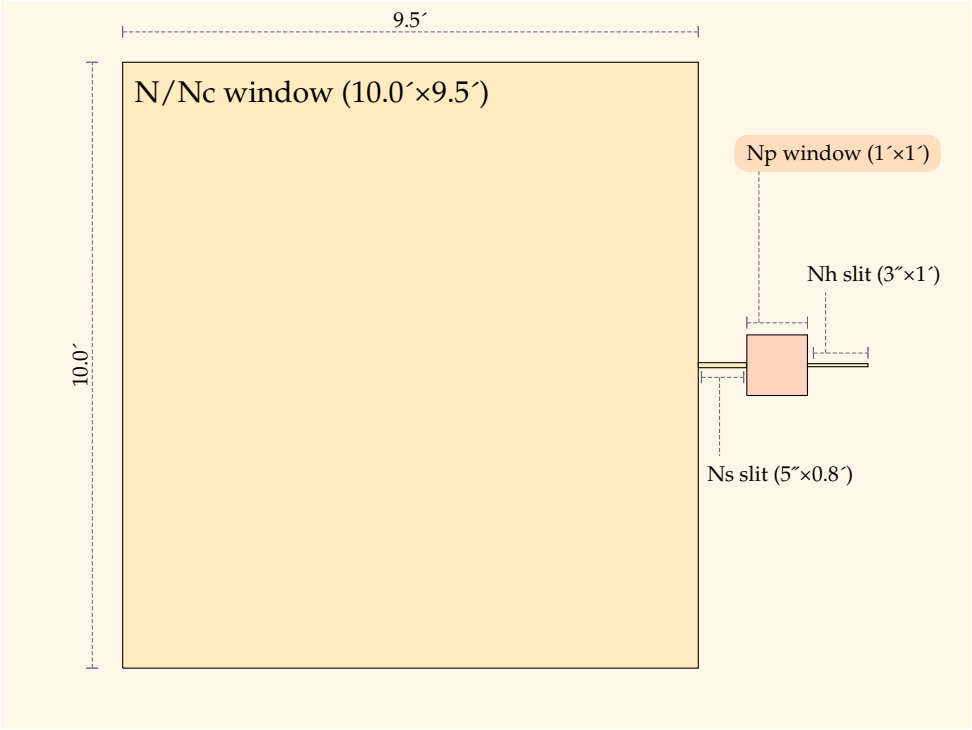

Figure 2.1 – Field of view of the *AKARI*/IRC NIR-channel. It has four regions, N/Nc-window, Ns-slit, Np-window, and Nh-slit from left to right (*see* text).

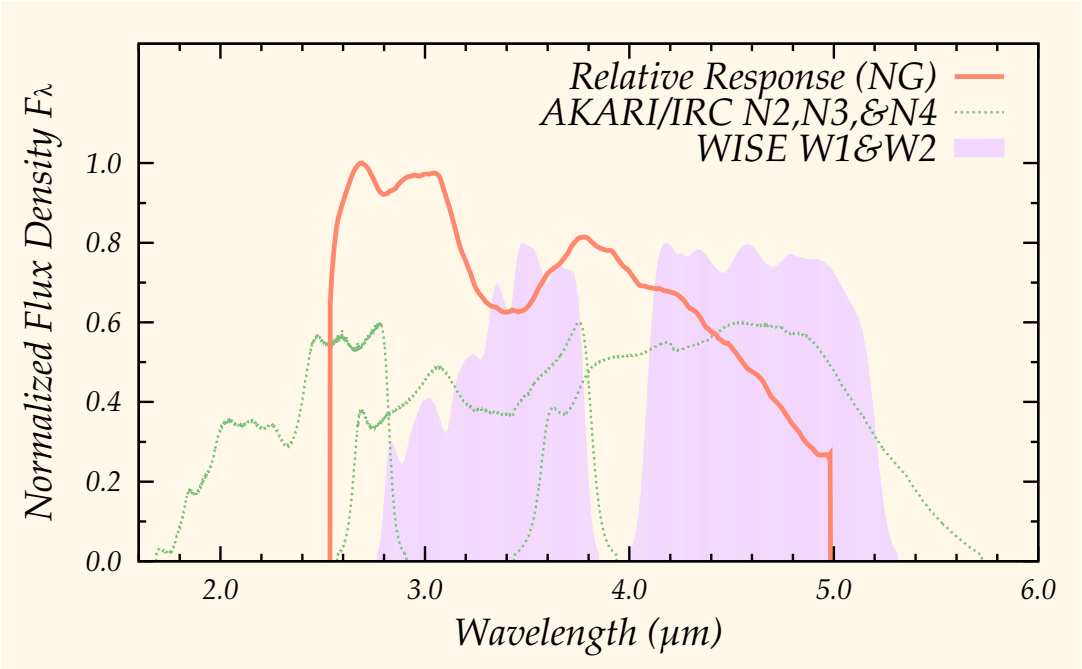

Figure 2.2 – Relative spectral response functions. The solid line shows the RSRF of the NG grism. The dotted lines are the RSRF of the imaging filters: N2, N3, and N4, respectively, from left to right. The filled regions show the RSRF of the WISE W1 (left) and W2 (right) filters.

We obtained near-infrared spectra with the NG grism in the Np-window in Phase 3. The full-width half maximum (FWHM) of the point spread function (PSF) for the IRC was about 4".7. The achieved spectral resolution (R[*5]) was about 120 at 3.6 μm (Ohyama et al., 2007). Observations were performed along with the Astronomical Observation Templates. The IRC spectroscopy mode consisted of four frames of spectroscopic images, then one image in the N3 filter, and lastly another five spectroscopic images. The last two frames were sometimes taken during maneuver and were not used for analysis. Every frame consisted of short (4.58 sec) and long (44.41 sec) exposures. Short exposure spectra were used to replace pixels saturated during the long exposure. The 5σ detection limit for point sources is about 2 mJy. The saturation limit is about 10 Jy.

2.2 *Spitzer*/Infrared Spectrograph

2.2.1 *Spitzer Space Telescope*

Spitzer Space Telescope, NASA's Great Observatory for infrared astronomy, was launched on August 25, 2003 and operated by Jet Propulsion Laboratory at California Institute of Technology. It consisted of a 85 cm-diameter telescope and three scientific instruments. The telescope was cooled down to a cryogenic temperature by liquid helium and able to observe in the mid- and far-infrared with a high sensitivity. *Spitzer* utilized an Earth-trailing solar orbit allowing it to stay cooler, compared to a low Earth orbit. Thanks to the unique orbit, *Spitzer* required only 170 liters of liquid helium to cool itself for five years. The Infrared Array Camera (IRAC) is an instrument for near- and mid-infrared (3–8 μm) imaging with four broad band filters. The Infrared Spectrograph (IRS) has a capability of mid-infrared spectroscopy in the 5.2–38 μm region with low (R~60–130) and moderate (R~600) spectral resolutions. The Multiband Imaging Photometer for *Spitzer* (MIPS) obtains images at 24, 70, 160 μm. It also has a capability of spectroscopy between 55 and 95 μm. Five and a half years after launch, *Spitzer* ran out of coolant and started its warm mission. Only the near-infrared imaging at 3.6 and 4.5 μm with the IRAC was available during this phase. Spitzer obtained a lot of scientific data and most of them are available as post-calibrated data in the *Spitzer* Heritage Archive[*6] (SHA).

2.2.2 Infrared Spectrograph (IRS)

In Section 5, we utilized the data obtained by the *Spitzer*/IRS. We summarize the basic characteristics of the IRS (Houck et al., 2004). It consists of four separate modules: Short-Low (SL), Short-High (SH), Long-Low (LL), and Long-High (LH). The SL and LL modules are intended for low-resolution spectroscopy, while the SH and LH offer moderate-resolution spectroscopy with a cross-dispersed echelle design. The wavelength coverage and resolving powers of the modules are listed in Table 2.2. The IRS obtains spectra in either Staring or Mapping mode. Imaging

[*5] R is the resolving power defined by $\lambda/\delta\lambda$, where $\delta\lambda$ is the smallest scale resolved at λ.

[*6] `http://sha.ipac.caltech.edu/applications/Spitzer/SHA/`

Table 2.2 – IRS Wavelength Coverage and Resolving Power

Name	Wavelength (μm)	Resolving Power
Short-Low (SL)	5.2–8.7 (2nd & bonus order)	60–127
	7.4–14.5 (1st order)	61–120
Long-Low (LL)	14.0–21.3 (2nd & bonus order)	57–126
	19.5–38.0 (1st order)	58–112
Short-High (SH)	9.9–19.6	~600
Long-High (LH)	18.7–37.2	~600

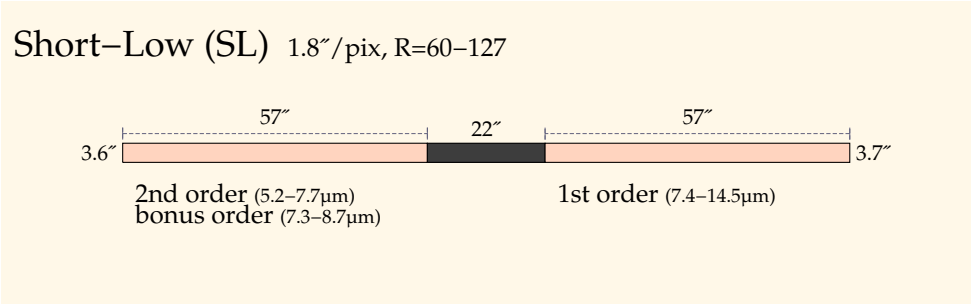

Figure 2.3 – Schematic view of the IRS SL-module slits.

observations are also available in two broad band filters (13–18 and 18–26 μm), which are usually used for the acquisition of the target and accurately place it on the intended slit.

The data obtained with the SL module are used in Section 5. The characteristics of the SL module are summarized in detail. The SL module covers the spectral range from 5.2 to 14.5 μm with $R = 60$–128 in two orders. The SL module has two slits as shown in Figure 2.3. When the object is set on the right slit, the light is filtered by the 7.5–15 μm band-pass filter and diffracted by the grating in the first order. After passing through the left slit, the light is filtered by the 5–7.5 μm band-pass filter and diffracted by the grating in the second order. A small spectral segment covering the 7.3–8.7 μm region is also produced. The overlapped segment is used as an aid in connecting the first and second order spectra. The 1σ point source continuum sensitivity for the Staring mode is about 0.2 mJy at 10 μm for 60-second integration. The saturation limit for the shortest exposure is about 5 Jy at 10 μm. The SHA provides calibrated datasets (Post Basic Calibrated Data, PBCD), which contain the spectra smoothly connected between the first and second order.

Chapter 3

Near-Infrared Spectral Atlas of Galactic Planetary Nebulae

For more than 70 Galactic planetary nebulae (PNe), 2–5 μm low-resolution (R∼100) spectra were obtained with the *AKARI*/IRC. The observations were carried out as part of the Phase 3 Open Time Program "Near-Infrared Spectroscopy of Planetary Nebulae" (PNSPC). The $1' \times 1'$ spectroscopy window installed in the IRC enabled us to obtain near-infrared spectra without any flux loss, due to the slit efficiency. The observed targets include 73 PNe, 3 evolved stars, and 1 compact HII region. A spectral catalog is produced from the PSPC observations. The spectra show several emission features including hydrogen recombination lines and the 3 μm PAH features. The catalog provides unique information for the interpretation of near-infrared emission of from PNe. In this chapter, the details of the observations and characteristics of the catalog are described.

3.1 Introduction

PNe are a late stage of the low- and intermediate-mass stellar evolution. They are surrounded by rich circumstellar materials (CSMs) ejected in the AGB phase. These CSMs are eventually injected into the interstellar medium and become ingredients of the next-generation star-forming activity. Investigating the evolution and processing of CSMs of PNe is important to understand the chemical evolution of galaxies.

Emission from CSMs generally appears in the infrared because of their low or intermediate temperatures. Observations in the infrared is important to investigate the CSM. Spectroscopy in the infrared is especially fruitful for studying CSM characteristics. Specific emission features of dust grains (e.g., PAHs and silicates) appear in the near- to mid-infrared (∼3–40 μm). There are several fine-structure lines as well as recombination lines in the infrared, which are used to diagnose the electron density and temperature of the nebulae.

Infrared spectroscopy of PNe has been intensively performed with space ob-

servatories because ground-based observations are constrained by heavy atmospheric absorption. Although their spectral resolution is limited, space observatories have the unique ability to take continuous infrared spectra. Volk & Cohen (1990) obtain 7–23 μm low-resolution spectra of 170 Galactic PNe with *IRAS*. The SWS and LWS[*1] on-board *ISO* cover 2.5–45 and 45–197 μm, respectively. A lot of emission lines are identified and the physical conditions of the circumstellar nebulae are investigated (e.g., Bernard-Salas & Tielens, 2005; Pottasch & Bernard-Salas, 2006). The Infrared Spectrograph (IRS) on-board *Spitzer* space telescope covers 5.5–40 μm. Stanghellini et al. (2012) obtain 157 spectra of Galactic compact PNe and investigate their dust emission. Spectra of PNe in the Magellanic Clouds are also obtained with the IRS (Bernard-Salas et al., 2009, 2008; Stanghellini & Haywood, 2010) thanks to its high sensitivity. The 2.5–5.0 μm wavelengths are covered by the *ISO*/SWS. The SWS obtained spectra of 85 Galactic PNe. However, a few of them have sufficient signal-to-noise ratio in the 2.5–5.0 μm because of its low sensitivity. The Infrared Camera (IRC) on-board the *AKARI* satellite has the capability to obtain a 2.5–5.0 μm spectrum with high sensitivity.

The *AKARI*/IRC obtained 2.5–5.0 μm spectra of Galactic PNe as part of the PNSPC program. Near-infrared spectra of 73 PNe, 3 evolved stars, and 1 HII region were obtained. The data were compiled into a near-infrared spectral catalog. In this chapter, we introduce the details of the observations and the characteristics of the catalog. This chapter is organized as follows: Detailed information about the observations is shown in Section 3.2. Section 3.3 describes the reduction procedures and the method to extract the spectra. The measurement of the intensity of spectral features and the format of the compiled catalog are given in Section 3.4. The spectra are investigated in comparison with observations with other facilities in Section 3.5. We summarize the chapter in Section 3.6.

3.2 Observations

3.2.1 Target Selection

The observed targets were selected by Takashi Onaka, the principal investigator of the PNSPC program, from the Strasbourg-ESO Catalogue of Galactic Planetary Nebulae (Acker et al., 1992) based on the limiting magnitude of the IRC and their angular size. The sensitivity of the IRC in the spectroscopy is ∼10 mJy in the 2–5 μm, while the IRC saturates when the flux density is larger than 10 Jy. The objects with the K-band magnitude of between 5 and 13 were selected as the targets. The observations were carried out in the $1' \times 1'$ Np-window. Since the Np-window provides a kind of slit-less spectroscopy, compact objects are preferred to avoid degrading the spectral resolution. The targets were selected with a criterion that the radius in the optical is smaller than $5''$, which is comparable to the size of the PSF of the IRC ($\sim 3''$). Finally, 77 objects were selected and their spectra were successfully obtained. Their PN G id, name, *AKARI* observation id, and coordinates are listed in Table 3.1.

[*1] Long-Wave Spectrometer
[*2] Degitized Sky Survey

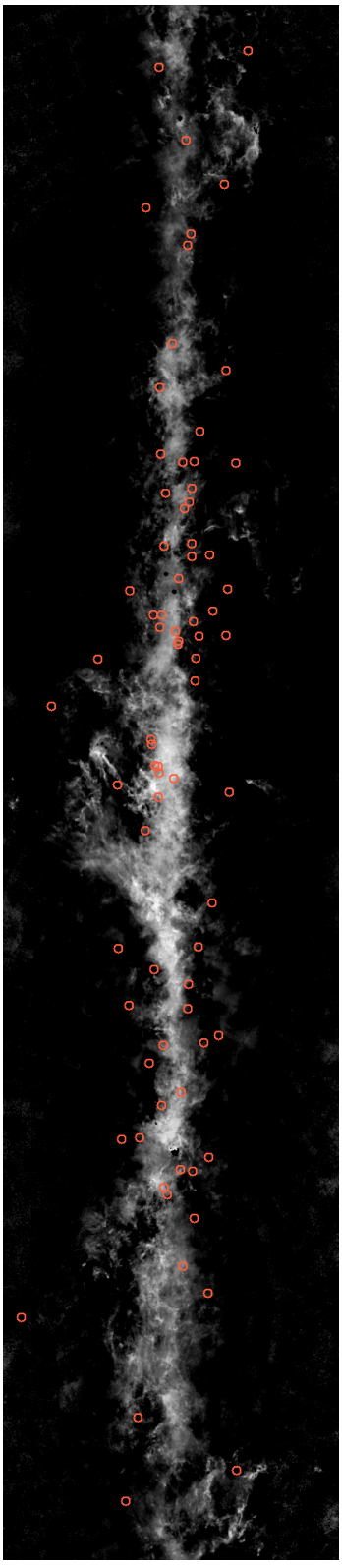

Figure 3.1 – Distribution of the observed PNe are shown by the circle symbols, overlaid on the extinction map in the Galactic coordinates created based on DSS[*2](Dobashi et al., 2005a). The map covers $l \simeq -180$–180° and $b \simeq -40$–40°.

The sixth column of Table 3.1 shows the object type in the Simbad[*3] Astronomical Database. According to Simbad, the observed targets include 73 PNe, 3 evolved stars, and 1 compact HII region. Although four of them are not categorized as PNe, they are included in the catalog.

The target selection is free from the chemistry and dust species of the nebula. The catalog is considered to have only a minor bias in terms of chemical abundance and dust composition. The objects were selected by their size and thus may be may be biased toward young PNe since PNe expand as they evolve. The detailed characteristics of the sample are discussed in Section 3.5.

Each object was observed either once, or twice, yielding either nine or eighteen frames. Some frames were not usable due to cosmic ray hist or unstable pointing during the exposure. When there are saturated pixels, their counts were scaled and replaced by the corresponding short-exposure frames. The effective total integration time was different for each object.

3.2.2 Hβ Intensity

The intensity of the hydrogen recombination line Hβ at 4861 Å was obtained from Cahn et al. (1992) and Acker et al. (1991). The intensity of Hβ was compared to that of Brackett-α at 4.051 μm and used to estimate the extinction towards the object.

3.3 Data Reduction

The basic data reduction, including dark frame subtraction, linearity correction, saturation masking, flat fielding, and subtracting background fluxes, was carried out with the IRC Spectroscopy Toolkit for Phase 3 (Version 20111121)[*4]. Some frames were affected by cosmic rays. The pixels affected by cosmic rays were masked by hand. There were a few frames showing a blurred spectrum caused by an abrupt telescope movement during the exposure. These frames were excluded from image stacking.

Most of the objects were observed twice, but the official toolkit does not provide a function to combine frames from different observations. Thus, we performed image stacking separately from the toolkit. All the frames were matched in order to maximize the correlation between the frames, before combination by median stacking.

One-dimensional spectra were extracted with an aperture wide enough to collect the fluxes from every object ($\gtrsim$10 pixels). Some objects were located in a crowded region, and a sufficiently wide aperture was difficult to use. In those cases, the contribution from nuisance objects was estimated and removed by profile fitting with a combination of Gaussian functions. A similar method is used in Noble et al. (2013).

[*3] http://simbad.u-strasbg.fr/simbad/

[*4] Available at http://www.ir.isas.jaxa.jp/ASTRO-F/Observation/DataReduction/IRC/

Table 3.1. List of the Observed Galactic Planetary Nebulae

PN G	Name	Obs. ID	RA (J2000) hh:mm:ss	DEC (J2000) dd:mm:ss	Type
002.0−13.4	IC 4776	3460003	18 : 45 : 50.7	−33 : 20 : 35.0	PN
003.1+02.9	PN Hb 4	3460005	17 : 41 : 52.8	−24 : 42 : 07.7	PN
011.0+05.8	NGC 6439	3460012	17 : 48 : 19.8	−16 : 28 : 44.0	PN
027.6−09.6	IC 4846	3460016	19 : 16 : 28.3	−09 : 02 : 37.0	PN
037.8−06.3	HD 182083	3460019	19 : 22 : 56.9	01 : 30 : 48.0	Star
038.2+12.0	PN Cn 3-1	3460020	18 : 17 : 34.0	10 : 09 : 05.0	PN
046.4−04.1	NGC 6803	3460021	19 : 31 : 16.4	10 : 03 : 21.7	PN
051.4+09.6	PN G05.4+09.6	3460022	18 : 49 : 47.6	20 : 50 : 39.5	PN
058.3−10.9	HD 193538	3460023	20 : 20 : 08.8	16 : 43 : 54.0	Star
060.1−07.7	NGC 6886	3460024	20 : 12 : 42.9	19 : 59 : 23.0	PN
060.5+01.8	Hen 2-440	3460025	19 : 38 : 08.4	25 : 15 : 42.0	PN
064.7+05.0	BD+30 3639	3460026	19 : 34 : 45.3	30 : 30 : 59.2	PN
071.6−02.3	PN M 3-35	3460027	20 : 21 : 03.8	32 : 29 : 24.0	PN
074.5+02.1	NGC 6881	3460028	20 : 10 : 52.5	37 : 24 : 41.0	PN
082.1+07.0	NGC 6884	3460029	20 : 10 : 23.7	46 : 27 : 39.0	PN
082.5+11.3	NGC 6833	3460030	19 : 49 : 46.6	48 : 57 : 40.0	PN
089.3−02.2	PN M 1-77	3460031	21 : 19 : 07.2	46 : 18 : 48.0	PN
089.8−05.1	IC 5117	3460032	21 : 32 : 31.0	44 : 35 : 47.7	PN
095.2+00.7	PN K 3-62	3460033	21 : 31 : 50.2	52 : 33 : 52.0	PN
100.6−05.4	IC 5217	3460034	22 : 23 : 55.7	50 : 58 : 00.0	PN
111.8−02.8	PN Hb 12	3460035	23 : 26 : 14.9	58 : 10 : 53.0	PN
211.2−03.5	PN M 1-6	3460036	06 : 35 : 45.1	−00 : 05 : 38.0	PN
232.8−04.7	PN M 1-11	3460037	07 : 11 : 16.7	−19 : 51 : 04.0	PN
235.3−03.9	PN M 1-12	3460038	07 : 19 : 21.5	−21 : 43 : 54.3	PN
258.1−00.3	Hen 2-9	3460039	08 : 28 : 28.0	−39 : 23 : 40.0	PN
264.4−12.7	Hen 2-5	3460040	07 : 47 : 20.0	−51 : 15 : 03.4	PN
268.4+02.4	PN PB 5	3460042	09 : 16 : 09.6	−45 : 28 : 42.8	PN
283.8+02.2	PN My 60	3460044	10 : 31 : 33.4	−55 : 20 : 50.5	PN
285.6−02.7	PN My 59	3460045	10 : 23 : 09.1	−60 : 32 : 42.3	PN
291.6−04.8	IC 2621	3460046	11 : 00 : 20.0	−65 : 14 : 57.8	PN
294.9−04.3	Hen 2-68	3460047	11 : 31 : 45.4	−65 : 58 : 13.7	PN
296.3−03.0	Hen 2-73	3460048	11 : 48 : 38.2	−65 : 08 : 37.3	PN
304.5−04.8	IC 4191	3460051	13 : 08 : 47.3	−67 : 38 : 37.6	PN
307.2−09.0	Hen 2-97	3460052	13 : 45 : 22.4	−71 : 28 : 55.7	PN
307.5−04.9	PN MyCn 18	3460053	13 : 39 : 35.1	−67 : 22 : 51.7	PN
315.1−13.0	Hen 2-131	3460054	15 : 37 : 11.2	−71 : 54 : 52.9	PN
315.4+09.4	V* V852 Cen	3460055	14 : 11 : 52.1	−51 : 26 : 24.1	Mira
320.9+02.0	Hen 2-117	3460056	15 : 05 : 59.2	−55 : 59 : 16.5	PN
321.0+03.9	Hen 2-113	3460057	14 : 59 : 53.5	−54 : 18 : 07.5	PN
322.5−05.2	NGC 5979	3460060	15 : 47 : 41.2	−61 : 13 : 05.6	PN
323.9+02.4	Hen 2-123	3460061	15 : 22 : 19.4	−54 : 08 : 13.1	PN
324.8−01.1	Hen 2-133	3460062	15 : 41 : 58.8	−56 : 36 : 25.6	PN
325.8−12.8	Hen 2-182	3460063	16 : 54 : 35.2	−64 : 14 : 28.4	PN
326.0−06.5	Hen 2-151	3460064	16 : 15 : 42.3	−59 : 54 : 01.0	PN
327.1−01.8	Hen 2-140	3460065	15 : 58 : 08.1	−55 : 41 : 50.3	PN
327.8−01.6	Hen 2-143	3460066	16 : 00 : 59.1	−55 : 05 : 39.7	PN
331.1−05.7	HD 149427	3460067	16 : 37 : 42.7	−55 : 42 : 26.5	PN
331.3+16.8	NGC 5873	3460068	15 : 12 : 50.8	−38 : 07 : 32.0	PN

Table 3.1 (cont'd)

PN G	Name	Obs. ID	RA (J2000) hh:mm:ss	DEC (J2000) dd:mm:ss	Type
336.3−05.6	Hen 2-186	3460069	16 : 59 : 36.1	−51 : 42 : 08.4	PN
350.9+04.4	PN H 2-1	3460070	17 : 04 : 36.2	−33 : 59 : 18.0	PN
355.9+03.6	PN H 1-9	3460075	17 : 21 : 31.8	−30 : 20 : 48.0	PN
356.1+02.7	PN Th 3-13	3460076	17 : 25 : 19.2	−30 : 40 : 41.0	PN
357.6+02.6	PN H 1-18	3460082	17 : 29 : 42.7	−29 : 32 : 50.0	PN
358.9−00.7	PN M 1-26	3460085	17 : 45 : 57.7	−30 : 12 : 01.0	PN
043.1+03.8	PN M 1-65	3460093	18 : 56 : 33.6	10 : 52 : 12.0	PN
052.2−04.0	PN M 1-74	3460094	19 : 42 : 18.7	15 : 09 : 09.0	PN
093.5+01.4	IRAS 21190+5140	3460095	21 : 20 : 44.7	51 : 53 : 26.1	H II
118.0−08.6	PN Vy 1-1	3460096	00 : 18 : 42.2	53 : 52 : 20.0	PN
146.7+07.6	PN M 4-18	3460097	04 : 25 : 50.8	60 : 07 : 12.7	PN
159.0−15.1	IC 351	3460098	03 : 47 : 33.0	35 : 02 : 48.9	PN
190.3−17.7	PN G190.3−17.7	3460099	05 : 05 : 34.3	10 : 42 : 23.8	PN
226.7+05.6	PN M 1-16	3460100	07 : 37 : 18.9	−09 : 38 : 50.0	PN
278.6−06.7	PN My 47	3460101	09 : 19 : 27.5	−59 : 12 : 00.3	PN
292.8+01.1	Hen 2-67	3460102	11 : 28 : 47.4	−60 : 06 : 37.3	PN
320.1−09.6	Hen 2-138	3460103	15 : 56 : 01.7	−66 : 09 : 09.2	PN
342.1+27.5	PN Me 2-1	3460104	15 : 22 : 19.3	−23 : 37 : 32.0	PN
349.8+04.4	PN M 2-4	3460105	17 : 01 : 06.2	−34 : 49 : 38.0	PN
000.3+12.2	IC 4634	3460107	17 : 01 : 33.6	−21 : 49 : 33.5	PN
086.5−08.8	PN G086.5−08.8	3460114	21 : 33 : 08.3	39 : 38 : 09.7	PN
123.6+34.5	IC 3568	3460115	12 : 33 : 06.8	82 : 33 : 50.1	PN
166.1+10.4	IC 2149	3460116	05 : 56 : 23.9	46 : 06 : 17.2	PN
194.2+02.5	PN G194.2+02.5	3460117	06 : 25 : 57.2	17 : 47 : 27.3	PN
221.3−12.3	IC 2165	3460118	06 : 21 : 42.7	−12 : 59 : 14.0	PN
285.4−05.3	IC 2553	3460120	10 : 09 : 20.8	−62 : 36 : 48.5	PN
285.7−14.9	IC 2448	3460121	09 : 07 : 06.3	−69 : 56 : 30.6	PN
305.1+01.4	Hen 2-90	3460122	13 : 09 : 36.4	−61 : 19 : 35.6	PN
312.6−01.8	Hen 2-107	3460123	14 : 18 : 43.3	−63 : 07 : 10.1	PN

In some observations, the target and the nuisance object were aligned in the direction of dispersion. In such a case, the spectra of these objects fully overlapped with each other and it was impossible to retrieve the target's spectrum by profile fitting (*see* Figure 3.2). To remove the contamination from the nuisance object, we developed a method to estimate the amount of contamination. The method basically follows the procedure used in Sakon et al. (2008). We assumed that the nuisance objects were stars since their spectra did not show any significant spectral features. Their 2.5–5.0 μm spectra ($\tilde{f}_\nu$) were estimated from the 2MASS, *AKARI*, and *WISE* photometric data by fitting with a blackbody function. Define d as the distance between the target and the nuisance object in the direction of the dispersion in units of a pixel and δ as the pixel scale of the spectrum in units of μm pixel^{-1}. The amount of the contamination was estimated by

$$f^c_\nu(\lambda) = \frac{\tilde{f}_\nu(\lambda-\delta d)R(\lambda-\delta d)}{R(\lambda)}, \tag{3.1}$$

where $R(\lambda)$ is the spectral response function of the IRC in units of ADU mJy^{-1}. Define f^{obs}_ν as the obtained spectrum including the contamination. The decon-

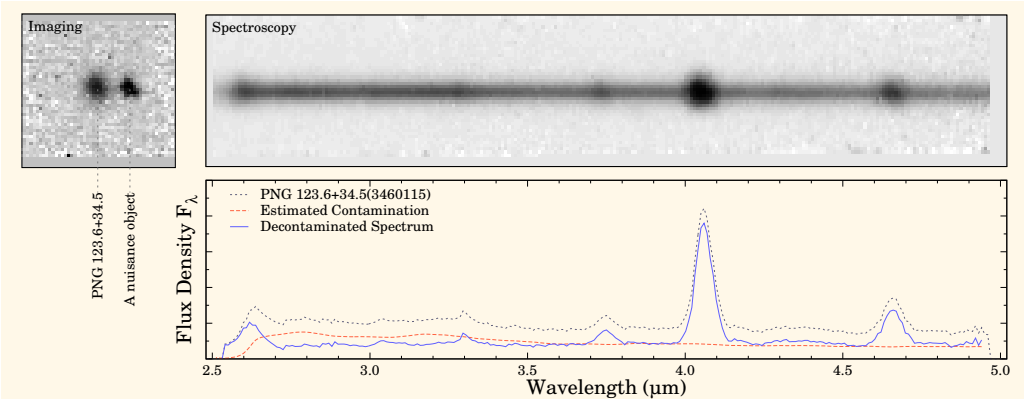

Figure 3.2 – Schematic view of decontamination. The upper left panel shows the locations of the object and the nuisance star, while the upper right panel shows the obtained spectrum. The spectrum contains the contribution from the nuisance star. The obtained spectrum is shown by the gray dotted line in the bottom panel. The red dashed line shows the estimated contribution from the nuisance star. The remaining spectrum of the PN is shown by the blue solid line.

taminated spectrum was given by $f_\nu^{obj} = f_\nu^{obs} - f_\nu^{c}$. The schematic view of the method is shown in Figure 3.2. The upper left panel shows the location of the target (PN G123.6+34.5, left) and the nuisance object (right). The direction of dispersion is from left to right. The obtained spectrum including the contamination is shown in the upper right panel. The contaminated spectrum (f_ν^{obs}) is shown by the gray dotted line in the bottom panel. The estimated contamination and decontaminated spectrum are shown by the red dashed and blue solid lines, respectively.

3.4 Results

3.4.1 Extinction

The extinction towards the object is estimated based on the intensity ratio of Hβ to Brackett-α (Brα). The intensity of Hβ is obtained from literature, while that of Brα is measured by fitting with a Gaussian function. We assume that the relative intensity of the hydrogen recombination lines is given by the ratios calculated where the nebula is totally opaque for the Lyman photons (Case B in Baker & Menzel, 1938). We adopt the Case B ratio calculated for the electron density of 10^4 cm^{-3} and the electron temperature of 10^4 K from Storey & Hummer (1995). Define $I_{H\beta}$ and $I_{Br\alpha}$ as the intensities of Hβ and Brα, respectively. The observed intensity ratio follows the relation:

$$\frac{I_{H\beta}^{obs}}{I_{Br\alpha}^{obs}} = \frac{I_{H\beta}^{0} e^{-\tau_{H\beta}}}{I_{Br\alpha}^{0} e^{-\tau_{Br\alpha}}}, \tag{3.2}$$

where I_X^{obs} and I_X^0 are the observed and intrinsic intensities of the line X, respectively, and τ_X is the extinction at the line X. We adopt the extinction curve given by Mathis (1990). From Equation (3.2), the extinction at the V-band is derived

as:

$$A_V(H\beta) = 2.39 - 0.95 \ln \left(\frac{I^{obs}_{H\beta}}{I^{obs}_{Br\alpha}} \right). \tag{3.3}$$

$A_V(H\beta)$ depends on the electron temperature and density. When the electron temperature increases to 2×10^4 K, A_V will increase by about 0.3. The variation in $A_V(H\beta)$ with the electron density is much smaller than 0.3 for the range from 10^2 to 10^6 cm^{-3}. The estimated $A_V(H\beta)$ values are included in the catalog.

3.4.2 Spectral Fitting

The intensity of the spectral features are measured by spectral fitting. The fitted function is given by a linear combination of spectral features as

$$F_\lambda(\lambda) = \left[f^{cont}_\lambda(\lambda) + f^{line}_\lambda(\lambda) + f^{dust}_\lambda(\lambda) \right] e^{-\tau(\lambda)}, \tag{3.4}$$

where f^{cont}_λ, f^{line}_λ, and f^{dust}_λ are respectively the components of continuum, line, and dust emission and $\tau(\lambda)$ is the optical depth at λ. The functional shape of $\tau(\lambda)$ is defined by interpolating the extinction curve given by Mathis (1990) with a spline curve. The amount of the extinction is taken as a free parameter.

f^{cont}_λ is given by a combination of a polynomial function and a step function. The step function, defined by the error function, is required to reproduce the sudden increase in the continuum emission at $\gtrsim$3.4 μm as mentioned in Boulanger et al. (2011). The line profile is approximated by a Gaussian function and f^{line}_λ is given by a linear combination of Gaussian functions. The emission from PAHs is included in the fitting. The profile of the PAH emission is approximated by a Lorentzian function. When the object is extended for the IRC, the effective spectral resolution is degraded. Thus, f^{dust}_λ is defined by a linear combination of Lorentzian functions convolved with the profile of the line emission. The details of the spectral profiles are described in Appendix B.

Accurately measuring the intensity of the 3.3 μm PAH feature is important. There is a hydrogen recombination line at 3.297 μm (Pfund-δ) and it is difficult to distinguish Pfund-δ from the 3.3 μm PAH feature, using the spectral resolution of the IRC. Since hydrogen recombination lines are strong in PNe, an accurate estimation of the Pfund-δ intensity is required. We assume that the relative intensity of the hydrogen recombination lines follows the Case B ratio calculated for the electron density of 10^4 cm^{-3} and the electron temperature of 10,000 K. The intensity of Pfund-δ is estimated from the intensity of other hydrogen recombination lines. The uncertainty of the estimated intensity is at most 5% even when the electron density ranges from 10^3 to 10^5 cm^{-3} and the electron temperature ranges from 5000 to 15,000 K. The intensity of the 3.3 μm PAH emission is derived by subtracting the estimated contribution from Pfund-δ.

We define the observed (decontaminated) flux density and its uncertainty as F^{obj}_λ and σ_λ, respectively. We assume that the residual $\Delta_\lambda(\lambda) = [F^{obj}_\lambda(\lambda) - F_\lambda](\lambda)$ follows the normal distribution of $\mathcal{N}(0, \sigma_\lambda(\lambda))$. The likelihood is defined as:

$$\mathcal{L} = \prod_i \frac{1}{\sqrt{2\pi}\sigma_\lambda(\lambda_i)} \exp\left[-\frac{1}{2} \left(\frac{\Delta_\lambda(\lambda_i)}{\sigma_\lambda(\lambda_i)} \right)^2 \right], \tag{3.5}$$

where λ_i is the wavelength of the i-th bin. Although we include the extinction as a free parameter, the extinction is not well defined by maximizing Equation (3.5) because of an insufficient signal-to-noise ratio (*see* Appendix A). To make the fitting stable, we put a constraint on the extinction in such a way that the probability density function of A_V should follow

$$\mathrm{prob}(A_V) \propto \exp\left[-\frac{1}{2}\left(\frac{A_V - A_V(H\beta)}{\sigma(A_V(H\beta))}\right)^2\right], \tag{3.6}$$

where $A_V(H\beta)$ is the extinction estimated from the Hβ to Brα intensity ratio and $\sigma(A_V(H\beta))$ is its uncertainty. The parameters are derived by maximizing the product of Equations (3.5) and (3.6) with the constraint that the value of A_V and the intensity of the spectral features should be non-negative. The uncertainty of the intensity is estimated based on a parameterized bootstrap analysis.

The extinction-corrected intensity and equivalent width of the spectral features were measured. The measured spectral features are listed in Table 3.2. They are widely detected in the PNSPC sample with sufficient signal-to-noise ratio. However, it is difficult to measure the intensities of the PAH features in 3.4–3.5 μm individually because of a low spectral resolution of the IRC. Thus, the "PAH3.4" in Table 3.2 means the summation of the intensity of these features.

Table 3.2 – Measured Spectral Features

Name	Wavelength (μm)	Name	Wavelength (μm)
Brackett-α	4.051	[Mg IV]	4.49
He II	3.09	[Ar VI]	4.53
He I	3.70	H_2	3.84
He I	4.12	H_2	4.18
He I	4.30	PAH3.3	3.2–3.3
He I	4.61	PAH3.4	3.4–3.5

3.4.3 Catalog Format

The PNSPC catalog consists of three tables. One table contains the basic information of the targets, the details of the observations, the estimated extinction, and the paths to the obtained spectrum. The others are for the intensities and equivalent widths, respectively. The format of the tables are shown in Tables 3.3 and 3.4. The first table contains the PN G id, AKARI observation id, the position in the equatorial coordinates, the object type, the number of frames, the total integration time, the saturation and contamination flags, the extinction estimated from Hβ and fitting, and the path to the spectrum. The second and third tables list the measured values as well as their uncertainties.

Table 3.3 – Format of the PNSPC Catalog: Basic Information

PN G	Obs. ID	RA (J2000)	DEC (J2000)	Type	N	t_{int}	Flag	$A_V(H\beta)$			A_V(IRC)			Path
		hh : mm : ss.s	dd : mm : ss.s			sec.		mag.	mag.	mag.	mag.	mag.	mag.	
(1)	(2)	(3)	(4)	(5)	(6)	(7)	(8)	(9)	(10)	(11)	(12)	(13)	(14)	(15)
002.0−13.4	3460003	18 : 45 : 50.7	−33 : 20 : 35.0	PN	16	710.56	00	0.270	0.248	0.298	0.172	0.167	0.194	—
003.1+02.9	3460005	17 : 41 : 52.8	−24 : 42 : 07.7	PN	9	399.69	01	3.286	3.254	3.319	3.274	3.197	3.346	—
011.0+05.8	3460012	17 : 48 : 19.8	−16 : 28 : 44.4	PN	18	799.38	00	1.776	1.734	1.818	1.800	1.797	1.836	—
027.6−09.6	3460016	19 : 16 : 28.3	−09 : 02 : 37.0	PN	9	399.69	00	1.014	0.970	1.067	1.032	1.025	1.091	—
⋮	⋮	⋮	⋮	⋮	⋮	⋮	⋮	⋮	⋮	⋮	⋮	⋮	⋮	⋮

Note. — (1) PN G ID; (2) *AKARI* Obs. ID; (5) Simbad object type; (6) the number of frames; (7) the integration time; (8) the saturation and contamination flag; (9) the extinction at the V-band based on the $I_{H\beta}/I_{Br\alpha}$ ratio; (10) the lower limit of confidence interval for $A_V(H\beta)$; (11) the upper limit of confidence interval for $A_V(H\beta)$; (12) the extinction at the V-band based on the IRC spectrum; (13) the lower limit of confidence interval for A_V(IRC); (14) the upper limit of confidence interval for A_V(IRC); (15) the path to the spectrum.

Table 3.4 – Format of the PNSPC Catalog: Intensity

PN G	Brackett-α			He II(3.09μm)			He I(3.70μm)			He I(4.12μm)			He I(4.30μm)			⋯
	10^{-16}W m^{-2}			10^{-16}W m^{-2}			10^{-16}W m^{-2}			10^{-16}W m^{-2}			10^{-16}W m^{-2}			⋯
(1)	(2)	(3)	(4)	(5)	(6)	(7)	(8)	(9)	(10)	(11)	(12)	(13)	(14)	(15)	(16)	⋯
002.0−13.4	2.003	1.957	2.086	0.000	0.000	0.000	0.070	0.070	0.700	0.064	0.064	0.088	0.456	0.456	0.456	⋯
003.1+02.9	3.169	3.064	3.215	0.457	0.274	0.536	0.198	0.177	0.247	0.182	0.166	0.219	0.428	0.398	0.459	⋯
011.0+05.8	1.094	1.058	1.138	0.128	0.100	0.162	0.004	0.000	0.041	0.032	0.000	0.066	0.088	0.060	0.131	⋯
027.6−09.6	1.113	1.099	1.128	0.000	0.000	0.000	0.023	0.018	0.032	0.043	0.035	0.056	0.100	0.091	0.115	⋯
⋮	⋮	⋮	⋮	⋮	⋮	⋮	⋮	⋮	⋮	⋮	⋮	⋮	⋮	⋮	⋮	⋮

Note. — (1) PN G ID; (2) the intensity of Brackett-α; (3) the lower limit of confidence interval for Brackett-α; (4) the upper limit of confidence interval for Brackett-α; the following columns are the same as the column (2), (3), and (4).

3.5 Characteristics

3.5.1 Evaluation of the Accuracy of the Flux Density

One of the major characteristics of the PNSPC catalog is the slit-less spectroscopy in the Np-window. The spectra of the PNSPC catalog should include all the flux from the target. Since the IRC spectrum totally covers the *WISE* W1 band (Figure 2.2), we compare the PNSPC spectra with the *WISE* W1 photometry from WISE All-Sky Source Catalog (Cutri et al., 2012a) and evaluate the accuracy of the flux density. Define R^{W1} as the relative response curve of the *WISE* W1 band (per photon; Wright et al., 2010). The flux in the W1 band estimated from the IRC spectrum is defined as

$$W1(\mathrm{IRC}) = \frac{\int F_\nu^{\mathrm{obj}}(\nu) R^{W1}(\nu) \frac{d\nu}{\nu}}{\int \left(\frac{\nu_{\mathrm{iso}}}{\nu}\right)^2 R^{W1}(\nu) \frac{d\nu}{\nu}}, \tag{3.7}$$

where ν_{iso} is the isophotal frequency of the W1 band and F_ν^{obj} is the observed flux density in units of Jy. Figure 3.3 shows the estimated flux density in the W1 band against the *WISE* W1 catalog data. It confirms that the W1 flux density estimated from the IRC spectra is consistent with the *WISE* W1 data in a wide range from about 0.01 to 5 Jy. The histogram of the *AKARI* to *WISE* W1 flux ratio is shown in Figure 3.4. The ratios are distributed with the mean of 1.01 ± 0.01 and the standard deviation of 0.22 ± 0.02, suggesting that the spectra provided by the PNSPC catalog are reliable in absolute flux density.

3.5.2 Galactic Distribution of the PNSPC Samples

We investigate the bias in the distribution of the PNSPC samples. The distribution of the PNSPC samples in the Galactic coordinates is compared with that of the PNe in Acker et al. (1992). The distribution of Acker's samples are assumed to represent the distribution of all the PNe in the Milky Way. The histograms of the Galactic longitude and latitude are respectively shown in the top and bottom panels of Figure 3.5. The histograms of the PNSPC samples are shown by the blue lines with $\sqrt{N}$ Poisson errors, while the histograms of Acker's PNe are shown by the gray filled bars. The total number of Acker's PNe is 1143.

The longitude histogram of the PNSPC samples looks broader than that of Acker's PNe, while the latitude histogram of the PNSPC samples does not show a large deviation from that of Acker's PNe. We investigate the differences by Kolmogorov-Smirnov test. The values of $\chi^2_{\nu=2}$ are about 16 and 4 for the longitude and latitude, respectively. The results suggest that the deviation of the longitude is highly significant and that the PNSPC samples are biased toward the PNe in the Galactic disk.

To confirm the hypothesis, we investigated the distribution of the PNSPC samples in terms of the distance from the Galactic Center. The distance to the objects from the Sun is collected from literature. Figure 3.6 shows the distribution of

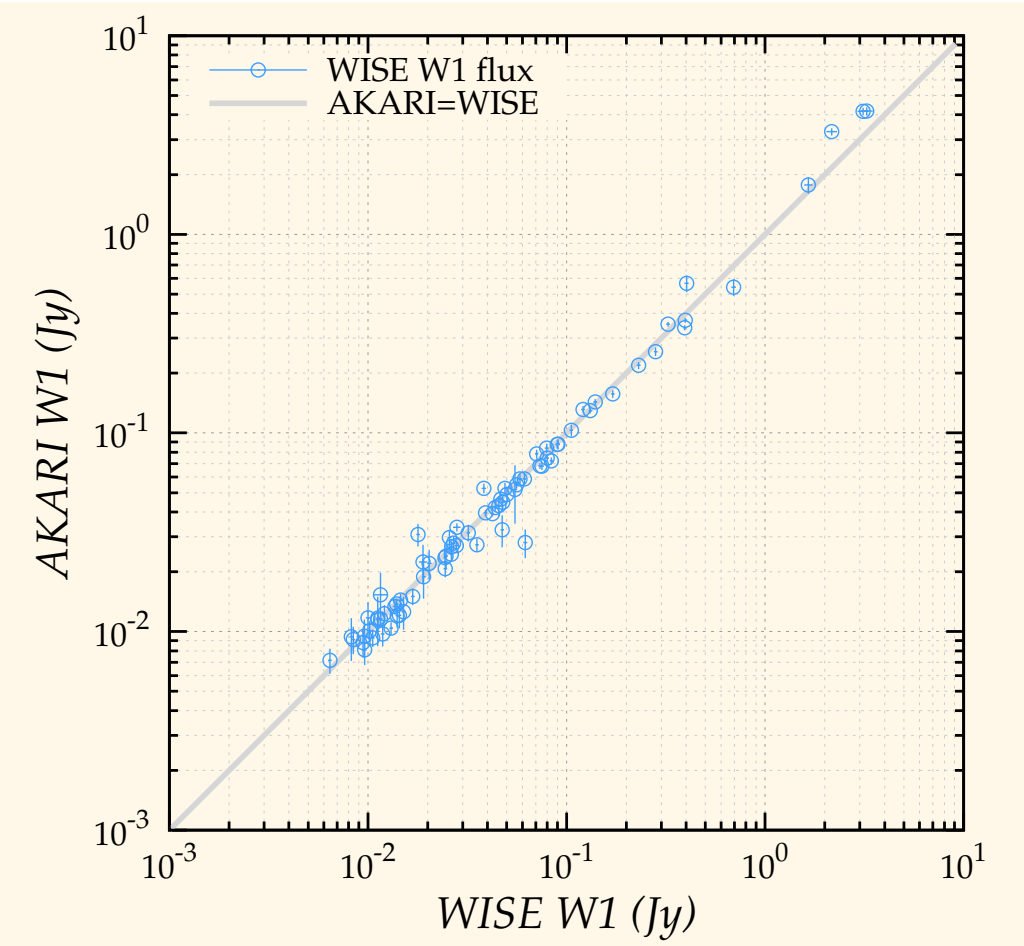

Figure 3.3 – Comparison with the *WISE* All-Sky Catalog. The horizontal axis shows the flux in the *WISE* W1 band in the *WISE* All-Sky Source Catalog, while the vertical axis shows the flux in the W1 band estimated from the *AKARI*/IRC spectrum.

the PNSPC samples in the Milky Way. Although we have to note that the uncertainty in the distance is generally quite large, Figure 3.6 clearly confirms that the PNSPC samples do not cover the PNe around the Galactic Center. The PNSPC samples thus represent the PNe in the Galactic disk.

3.5.3 Effective Temperature of the PNSPC Samples

The PNSPC samples are selected by the apparent size and they may be biased toward younger PNe. The effective temperature, which can be an indicator of the evolutionary stage of a PN, is investigated to evaluate the bias. The effective temperatures are collected from literature. The references are listed in Table 3.5. The effective temperature is estimated in several different methods. We adopt a weighted mean of the temperatures assuming the weight listed in Table 3.5. The weight is tentatively defined based on a typical uncertainty. Zanstra temperature is estimated based on H I, He I, and He II recombination lines. Only the He II Zanstra temperature is used when it is available. If not, the He I Zanstra temperature is used. The H I Zanstra temperature is only used when

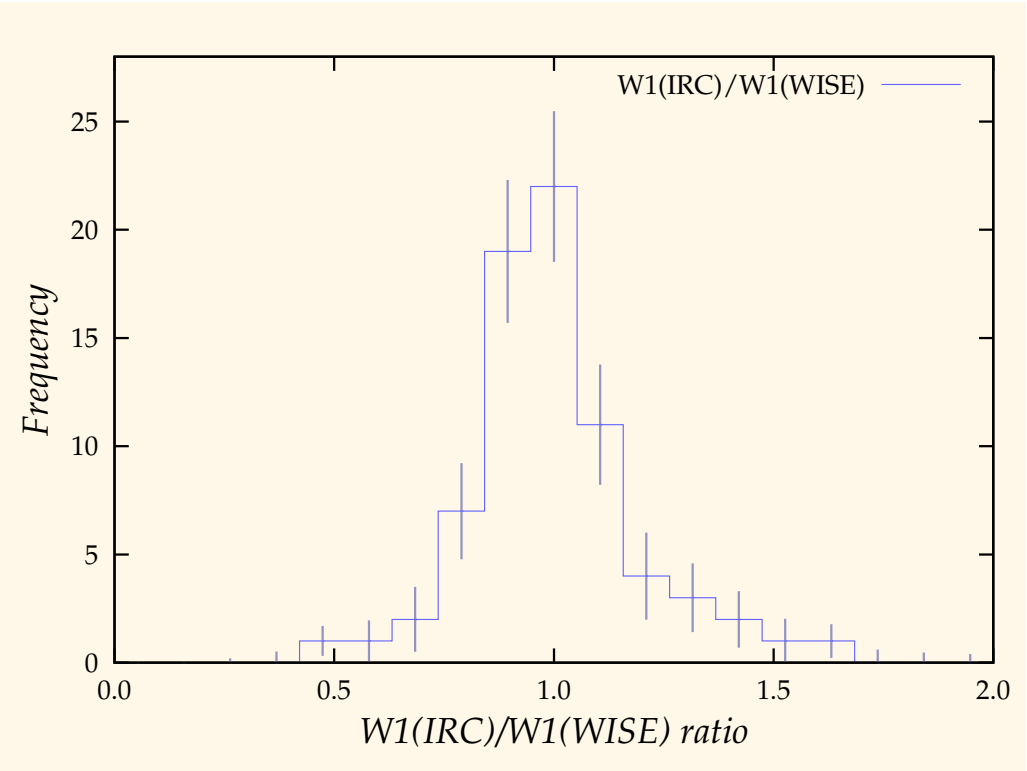

Figure 3.4 – Histogram of the ratio of the *AKARI* to *WISE* W1 band flux.

Table 3.5 – References of the Effective Temperature

Method	Source	Weight
UV color	GN90[a]	1
Stoy & Energy Balance	Lu01[b], PM89[c], PM91[d], Ka76[e]	3
Zanstra (H I, He I, He II)	Ph03[f], KJ91[g]	3
Atmosphere Model	Me88[h], HF83[i]	5

References. — a: Grewing & Neri (1990), b: Lumsden et al. (2001), c: Preite-Martinez et al. (1989), d: Preite-Martinez et al. (1991), e: Kaler (1976) ,f: Phillips (2003), g: Kaler & Jacoby (1991), h: Mendez et al. (1988), i: Harrington & Feibelman (1983).

the other two are not available. Finally, the effective temperature was obtained for 72 of 77 objects in the catalog. Figure 3.7 shows the cumulative histogram of the effective temperatures by the blue solid line. The effective temperatures adopted from Phillips (2003) are shown by the gray dashed line. We assume that the temperature distribution of Phillips' samples represents that of the whole Galactic PNe. The median of the effective temperature for the PNSPC samples is about 50 000 K, while that for Phillips' data is about 80 000 K. Figure 3.7 indicates that the PNSPC samples are significantly biased toward young PNe.

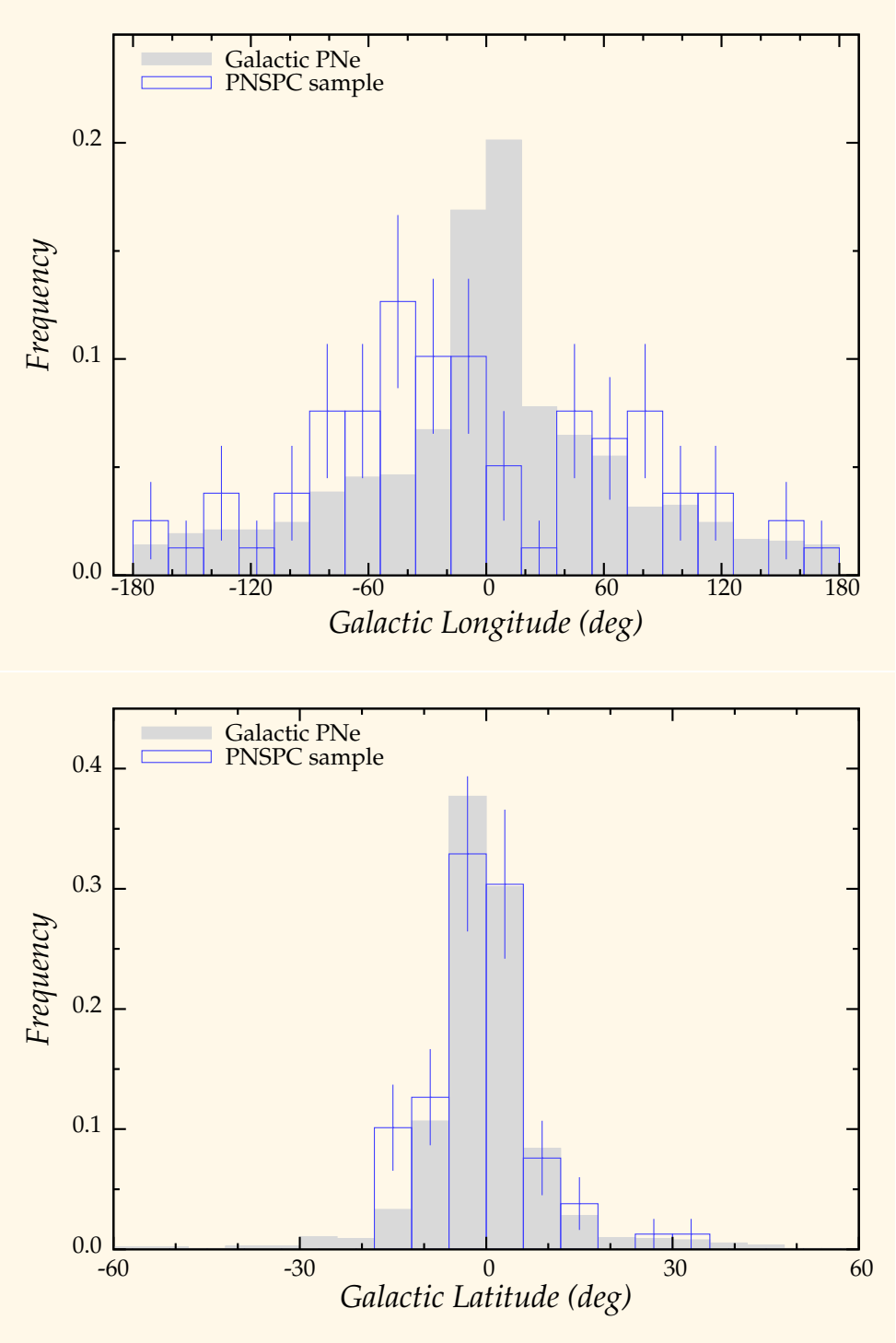

Figure 3.5 – Distributions of the PNSPC samples in the Galactic Coordinates. The upper panel shows the histograms of the Galactic Longitude of the PNe, while the lower panel shows those of the Galactic Latitude. The blue solid line shows the histograms for the PNSPC samples and the gray filled areas show those for the whole Galactic PNe adopted from Acker et al. (1992).

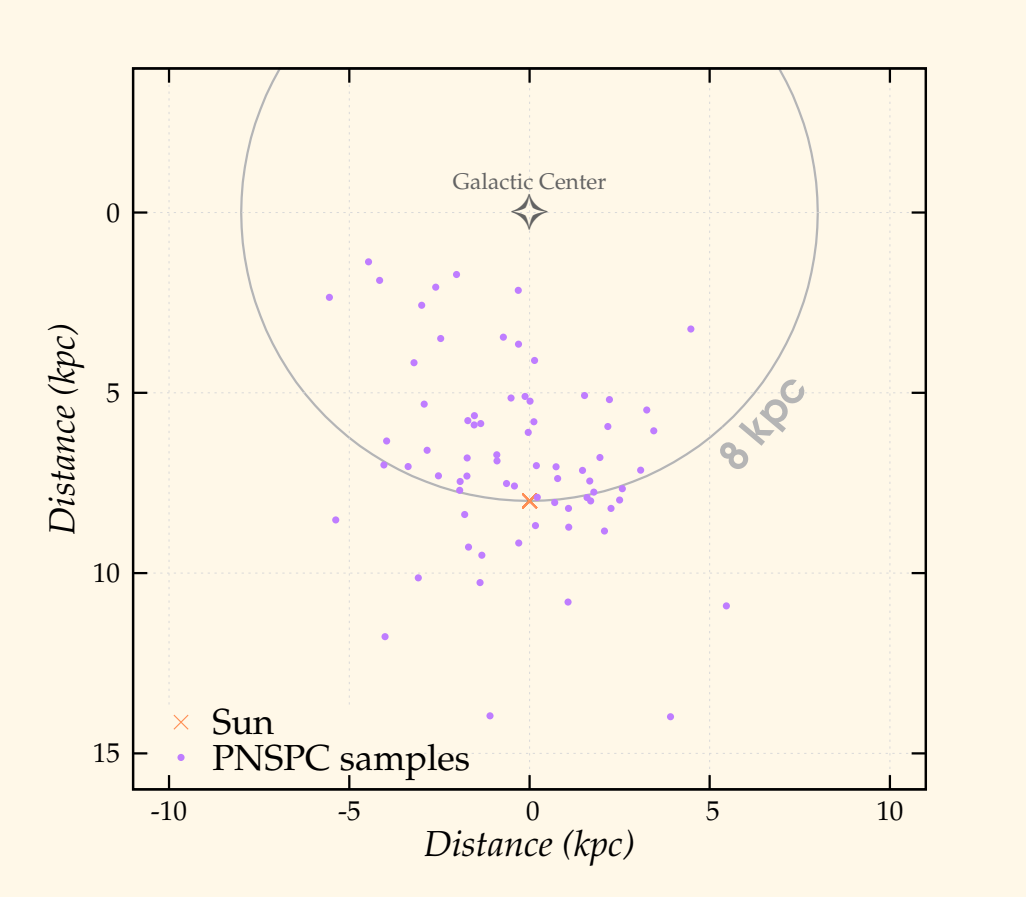

Figure 3.6 – Distribution of the PNSPC samples in the Galactic Plane (top view). The red cross shows the Sun. The purple circles show the positions of the PNSPC samples. The distances are taken from Acker (1978), Pottasch (1983), Maciel (1984), Amnuel et al. (1984), Gathier et al. (1986b), Gathier et al. (1986a), Sabbadin (1986), Cahn et al. (1992), Acker et al. (1992), and references therein.

3.6 Summary

We observe more than 70 Galactic PNe and obtained their 2.5–5.0 μm spectra with a high sensitivity of ~10 mJy using the *AKARI*/IRC. The PNSPC program successfully provided a set of the near-infrared spectra which collect all the flux from the object. The accuracy in the absolute flux density is evaluated based on the comparison with the *WISE* All-Sky source catalog. The spectra provided by the PNSPC program are consistent with the *WISE* catalog with an accuracy of ~20%. These spectra are compiled into a spectral catalog. The *AKARI*/IRC spectra include several spectral features, such as recombination lines, fine-structure lines, molecular lines, and dust emission. The intensity and equivalent width of these spectral features were measured by spectral fitting. They are also included in the catalog.

The possible biases in the PNSPC catalog are investigated in terms of the Galactic coordinates and effective temperature of the central star. The distribution

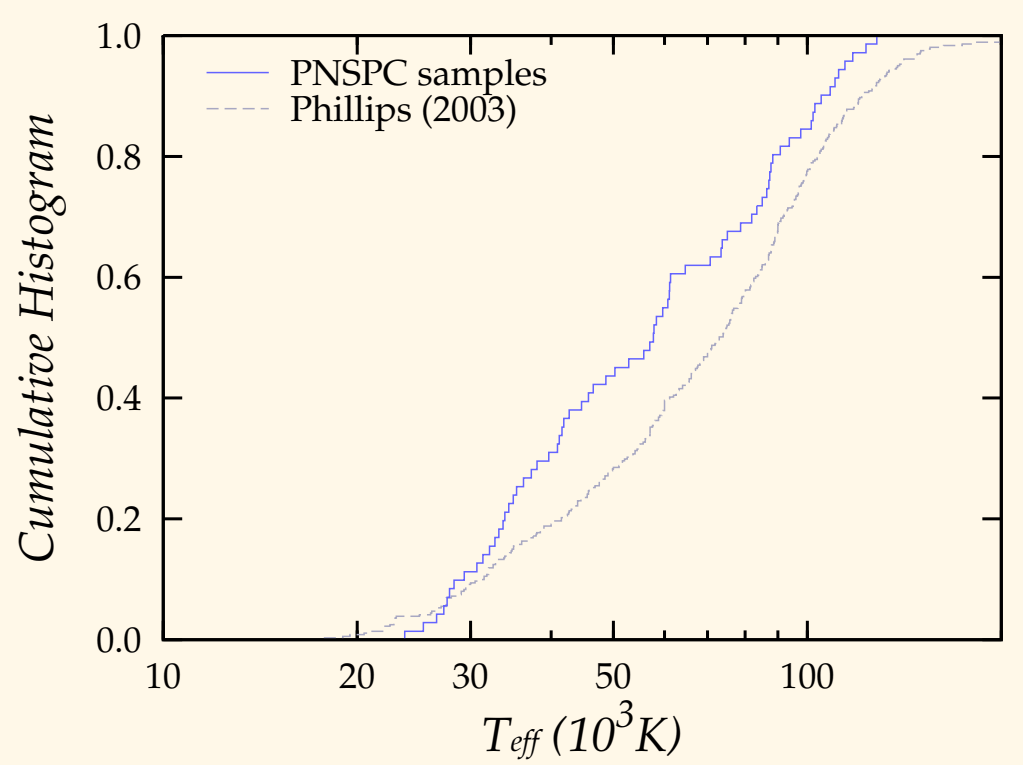

Figure 3.7 – Cumulative histograms of the effective temperature of the PNe. The blue solid line shows the temperature distribution of the PNSPC samples ($N_{obj} = 72$), while the gray dashed line shows that of the Galactic PNe (Phillips, 2003, $N_{obj} = 362$).

of the PNSPC sample shows that the PNSPC samples are mostly located in the Galactic disk. A typical effective temperature of the PNSPC samples is significantly lower than that of the whole Galactic PNe. This indicates that the PNSPC samples are biased toward young PNe. This bias possibly originates in the small apparent size in the target selection.

Although the PNSPC catalog does not represent the characteristics of the whole Galactic PNe, this catalog is the largest near-infrared spectral catalog available so far. It provides unique information to investigate the 2.5–5.0 μm spectra of Galactic PNe. The statistical characteristics of the emission features will be discussed in the following chapter.

Chapter 4

Near-Infrared PAH emission in Galactic Planetary Nebulae

Characteristics of the PAH emission in Galactic planetary nebulae (PNe) are statistically investigated based on the PNSPC catalog. The detection rate of the PAH emission is about 80%. The intensity of the 3.3 μm PAH feature is investigated in terms of the intrinsic extinction and effective temperature, indicating that the strength of the PAH feature is sensitive to the amount of dust and the evolutionary phase of the PN. The amount of aliphatic components in PAHs increases as the effective temperature gets higher. The results indicate that the PAH features evolve together with PNe.

4.1 Introduction

The previous chapter introduces the near-infrared spectral catalog of Galactic planetary nebulae (PNe) based on the *AKARI* observation program "PNSPC" (hereafter PNSPC catalog). The PNSPC catalog is the largest spectral catalog of Galactic PNe with the sensitivity of ~10 mJy around 3 μm. The catalog is useful for the statistical investigation of the PAH features in Galactic PNe.

The PAH features are attributed to specific vibrational modes of C—H or C—C chemical bonds. The PAH feature at 3.3 μm is dominant in the 3 μm region and attributed to a stretching mode of aromatic C—H bonds, while the PAH features around 3.4–3.5 μm are attributed to stretching modes of aliphatic C—H bonds (Duley & Williams, 1981). Theoretical studies (e.g., Schutte et al., 1993) indicate that the 3 μm PAH features are effectively emitted by PAHs with the number of carbon atoms less than ~100. Smaller PAHs are processed more easily than larger ones (e.g., Allain et al., 1996a,b). Observations of the 3 μm PAH emission should be effective to investigate processing of PAHs. Sloan et al. (1997) and Joblin et al. (1996) report that the variation in the intensity ratio of the 3.4 to 3.3 μm PAH features ($I_{3.4}/I_{3.3}$) is attributable to the processing of aliphatic C—H bonds by UV-photons. Mori et al. (2012b) investigate the intensity ratio of the 3.3 to 11.3 μm PAH features ($I_{3.3}/I_{11.3}$) in H II complexes in the LMC with different star-forming

activities and discuss possible destruction of small-sized PAHs in regions with an intense star-forming activity.

Investigations of the 3 μm PAH features of evolved stars (post-AGB stars and PNe) have been performed both with space and ground-based telescopes. Bernard et al. (1994) investigate the spatial distribution of the 3.3 μm PAH emission in a Galactic PN, BD+30° 3639, and discuss the excitation and processing of PAHs. Beintema et al. (1996) measure the peak wavelength and band width of the PAH features of a post-AGB star and two PNe based on the *ISO*/SWS spectra. Geballe & van der Veen (1990) and Geballe et al. (1992) report that the $I_{3.4}/I_{3.3}$ ratio is unusually high in some post-AGB stars, suggesting that the variation in the ratio may be related to processing of PAHs. Goto et al. (2003) obtain spatially resolved 3 μm spectra of a post-AGB star, IRAS 22272+5435, and discuss the variation in the $I_{3.4}/I_{3.3}$ ratio in terms of thermal processing of dust grains. Roche et al. (1996) investigate 3.2–3.6 μm spectra of 21 Galactic PNe with the *UKIRT*/CGS4[*1]. They report that the $I_{3.4}/I_{3.3}$ ratio increases with the size of the PNe, and that the strength of the PAH feature is strongly correlated with the C/O ratio. Recently, Smith & McLean (2008) obtain 3.0–3.4 μm spectra of 20 Galactic PNe using the FLITECAM[*2] and investigate the 3.3 μm PAH equivalent width in terms of the C/O ratio. However, limited by the insufficient sensitivity, the number of the available targets is small in these studies and the targets are biased toward bright ones. The evolution and statistical characteristics of the 3 μm PAH features have not been well investigated.

The PNSPC catalog is useful for statistical investigations of the 3 μm PAH features of Galactic PNe. More than 70 Galactic PNe are included in the catalog thanks to high sensitivity of the IRC. They are selected only by the brightness and the angular size, suggesting that the catalog is only slightly biased in terms of the chemistry and the amount of dust. Although a moderate spectral resolution ($R \sim 600$) is usually required to distinguish Pfund-δ and the 3.3 μm PAH feature, the wide spectral coverage of the IRC enables us to estimate the contribution from Pfund-δ accurately. The PNSPC catalog is the most useful database so far to investigate the statistical characteristics of the 3 μm PAH features.

In this chapter, we investigate the detection rate of the PAH features in Galactic PNe and the evolution of the PAH features along with PN evolution based on the PNSPC catalog. This chapter is organized as follows: Section 4.2 describes the data we used. The statistical characteristics and the evolution of the PAH features are shown in Section 4.3. The interpretations of the results are given in Section 4.4. The chapter is summarized in Section 4.5.

4.2 Data

4.2.1 Data from the PNSPC Catalog

The intensity and equivalent width of the PAH features (3.3 and 3.4 μm) were obtained from the PNSPC catalog. Because of low spectral resolution, the

[*1] United Kingdom Infrared Telescope/Cooled Grating Spectrometer 4

[*2] First Light Test Experiment Camera, which is developed for *SOFIA* project

AKARI/IRC cannot distinguish the sub-features in the 3.4–3.5 μm region. Thus, the intensity of the 3.4 μm PAH emission in the PNSPC catalog indicates the summation of the sub-features. The extinction estimated based on the intensity ratio of Hβ to Brackett-α ($I_{H\beta}/I_{Br\alpha}$) was also adopted from the catalog. It was used to estimate the extinction caused by circumstellar dust.

4.2.2 Effective Temperature

Effective temperatures were obtained in the same way as in Chapter 3. We collected the effective temperature estimated by several methods (e.g., Zanstra, Energy Balance, and Atmosphere modeling) from the literature. The weights were assigned for each method based on a typical uncertainty. We then adopted a weighted mean of the collected temperatures. The effective temperatures were obtained for 72 of the 77 objects in the PNSPC catalog. Details are described in Section 3.5.3.

4.2.3 Total Infrared Intensity

The total infrared intensity of each PN was estimated based on the all-sky broad band photometry data. The 22.1 μm fluxes were retrieved from the *WISE* All-Sky Catalog (Cutri et al., 2012a,b). The 18 μm fluxes were retrieved from the *AKARI*/IRC Point Source Catalog (Ishihara et al., 2010a), while the 65, 90, 140, and 160 μm fluxes were retrieved from the *AKARI*/FIS Bright Source Catalog (Yamamura et al., 2010). Some objects are too bright and their far-infrared flux densities are not provided by the *AKARI* and *WISE* catalogs. For these objects, we used the flux densities at 25, 65, and 100 μm from the *IRAS* point-source catalog (Joint Iras Science, 1994; Neugebauer et al., 1984). The infrared spectral energy distribution was fitted by a single- or two-temperature graybody function with a varying emissivity. The total infrared intensity was calculated by integrating the fitted graybody function.

4.2.4 Interstellar Extinction

Interstellar extinction toward the objects was estimated based on the DSS extinction map (Figure 3.1; Dobashi et al., 2005a,b). The extinction map was given in a resolution of $2' \times 2'$. We averaged the extinction values within a $6'$ radius around the objects and assumed it as the interstellar extinction towards the objects. Since there is no information about the line-of-sight distribution of interstellar dust, the extinction values derived from the DSS map should be considered as an upper limit on interstellar extinction.

4.3 Results

4.3.1 Statistical Characteristics

As described in Section 3.5.3, the PNSPC samples are biased toward young PNe. This bias is not negligible in investigating statistical characteristics of Galactic

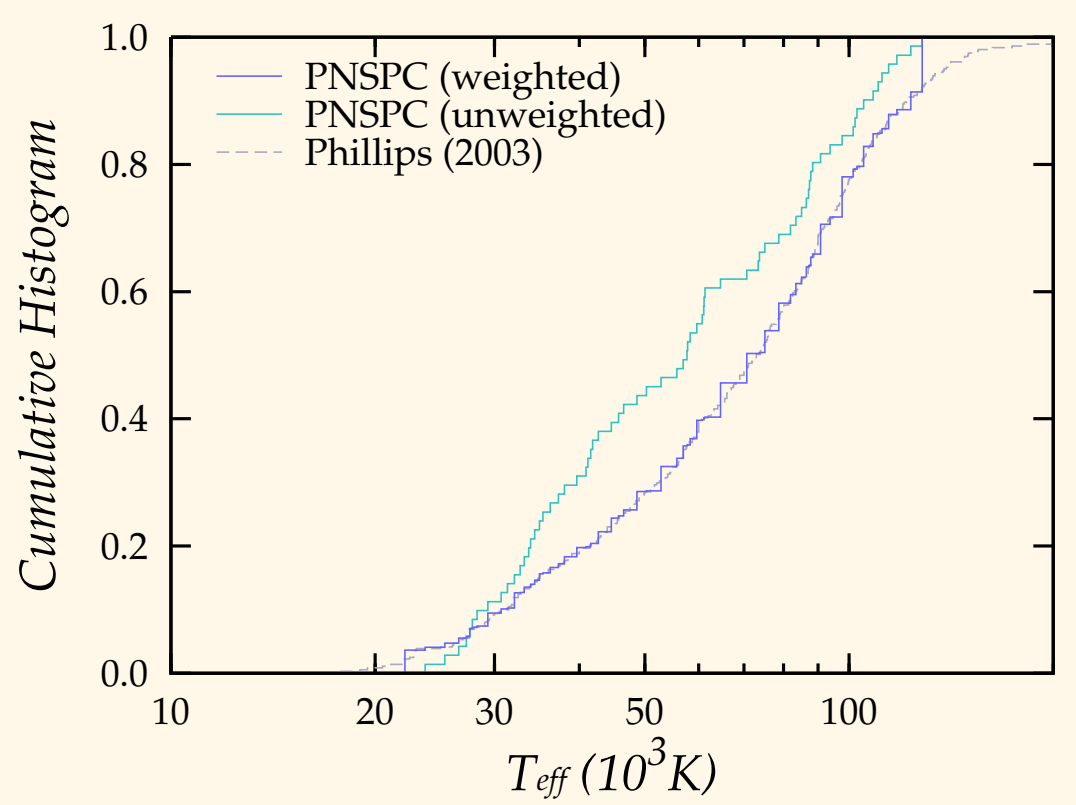

Figure 4.1 – Cumulative histograms of the effective temperature. The cyan solid line shows the temperature distribution of the PNSPC samples ($N_{obj} = 72$), while the gray dashed line illustrates that of Galactic PNe (Phillips, 2003, $N_{obj} = 362$). The blue solid line shows the weighted cumulative histogram of the temperature for the PNSPC samples (*see* text).

PNe. To evaluate the effect of the sample bias, we calculate a weight for each object so that the temperature distribution should follow Galactic PNe. We assume that the temperature distribution adopted from Phillips (2003) represents that of Galactic PNe. Figure 4.1 shows the weighted and unweighted cumulative histograms of the effective temperature for the PNSPC samples by the blue and cyan lines, respectively. The weights are typically larger for the PNe with a higher temperature. When the weighted and unweighted histograms are significantly different, the result should be sensitive to the sample bias of the PNSPC catalog.

The distribution of the extinction at the *V*-band is illustrated in Figure 4.2. The cyan lines show the extinction estimated from the $I_{H\beta}/I_{Br\alpha}$ ratio ($A_V(H\beta)$). The solid and dashed lines are the weighted and unweighted histograms, respectively. We assume that the extinction from interstellar dust is given by the DSS extinction map ($A_V(DSS)$). The difference of $\Delta A_V = A_V(H\beta) - A_V(DSS)$ is assumed to represent the extinction from circumstellar dust. Note that the circumstellar extinction can be underestimated since $A_V(DSS)$ is only an upper limit for interstellar extinction. The distribution of the circumstellar extinction is shown by the blue lines. The circumstellar extinction is less than unity for about 80% of the PNSPC samples.

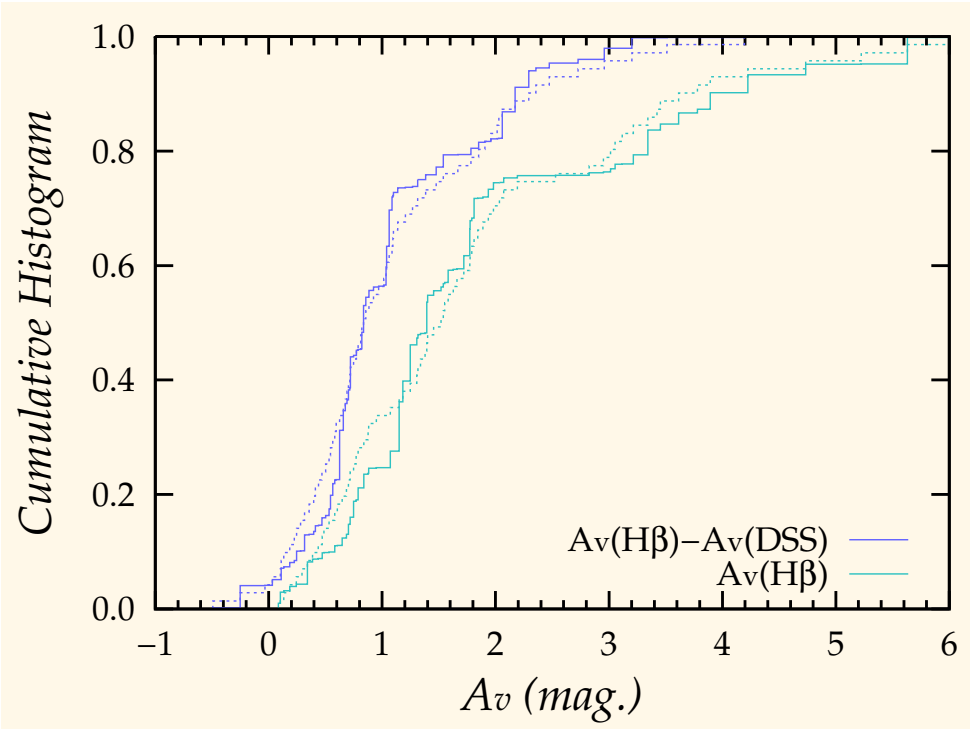

Figure 4.2 – Cumulative histograms of the extinction at the V-band ($N_{obj} = 72$). The cyan lines show the extinction values from the $I_{H\beta}/I_{Br\alpha}$ ratio. The blue lines also show the extinction from circumstellar dust. The solid and dashed lines show the weighted and unweighted histograms, respectively.

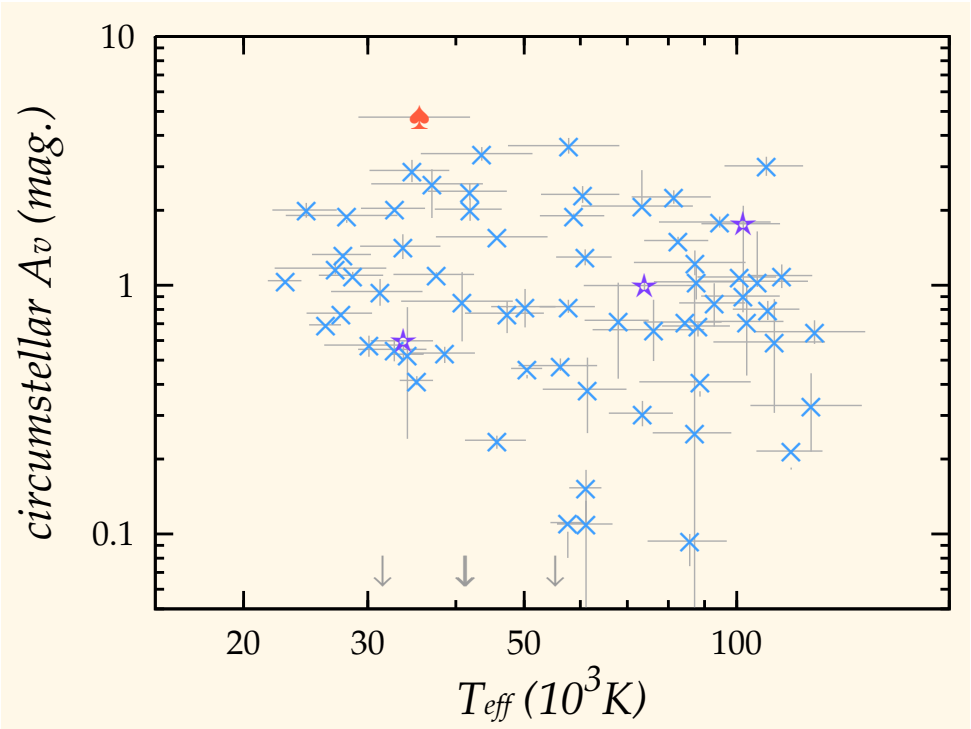

Figure 4.3 – Variation in the circumstellar extinction against the effective temperature ($N_{obj} = 72$). The cross, star, and spade symbols show the PNe, evolved stars, and a H II region, respectively.

The extinction is expected to decrease with the expansion of the envelope. Figure 4.3 shows the circumstellar extinction value against the effective temperature. The effective temperature can be a good indicator of the evolutionary phase of PNe (*see* Section 4.3.2). The cross, star, and spade symbols represent a PN, an evolved star and a H II region, respectively, based on the classification in the Simbad Database. The extinction decreases slightly along with increasing temperature. This is possibly attributed to the nebular expansion, since evolved PNe have higher temperatures. Note that there is a large scatter in the circumstellar extinction at the same temperature. The scatter is attributed to the difference in the evolutionary timescale or the amount of dust in the envelope. Figure 4.4 illustrates the relationship between the dust amount and extinction. The top panel shows the equivalent width of the 3.3 μm PAH feature ($EW(3.3\,\mu m)$) against the circumstellar extinction, showing a weak positive correlation. The bottom panel shows cumulative histograms of the circumstellar extinction. The blue lines show the histograms for $EW(3.3\,\mu m) > 150$ Å, while the cyan lines show those for for $EW(3.3\,\mu m) < 150$ Å. The histograms for $EW(3.3\,\mu m) > 150$ Å are systematically shifted toward large extinction. The results indicate that the PAH emission is strong in the PNe with large extinction.

The detection rate of the PAH features is investigated. Figure 4.5 shows the cumulative histograms of the signal-to-noise ratio of the 3.3 μm PAH feature intensity ($S/N(I_{3.3})$). If we accept a 3σ detection limit, the detection rate of the 3.3 μm PAH feature in the PNSPC samples is about 80%. However, the detection rate is significantly different between the weighted and unweighted histograms, because evolved PNe tend to show strong PAH emission (*see* Section 4.3.2). The detection rate may change by about 10–15% due to the uncertainty in the bias in the PNSPC samples.

The distribution of the $I_{3.4}/I_{3.3}$ ratio is shown in Figure 4.6. The ratio ranges from about 0.0 to 0.6. The median of the ratio is about 0.4. Note that the intensity of the 3.4 μm PAH feature ($I_{3.4}$) indicates the summation of the intensity of the 3.4–3.5 μm sub-features. Mori et al. (2014) report that the $I_{3.4}/I_{3.3}$ ratio for Galactic H II regions typically is about 0.1–0.4. A large $I_{3.4}/I_{3.3}$ ratio of Galactic PNe versus that of Galactic H II regions is notable.

4.3.2 Evolution of the PAH Emission

The evolution of the PAH features is investigated in terms of the effective temperature. The effective temperature can be used to estimate the evolutionary phase of the PN, since the effective temperature increases with PN evolution. Figure 4.7 shows the *AKARI*/FIS 65 to 90 μm color against the effective temperature. The *AKARI* color, which represents the temperature of the circumstellar dust, decreases with increasing temperature. The decreased dust temperature may be attributed to nebular expansion. Figure 4.7 confirms that the effective temperature is useful to estimate the evolutionary phase of PNe, and this fact is applied in the following sections.

The evolution of the $I_{3.4}/I_{3.3}$ ratio, which represents the amount of aliphatic components in PAHs, is illustrated in Figure 4.8. The top panel shows the $I_{3.4}/I_{3.3}$ ratio against the effective temperature. The effective temperature tends to be

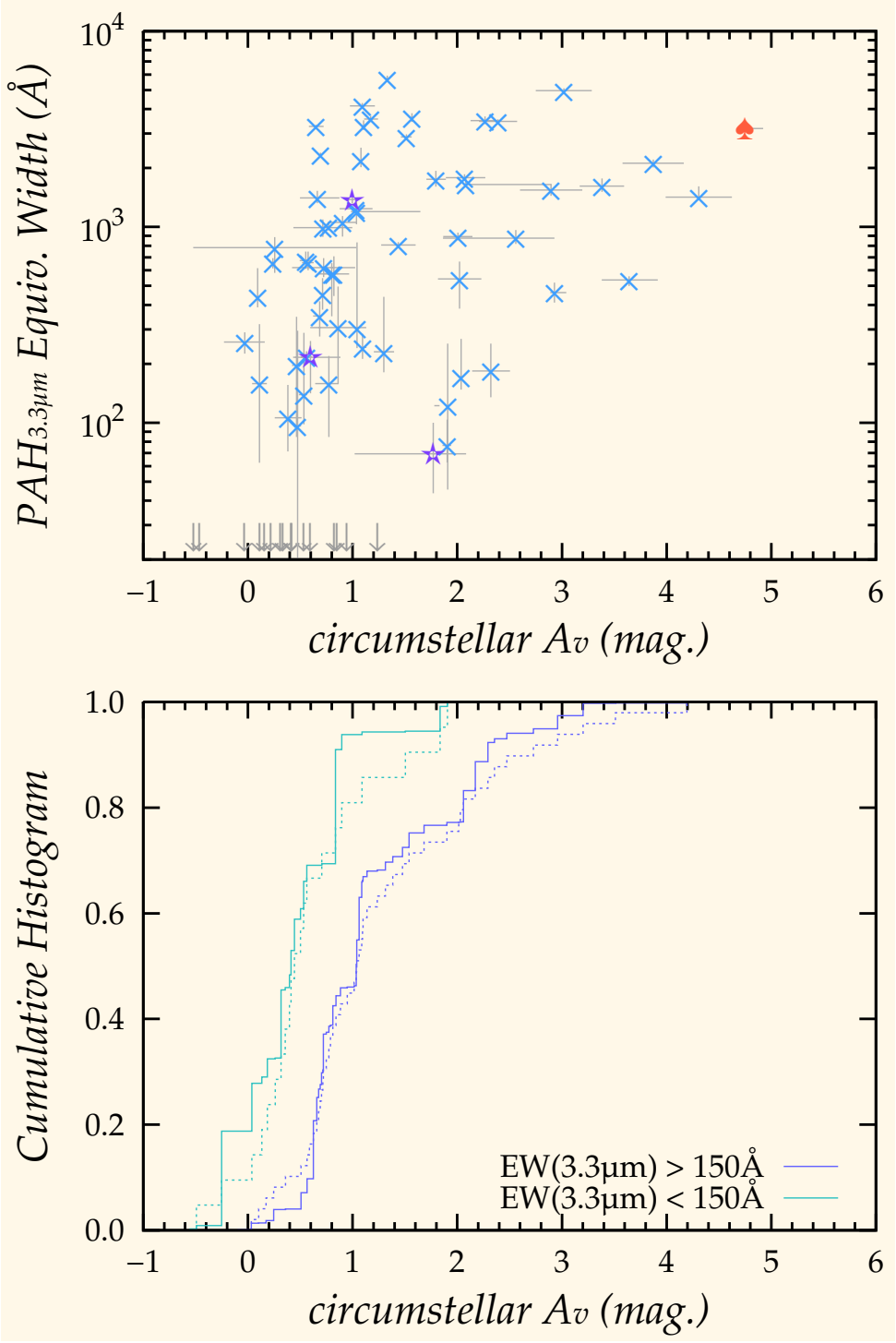

Figure 4.4 – Top: $EW(3.3\,\mu m)$ against the circumstellar extinction ($N_{obj} = 77$). The symbols are the same as in Figure 4.3. Bottom: Cumulative histograms of the extinction. The cyan lines show the histograms with $EW(3.3\,\mu m) < 150\,Å$ ($N = 22$), while the blue lines show those with $EW(3.3\,\mu m) > 150\,Å$ ($N = 50$). The solid and dashed lines are the same as in Figure 4.2.

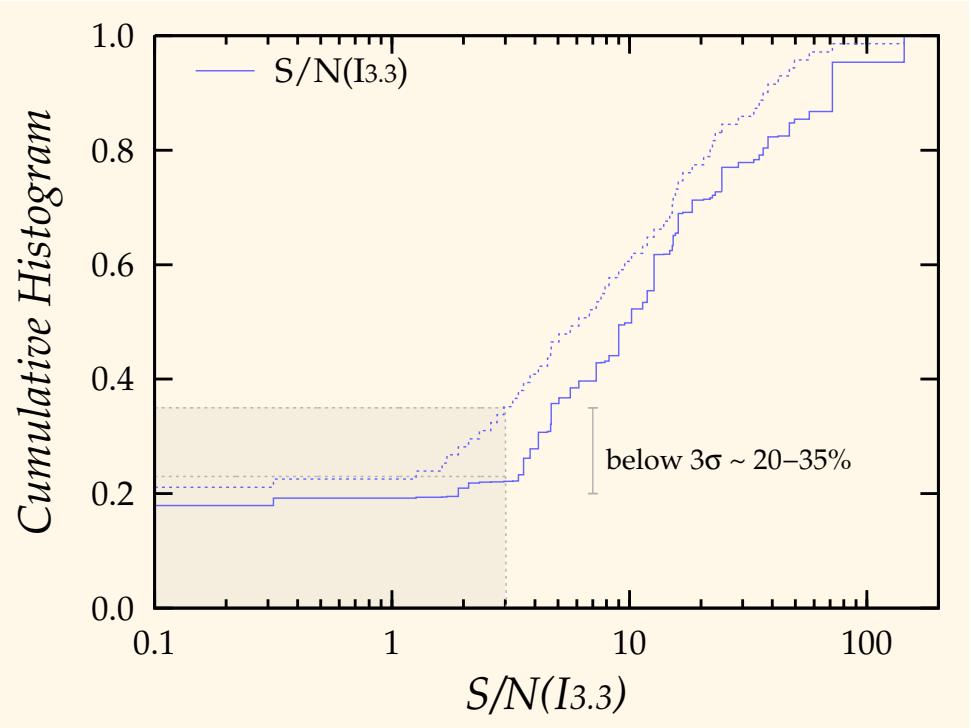

Figure 4.5 – Cumulative histograms of $S/N(I_{3.3})$ ($N_{obj} = 72$). The region with $S/N(I_{3.3})$ less than three is filled with grayed color. The solid and dashed lines are the same as in Figure 4.2.

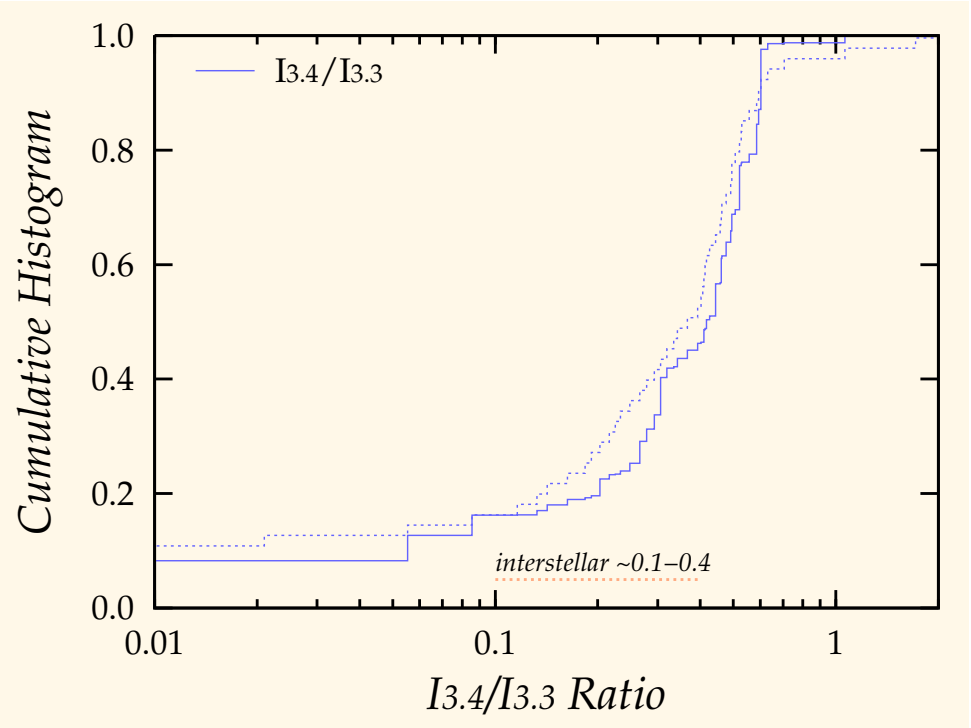

Figure 4.6 – Cumulative histograms of the $I_{3.4}/I_{3.3}$ ratio ($N_{obs} = 72$). The solid and dashed lines are the same as in Figure 4.2.

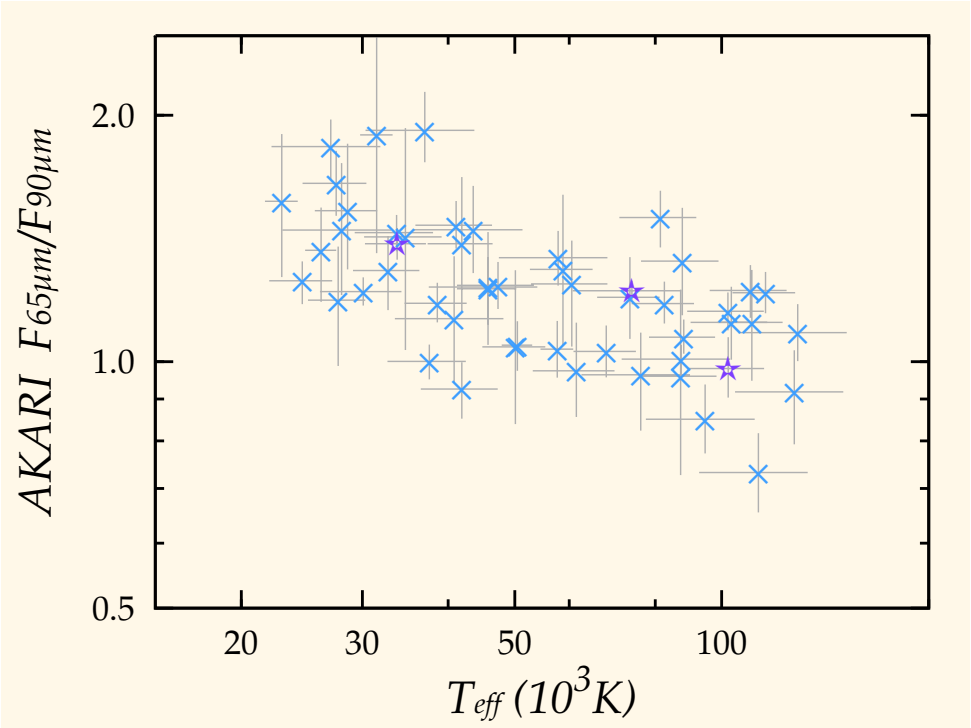

Figure 4.7 – Variation in *AKARI*/FIS 65/90 μm color with the effective temperature ($N_{obj} = 52$). The symbols are the same as in Figure 4.3.

low for the PNe with a low $I_{3.4}/I_{3.3}$ ratio. The trend is obvious in the bottom panel, which shows the cumulative histograms of the effective temperature for $I_{3.4}/I_{3.3} > 0.25$ and $I_{3.4}/I_{3.3} < 0.25$ by the blue and cyan lines, respectively. A typical effective temperature for $I_{3.4}/I_{3.3} > 0.25$ is significantly higher than that for $I_{3.4}/I_{3.3} < 0.25$. The results suggest that the amount of the aliphatic components increases with PN evolution.

The evolution of the fractional strength of the 3.3 μm PAH feature to the total infrared intensity ($I_{3.3}/I_{IR}$) is assumed to represent the amount of PAHs excited by a UV-photon. When more PAHs are excited by a UV-photon, the $I_{3.3}/I_{IR}$ ratio is expected to increase. The top panel in Figure 4.9 shows the $I_{3.3}/I_{IR}$ ratio against the effective temperature. Assuming that PAHs are mostly excited in the envelope, the $I_{3.3}/I_{IR}$ ratio indicates the amount of PAHs in the envelope. The symbols show a "U"-like distribution with a minimum around 50 000 K. The bottom panel shows the equivalent widths of the 3.3 μm PAH feature. Although scatter is much larger, they show a similar distribution as in the top panel.

4.4 Discussion

4.4.1 Strength of the PAH Emission

Since PAHs are carbonaceous, the existence of the PAH features should be closely related to the chemistry of PNe. Roche et al. (1996) report that $EW(3.3\ \mu m)$ almost linearly increases with the C/O ratio of the PN. A PAH detection threshold is

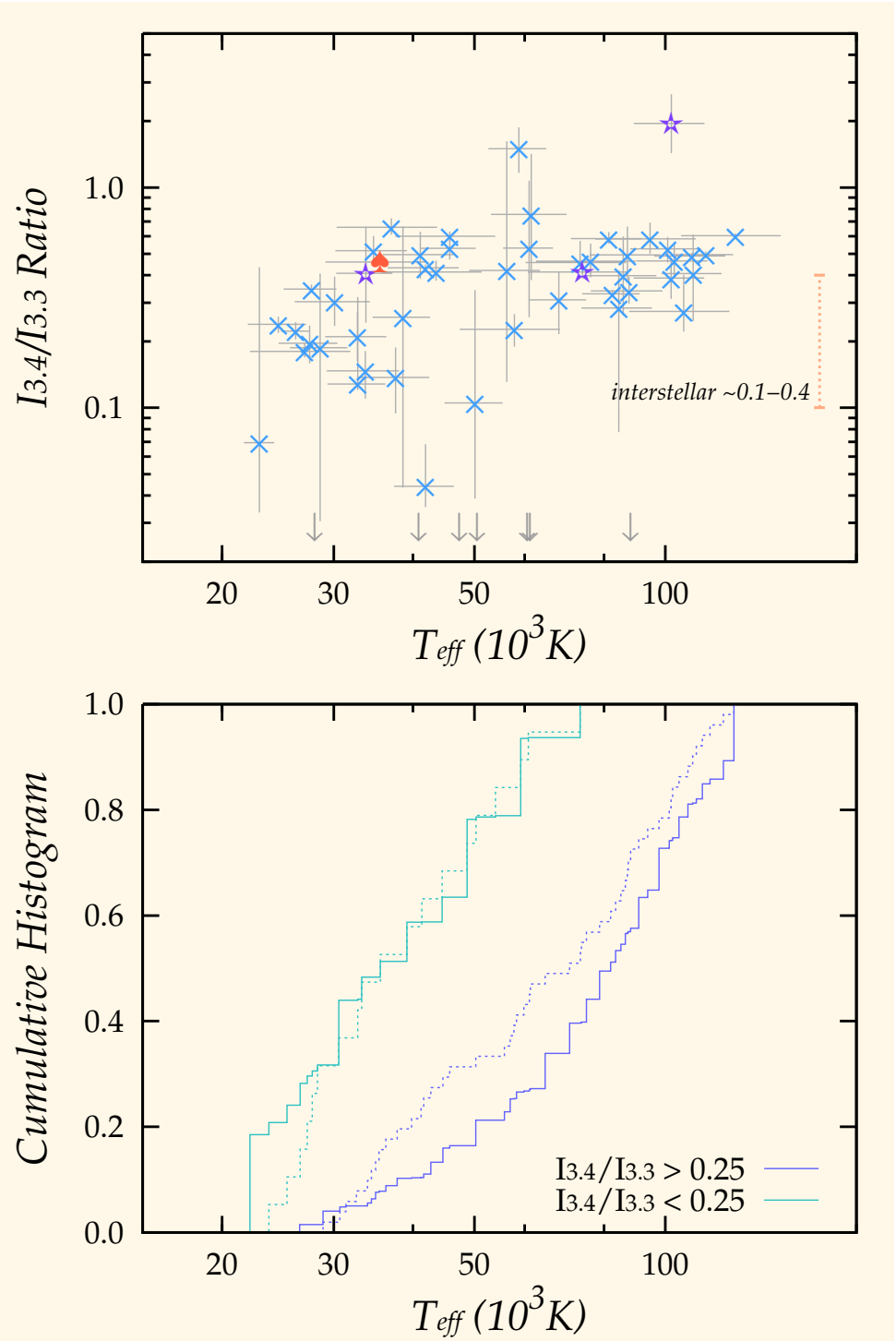

Figure 4.8 – Top: Variation in the $I_{3.4}/I_{3.3}$ ratio with the effective temperature. The symbols are the same as in Figure 4.3. The dashed line on the right shows a typical range of the $I_{3.4}/I_{3.3}$ ratio for Galactic star-forming regions (Mori et al., 2014). Bottom: Cumulative histograms of the effective temperature. The cyan and blue lines show the histograms with $I_{3.4}/I_{3.3} < 0.25$ ($N_{obj} = 20$) and $I_{3.4}/I_{3.3} > 0.25$ ($N_{obj} = 52$), respectively. The solid and dashed lines are the same as in Figure 4.4.

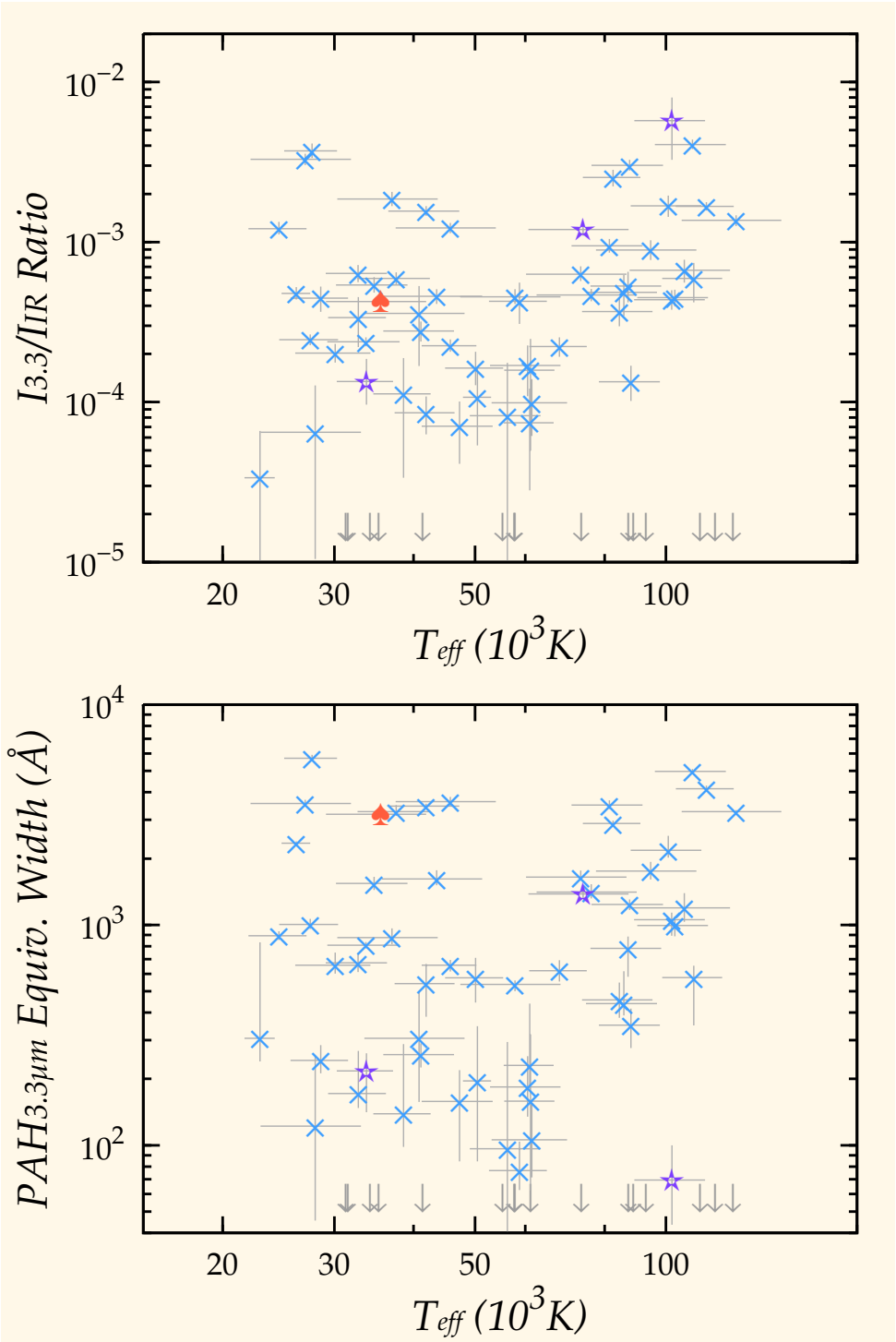

Figure 4.9 – Top: Variation in the $I_{3.3}/I_{IR}$ ratio with the effective temperature ($N_{obj} = 72$). Bottom: $EW(3.3\,\mu m)$ against the effective temperature ($N_{obj} = 72$). The symbols are the same as in Figure 4.3.

obtained at C/O $\sim$ 0.6 based on fitting with a linear function. They propose that PAHs can be formed even when the C/O ratio is less than unity. Smith & McLean (2008) also investigate the correlation between $EW(3.3\,\mu m)$ and the C/O ratio and report a PAH detection threshold at C/O $= 0.65 \pm 0.28$. A similar investigation is performed for the mid-infrared PAH features by Cohen & Barlow (2005). They report a threshold consistent with the results reported by Roche et al. (1996) and Smith & McLean (2008).

The present results suggest that there is a large scatter in the amount of dust in the PN envelope. $EW(3.3\,\mu m)$ increases with the amount of circumstellar dust. Furthermore, $EW(3.3\,\mu m)$ changes along with PN evolution. Figure 4.9 shows that $EW(3.3\,\mu m)$ could increase by about 10 times when the effective temperature increases from 50 000 to 100 000K. The variation in $EW(3.3\,\mu m)$, with PN evolution, is almost comparable with that of the C/O ratio reported by Roche et al. (1996) and Smith & McLean (2008). We propose that $EW(3.3\,\mu m)$ depends on several factors such as the amount of dust and the evolutionary phase, and that the C/O ratio may not be the most important one.

4.4.2 Detection Rate of the PAH Emission

The present results suggest that the 3.3 μm PAH detection rate is about 65–80%. The 3.3 μm PAH feature is suitable to measure the PAH detection rate because the PAH features in 6–9 μm are possibly contaminated by plateau emission and emission from hydrogenated amorphous carbons (HACs). The sample selection of the PNSPC catalog is free from the chemistry of the nebula. The PNSPC samples are selected by the K-band brightness, which does not include dust emission. The PNSPC samples are assumed to be slightly biased toward dusty PNe. We presume that the PAH detection rate provided by the PNSPC catalog is robust.

Roche et al. (1996) detect the 3.3 μm PAH feature in 18 of 21 PNe (85%), while Smith & McLean (2008) detect the 3.3 μm PAH feature in 13 of 20 PNe (65%). Their results are consistent with our results within the range of the uncertainty. Their objects, however, may be biased toward bright PNe in the mid-infrared, which tend to have a large amount of dust.

Stanghellini et al. (2012) report that the ratio of Galactic PNe with carbon-rich and mixed-chemistry dust emission is about 53% (80 of 150 PNe) based on mid-infrared spectra obtained with the *Spitzer*/IRS. Their detection rate is significantly lower than the present result. Their survey area is large enough to cover PNe near the Galactic center. Ishihara et al. (2011) report that the distribution of oxygen-rich AGB stars is concentrated around the Galactic center, while carbon-rich AGB stars are widely distributed over the Galactic disk. If oxygen-rich PNe are concentrated around the Galactic center and carbon-rich PNe are not, we surmise that the PAH detection rate in the Galactic disk is higher than in the Galactic bulge. *Spitzer* observes in the mid-infrared, and could possibly observe PNe with a smaller core mass than with *AKARI*. While massive PNe become oxygen-rich due to hot bottom burning (Iben & Renzini, 1983), PNe with a smaller core mass than $\sim 0.6\,M_{\odot}$ are not supposed to be carbon-rich (Ferrarotti & Gail, 2006; Iben, 1982). We must note that the discrepancy of the PAH detection rate may be attributed in part to the different detection limits on the core mass

of PNe, between *Spitzer* and *AKARI*.

4.4.3 Evolution of the PAH Emission

The present results indicate that the $I_{3.4}/I_{3.3}$ ratio increases with PN evolution. The increase may be attributed to an increase of aliphatic components in envelope PAHs.

The amount of aliphatic components may be decreased by processing due to UV-photons (Jones, 2012a,b). When PAHs are processed by UV-photons, the most fragile parts of PAHs are expected to be broken first. The strength of aliphatic bonds is weaker than that of aromatic bonds. When hydrogenation of PAHs is promoted, the amount of aliphatic bonds in PAHs may be increased. The amount of aliphatic components may be sensitive to the equilibrium between hydrogenation and dehydrogenation. Allain et al. (1996a,b) show that the degree of hydrogenation is controlled by G_0/n_H, where G_0 is the strength of the radiation field normalized by the Solar neighborhood value and n_H is the density of hydrogen. Their results indicate that G_0/n_H should decrease by one or two orders of magnitude, in order to significantly promote hydrogenation. Such a sudden decrease in G_0/n_H is not feasible in the PN phase since the luminosity remains almost constant during PN evolution. The evolution of the $I_{3.4}/I_{3.3}$ ratio is not attributable to processing of PAHs.

Dust shattering may increase the amount of aliphatic components. When large carbonaceous grains are shattered, they are fragmented and a large amount of VSGs can be produced (Jones et al., 1996). If the grain size is sufficiently small, such a small grain may show the PAH features when they are excited by a single UV-photon. Kaneda et al. (2012) and Yamagishi et al. (2012) report PAH features with a large $I_{3.4}/I_{3.3}$ ratio, respectively, in two shocked regions: the root of a Galactic molecular loop and the galactic super wind of M 82. Their results suggest that the PAHs produced by shattering may contain a large amount of aliphatic components. Hirashita (2010) report that a typical timescale of dust shattering ($\tau_{\rm shat}$) is given by

$$\tau_{\rm shat} = 10^8 \left(\frac{\mathcal{R}}{\mathcal{R}_0}\right) \left(\frac{n_{\rm H}}{0.3\,{\rm cm^{-3}}}\right)^{-1} \left(\frac{a}{0.1\,\mu{\rm m}}\right) \left(\frac{V_{\rm shat}}{20\,{\rm km\,s^{-1}}}\right)^{-\alpha}, \tag{4.1}$$

where $\mathcal{R}$ and $\mathcal{R}_0$ are the local and nominal dust-to-hydrogen mass ratios, $n_{\rm H}$ is the density of hydrogen, a is the grain radius, $V_{\rm shat}$ is the shattering velocity, and α is estimated to be about two. $n_{\rm H}$ in PNe typically ranges from 10^2 to $10^4\,{\rm cm^{-3}}$ (Schönberner et al., 2005b; Villaver et al., 2002). There is no direct measurement of $V_{\rm shat}$ in PNe. Sabbadin et al. (2008) estimate the gas turbulence velocity of a PN, NGC 7009 to be 2–8 $\rm km\,s^{-1}$. We assume that $V_{\rm shat}$ is as large as the gas turbulence velocity. By substituting $10^3\,{\rm cm^{-3}}$ and $5\,{\rm km\,s^{-1}}$ into $n_{\rm H}$ and $V_{\rm shat}$, respectively, $\tau_{\rm shat}$ becomes 5×10^4 years. $\tau_{\rm shat}$ is estimated to be much larger than a typical lifetime of PNe. Dust shattering does not account for the increase in the $I_{3.4}/I_{3.3}$ ratio unless there is a mechanism to significantly decrease $\tau_{\rm shat}$.

The nebular expansion may contribute to the increase in the $I_{3.4}/I_{3.3}$ ratio. The vibrational modes of PAHs are excited only when PAHs absorb a single UV-photon. PAHs outside the photo-dissociation region do not show the PAH features.

The AGB wind region spreads outside the envelope (Figure 1.5). PAHs may reside also in the AGB wind region, but they are not excited by UV-photons. As the envelope expands, PAHs in the AGB wind region are taken in the envelope. Geballe & van der Veen (1990) report that some post-AGB stars show unusually strong 3.4 μm features. If the carriers of those strong 3.4 μm features survive in the AGB wind region, the $I_{3.4}/I_{3.3}$ ratio could increase along with the expansion of the envelope.

The explanation mentioned above may require an increase in the amount of PAHs in the envelope. The amount of PAHs in the envelope is examined in terms of the $I_{3.3}/I_{IR}$ ratio shown in Figure 4.9. The optical depth of the circumstellar dust and PAHs at ν, are defined as τ_ν^{dust} and τ_ν^{PAH}, respectively. The total infrared intensity (I_{IR}) and the total intensity of the PAH features (I_{PAH}) are approximated by

$$I_{IR} + I_{PAH} \simeq \int \left(1 - e^{-\tau_\nu^{dust} - \tau_\nu^{PAH}}\right) F_\nu d\nu \simeq \left(1 - e^{-\tau_{UV}^{dust}} + \tau_{UV}^{PAH} e^{-\tau_{UV}^{dust}}\right) I_{UV}, \quad (4.2)$$

where F_ν is the flux density of the incident radiation and I_{UV} is the UV intensity. τ_ν^{PAH} is assumed to be optically thin. Thus, the $I_{3.3}/I_{IR}$ ratio is given by

$$\frac{I_{3.3}}{I_{IR}} \simeq \frac{I_{3.3}}{I_{PAH}} \frac{\tau_{UV}^{PAH}}{e^{\tau_{UV}^{dust}} - 1}. \quad (4.3)$$

Assuming that the $I_{3.3}/I_{PAH}$ ratio is constant, the $I_{3.3}/I_{IR}$ ratio linearly depends on the optical depth or the amount of PAHs. A decrease in τ_{UV}^{dust} may contribute to an increase in the $I_{3.3}/I_{IR}$ ratio. Figure 4.3 shows that a typical extinction value decreases from 1 to 0.8 mag. when the effective temperature increases from 50 000 to 100 000 K. The decrease in τ_ν can increase the $I_{3.3}/I_{IR}$ ratio only by a factor of about two. The increase seen in the $I_{3.3}/I_{IR}$ ratio is not fully explained by the decrease in τ_{UV}^{dust} and may be attributable to an increase in the amount of PAHs in the envelope. This result is also consistent with the explanation described above. On the other hand, the $I_{3.3}/I_{PAH}$ ratio decreases when T_{eff} changes from 20,000 to 50,000 K. We assume that the decrease may be attributable to PAH destruction. The $I_{3.3}/I_{PAH}$ ratio, however, could also change with the ionization fraction and the size distribution of PAHs. Part of the variation in Figure 4.9 could come from the variation in the $I_{3.3}/I_{PAH}$ ratio.

4.5 Summary

The PNSPC catalog is the largest near-infrared spectral catalog of Galactic PNe. The catalog is slightly biased in terms of the amount of dust and chemistry of PNe. The statistical characteristics of the PAH features in the 3 μm region is investigated based on the PNSPC catalog.

The 3.3 μm PAH detection rate is obtained based on large and less-biased samples. The PAH detection rate is estimated to be about 65–80% in Galactic PNe. The result suggests that the PAH detection rate of PNe in the Galactic disk is higher than that around the Galactic center.

The $I_{3.4}/I_{3.3}$ ratio increases along with PN evolution. We propose that aliphatic-rich PAHs reside in the AGB wind region and that they are taken in the envelope

with the nebular expansion. The behavior of the $I_{3.3}/I_{IR}$ ratio is consistent with the proposed hypothesis. The hypothesis suggests that PAHs are already formed in the AGB phase and that properties of PAHs gradually change with the distance from the central star. The variations in properties of PAHs can be rooted in PAH formation in the AGB phase. The mid-infrared PAH features are indispensable to examine the properties of PAHs. It is important to investigate the hypothesis based on both the near- and mid-infrared PAH features.

Chapter 5

Evolution of PAHs and PNe

Near- to mid-infrared spectra of 18 Galactic Planetary Nebulae (PNe), which show prominent C-rich dust features, are obtained with the *AKARI*/IRC and *Spitzer*/IRS. Relative intensities of the PAH features are investigated. The intensity ratio of the 3.3 to 11.3 μm PAH feature in PNe is significantly smaller than that predicted by a model calculation, suggesting that small-sized PAHs in PNe are sensitive to dehydrogenation or destruction. The evolution of the PAH features is investigated in terms of the evolution of the central stars. As a PN evolves, the ionization fraction of PAHs becomes small, the 3.4 μm aliphatic features become strong, and the peak position of the 6.2 μm feature moves toward shorter wavelengths. A possible explanation is proposed to account for these transitions.

5.1 Introduction

Emission from PAHs is widely observed both in interstellar and circumstellar objects (Acke & van den Ancker, 2004; Peeters et al., 2002b). Their emission accounts for about 10% of the total infrared luminosity of our Galaxy and other star-forming galaxies (Draine & Li, 2007; Smith et al., 2007). PAHs are believed to be common grain species in the Universe. Although the PAH emission features are almost identical among objects, variations in the spectral profile of the PAH features have been reported (Peeters et al., 2002a).

Theoretical studies indicate that the relative intensity of the PAH features depends on the physical conditions of PAHs and radiation field (Schutte et al., 1993). The intensity ratio of the 7.7 to 11.3 μm features ($I_{7.7}/I_{11.3}$) is used as an indicator of the PAH ionization fraction (Bregman & Temi, 2005) as well as the intensity ratio of the 6.2 to 11.3 μm features ($I_{6.2}/I_{11.3}$). Systematic variations in the PAH features around 6–11 μm with the distance from the illuminating star in the reflection nebula, NGC 7023, have been reported (Berné et al., 2007, 2008). They conclude that the variations can be attributed to the variation in the radiation intensity. Mori et al. (2012b) report that the intensity ratio of the 3.3 to 11.3 μm features ($I_{3.3}/I_{11.3}$) in a star-forming regions in the LMC decreases when the star-

forming activity is intense. They propose that the decrease is attributed to the destruction of small-sized PAHs. The relative intensity of the PAH features is a useful tool to investigate the conditions of PAHs.

Peeters et al. (2002a) categorize the profiles of the PAH features around 6–9 μm into three classes (Class $\mathcal{A}$, $\mathcal{B}$, and $\mathcal{C}$). Interstellar objects such as star-forming regions tend to show Class $\mathcal{A}$ features, while circumstellar objects like PNe and post-AGB stars tend to show Class $\mathcal{B}$ or $\mathcal{C}$ features. A similar trend has been reported for the profiles of the PAH features at 3.3 and 11.3 μm by van Diedenhoven et al. (2004). However, the origin of this difference remains unclear.

PAHs are thought to be vulnerable to harsh environments such as a strong radiation field (Allain et al., 1996a,b), hot plasma (Micelotta et al., 2010b), and interstellar shocks (Micelotta et al., 2010a). A steep decline in the intensity of the 3.3 μm PAH emission at the ionization front of the Orion Nebula is observationally confirmed (Giard et al., 1994; Sellgren et al., 1990), indicating PAH destruction in the ionized region. Dehydrogenation is proposed as a PAH processing mechanism. Montillaud et al. (2013) investigate PAHs under photo-dissociation region (PDR) conditions and propose that small-sized PAHs ($N_C \lesssim 50$, where N_C is the number of carbon atoms in PAHs) can be totally dehydrogenated in NGC 7023.

Planetary nebulae (PNe) are a late phase of low- and intermediate-mass stellar evolution. They are generally surrounded by a dusty envelope and sometimes show PAH emission. Like other dust grains, PAHs are thought to be formed around evolved stars and then ejected into the interstellar region (e.g., Buss et al., 1991). PAHs in PNe tend to show Class $\mathcal{B}$ features, while Class $\mathcal{A}$ features are widely detected in interstellar space. Hony et al. (2001) report that the 12.7 μm feature is significantly weak in PNe compared to that in interstellar space. They propose that the difference in the 11–14 μm features reflects the structure of PAHs. PAHs in PNe should be in a transitional phase from the circumstellar to interstellar regions. Central stars of PNe are among the hottest stars in the Universe. Thus, PAHs in PNe would be exposed to a harsh environment. Whether PAHs are be processed in PNe should be investigated. The PN is an ideal object for the investigation of the evolution and processing of PAHs.

In the previous chapter, the evolution of the PAH features in the 3 μm region is investigated. To account for the variation of the PAH features with PN evolution, we proposed a hypothesis: PAHs with rich aliphatic components are taken into the envelope as the envelope expands. The explanation can be tested with the mid-infrared PAH features, since the proposed mechanism also affects the mid-infrared PAH features.

This chapter is intended to interpret the variations seen in the near- to mid-infrared PAH features. The relative intensity and peak wavelength of the PAH features are measured. Both are investigated in terms of the PN evolution. Details of the data we used are described in Section 5.2. The results are shown in Section 5.3. In Section 5.4, the origin of the variations in the PAH features are discussed. The conclusion is summarized in Section 5.5.

Table 5.1. List of the Galactic Planetary Nebulae

PN G	Name	*AKARI* ID	*Spitzer* AOR	Note
002.0−13.4	IC 4776	3460003	11337216	mixed-chemistry
060.1−07.7	NGC 6886	3460024	19902976	···
074.5+02.1	NGC 6881	3460028	19904000	···
095.2+00.7	K 3-62	3460033	25847808	SiC, fullerene
146.7+07.6	M 4-18	3460097	21957632	···
194.2+02.5	J 900	3460117	27018752	···
211.2−03.5	M 1-6	3460036	21953024	SiC, fullerene
226.7+05.6	M 1-16	3460100	21955584	···
235.3−03.9	M 1-12	3460038	25849856	SiC, fullerene
278.6−06.7	He 2-26	3460101	25851136	SiC
294.9−04.3	He 2-68	3460047	25852417	SiC
296.3−03.0	He 2-73	3460048	25852929	mixed-chemistry
307.5−04.9	MyCn 18	3460053	25853696	mixed-chemistry
324.8−01.1†	He 2-133	3460062	25855232	mixed-chemistry
327.1−01.8	He 2-140	3460065	25856256	···
336.3−05.6	He 2-186	3460069	25857792	···
356.1+02.7	Th 3-13	3460076	10499072	···
357.6+02.6	H 1-18	3460082	25865216	···

Note. — †: the effective temperature is not available.

5.2 Data

5.2.1 Target Selection

We selected 18 PNe in the PNSPC catalog. They are also observed by the *Spitzer*/IRS and their mid-infrared spectra show prominent PAH features. Most targets are considered to be a PN with carbon-rich dust, suggesting that they are similar in terms of the initial mass and metalicity (Stanghellini & Haywood, 2010). Table 5.1 lists the name of the targets, the pointing ID of the *AKARI*/IRC spectrum, and the Astronomical Observation Requests (AORs) key of the *Spitzer*/IRS spectrum.

5.2.2 Near-Infrared PAH Features

Intensities of the near-infrared PAH features were obtained from the PNSPC catalog. The intensities were measured by spectral fitting with a combination of Lorentzian functions. The intensity of the 3.4 μm PAH feature ($I_{3.4}$) is the summation of the intensities of the sub-features in the 3.4–3.5 μm region. Details of

the near-infrared spectral fitting are written in Appendix B.

5.2.3 Extinction

The extinction value toward the objects at the V-band was adopted from the PNSPC catalog. We assumed the same A_V values for the near- and mid-infrared spectra. The extinction values in the PNSPC catalog were the total extinction from interstellar and circumstellar dust. The contribution from the circumstellar dust was not negligible (*see* Section 4.3.1). However, the extinction curve of the circumstellar dust was not known. We tentatively adopted the extinction curve provided by Mathis (1990).

5.2.4 Effective Temperature of PNe

Effective temperature was collected from literature (Grewing & Neri, 1990; Kaler, 1976; Kaler & Jacoby, 1991; Lumsden et al., 2001; Mendez et al., 1992; Phillips, 2003; Preite-Martinez et al., 1989, 1991). For 17 of 18 PNe, the effective temperature was obtained. For some PNe, the effective temperature was estimated by different methods. We adopted a weighted mean for them based on typical uncertainties. Details are given in Section 3.5.3.

5.2.5 Total Infrared Intensity

The total infrared intensity of each PN (I_{IR}) was estimated based on the *WISE* All-Sky Catalog (Cutri et al., 2012a,b), the *AKARI*/IRC Point Source Catalog (Ishihara et al., 2010b), the *AKARI*/FIS Bright Source Catalog (Yamamura et al., 2010), and the *IRAS* point-source catalog (Joint Iras Science, 1994; Neugebauer et al., 1984). The infrared spectral energy distribution was fitted by single- or two-temperature graybody functions with a varying emissivity. The total infrared intensity was obtained by integrating the fitted function.

5.2.6 Mid-Infrared PAH Features

We obtained 5.5–14.0 μm spectra of the targets from SHA. The PBCD spectra were obtained from the program IDs of 1451, 3235, 3633, 30430, 40035, and 50261. Observations were performed with the SL-module of the *Spitzer*/IRS. The achieved spectral resolution was about 80 at 10 μm. The spectra in the different orders were combined to obtain the continuous spectrum.

The IRS spectroscopy was performed with the slit, which was about $\sim 4''$ in width. Some targets were extended for the PSF of the IRS and there could be loss in flux due to the slit efficiency. Flux calibration of the IRS spectra was important to discuss the relative intensity of the PAH features in the near- and mid-infrared. Since the IRS spectrum totally covered the wavelength coverage of the S9W band, we used the 9 μm flux in the *AKARI*/IRC Point Source Catalog to scale the IRS spectra. Define F_ν^{obs} as the observed flux density of the IRS spectrum. The flux

density observed with the S9W band was estimated as

$$F_\nu^{\rm IRS}({\rm S9W}) = \frac{\int F_\nu^{\rm obs} R^{\rm S9W}(\nu)\frac{d\nu}{\nu}}{\int \left(\frac{\nu_0}{\nu}\right) R^{\rm S9W}(\nu)\frac{d\nu}{\nu}}, \tag{5.1}$$

where $R^{\rm S9W}$ and ν_0 are the RSRF and the nominal frequency of the S9W band, respectively. The IRS spectra were scaled by the ratio of $F_\nu^{\rm IRC}({\rm S9W})/F_\nu^{\rm IRS}({\rm S9W})$, where $F_\nu^{\rm IRC}({\rm S9W})$ is the flux density in the *AKARI*/IRC Point Source Catalog.

5.3 Results

5.3.1 Obtained Spectra

The obtained near- to mid-infrared spectra are shown in Figure 5.1 with 1-σ error bars. The spectra show the major PAH features at 3.3, 6.2, 7.7, 8.6, and 11.3 μm. Some spectra show PAH features at 5.7, 12.0, and 12.7 μm, although they are weaker than the major features. The emission features at 3.4–3.5 μm are usually attributed to aliphatic C—H bonds in PAHs (e.g., Joblin et al., 1996).

Some PNe (e.g., PN G095.2+00.7) show a broad emission feature peaking around 12 μm. This emission is typically attributed to silicon carbide (SiC; Bernard-Salas et al., 2009; Speck et al., 2009) or hydrogenated amorphous carbons (Stanghellini et al., 2012). Some of them are known as PNe with fullerene emission (García-Hernández et al., 2010; Otsuka et al., 2013). On the other hand, some PNe (e.g., PN G002.0−13.4) show another broad emission feature peaking around 10 μm, which is attributed to amorphous silicate. They are usually referred to as PNe with mixed-chemistry dust (Perea-Calderón et al., 2009). The PNe with SiC, fullerene, or silicate emission are noted in the fifth column of Table 5.1.

5.3.2 Spectral Fitting in the Mid-Infrared

The intensities of the PAH features in the mid-infrared are measured by spectral fitting. A model spectrum is constructed for the fitting by a linear combination of spectral features as

$$F_\lambda(\lambda) = \left[f_\lambda^{\rm cont}(\lambda) + f_\lambda^{\rm line}(\lambda) + f_\lambda^{\rm dust}(\lambda)\right] e^{-\tau(\lambda)}, \tag{5.2}$$

where $f_\lambda^{\rm cont}(\lambda)$, $f_\lambda^{\rm line}(\lambda)$, and $f_\lambda^{\rm dust}(\lambda)$ are the components of continuum, line, and dust emission, respectively, and $\tau(\lambda)$ is the extinction at λ. $f_\lambda^{\rm cont}(\lambda)$ is given by a combination of graybody functions and a plateau emission around 6–9 μm. $f_\lambda^{\rm line}(\lambda)$ is given by a combination of Gaussian functions. The position and width of the line profiles are fixed. $f_\lambda^{\rm dust}(\lambda)$ is given by a combination of the PAH features and the broad emission features such as SiC and silicate. The spectral profile of the PAH features is given by a Lorentzian function convolved with the profile of the line emission. The position and width of the PAH features are defined according

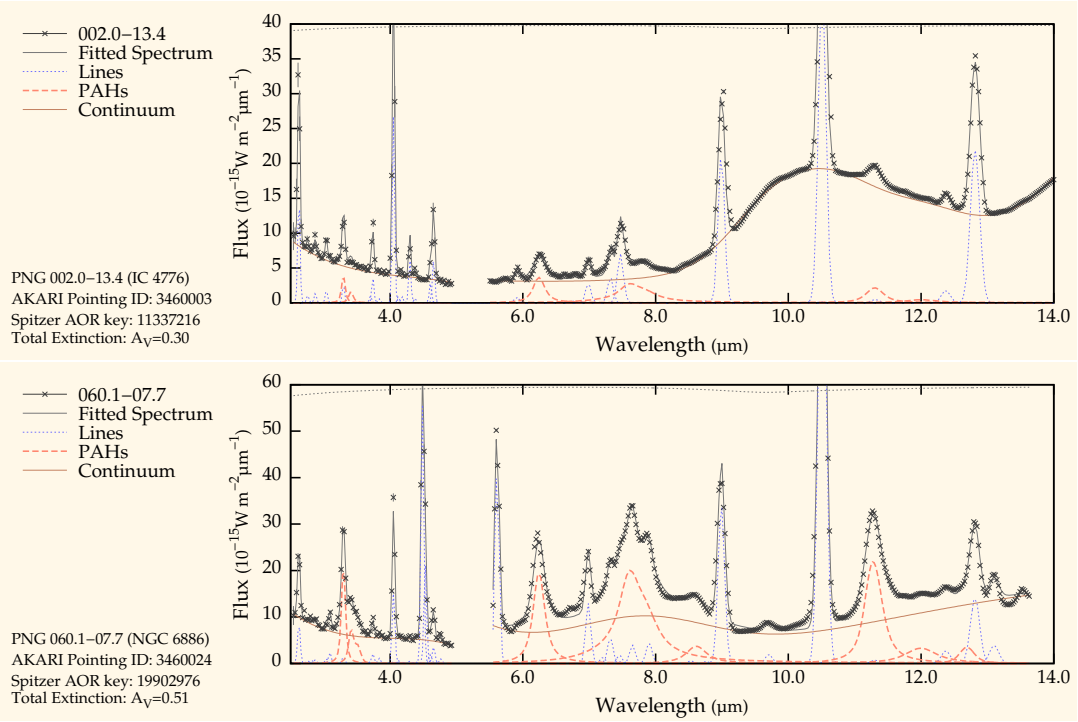

Figure 5.1 – The list of the 2.5–14.0 μm spectra of PNe. The 2.5–5.0 μm part is obtained with the *AKARI*/IRC, while the 5.5–14.0 μm part is obtained with the *Spitzer*/IRS. The symbols with error bars show the observed spectra. The results of the spectral fitting are shown by the solid, dotted, and dashed lines (*see* text).

to PAHFIT[*1] (Smith et al., 2007). The broad emission features are approximated by a combination of Gaussian functions. In the fitting, the intensities of the spectral features are taken as free parameters with a constraint that the spectral features should be non-negative. The uncertainty of the intensity is calculated by a parameterized bootstrap method. Details are described in Appendix C.

The results of the spectral fitting are also given in Figure 5.1. The fitted spectrum is shown by the gray solid line. The summation of the continuum emission and the broad emission features is given by the brown solid line. The emission line components are given by the blue dotted lines. The PAH features are shown by the red dashed lines. The gray dotted line shows the extinction curve.

The intensities of the 6.2, 7.7, and 11.3 μm PAH features are summarized in Table 5.2 as well as the intensities of the 3 μm PAH features. Although the PAH features at 5.7, 8.6, 12.0, and 12.7 μm are included in fitting, they are weak or contaminated with other spectral features. These features are not used in the following sections.

5.3.3 Peak Wavelength of the 6.2 μm PAH Feature

The peak wavelength of the 6.2 μm PAH feature ($\lambda^{6.2}$) is a good indicator of the PAH emission classes (Peeters et al., 2002a). Although the spectral profile of the

[*1] IDL routine developed for spectral fitting of the mid-infrared PAH features, available at `http://tir.astro.utoledo.edu/jdsmith/`

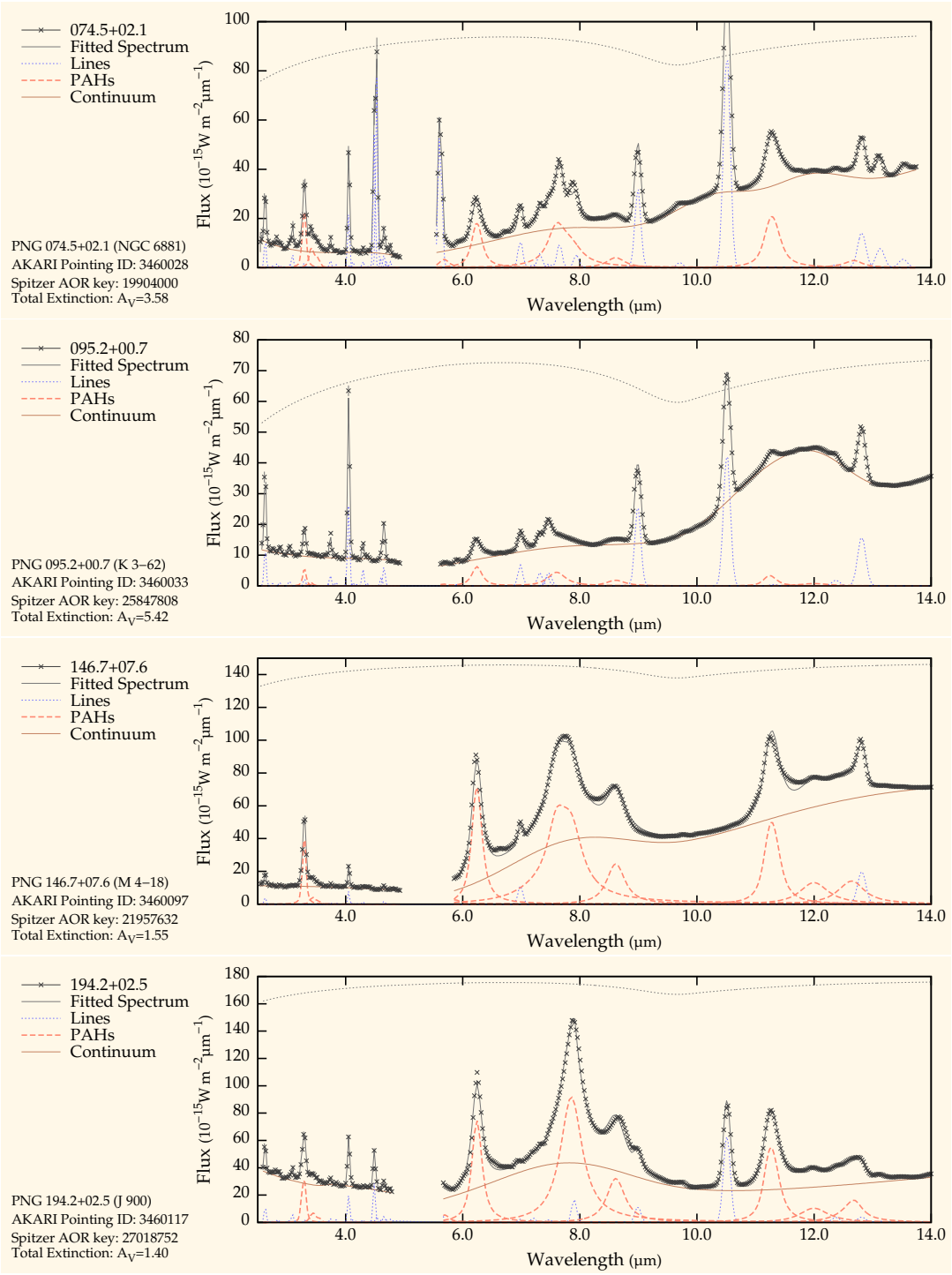

Figure 5.1 – *Cont.*

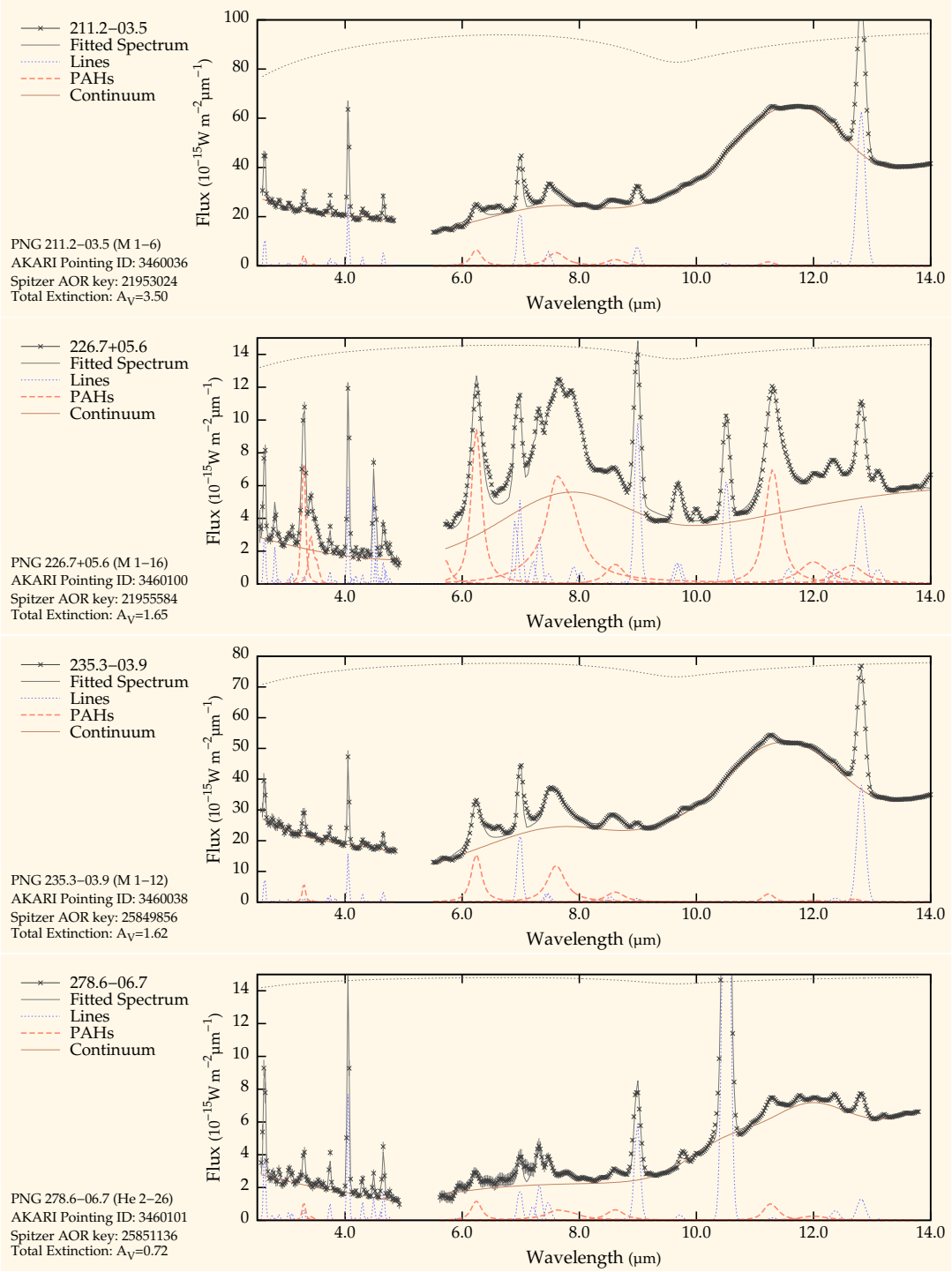

Figure 5.1 – *Cont.*

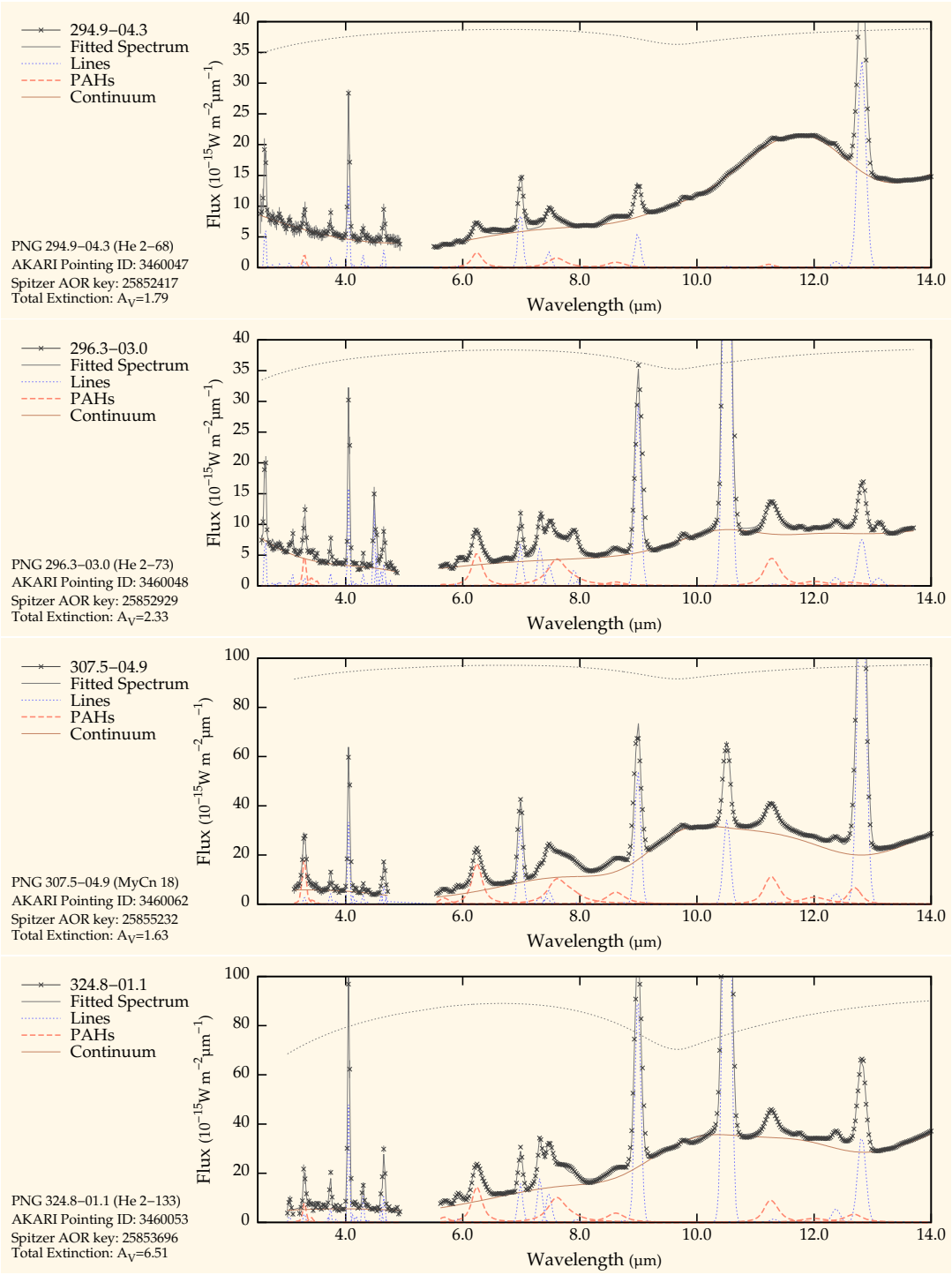

Figure 5.1 – *Cont.*

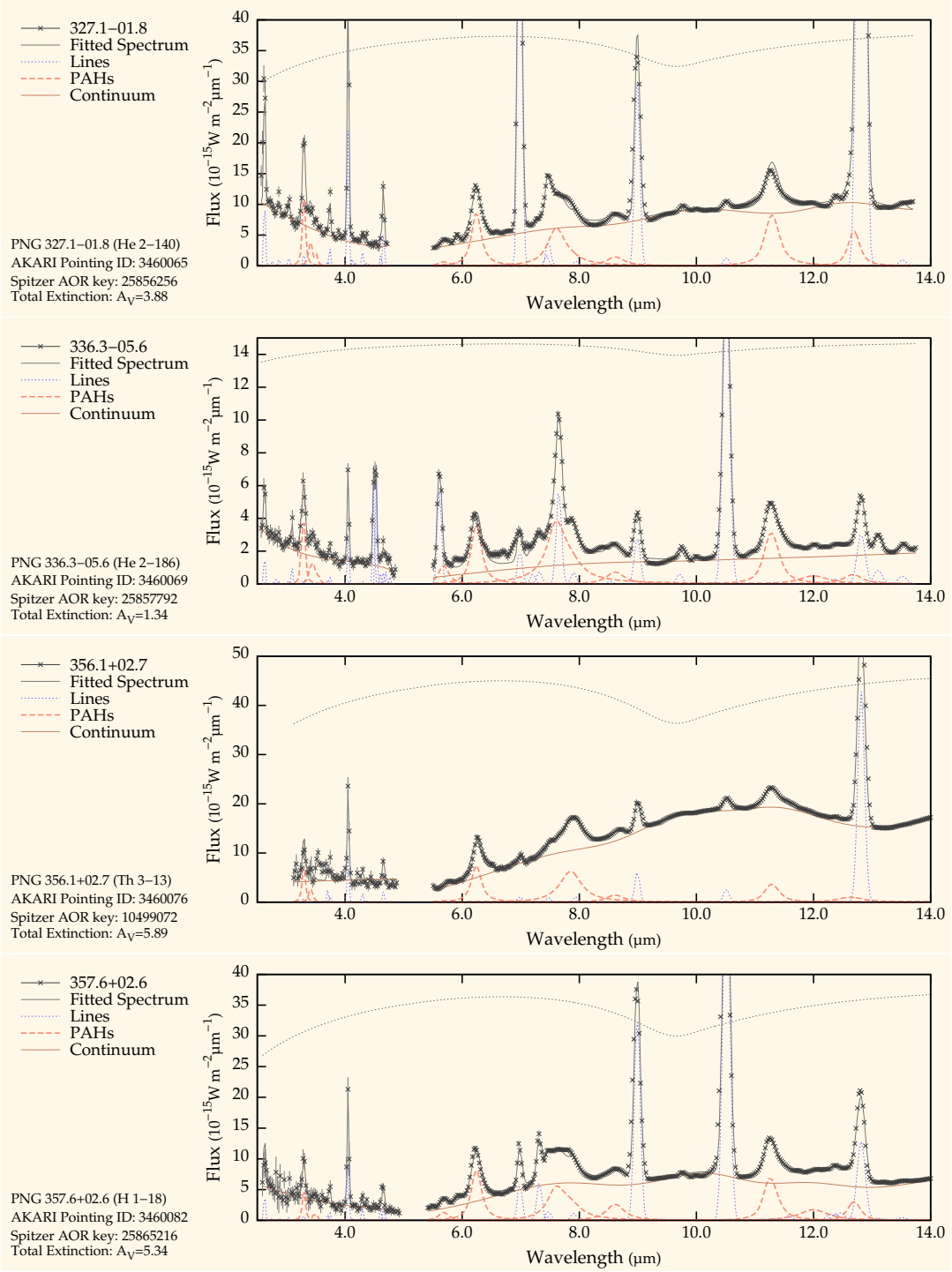

Figure 5.1 – *Cont.*

Table 5.2. Intensities of the PAH emission

PN G	3.3 μm	3.4 μm	6.2 μm	7.7 μm	11.3 μm
002.0−13.4	$3.52^{+0.20}_{-0.22}$	$1.86^{+0.15}_{-0.18}$	$11.28^{+0.80}_{-0.68}$	$23.78^{+1.90}_{-1.85}$	$9.80^{+0.65}_{-0.70}$
060.1−07.7	$22.03^{+0.40}_{-0.28}$	$13.31^{+0.33}_{-0.24}$	$60.57^{+0.36}_{-0.35}$	$171.21^{+1.62}_{-1.58}$	$96.70^{+0.45}_{-0.45}$
074.5+02.1	$27.84^{+1.41}_{-1.08}$	$16.32^{+1.24}_{-0.73}$	$59.99^{+0.70}_{-0.71}$	$144.91^{+11.12}_{-9.29}$	$101.76^{+1.26}_{-1.30}$
095.2+00.7	$6.89^{+0.30}_{-0.48}$	$1.55^{+0.23}_{-0.24}$	$21.09^{+0.89}_{-0.88}$	$27.21^{+2.74}_{-1.20}$	$14.42^{+1.67}_{-1.71}$
146.7+07.6	$42.17^{+1.61}_{-1.18}$	$7.61^{+0.96}_{-0.35}$	$221.42^{+0.32}_{-0.35}$	$627.71^{+0.95}_{-1.00}$	$227.22^{+0.59}_{-0.59}$
194.2+02.5	$38.48^{+2.05}_{-2.22}$	$12.99^{+2.16}_{-1.65}$	$231.84^{+0.39}_{-0.46}$	$645.26^{+1.68}_{-1.68}$	$239.68^{+0.72}_{-0.74}$
211.2−03.5	$4.60^{+2.57}_{-0.64}$	$0.59^{+1.70}_{-0.33}$	$21.57^{+0.25}_{-0.27}$	$31.63^{+0.45}_{-0.45}$	$5.67^{+0.19}_{-0.19}$
226.7+05.6	$8.62^{+0.44}_{-0.44}$	$5.18^{+0.23}_{-0.17}$	$29.51^{+0.27}_{-0.26}$	$64.88^{+1.10}_{-1.23}$	$33.01^{+0.11}_{-0.12}$
235.3−03.9	$5.72^{+0.99}_{-0.72}$	$1.09^{+1.13}_{-0.89}$	$49.13^{+0.89}_{-0.94}$	$67.37^{+2.18}_{-1.51}$	$8.75^{+0.52}_{-0.56}$
278.6−06.7	$1.03^{+0.21}_{-0.18}$	$0.31^{+0.15}_{-0.19}$	$3.66^{+0.38}_{-0.38}$	$5.97^{+1.07}_{-0.97}$	$4.28^{+0.81}_{-0.79}$
294.9−04.3	$2.08^{+1.30}_{-1.01}$	< 1.25	$7.86^{+0.58}_{-0.56}$	$8.97^{+0.68}_{-0.66}$	$1.76^{+0.37}_{-0.35}$
296.3−03.0	$5.01^{+0.49}_{-0.52}$	$2.30^{+0.40}_{-0.23}$	$16.96^{+0.92}_{-0.89}$	$29.89^{+2.98}_{-3.55}$	$20.96^{+1.14}_{-1.16}$
307.5−04.9	$20.69^{+1.49}_{-0.89}$	$2.80^{+1.14}_{-0.79}$	$52.50^{+0.93}_{-0.89}$	$73.50^{+2.55}_{-2.55}$	$49.40^{+1.46}_{-1.50}$
324.8−01.1	$10.65^{+1.42}_{-0.03}$	$3.24^{+1.15}_{-0.28}$	$50.00^{+1.11}_{-1.03}$	$70.18^{+2.85}_{-3.01}$	$44.97^{+1.95}_{-1.93}$
327.1−01.8	$12.54^{+0.88}_{-0.83}$	$6.49^{+1.02}_{-0.72}$	$27.39^{+0.82}_{-0.79}$	$39.42^{+4.43}_{-1.92}$	$39.71^{+0.82}_{-0.82}$
336.3−05.6	$4.35^{+0.71}_{-0.32}$	$2.31^{+0.36}_{-0.21}$	$11.51^{+0.41}_{-0.38}$	$29.26^{+1.23}_{-1.26}$	$14.03^{+0.47}_{-0.46}$
356.1+02.7	$8.69^{+0.61}_{-0.03}$	$3.96^{+1.22}_{-0.00}$	$24.78^{+1.34}_{-1.47}$	$48.15^{+3.53}_{-3.28}$	$18.54^{+1.48}_{-1.51}$
357.6+02.6	$5.80^{+0.95}_{-0.79}$	$1.46^{+1.15}_{-0.03}$	$27.99^{+0.91}_{-0.87}$	$43.48^{+2.74}_{-2.39}$	$32.74^{+1.23}_{-1.19}$

Note. — The intensities are given in units of 10^{-16}W m^{-2}.

7.7 μm PAH feature is also sensitive to the PAH classes, it is difficult to properly estimate the emission classes by the 7.7 μm feature due to contamination of emission lines and the uncertainty in the continuum emission. Thus, the PAH emission class is investigated based on the peak wavelength of the 6.2 μm feature. We calculate a correlation given by

$$C(\lambda_c) = \sum_{\lambda} f_\lambda(\lambda)\mathcal{G}_{6.2}(\lambda;\lambda_c), \tag{5.3}$$

where $f_\lambda(\lambda)$ is the continuum-subtracted and extinction-corrected flux density at λ and $\mathcal{G}_{6.2}(\lambda;\lambda_c)$ is the profile of the 6.2 μm feature peaking at λ_c. $\lambda^{6.2}$ was defined in such a way that $C(\lambda_c)$ should be maximum. The uncertainty in $\lambda^{6.2}$ is estimated based on a parameterized bootstrap method.

5.3.4 Model Calculation of the PAH Features

The relative intensity of the PAH features is calculated by a simple PAH model to investigate the observed intensity ratio. The calculation is based on the PAH emission model developed by Schutte et al. (1993) and modified to include the latest parameters (Draine & Li, 2001, 2007). Details of the calculation are described in Mori et al. (2012b).

The emission model includes the incident radiation field, the size distribution of PAHs, and the PAH ionization fraction as parameters. The incident radiation field is approximated by the blackbody radiation with the temperature of

Table 5.3 – PAH Emission Model Parameters

Parameters	Values
Radiation field	$B_\nu(50\,000\,\mathrm{K})^\dagger$ for $h\nu \leq 13.6\,\mathrm{eV}$
Size Distribution	$dN_{PAH} \propto N_C^{-1.83} dN_C$, $N_C \in (20, 4\,000)$
Ionization Fraction	$f_{ion} = (0.0, 0.2, 0.4, 0.6, 0.8, 1.0)$

Note. — † a blackbody radiation function.

$50,000\,\mathrm{K}$. We assume that PAHs are located in the envelope. If the HII region is radiation-bounded, all the hydrogen-ionizing photons are trapped and unable to reach the envelope. Thus, the photons with $h\nu > 13.6\,\mathrm{eV}$ are removed. The PAH size distribution is given by a power-law function (Mathis et al., 1977), $dN_{PAH} \propto a^{-3.5} da$, where a is the radius of PAHs and N_{PAH} is the number of PAHs with the size between a and $a+da$. The number of carbon atoms in PAHs (N_C) is given by $N_C \propto a^3$ and ranges from 20 to 4 000 as assumed in Mori et al. (2012a,b). The ionization fraction of PAHs is given as a free parameter. Define f_{ion} as the PAH ionization fraction. Since the dependence of f_{ion} on N_C is small (Allain et al., 1996b), f_{ion} is assumed to be constant with N_C. The relative intensity is calculated for $f_{ion} = 0.0, 0.2, \ldots$, and 1.0. The parameters are listed in Table 5.3.

Allain et al. (1996b) suggest that small-sized PAHs can be dehydrogenated when they are exposed to a strong radiation field. Small-sized PAHs in PNe can be significantly dehydrogenated since the central star of PNe is hot and bright. Le Page et al. (2001) report that the dehydrogenation rate of PAHs rapidly drops when N_C becomes larger than 30. Montillaud et al. (2013) propose that smaller PAHs ($N_C \lesssim 50$–70) are fully dehydrogenated in PDRs, while larger PAHs are insensitive to dehydrogenation. Thus, we assume that there is a threshold in N_C such that PAHs are totally dehydrogenated when N_C is smaller than the threshold. We define the threshold as $N_{C\,Hmin}$, which defines the minimum size of PAHs which retain peripheral hydrogen atoms. The relative intensities are calculated in such a way that the vibrational modes corresponding to the 3.3 and 11.3 μm features are disabled when N_C is smaller than $N_{C\,Hmin}$. For $N_{C\,Hmin} = 20$, which is the minimum N_C, no PAH dehydrogenation is assumed. Note that the calculated intensities may change significantly when basic parameters of PAH model such as Einstein's A-coefficients are modified.

5.3.5 Properties of PAHs

The PAH features at 6.2, 7.7, and 8.6 μm become strong when PAHs are ionized, while the 3.3 and 11.3 μm PAH features strengthen when PAHs are neutral. Figure 5.2 shows the observed $I_{7.7}/I_{11.3}$ ratio against the $I_{6.2}/I_{11.3}$ ratio. The star, and spade symbols show the PNe with the fullerene and silicate emission, respectively, while the cross symbols are the ones without neither fullerene nor silicate emission. The arrow shows the dependence of the ratios on the uncertainty in A_V: the data points range within the size of the arrow when A_V increases by

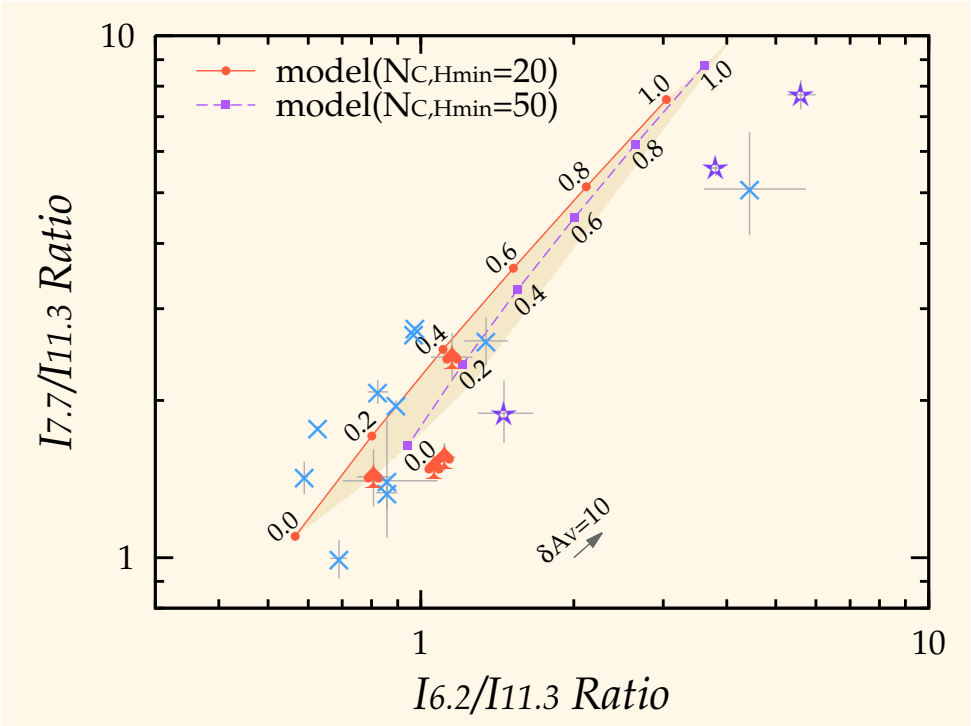

Figure 5.2 – The $I_{7.7}/I_{11.3}$ ratio against the $I_{6.2}/I_{11.3}$ ratio. The cross, star, and spade symbols are, respectively, normal, fullerene, and mixed-chemistry PNe (*see* text). The lines with symbols show the intensity ratios provided by the PAH emission model. The gray-shaded region indicates the region explained by the PAH emission model when $N_{C\,Hmin}$ changes from 20 to 100. The arrow on the bottom shows the effect from the uncertainty in the extinction (*see* text).

10 mag. A typical uncertainty in A_V is assumed to be no greater than 1 mag. The uncertainty in A_V is almost negligible in Figure 5.2. The ratios are well correlated with each other. Similar results have been reported by Bernard-Salas et al. (2009) for PNe in the MCs.

The results of the model calculation are overlaid by the lines with symbols. The number beside the symbols shows the ionization fraction f_{ion}. The solid line with the circles shows the model without any dehydrogenation, while the dashed line with the squares shows the model with $N_{C\,Hmin} = 50$. The gray-shaded region indicates the intensity ratio reproduced by the model when $N_{C\,Hmin}$ varies from 20 to 100 and f_{ion} changes from 0.0 to 1.0, suggesting that the effect of hydrogenation is small in the $I_{6.2}/I_{11.3}$ and $I_{7.7}/I_{11.3}$ ratios.

The $I_{6.2}/I_{11.3}$ ratio typically ranges between 0.6 and 2.0, while the $I_{7.7}/I_{11.3}$ ratio varies from 1.0 to 3.0. This indicates that the ionization fraction of PAHs in PNe is typically $\lesssim$0.4. Bernard et al. (1994) report a low ionization fraction of PAHs for the Galactic PN, BD+30° 3639. The present results are consistent with theirs. Three PNe (PN G211.2−03.5, 235.3−03.9, and 294.9−04.3), however, show significantly higher $I_{6.2}/I_{11.3}$ and $I_{7.7}/I_{11.3}$ ratios. The ionization fraction of PAHs is considered to be large for these PNe. Their $I_{6.2}/I_{11.3}$ ratio is slightly higher than the region reproduced by the model with varying $N_{C\,Hmin}$. This displacement may be attributed to the size distribution of PAHs: the $I_{6.2}/I_{11.3}$ ratio

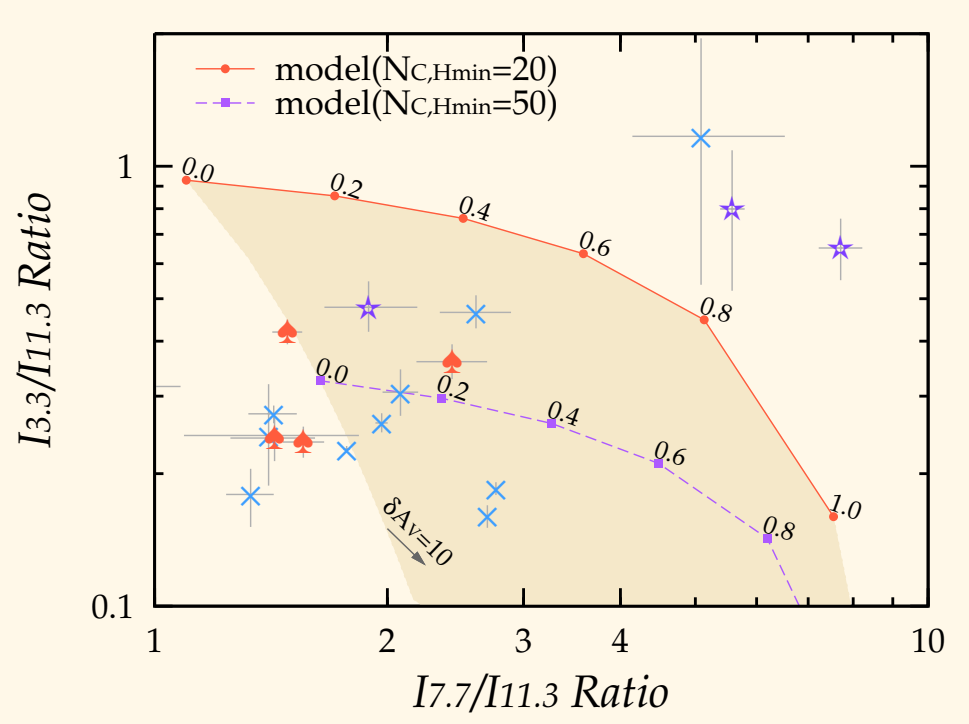

Figure 5.3 – The $I_{3.3}/I_{11.3}$ ratio against the $I_{7.7}/I_{11.3}$ ratio. The symbols, lines, shaded region, and arrow are the same as in Figure 5.2.

becomes high when small-sized PAHs are abundant.

Both the 3.3 and 11.3 μm PAH features are attributed to vibrational modes of C—H bonds and strengthen when PAHs are neutral. The $I_{3.3}/I_{11.3}$ ratio is sensitive to neither the C/H ratio nor the ionization fraction of PAHs. On the other hand, the 3.3 μm feature is most efficiently emitted by small-sized PAHs because of their small heat capacity (Schutte et al., 1993). The $I_{3.3}/I_{11.3}$ ratio can be a good indicator of the PAH excitation, or the fraction of small-sized PAHs.

Figure 5.3 shows the $I_{3.3}/I_{11.3}$ ratio against the $I_{7.7}/I_{11.3}$ ratio. The $I_{3.3}/I_{11.3}$ ratio tends to be low for PNe with a low $I_{7.7}/I_{11.3}$ ratio. On the other hand, three PNe with a high $I_{7.7}/I_{11.3}$ ratio show a high $I_{3.3}/I_{11.3}$ ratio. Small-sized PAHs should be abundant in these three PNe, consistent with the high $I_{6.2}/I_{11.3}$ ratios in Figure 5.2.

The relative intensities provided by the model calculation are shown by the lines with the symbols as in Figure 5.2. The model without dehydrogenation overestimates the $I_{3.3}/I_{11.3}$ ratio for most PNe. The observed $I_{3.3}/I_{11.3}$ ratios are consistent with the model with $N_{C\,Hmin} \simeq 50$. Montillaud et al. (2013) conclude that PAHs with $N_C \lesssim 50$ are totally dehydrogenated in the reflection nebula, NGC 7023. The present result is consistent with their conclusion. Some PNe, however, show a small $I_{7.7}/I_{11.3}$ ratio which is not reproduced by the PAH emission model with varying $N_{C\,Hmin}$. The $I_{7.7}/I_{11.3}$ ratio may decrease when the amount of small-sized PAHs is reduced. Thus, these PNe may have fewer small-sized PAHs. The deficiency of small-sized PAHs could also decrease the $I_{3.3}/I_{11.3}$ ratio. The low $I_{3.3}/I_{11.3}$ ratio in PNe could be attributed to a combination of PAH

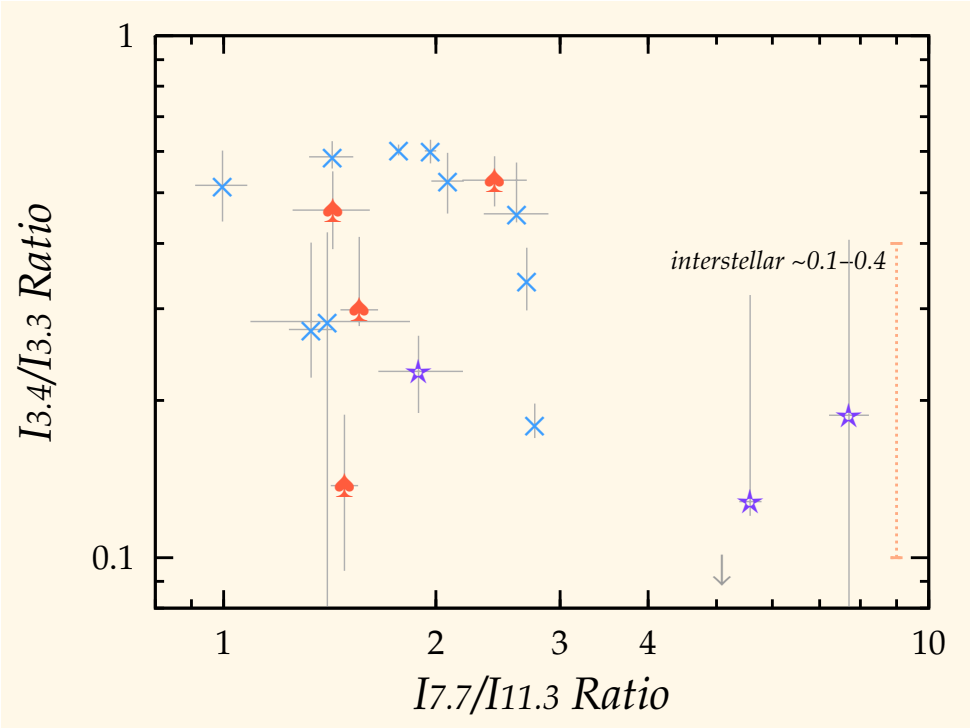

Figure 5.4 – The $I_{3.4}/I_{3.3}$ ratio against the $I_{7.7}/I_{11.3}$ ratio. The value is replaced by the upper limit when $S/N < 1$. The symbols are the same as in Figure 5.2. The dotted line on the right shows a typical range of the $I_{3.4}/I_{3.3}$ ratio for Galactic compact H II regions (Mori et al., 2014).

dehydrogenation and a deficiency of small-sized PAHs.

The 3.4–3.5 μm features are usually attributed to stretching modes of aliphatic C—H bonds (e.g., Joblin et al., 1996; Schutte et al., 1993). The 3.4–3.5 μm features are supposed to be effectively emitted by small-sized PAHs as the 3.3 μm PAH feature (Jones, 2012b). The intensity ratio of the 3.4 to 3.3 μm features ($I_{3.4}/I_{3.3}$) is assumed to be insensitive to the PAH size distribution. The $I_{3.4}/I_{3.3}$ ratio can be an indicator of the relative amount of aliphatic components in PAHs.

Figure 5.4 shows the $I_{3.4}/I_{3.3}$ ratio against the $I_{7.7}/I_{11.3}$ ratio. It is notable that the aliphatic features are weak or not detected for the three PNe with a large PAH ionization fraction. On the other hand, PNe with a small PAH ionization fraction show a relatively high $I_{3.4}/I_{3.3}$ ratio. The figure indicates that the $I_{3.4}/I_{3.3}$ ratio decreases when PAHs are ionized. Joblin et al. (1996) and Bregman & Temi (2005) report the same trend for reflection nebulae.

The vertical dotted line on the right of Figure 5.4 shows a typical range of the $I_{3.4}/I_{3.3}$ ratio for Galactic compact H II regions indicated by Mori et al. (2014). In Section 4.3.1, we report that about a half of Galactic PNe show a significantly higher $I_{3.4}/I_{3.3}$ ratio than a typical Galactic H II region. Figure 5.4 indicates that only PNe with a small PAH ionization fraction show such a high $I_{3.4}/I_{3.3}$ ratio.

The spectral profile of the 6.2 μm PAH feature is intensively investigated by Peeters et al. (2002a). The 6.2 μm PAH feature is classified by $\lambda^{6.2}$ into three classes (Class $\mathcal{A}$, $\mathcal{B}$, and $\mathcal{C}$) as follows: The 6.2 μm feature is regarded as Class $\mathcal{A}$ when $\lambda^{6.2}$ is about 6.22 μm. When $\lambda^{6.2}$ is in the range of 6.24–6.28 μm, the feature

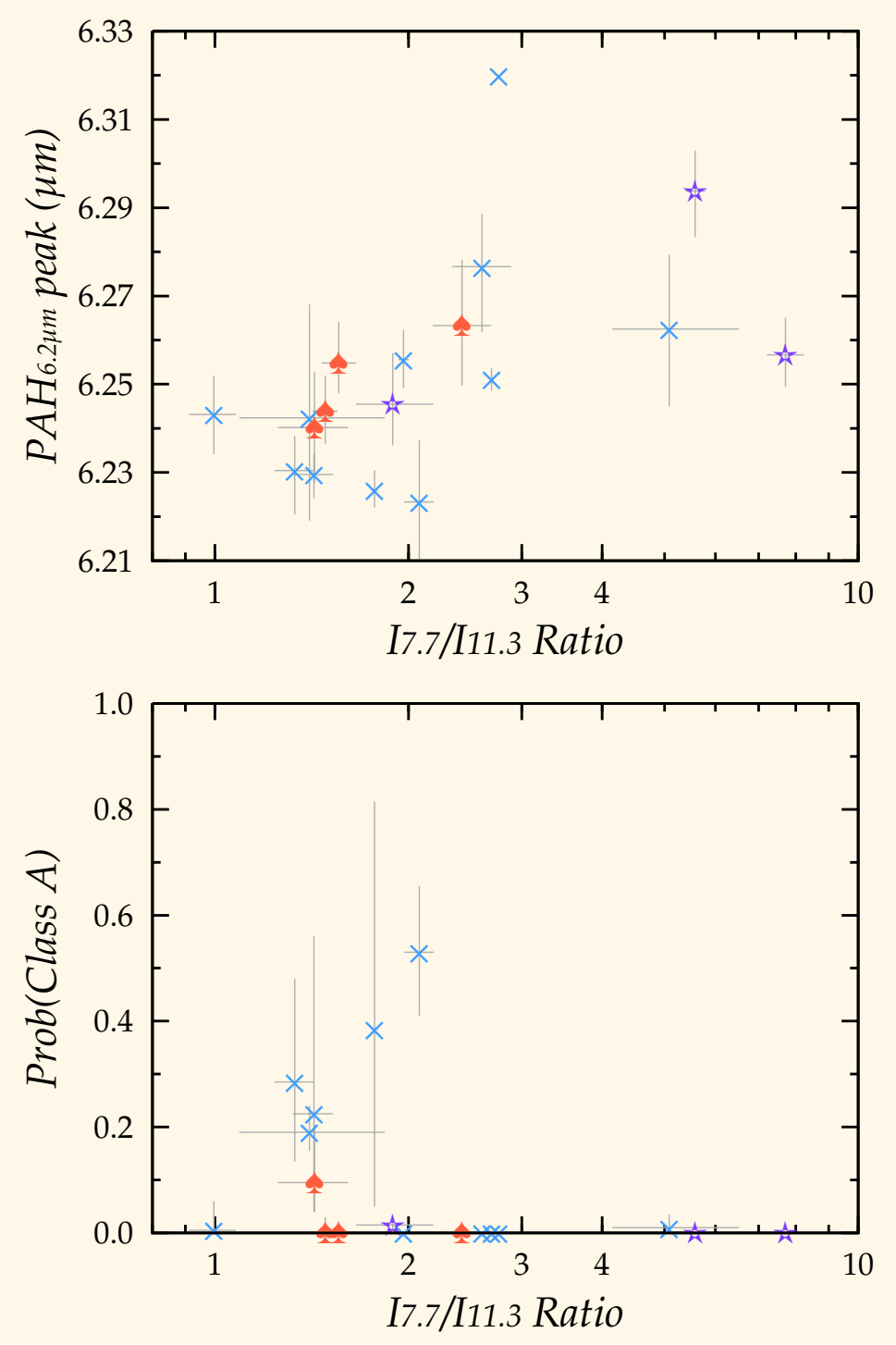

Figure 5.5 – Top: $\lambda^{6.2}$ in units of μm against the $I_{7.7}/I_{11.3}$ ratio. r_s is about 0.71 for $N_{obj} = 18$. Bottom: prob(Class $\mathcal{A}$) against the the $I_{7.7}/I_{11.3}$ ratio. The symbols are the same as in Figure 5.2.

is classified as Class $\mathcal{B}$. If $\lambda^{6.2}$ is about 6.3 μm or longer, the feature is classified as Class $\mathcal{C}$. $\lambda^{6.2}$ can be used as an indicator of the PAH emission class.

The top panel of Figure 5.5 shows $\lambda^{6.2}$ against the $I_{7.7}/I_{11.3}$ ratio. There is a

clear trend such that $\lambda^{6.2}$ decreases with decreasing $I_{7.7}/I_{11.3}$ ratio. The Spearman's correlation coefficient (r_s) is about 0.71 for $N_{obj} = 18$, suggesting that the trend is statistically significant at a 99.5% confidence level.

To quantitatively investigate the PAH emission class, the probability that the 6.2 μm feature is Class $\mathcal{A}$ (prob(Class $\mathcal{A}$)) is defined as:

$$\text{prob(Class } \mathcal{A}) = \text{prob}(\lambda^{6.2} < 6.225\,\mu\text{m}). \tag{5.4}$$

The right hand side is calculated in such a way that the probability density function of $\lambda^{6.2}$, which is obtained by a parameterized bootstrap method, is integrated up to 6.225 μm. The bottom panel of Figure 5.5 shows prob(Class $\mathcal{A}$) against the $I_{7.7}/I_{11.3}$ ratio. The results indicate that some PNe have the Class $\mathcal{A}$ 6.2 μm feature, while prob(Class $\mathcal{A}$) is small for most PNe. The Class $\mathcal{A}$ 6.2 μm feature is detected only in PNe with a small PAH ionization fraction.

5.3.6 Evolution of the PAH Emission

As shown in Section 4.4.3, the effective temperature can be a good indicator of the evolutionary phase of PNe. The evolution of the PAH features is investigated in terms of the effective temperature.

The $I_{7.7}/I_{11.3}$ ratio is an indicator of the ionization fraction of PAHs. Figure 5.6 shows the evolution of the PAH ionization fraction. The effective temperatures of PNe with a large PAH ionization fraction are typically low, while the ionization fraction is small when PNe become evolved. The Spearman's correlation coefficient is about −0.49 for $N_{obj} = 17$, suggesting that the anti-correlation in Figure 5.6 is statistically significant at a 95% confidence level. The result indicates that the ionization fraction of PAHs decreases with the evolution of PNe.

The evolution of the PAH size distribution is investigated in terms of the variation in the $I_{3.3}/I_{11.3}$ ratio with the effective temperature. The evolution of the $I_{3.3}/I_{11.3}$ ratio is shown in Figure 5.7. The $I_{3.3}/I_{11.3}$ ratio decreases with increasing effective temperature, suggesting that the relative amount of small-sized PAHs decreases with PN evolution.

The evolution of the fractional amount of aliphatic components in PAHs is investigated in terms of the variation in the $I_{3.4}/I_{3.3}$ ratio with the effective temperature. Figure 5.8 shows the $I_{3.4}/I_{3.3}$ ratio against the effective temperature. The effective temperature tends to be low for PNe with a low $I_{3.4}/I_{3.3}$ ratio, while the $I_{3.4}/I_{3.3}$ ratio becomes high when the effective temperature is high. The Spearman's correlation coefficient, which is calculated for PNe with $S/N > 3$ for the $I_{3.4}/I_{3.3}$ ratio, is about 0.49 for $N_{obj} = 14$, suggesting that the trend is statistically significant at about a 90% confidence level. The result indicates that the fractional amount of aliphatic components in PAHs increases with PN evolution.

Figure 5.9 illustrates the evolution of the PAH emission class with the effective temperature. The vertical axis shows prob(Class $\mathcal{A}$) defined by the 6.2 μm PAH feature. prob(Class $\mathcal{A}$) is below 0.05 when the effective temperature is lower than 60 000 K. When the effective temperature becomes higher than 60 000 K, prob(Class $\mathcal{A}$) suddenly increases. The present result indicates that the PAH features in PNe evolve from Class $\mathcal{B}$ to $\mathcal{A}$ along with the evolution of PNe.

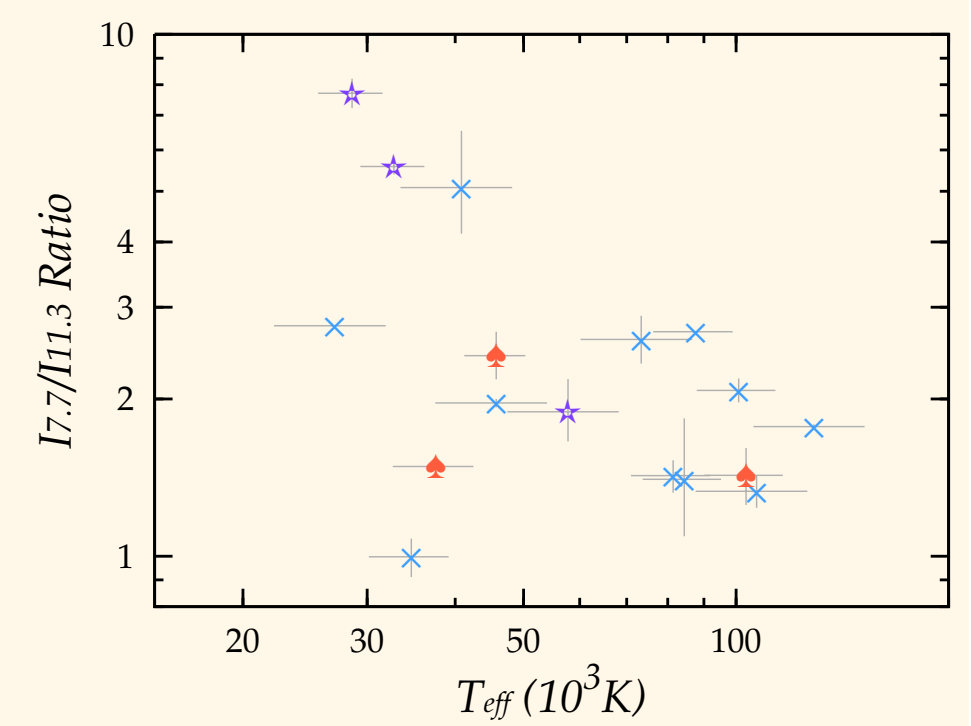

Figure 5.6 – Evolution of the $I_{7.7}/I_{11.3}$ ratio with the effective temperature. r_s is about -0.49 for $N_{obs} = 17$. The symbols are the same as in Figure 5.2.

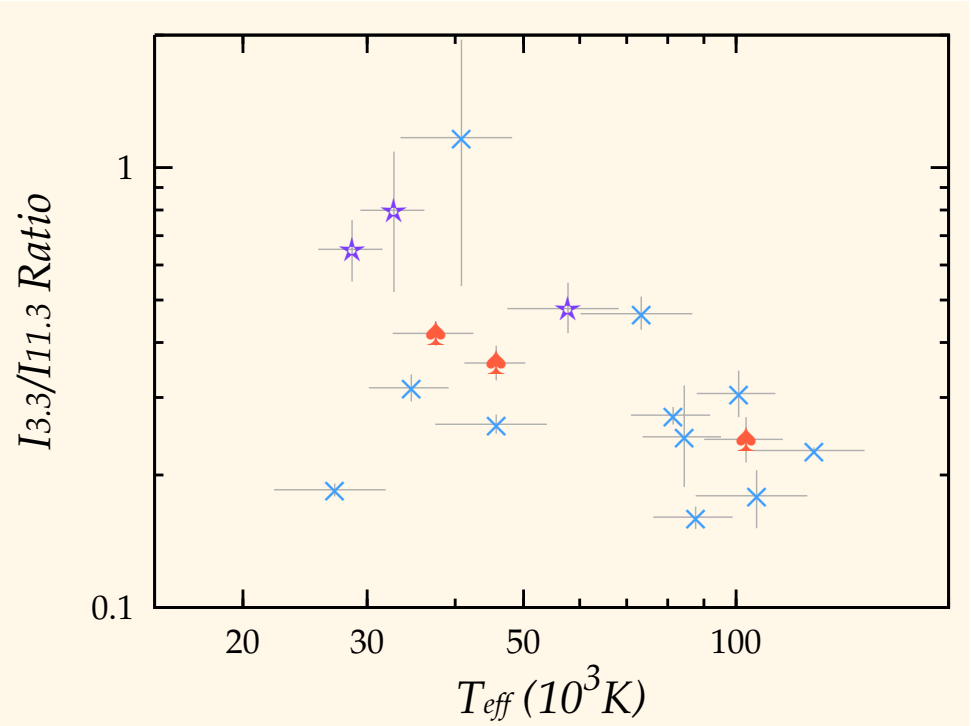

Figure 5.7 – Evolution of the $I_{3.3}/I_{11.3}$ ratio against the effective temperature. r_s is about -0.56 for $N_{obs} = 17$. The symbols are the same as in Figure 5.2.

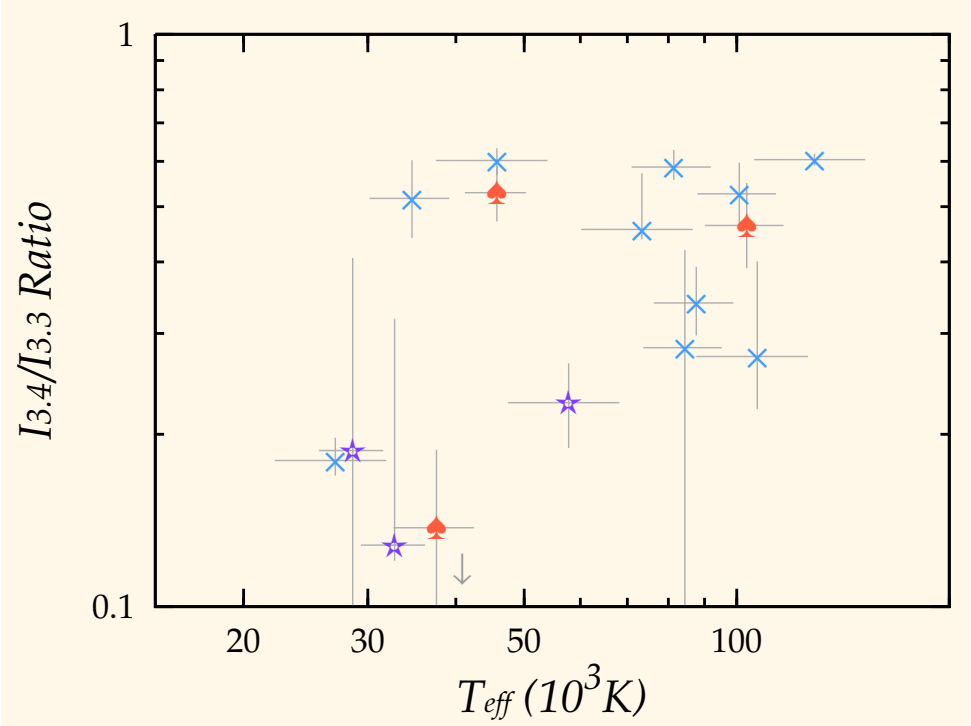

Figure 5.8 – Evolution of the $I_{3.4}/I_{3.3}$ ratio against the effective temperature. r_s is about 0.49 for $N_{obs} = 14$. The symbols are the same as in Figure 5.2.

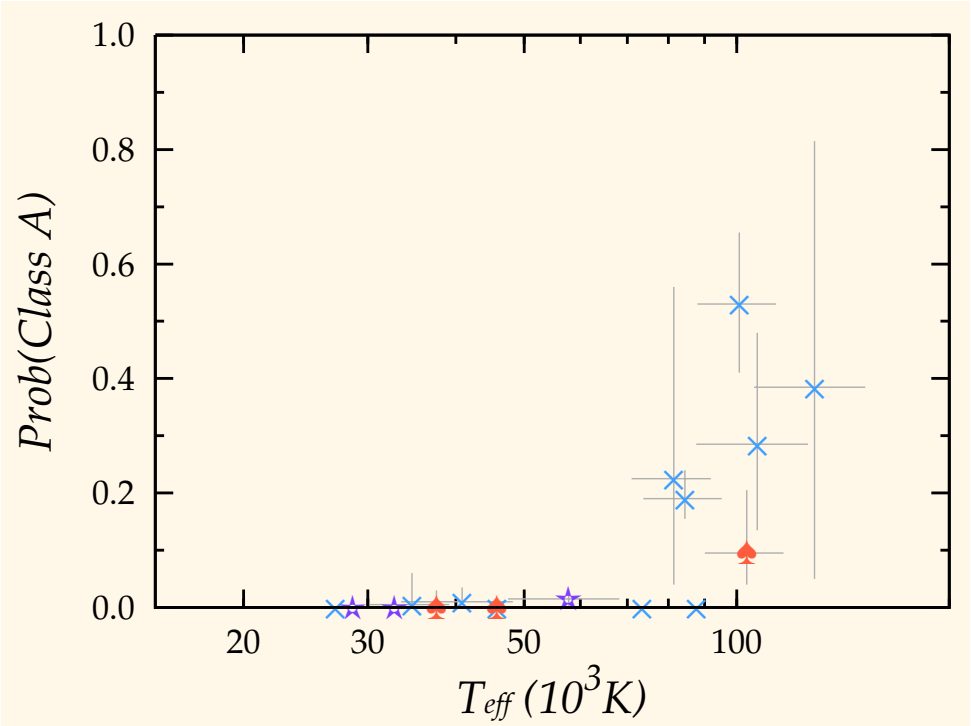

Figure 5.9 – prob(Class $\mathcal{A}$) against the effective temperature. The symbols are the same as in Figure 5.2.

5.4 Discussion

5.4.1 Properties of PAHs in Typical PNe

The present results indicate that, for typical PNe, the ionization fraction of PAHs is as low as about 0.0–0.4 and PAHs with $N_C \lesssim 50$ are totally dehydrogenated. The amount of aliphatic components of PAHs in PNe is typically larger than in H II regions except for PNe with a large PAH ionization fraction. The 6.2 μm feature is Class $\mathcal{B}$ for most PNe, but tends to become Class $\mathcal{A}$ with PN evolution.

The ionization fraction of PAHs is roughly determined by the G_0/n_e ratio (Bregman & Temi, 2005), where G_0 is the intensity of UV radiation field normalized by the Solar neighborhood value (Habing, 1968) and n_e is the electron density. Galliano et al. (2008) report that the $I_{6.2}/I_{11.3}$ ratio approximately follows the relationship as:

$$\frac{I_{6.2}}{I_{11.3}} \simeq 5 \left(\frac{G_0}{10^4}\right) \left(\frac{1\,\mathrm{cm}^{-3}}{n_e}\right) \left(\frac{T_{\mathrm{gas}}}{10^3\,\mathrm{K}}\right)^{\frac{1}{2}} + 0.26, \tag{5.5}$$

where T_{gas} is the gas temperature. Bregman & Temi (2005) report that the equation is valid when the G_0/n_e ratio ranges between 10^2 and 10^4 cm^3. The G_0/n_e ratio is calculated using Equation (5.5) assuming that T_{gas} is 8000 K. Figure 5.10 shows the calculated G_0/n_e ratio against the effective temperature. The G_0/n_e ratio ranges typically between 200 and 800 cm^3. Galliano et al. (2008) estimate the G_0/n_e ratio of the Galactic PN, NGC 7027, to be about 400 cm^3. The present results are consistent with that. Assuming that the radiation field is a 100 000 K blackbody with a luminosity of 10^4 $L_\odot$ and the radius of the envelope is 0.05 pc, the electron density ne corresponding to $G_0/n_e = 400$ is about 20 cm^{-3}. The gas density in the envelope (n_H) is about 10^3 cm^{-3}. In PDRs, electrons are mostly provided by carbon atoms and the n_e/n_H ratio should be as large as the C/H ratio (e.g., Draine, 2011). The C/H ratio in PNe is estimated to be about 5–8 $\times$ 10^{-4} (Bernard-Salas & Tielens, 2005). The present n_e/n_H ratio is significantly higher than the C/H ratio. The present results indicate that the PAH features are emitted in part within the H II region, as suggested in Bernard et al. (1994).

The number of peripheral hydrogen atoms in PAHs is in equilibrium between hydrogenation and dehydrogenation. Allain et al. (1996a,b) suggest that the degree of PAH hydrogenation is determined by the G_0/n_H ratio. Montillaud et al. (2013) report a similar result based on their detailed PAH modeling in the reflection nebula, NGC 7023. Assuming that n_H is about 10^4 cm^{-3}, $\log_{10}[G_0/(n_H(\mathrm{cm}^{-3}))]$ is estimated about 0.1. Based on observations of [O III]$_{63\,\mu\mathrm{m}}$ and [C II]$_{158\,\mu\mathrm{m}}$, Chokshi et al. (1988) report that $\log_{10}[G_0/(n_H(\mathrm{cm}^{-3}))]$ is about 0.15 in NGC 7023, suggesting that $\log_{10}[G_0/(n_H(\mathrm{cm}^{-3}))]$ in PNe is as large as in NGC 7023. The $G_0/(n_H(\mathrm{cm}^{-3}))$ ratio is required to change by one or two orders of magnitude to significantly affect the degree of hydrogenation (Allain et al., 1996b). The present results indicate that the degree of PAH dehydrogenation in PNe is almost the same as in NGC 7023, which is quite consistent with the previous theoretical calculations.

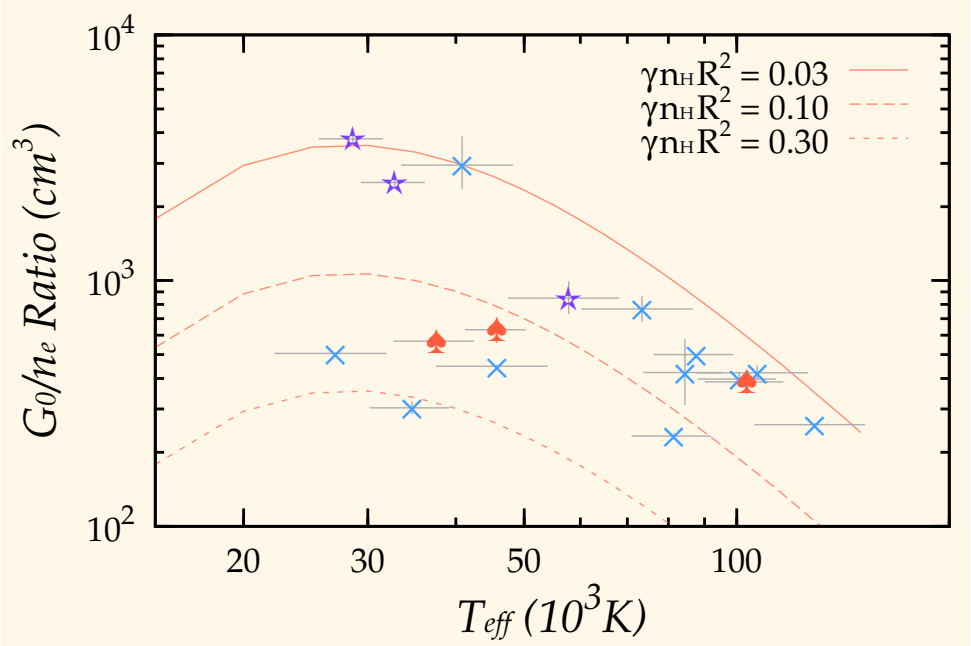

Figure 5.10 – Dependence of G_0/n_e on the effective temperature. The solid, dashed and dotted lines show the G_0/n_e ratio expected from Equation (5.6) for $\gamma n_H R^2 = 0.03$, 0.1, and 0.3, respectively (*see* text). The symbols are the same as in Figure 5.2.

The origin of the different PAH emission classes is not identified. Hudgins et al. (2005) propose that $\lambda^{6.2}$ may represent the N/C ratio in nitrogen-substituted PAHs. Bauschlicher et al. (2008) suggest that small and large PAHs tend to show the Class $\mathcal{A}$ and $\mathcal{B}$ 7.7 μm features, respectively. Wada et al. (2003) report that $\lambda^{6.2}$ changes with the C^{13}/C^{12} ratio. Bregman & Temi (2005) investigate the variation in the profile of the 7.7 μm PAH feature with the $I_{7.7}/I_{11.3}$ ratio and conclude that the Class $\mathcal{A}$ and $\mathcal{B}$ 7.7 μm features are, respectively, attributed to cation and anion PAHs. Pino et al. (2008) experimentally suggest that $\lambda^{6.2}$ moves from 6.3 toward 6.2 μm when the amount of aliphatic components in PAHs decreases. However, the present results indicate that the Class $\mathcal{A}$ 6.2 μm feature in PNe is compatible with a small PAH ionization fraction and a high aliphatic-to-aromatic ratio. None of the explanations above is strongly supported by the present observations.

5.4.2 Coevolution of the PAH Emission with PNe

The present results show systematic variations in the relative intensities of the PAH features and the peak wavelength of the 6.2 μm feature: As the effective temperature increases, the ionization fraction of PAHs decreases, the amount of small-sized PAHs decreases, the fraction of aliphatic components in PAHs increases, and the 6.2 μm PAH feature changes from Class $\mathcal{B}$ to $\mathcal{A}$. The origin of these transitions should be strongly related to the evolution of PNe.

As mentioned above, the ionization fraction of PAHs is determined by the G_0/n_e ratio. The intensity of radiation field G_0 and electron density n_e decreases with the expansion of the envelope. Define the radius of the envelope by R. The G_0/n_e

ratio should be proportional to $(n_e R^2)^{-1}$:

$$\frac{G_0}{n_e} \propto \frac{1}{n_e R^2} = \frac{1}{\gamma n_H R^2}, \tag{5.6}$$

where γ is the gas ionization fraction defined by n_e/n_H. Schönberner et al. (2005b) report that the gas density of the envelope (n_H) is roughly proportional to R^{-2}. Therefore, $n_H R^2$ is expected to be constant along with PN evolution. The G_0/n_e ratio is calculated for $\gamma n_H R^2 = 0.03$, 0.1, and $0.3\,\mathrm{cm^{-3}\,pc^2}$, assuming that the luminosity of the central star is $10^4\,L_\odot$. They are shown in Figure 5.10 by the lines. The present results indicate that the observed G_0/n_e ratio suddenly decreases at ~30 000 K. Such a sudden decrease is not explained by the expansion of the envelope. The decrease in G_0/n_e should be attributed to the increase in the gas ionization fraction γ. The PAH features in PNe are thought to be emitted in the envelope, which contains the PDR and the H II region. In the H II region, electrons are provided by hydrogen atoms ($\gamma \sim 1$), while electrons in the PDR are provided by carbon atoms ($\gamma \sim \mathrm{C/H} \sim 10^{-4}$). The observed G_0/n_e ratio is expected to decrease when the PAH features from the H II region become dominant. The evolution of the PAH ionization fraction may be attributed to the increasing fraction of the PAH features emitted in the H II region. Note that the G_0/n_e ratio may be smaller than $10^2\,\mathrm{cm^3}$ in the H II region of PNe, where Equation (5.5) is not valid. The discussion above is too simple to quantitatively investigate the gas ionization fraction γ and the fraction of PAHs in the H II region. The limitation in Equation (5.5), however, does not change the present conclusion.

The amount of small-sized PAHs decreases with PN evolution. The deficiency in small-sized PAHs is usually attributed to the destruction of small-sized PAHs. Probable mechanisms of PAH destruction in PNe are ion-sputtering and photo-dissociation. PAH destruction by ion-sputtering is investigated by Micelotta et al. (2010a). They suggest that a typical lifetime of PAHs is about 1.3×10^7 years when $n_H \simeq 10^4\,\mathrm{cm^{-3}}$ and $T_{gas} \simeq 7\,000$ K. That is much longer than a typical lifetime of PNe. In addition, the lifetime of PAHs does not depend on the size of PAHs when ion-sputtering is the most effective in the PAH destruction. The evolution of the $I_{3.3}/I_{11.3}$ ratio is not attributable to the PAH destruction by ion-sputtering. PAH destruction by photo-dissociation is investigated by Allain et al. (1996a,b). They assume that PAHs are in equilibrium between loss and accretion of acetylene molecules. They suggest that small-sized PAHs are destroyed faster by photo-dissociation than large-sized PAHs. PAH destruction by photo-dissociation could change the amount of small-sized PAHs. They propose that the smallest size of the PAHs which can survive the photo-dissociation ($N_{C\,min}$) is determined by the G_0/n_H ratio. The amount of small-sized PAHs could decrease if $N_{C\,min}$ increases. Their results show that the G_0/n_H ratio should increase about by one or two orders of magnitude to significantly increase $N_{C\,min}$. Such a large increase in G_0/n_H, however, is not expected with PN evolution (*see* Figure 5.10). A decrease in the $I_{3.3}/I_{11.3}$ ratio, caused by PAH destruction due to photo-dissociation, is unlikely. Micelotta et al. (2010b) suggest that PAHs are totally dehydrogenated before their destruction. Since aliphatic C—H bonds in PAHs are more fragile than aromatic C—H bonds, the $I_{3.4}/I_{3.3}$ ratio should decrease if the decrease in the $I_{3.3}/I_{11.3}$ ratio is caused by the destruction of small-sized PAHs. The present results show

that the $I_{3.4}/I_{3.3}$ ratio increases with PN evolution, indicating that the decrease in the $I_{3.3}/I_{11.3}$ ratio is not caused by any kind of PAH destruction.

Shattering of large carbonaceous dust grains can increase the amount of small-sized dust grains (Hirashita, 2010). Dust shattering in the envelope, if any, could provide newly-produced PAHs, and the PAH size distribution and the amount of aliphatic components in PAHs could be changed as discussed in Section 4.4.3. Assuming that the shattering produces relatively large PAHs with abundant aliphatic components from fragments of large carbonaceous grains, the variations in the $I_{3.3}/I_{11.3}$ and $I_{3.4}/I_{3.3}$ ratios with PN evolution are explained at the same time. As discussed in Section 4.4.3, a typical timescale of dust shattering ($\tau_{\rm shat}$) should be much longer than a typical lifetime of PNe when we assume that $n_{\rm H} \simeq 10^3\,{\rm cm}^{-3}$ and $V_{\rm shat} \simeq 5\,{\rm km\,s}^{-1}$, where $V_{\rm shat}$ is the shattering velocity (*see* Equation (4.1)). Dust shattering may be negligible in PNe unless $\tau_{\rm shat}$ decreases significantly.

The PAH features are emitted only when PAHs are excited by a UV-photon. Although PAHs may reside in the AGB wind region, the PAH features are not emitted from PAHs there since the AGB wind region is outside the PDR. The observed PAH features in PNe represent the properties of PAHs only in the envelope. As PNe evolve, the envelope expands and collects materials in the AGB wind region as well as PAHs. Theoretical studies suggest that the total mass in the envelope increases as approximately proportional to R (e.g., Bedogni & Dercole, 1986). PAHs located farther from the central star (hereafter *far-side PAHs*) have been formed earlier in the AGB phase, while PAHs located closer to the central star (*near-side PAHs*) have been formed later in the AGB phase or in the post-AGB phase. As the envelope expands, far-side PAHs are accumulated in the envelope. If the properties of PAHs formed in the AGB phase systematically change with the evolution of the AGB stars, the properties of PAHs in the envelope are expected to change with the expansion of the envelope. The variations in the PAH features are simultaneously explained assuming that far-side PAHs are larger in size, contain more aliphatic components, and show the Class $\mathcal{A}$ 6.2 μm feature, while near-side PAHs are smaller, more associated with aromatic components, and show the Class $\mathcal{B}$ feature.

If the envelope takes in PAHs in the AGB wind region as it expands, the total amount of PAHs in the envelope should increase with PN evolution. The variation in the total PAH amount in the envelope is investigated in terms of the ratio of the total intensity of the PAH features to the total infrared intensity ($I_{\rm PAH}/I_{\rm IR}$). The total intensity of the PAH features ($I_{\rm PAH}$) is defined by

$$I_{\rm PAH} = I_{3.3} + I_{6.2} + I_{7.7} + I_{8.6} + I_{11.3}, \tag{5.7}$$

where I_x is the intensity of the PAH feature at x μm. As discussed in Section 4.4.3, the $I_{\rm PAH}/I_{\rm IR}$ ratio is approximated by

$$\frac{I_{\rm PAH}}{I_{\rm IR}} \simeq \frac{\tau_{\rm UV}^{\rm PAH}}{e^{\tau_{\rm UV}^{\rm dust}} - 1}, \tag{5.8}$$

where $\tau_{\rm UV}^{\rm dust}$ and $\tau_{\rm UV}^{\rm PAH}$ are the optical depth of circumstellar dust and PAHs in the envelope, respectively. Therefore, the $I_{\rm PAH}/I_{\rm IR}$ ratio approximately represents

the fractional amount of PAHs in the envelope. Figure 5.11 shows the I_{PAH}/I_{IR} ratio against the effective temperature. Although there is large scatter, the result shows a "U"-like distribution with a minimum around 50 000 K as seen in Figure 4.9. The I_{PAH}/I_{IR} ratio increases by about one order of magnitude when the effective temperature changes from about 50 000 to 100 000 K. Although the I_{PAH}/I_{IR} ratio could increase when τ_{UV}^{dust} decreases, Figure 4.3 indicates that τ_{UV}^{dust} the variation in τ_{UV}^{dust} with PN evolution is too small to explain the increase in the I_{PAH}/I_{IR} ratio. We suggest that the increase in the I_{PAH}/I_{IR} ratio is attributable in part to an increase in the PAH abundance in the envelope. The I_{PAH}/I_{IR} ratio decreases when the effective temperature changes from about 30 000 to 50 000 K. The origin of the decrease is not identified. PAHs in the inner rim of the envelope may evaporate into the hot bubble, where the gas temperature is more than 10^6 K. Micelotta et al. (2010a) estimate a typical lifetime of PAHs with $N_C = 200$ to be about 8^{+63}_{-6} years in a Galactic H II region, M 17, with $n_H \simeq 0.3\,cm^{-3}$ and $T_{gas} \simeq 7\times10^6$ K. We expect that PAHs in the H II region of PNe are immediately destroyed as in M 17. In the H II region, PAHs may be dissociated by absorbing a photon with $h\nu > 13.6$ eV. The number of ionizing photons from the central star (Q_0) changes along with PN evolution. The radius R_{dis}, within which PAHs are dissociated, become larger with increasing G_0. The dependence of Q_0 on the effective temperature is shown by the dotted line in Figure 5.11, assuming that the radiation field is given by the blackbody function and the luminosity is $10^4\,L_\odot$. Q_0 peaks at about 50, 000 K, corresponding to the effective temperature of the minimum I_{PAH}/I_{IR} ratio. Although it is unclear which processes is dominant in PAH destruction, both processes are efficient in the inner rim of the envelope. If PAHs in the envelope are not well-mixed, near-side PAHs are abundant near the inner rim of the envelope. We presume that near-side PAHs are selectively eliminated in PAH destruction. The PAH destruction in the inner rim may accelerate the replacement of near-side PAHs by far-side PAHs and the evolution of the PAH features.

5.5 Summary

We obtain 2.5–14.0 μm spectra of 18 Galactic C-rich PNe with *AKARI* and *Spitzer*. Properties of PAHs are investigated based on the relative intensity of the PAH features. A typical ionization fraction of PAHs in PNe is small compared to other PAH emission objects (e.g., star-forming galaxies) partly because of a high electron density in the envelope. PAHs with $N_C \lesssim 50$ in PNe are found to be totally dehydrogenated. The degree of PAH dehydrogenation in PNe is as high as reflection nebulae. The result is consistent with theoretical predictions. Amount of aliphatic components in PAHs decreases with increasing ionization fraction. Most PNe show the Class $\mathcal{B}$ 6.2 μm feature as previously reported, while PNe with a high effective temperature tend to show the Class $\mathcal{A}$ 6.2 μm feature.

Systematic variations in the relative intensity of the PAH features are discovered. We find that the $I_{7.7}/I_{11.3}$ and $I_{3.3}/I_{11.3}$ ratios decrease and the $I_{3.4}/I_{3.3}$ ratio increases along with PN evolution. The evolution of the $I_{7.7}/I_{11.3}$ ratio can be explained by a decreasing fraction of the PAH features from the H II region of

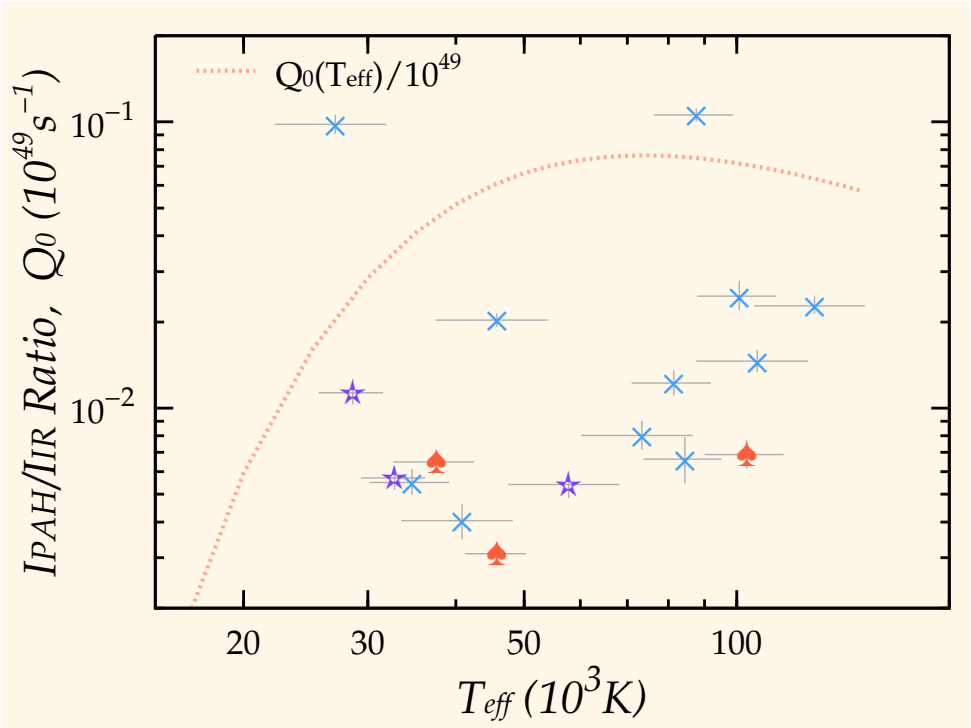

Figure 5.11 – Evolution of the I_{PAH}/I_{IR} ratio against the effective temperature. The symbols are the same as in Figure 5.2. The dotted line shows the variation of Q_0 against the effective temperature (*see* text).

the envelope with the effective temperature. The decrease in the $I_{3.3}/I_{11.3}$ ratio and the increase in the $I_{3.4}/I_{3.3}$ ratio are not attributed to PAH dehydrogenation or destruction. To account for the evolution of the PAH features at the same time, we propose a hypothesis: As the envelope expands, PAHs in the AGB wind region are accumulated in the envelope. Along with the evolution of PNe, far-side PAHs become dominant in the envelope and the observed PAH features change. Assuming that far-side PAHs are typically large in size and have more aliphatic components, and show the Class $\mathcal{A}$ feature while near-side PAHs are smaller and more associated with aromatic, and show the Class $\mathcal{B}$ feature, the observed transitions of the PAH features are reproduced along with PN evolution. The amount of PAHs in the envelope (I_{PAH}/I_{IR}) decreases at first when the effective temperature is about 30 000–50 000 K and then increase as the effective temperature changes from about 50 000 to 100 000 K. We propose that the decrease in the I_{PAH}/I_{IR} ratio is related to the PAH destruction in the inner rim. The PAH destruction at the inner rim of the envelope may accelerate the replacement of near-side PAHs by far-side PAHs in the envelope. The increase in the I_{PAH}/I_{IR} ratio is accounted for in part by accumulating PAHs in the AGB wind region with expanding envelope.

The present results indicate that the evolution of the PAH features in PNe is closely related to the evolution of the effective temperature and the expanding envelope. We conclude that photo-dissociation and dehydrogenation of PAHs are not effective in the evolution of the PAH features during the PN phase. Dynamical evolution of the nebula plays the most important role to account for the evolution of the PAH features by replacing near-side PAHs by far-side PAHs in the envelope.

The characteristics of PAHs in young PNe (small, aromatic-rich, and Class $\mathcal{B}$) are attributed to near-side PAHs, which are made in the late AGB or post-AGB phases. We propose that the variations in the PAH features are derived in part from physical conditions where PAHs are formed. Investigation of dust formation in stellar wind with a different mass loss rate, wind velocity, chemical abundance, and radiation field is crucial to understand the variation in the PAH features.

Chapter 6
Conclusion

In this paper, the PAH features in Galactic PNe are investigated using the spectra provided by the *AKARI*/IRC and *Spitzer*/IRS. The detection rate of the PAH features in PNe is measured for the first time with a large number of samples. We find the variations in the PAH features along with the evolution of PNe. We obtain the first observational results which strongly support the hypothesis that PAHs in PNe have already been formed in the AGB phase. Based on the observed variations, we propose that the characteristics of the PAH features in PNe originate in PAHs formed in the late AGB or post-AGB phases: they are smaller in size, contain less aliphatic components, and show Class $\mathcal{B}$ emission. The background of this research and the present results are summarized in this chapter.

PAHs, which are considered to be common dust species in the Universe, are composed of fused aromatic rings with hydrogen atoms. PAHs emit strong broad emission in the infrared, usually referred as the Unidentified Infrared bands or the PAH features, when they are excited by a single UV-photon. The PAH features are widely observed in a variety of objects such as post-AGB stars, PNe, reflection nebulae, and star-forming galaxies (Acke & van den Ancker, 2004; Peeters et al., 2002b). The spectral profile of the PAH features is almost identical among objects because of the single-photon excitation process. The variations in the spectral profile and the relative intensity of the PAH features have been reported, however, and these variations are believed to be related to the physical conditions and properties of PAHs.

The mechanism of PAH formation is not fully understood. PAHs are widely believed to be formed in ejecta of the AGB wind (Buss et al., 1991). The PAH features, however, are rarely observed around AGB stars because the effective temperature of AGB stars is too low to excite PAHs (Boersma et al., 2006). PAH formation around AGB stars has not been observationally confirmed. Several studies suggest that UV or thermal processing is important to form aromatic components in small carbonaceous dust (Goto et al., 2003, 2000). By examining whether PAHs are formed in the AGB phase, we can constrain the physical conditions required for PAH formation around evolved stars.

The variations in the spectral profile of the PAH features have been investigated. The variations in the 6–9 μm PAH features are categorized into three classes (Class $\mathcal{A}$, $\mathcal{B}$, and $\mathcal{C}$; Peeters et al., 2002a). Several mechanisms have been proposed to account for the variations (e.g., Bauschlicher et al., 2008; Hudgins et al., 2005; Pino et al., 2008). The origin of the different emission classes, however, remains to be identified. It is notable that evolved stars such as post-AGB stars and PNe tend to show Class $\mathcal{B}$ emission, while Class $\mathcal{A}$ emission is usually observed in interstellar objects such as reflection nebulae and star-forming regions. Evolution of the PAH features is expected when PAHs are injected from circumstellar environments into interstellar space.

PNe are a late stage of the low- and intermediate-mass stellar evolution and the PAH features are frequently observed in PNe. PAHs in PNe are believed to be formed in the AGB and post-AGB phase and they are about to be injected into interstellar space after the PN phase. PAHs in PNe are in a transitional phase from circumstellar to interstellar environments. Investigating the properties of PAHs in PNe is important to understand the evolution of the PAH features.

To understand the properties of PAHs, investigating the near- to mid-infrared PAH features together, is crucial. Due to the insufficient sensitivity, however, the number of objects available in the near-infrared (2–5 μm) has been limited (Roche et al., 1996; Smith & McLean, 2008). In Chapter 3, we compile a near-infrared spectral catalog of Galactic PNe (PNSPC catalog) based on observations of the *AKARI*/IRC (Onaka et al., 2007), the detection limit of which is as low as ∼10 mJy at 3 μm. More than 70 near-infrared spectra of PNe are included in the PNSPC catalog. The catalog is the largest near-infrared spectral catalog of Galactic PNe. The obtained spectra are consistent with the photometric data from the *WISE* All-Sky catalog (Cutri et al., 2012b; Wright et al., 2010), suggesting that the measured intensity and equivalent width in the PNSPC catalog are reliable. The catalog, for the first time, enables us to statistically investigate the characteristics of the near-infrared spectra of Galactic PNe.

In Chapter 4, we investigate the statistical characteristics of the near-infrared PAH features and their evolution. The effective temperature is used as an indicator of PN evolution. The 3.3 μm PAH feature is not contaminated by emission from HACs and plateau emission. The 3.3 μm PAH feature is ideal to measure the PAH detection rate in PNe. The PAH detection rate is estimated to be about 65–80%. The amount of aliphatic components, indicated by the $I_{3.4}/I_{3.3}$ ratio, is typically higher than that in typical Galactic star-forming regions and increases along with the evolution of PNe. The $I_{3.3}/I_{IR}$ ratio shows a "U"-shaped variation along with the evolution of PNe, indicating the increase in the total amount of PAHs in the envelope. To further give an insight into the origin of the variations in the near-infrared PAH features, it is indispensable to investigate the near- to mid-infrared PAH features together.

Together with mid-infrared spectra provided by the *Spitzer*/IRS, we investigate the properties of PAHs and the evolution of the PAH features in Chapter 5. As suggested in previous studies, the ionization fraction of PAHs in PNe is lower than other PAH emitting objects such as star-forming galaxies. The $I_{3.3}/I_{11.3}$ ratio is significantly lower than that predicted by the model, suggesting that PAHs with $N_C \lesssim 50$ are totally dehydrogenated in PNe. The degree of PAH dehydrogenation

Table 6.1 – Summary of the Evolution of the PAH Features in PNe

Observation	Physical Meanings	Variation
$I_{7.7}/I_{11.3}$	ionization fraction	decreasing
$I_{3.3}/I_{11.3}$	amount of small-sized PAHs	decreasing
$I_{3.4}/I_{3.3}$	amount of aliphatic components	increasing
I_{PAH}/I_{IR}	amount of PAHs in the envelope	"U"-shaped

in PNe is as high as that in the reflection nebula, NGC 7023. The result is consistent with previous theoretical studies. The variation in the $I_{3.3}/I_{11.3}$ ratio with the evolution of PNe indicates that the amount of small-sized PAHs decreases as a PN evolves. The evolution of $\lambda^{6.2}$ indicates that the 6.2 μm PAH feature changes from Class $\mathcal{B}$ to $\mathcal{A}$. The observed variations in the PAH features are summarized in Table 6.1. These variations are investigated in terms of processing of PAHs and the evolution of PNe.

We conclude that processing of PAHs is not the principal cause of the variations in the PAH features. In a PDR region such as the PN envelope, the gas temperature is not so high that PAH destruction by electron-sputtering is negligible (Micelotta et al., 2010a). A typical timescale for PAH destruction by ion-sputtering is estimated to be about 10^7 years, which is much longer than a typical lifetime of PNe. PAH destruction by photo-dissociation could affect the size distribution of PAHs, but the G_0/n_H ratio is required to change by about one or two orders of magnitude to significantly affect the relative intensity of the PAH features (Allain et al., 1996a,b). Such a large variation in the G_0/n_H ratio is not expected during the PN phase (Section 5.4). Therefore, the observed variations in the PAH features should be attributed to other mechanisms.

A mechanism is proposed to account for the observed variation in the PAH features. Figure 6.1 shows a schematic view of the proposed mechanism. We assume that PAHs reside in the AGB wind region but they are not excited by a UV-photon. We also assume that properties of PAHs formed in the stellar wind could change with the evolution of AGB stars. PAHs formed in an earlier phase should be located far from the central star (far-side PAHs), while PAHs formed in a later phase are located closer (near-side PAHs). As the envelope expands with PN evolution, far-side PAHs are accumulated in the envelope. As the fractional abundance of far-side to near-side PAHs increases, the observed characteristics of the PAH features change. In the hot bubble, PAHs are immediately destroyed by electron-sputtering (Micelotta et al., 2010a). In the inner rim of the envelope, PAHs may be exposed to a hard radiation field and eliminated by photo-dissociation. If PAHs in the envelope are not well-mixed, near-side PAHs are destroyed first. The PAH destruction accelerates the replacement of near-side PAHs by far-side PAHs. The present results indicate that PAHs in young PNe tend to be small in size, have less aliphatic components, and show the Class $\mathcal{B}$ feature. These characteristics of PAHs in young PNe are attributed to near-side PAHs. As PNe evolve, PAHs becomes larger in size, have more aliphatic components, and start to show the Class $\mathcal{A}$ feature. These are attributed to far-side PAHs. The observed variations in the PAH features are explained in such a way that the fractional amount of

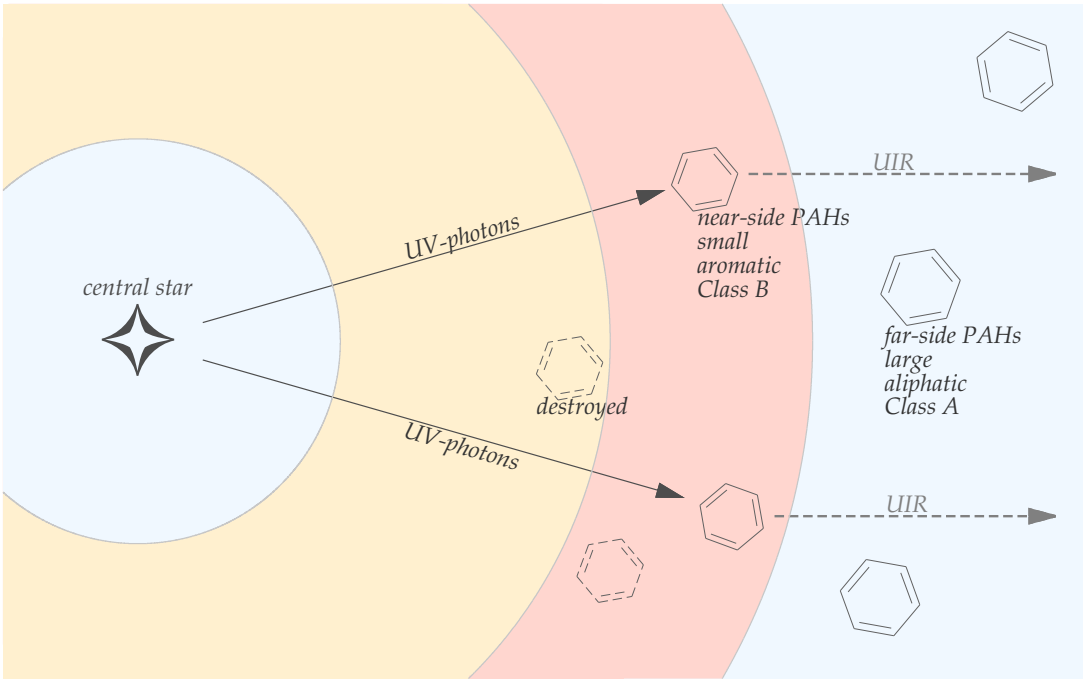

Figure 6.1 – Schematic view of the proposed mechanism to account for the variations in the PAH features. The definitions of the regions are the same as in Figure 1.5. In an early stage, only near-side PAHs are in the envelope. As the envelope expands, far-side PAHs are collected in the envelope. Since PAH destruction is efficient near the inner rim of the envelope, the amount of near-side PAHs in the envelope decreases with PN evolution.

far-side PAHs increases with the evolution of the envelope.

In this paper, we propose that the observed PAH features only reflect the properties of PAHs in the envelope and the expansion of PNe significantly affect the PAH features. To understand the variations in the PAH features around evolved stars, the dynamical evolution of the nebula can be important as well as processing of PAHs itself. In the post-AGB phase, the effective temperature is low so that the ionization front cannot penetrate into the circumstellar envelope. PAHs are not excited except for PAHs near the inner boundary of the envelope (near-side PAHs). The PAH features are emitted from the inner boundary of the circumstellar envelope. Since post-AGB stars are young objects, their circumstellar envelope is close to the central star. PAHs in post-AGB stars can be processed by UV-absorption. Matsuura et al. (2014) and Sloan et al. (2007) report that the PAH features in post-AGB stars systematically change with the effective temperature of the central star. They attribute the transition to the processing of PAHs. In the post-AGB phase, PAH processing is quite important to understand the variation of the PAH features. Then, in the PN phase, the effective temperature increases as the star evolves. The ionization front starts to penetrate into the circumstellar envelope and the outer shell and inner rim are created (*see* Figure 1.5). PAHs distant from the central star (far-side PAHs) become excited by a UV-photon. Along with PN evolution, more and more far-side PAHs are collected in the envelope and excited. Since the nebula gets large by expansion and the gas temperature is not high, processing of PAHs is not efficient any more in the PN phase. We present

that the PAH features also change systematically along with the effective temperature of the central star during the PN phase. Evolution of the PAH features during the PN phase should not be attributed to PAH processing. We conclude that the properties of the near-side and far-side PAHs are different and that the evolution of the PAH features is caused by the replacement of near-side PAHs by far-side PAHs with the PN expansion. After the PN phase, PAHs around PNe are injected into interstellar space. Since near-side PAHs can be eliminated near the inner rim, we expect that far-side PAHs are mainly injected into the interstellar space. As discussed in Section 5.4.2, far-side PAHs tend to show the Class A PAH features as PAHs in interstellar space. The present results are consistent with the hypothesis that PAHs in interstellar space are provided by evolved stars.

We feature the two unsolved issues on PAHs: whether PAHs are formed in the AGB phase and what is the origin of the PAH emission classes. The proposed mechanism strongly supports the idea that PAHs have already been formed in the AGB phase and indicates that the variation of the PAH properties could originate in the physical conditions of PAH formation. We propose that the understanding of PAH formation around AGB and post-AGB stars is important to identify the origin of the PAH classes. The investigation of the physical conditions of PAH formation in the late AGB and post-AGB phases is especially important. These conditions should be closely related to the properties of near-side PAHs. In this research, we regard the targets as point-source objects since they are not resolved with the *AKARI*/IRC and *Spitzer*/IRS. PNe are known to show a variety of morphologies. The morphology of PNe cannot be ignored in investigation of the expansion of the envelope. The proposed model should be investigated by spatially-resolved observations in the future.

Bibliography

Acke, B., & van den Ancker, M. E. 2004, A&A, 426, 151
Acker, A. 1978, A&AS, 33, 367
Acker, A., Marcout, J., Ochsenbein, F., Stenholm, B., & Tylenda, R. 1992, Strasbourg-ESO Catalogue of Galactic Planetary Nebulae, Parts I, II (Garching: European Southern Observatory)
Acker, A., Raytchev, B., Stenholm, B., & Tylenda, R. 1991, A&AS, 90, 89
Allain, T., Leach, S., & Sedlmayr, E. 1996a, A&A, 305, 602
—. 1996b, A&A, 305, 616
Allamandola, L. J., Tielens, A. G. G. M., & Barker, J. R. 1989, ApJS, 71, 733
Aller, L. H., & Czyzak, S. J. 1983, ApJS, 51, 211
Amnuel, P. R., Guseinov, O. K., Novruzova, K. I., & Rustamov, I. S. 1984, Astrophysics and Space Science, 107, 19
Arnaboldi, M., Freeman, K. C., Gerhard, O., Matthias, M., Kudritzki, R. P., Méndez, R. H., Capaccioli, M., & Ford, H. 1998, ApJ, 507, 759
Baker, J. G., & Menzel, D. H. 1938, ApJ, 88, 52
Bauschlicher, C. W., Peeters, E., & Allamandola, L. J. 2008, ApJ, 678, 316
—. 2009, ApJ, 697, 311
Beaulieu, S. F., Freeman, K. C., Kalnajs, A. J., Saha, P., & Zhao, H. 2000, AJ, 120, 855
Bedogni, R., & Dercole, A. 1986, A&A, 157, 101
Beintema, D. A., et al. 1996, A&A, 315, L369
Bernard, J. P., Giard, M., Normand, P., & Tiphene, D. 1994, A&A, 289, 524
Bernard-Salas, J., Peeters, E., Sloan, G. C., Cami, J., Guiles, S., & Houck, J. R. 2006, ApJ, 652, L29
Bernard-Salas, J., Peeters, E., Sloan, G. C., Gutenkunst, S., Matsuura, M., Tielens, A. G. G. M., Zijlstra, A. A., & Houck, J. R. 2009, ApJ, 699, 1541
Bernard-Salas, J., Pottasch, S. R., Gutenkunst, S., Morris, P. W., & Houck, J. R. 2008, ApJ, 672, 274
Bernard-Salas, J., & Tielens, A. G. G. M. 2005, A&A, 431, 523
Berné, O., et al. 2007, A&A, 469, 575
Berné, O., Joblin, C., Rapacioli, M., Thomas, J., Cuillandre, J.-C., & Deville, Y. 2008, A&A, 479, L41
Blöcker, T. 1995, A&A, 299, 755
Boersma, C., Bauschlicher, C. W., J., Ricca, A., Mattioda, A. L., Peeters, E., Tielens, A. G. G. M., & Allamandola, L. J. 2011, ApJ, 729, 64
Boersma, C., Hony, S., & Tielens, A. G. G. M. 2006, A&A, 447, 213

Boersma, C., Mattioda, A. L., Bauschlicher, C. W., Peeters, E., Tielens, A. G. G. M., & Allamandola, L. J. 2009, ApJ, 690, 1208

Boulanger, F., Onaka, T., Pilleri, P., & Joblin, C. 2011, in EAS Publications Series, Vol. 46, PAHs and the Universe: A Symposium to Celebrate the 25th Anniversary of the PAH Hypothesis, 399–405

Bregman, J., & Temi, P. 2005, ApJ, 621, 831

Buss, R. H., Tielens, A. G. G. M., & Snow, T. P. 1991, ApJ, 372, 281

Cahn, J. H., Kaler, J. B., & Stanghellini, L. 1992, A&AS, 94, 399

Cau, P. 2002, A&A, 392, 203

Cernicharo, J., Heras, A. M., Pardo, J. R., Tielens, A. G. G. M., Guélin, M., Dartois, E., Neri, R., & Waters, L. B. F. M. 2001a, ApJLetters, 546, L127

Cernicharo, J., Heras, A. M., Tielens, A. G. G. M., Pardo, J. R., Herpin, F., Guélin, M., & Waters, L. B. F. M. 2001b, ApJLetters, 546, L123

Chokshi, A., Tielens, A. G. G. M., Werner, M. W., & Castelaz, M. W. 1988, ApJ, 334, 803

Ciardullo, R. 2004, in Planetary Nebulae beyond the Milky Way, ESO Astrophysics Symposia (Garching, Germany: Springer Berlin Heidelberg New York), 79–90

Ciardullo, R., Jacoby, G. H., & Ford, H. C. 1989a, ApJ, 344, 715

Ciardullo, R., Jacoby, G. H., Ford, H. C., & Neill, J. D. 1989b, ApJ, 339, 53

Cohen, M., & Barlow, M. J. 2005, MNRAS, 362, 1199

Compiègne, M., et al. 2011, A&A, 525, 103

Cutri, R. M., Wright, E. L., Conrow, T., Bauer, J., Benford, D., Brandenburg, H., & Dailey, J. 2012a, VizieR Online Data Catalog, 2311, 0

Cutri, R. M., et al. 2012b, Explanatory Supplement to the WISE All-Sky Data Release Products, Tech. rep.

Daub, C. T. 1982, ApJ, 260, 612

DeFrees, D. J., Miller, M. D., Talbi, D., Pauzat, F., & Ellinger, Y. 1993, ApJ, 408, 530

Désert, F.-X., Boulanger, F., & Puget, J. L. 1990, A&A, 237, 215

Dobashi, K., Uehara, H., Kandori, R., Sakurai, T., Kaiden, M., Umemoto, T., & Sato, F. 2005a, PASJ, 57, 1

—. 2005b, PASJ, 57, 417

Draine, B. T. 2011, Physics of the Interstellar and Intergalactic Medium

Draine, B. T., & Li, A. 2001, ApJ, 551, 807

—. 2007, ApJ, 657, 810

Duley, W. W., & Williams, D. A. 1981, MNRAS, 196, 269

Durand, S., Acker, A., & Zijlstra, A. 1998, A&AS, 132, 13

Dwek, E., et al. 1997, ApJ, 475, 565

Ferrarotti, A. S., & Gail, H.-P. 2006, A&A, 447, 553

Galliano, F., Madden, S. C., Tielens, A. G. G. M., Peeters, E., & Jones, A. P. 2008, ApJ, 679, 310

García-Hernández, D. A., Manchado, A., García-Lario, P., Stanghellini, L., Villaver, E., Shaw, R. A., Szczerba, R., & Perea-Calderón, J. V. 2010, ApJLetters, 724, L39

García-Lario, P., & Perea Calderón, J. V. 2003, in Exploiting the ISO Data Archive - Infrared Astronomy in the Internet Age, Vol. 511 (ESA SP-511; Noordwijk:

European Space Agency), 97
Gathier, R., Pottasch, S. R., & Goss, W. M. 1986a, A&A, 157, 191
Gathier, R., Pottasch, S. R., & Pel, J. W. 1986b, A&A, 157, 171
Geballe, T. R., Tielens, A. G. G. M., Kwok, S., & Hrivnak, B. J. 1992, ApJ, 387, L89
Geballe, T. R., & van der Veen, W. E. C. J. 1990, A&A, 235, L9
Gesicki, K., Acker, A., & Zijlstra, A. A. 2003, A&A, 400, 957
Giard, M., Bernard, J. P., Lacombe, F., Normand, P., & Rouan, D. 1994, A&A, 291, 239
Gomez, Y., Rodriguez, L. F., & Moran, J. M. 1993, ApJ, 416, 620
Goto, M., et al. 2003, ApJ, 589, 419
Goto, M., Maihara, T., Terada, H., Kaito, C., Kimura, S., & Wada, S. 2000, A&AS, 141, 149
Grewing, M., & Neri, R. 1990, A&A, 236, 223
Habing, H. J. 1968, Bulletin of the Astronomical Institutes of the Netherlands, 19, 421
Harrington, J. P., & Feibelman, W. A. 1983, ApJ, 265, 258
Hirashita, H. 2010, MNRAS, 407, L49
Hirashita, H., Nozawa, T., Yan, H., & Kozasa, T. 2010, MNRAS, 404, 1437
Hony, S., van Kerckhoven, C., Peeters, E., Tielens, A. G. G. M., Hudgins, D. M., & Allamandola, L. J. 2001, A&A, 370, 1030
Houck, J. R., et al. 2004, ApJS, 154, 18
Hudgins, D. M., Bauschlicher, C. W., & Allamandola, L. J. 2005, ApJ, 632, 316
Iben, I., J. 1982, ApJ, 260, 821
Iben, I., J., & Renzini, A. 1983, ARA&A, 21, 271
Ishihara, D., Kaneda, H., Onaka, T., Ita, Y., Matsuura, M., & Matsunaga, N. 2011, A&A, 534, 79
Ishihara, D., et al. 2010a, A&A, 514, 1
—. 2010b, VizieR Online Data Catalog, 2297, 0
Joblin, C., Tielens, A. G. G. M., Allamandola, L. J., & Geballe, T. R. 1996, ApJ, 458, 610
Joint Iras Science, W. G. 1994, VizieR Online Data Catalog, 2125, 0
Jones, A. P. 2012a, A&A, 540, 2
—. 2012b, A&A, 542, 98
Jones, A. P., Tielens, A. G. G. M., & Hollenbach, D. J. 1996, ApJ, 469, 740
Kaler, J. B. 1976, ApJ, 210, 843
Kaler, J. B., & Jacoby, G. H. 1991, ApJ, 372, 215
Kaneda, H., et al. 2012, PASJ, 64, 25
Khromov, G. S. 1989, Space Science Reviews, 51, 339
Kohoutek, L. 2001, A&A, 378, 843
Koyama, Y. 2011, Ph.D thesis, University of Tokyo, Tokyo, Japan
Kwok, S., Purton, C. R., & Fitzgerald, P. M. 1978, ApJ, 219, L125
Le Page, V., Snow, T. P., & Bierbaum, V. M. 2001, ApJS, 132, 233
Lumsden, S. L., Puxley, P. J., & Hoare, M. G. 2001, MNRAS, 320, 83
Maciel, W. J. 1984, A&AS, 55, 253
Maciel, W. J., & Pottasch, S. R. 1980, A&A, 88, 1
Magrini, L., Corbelli, E., & Galli, D. 2007, A&A, 470, 843

Magrini, L., Stanghellini, L., & Villaver, E. 2009, ApJ, 696, 729
Manchado, A., Guerrero, M. A., Stanghellini, L., & Serra-Ricart, M. 1996, The IAC morphological catalog of northern Galactic planetary nebulae (La Laguna, Tenerife, Spain : Instituto de AstrofiÌĄsica de Canarias)
Marten, H., & Schönberner, D. 1991, A&A, 248, 590
Mathis, J. S. 1990, ARA&A, 28, 37
Mathis, J. S., Rumpl, W., & Nordsieck, K. H. 1977, ApJ, 217, 425
Matsumoto, H., Fukue, T., & Kamaya, H. 2006, PASJ, 58, 861
Matsumoto, H., et al. 2008, ApJ, 677, 1120
Matsuura, M., et al. 2009, MNRAS, 396, 918
—. 2014, ArXiv e-prints, 1401, 728
Mellema, G. 1994, A&A, 290, 915
Mendez, R. H., Kudritzki, R. P., & Herrero, A. 1992, A&A, 260, 329
Mendez, R. H., Kudritzki, R. P., Herrero, A., Husfeld, D., & Groth, H. G. 1988, A&A, 190, 113
Micelotta, E. R., Jones, A. P., & Tielens, A. G. G. M. 2010a, A&A, 510, 37
—. 2010b, A&A, 510, 36
Montillaud, J., Joblin, C., & Toublanc, D. 2013, A&A, 552, 15
Mori, T. I., Onaka, T., Sakon, I., Ishihara, D., Shimonishi, T., Ohsawa, R., & Bell, A. C. 2014, ApJ, in prep
Mori, T. I., Sakon, I., Onaka, T., Kaneda, H., Umehata, H., & Ohsawa, R. 2012a, in Galactic Archaeology: Near-Field Cosmology and the Formation of the Milky Way, Vol. 458 (Astronomical Society of the Pacific), 133
Mori, T. I., Sakon, I., Onaka, T., Kaneda, H., Umehata, H., & Ohsawa, R. 2012b, ApJ, 744, 68
Murakami, H., et al. 2007, PASJ, 59, 369
Neugebauer, G., et al. 1984, ApJLetters, 278, L1
Noble, J. A., Fraser, H. J., Aikawa, Y., Pontoppidan, K. M., & Sakon, I. 2013, ApJ, 775, 85
Ohsawa, R., Onaka, T., Sakon, I., Mori, T. I., Miyata, T., Asano, K., Matsuura, M., & Kaneda, H. 2012, ApJLetters, 760, L34
Ohyama, Y., et al. 2007, PASJ, 59, 411
Onaka, T., et al. 2007, PASJ, 59, 401
Otsuka, M., Kemper, F., Cami, J., Peeters, E., & Bernard-Salas, J. 2013, MNRAS, 2800
Paczyński, B. 1971, Acta Astronomica, 21, 417
Parker, Q. A., et al. 2006, MNRAS, 373, 79
—. 2012, MNRAS, 427, 3016
Parker, Q. A., & Frew, D. J. 2011, in Asymmetric Planetary Nebulae 5 (Bowness-on-Windermere: Jodrell Bank Centre for Astrophysics), 1
Peeters, E., Hony, S., van Kerckhoven, C., Tielens, A. G. G. M., Allamandola, L. J., Hudgins, D. M., & Bauschlicher, C. W. 2002a, A&A, 390, 1089
Peeters, E., et al. 2002b, A&A, 381, 571
Perea-Calderón, J. V., García-Hernández, D. A., García-Lario, P., Szczerba, R., & Bobrowsky, M. 2009, A&A, 495, L5
Perinotto, M., Schönberner, D., Steffen, M., & Calonaci, C. 2004, A&A, 414, 993
Phillips, J. P. 2003, MNRAS, 344, 501

Pino, T., et al. 2008, A&A, 490, 665
Pottasch, S. R. 1983, in Planetary nebulae, Vol. 103 (London, England: Dordrecht, D. Reidel Publishing Co.), 391–407
Pottasch, S. R., & Bernard-Salas, J. 2006, A&A, 457, 189
Preite-Martinez, A., Acker, A., Köppen, J., & Stenholm, B. 1989, A&AS, 81, 309
—. 1991, A&AS, 88, 121
Puget, J. L., & Leger, A. 1989, ARA&A, 27, 161
Renzini, A. 1981, in Physical Processes in Red Giants, Vol. 88, Erice, Italy, 431–446
Robinson, G. J., Reay, N. K., & Atherton, P. D. 1982, MNRAS, 199, 649
Roche, P. F., Lucas, P. W., Hoare, M. G., Aitken, D. K., & Smith, C. H. 1996, MNRAS, 280, 924
Sabbadin, F. 1986, A&AS, 64, 579
Sabbadin, F., Gratton, R. G., Bianchini, A., & Ortolani, S. 1984, A&A, 136, 181
Sabbadin, F., Turatto, M., Benetti, S., Ragazzoni, R., & Cappellaro, E. 2008, A&A, 488, 225
Sabin, L., Zijlstra, A. A., Wareing, C., Corradi, R. L. M., Mampaso, A., Viironen, K., Wright, N. J., & Parker, Q. A. 2010, Publications of the Astronomical Society of Australia, 27, 166
Sahai, R., Morris, M., Sánchez Contreras, C., & Claussen, M. 2007, AJ, 134, 2200
Sakon, I., Onaka, T., Okamoto, Y. K., Kataza, H., Kaneda, H., & Honda, M. 2006, Advances in Geosciences, Volume 7: Planetary Science (PS), 7, 133
Sakon, I., et al. 2008, in Society of Photo-Optical Instrumentation Engineers (SPIE) Conference Series, Vol. 7010, Space Telescopes and Instrumentation 2008: Optical, Infrared, and Millimeter, 88
Sanduleak, N., MacConnell, D. J., & Philip, A. G. D. 1978, Publications of the Astronomical Society of the Pacific, 90, 621
Schmidt-Voigt, M., & Köppen, J. 1987, A&A, 174, 211
Schönberner, D. 1981, A&A, 103, 119
Schönberner, D., Jacob, R., & Steffen, M. 2005a, A&A, 441, 573
Schönberner, D., Jacob, R., Steffen, M., Perinotto, M., Corradi, R. L. M., & Acker, A. 2005b, A&A, 431, 963
Schutte, W. A., Tielens, A. G. G. M., & Allamandola, L. J. 1993, ApJ, 415, 397
Sellgren, K., Tokunaga, A. T., & Nakada, Y. 1990, ApJ, 349, 120
Seok, J. Y., Hirashita, H., & Asano, R. S. 2014, ArXiv e-prints, 1401, 3943
Shklovsky, I., S. 1956, Astronomicheskii Zhurnal, 315, 222
Sloan, G. C., Bregman, J. D., Geballe, T. R., Allamandola, L. J., & Woodward, C. E. 1997, ApJ, 474, 735
Sloan, G. C., Hayward, T. L., Allamandola, L. J., Bregman, J. D., Devito, B., & Hudgins, D. M. 1999, ApJLetters, 513, L65
Sloan, G. C., et al. 2007, ApJ, 664, 1144
Smith, E. C. D., & McLean, I. S. 2008, ApJ, 676, 408
Smith, J. D. T., et al. 2007, ApJ, 656, 770
Speck, A. K., Corman, A. B., Wakeman, K., Wheeler, C. H., & Thompson, G. 2009, ApJ, 691, 1202
Stanghellini, L., García-Hernández, D. A., García-Lario, P., Davies, J. E., Shaw, R. A., Villaver, E., Manchado, A., & Perea-Calderón, J. V. 2012, ApJ, 753, 172

Stanghellini, L., García-Lario, P., García-Hernández, D. A., Perea-Calderón, J. V., Davies, J. E., Manchado, A., Villaver, E., & Shaw, R. A. 2007, ApJ, 671, 1669

Stanghellini, L., Guerrero, M. A., Cunha, K., Manchado, A., & Villaver, E. 2006, ApJ, 651, 898

Stanghellini, L., & Haywood, M. 2010, ApJ, 714, 1096

Stanghellini, L., Shaw, R. A., & Villaver, E. 2008, ApJ, 689, 194

Stanghellini, L., Villaver, E., Manchado, A., & Guerrero, M. A. 2002, ApJ, 576, 285

Storey, P. J., & Hummer, D. G. 1988, MNRAS, 231, 1139

—. 1995, MNRAS, 272, 41

van Diedenhoven, B., Peeters, E., van Kerckhoven, C., Hony, S., Hudgins, D. M., Allamandola, L. J., & Tielens, A. G. G. M. 2004, ApJ, 611, 928

Villaver, E., Manchado, A., & García-Segura, G. 2002, ApJ, 581, 1204

Volk, K., & Cohen, M. 1990, AJ, 100, 485

Wada, S., Onaka, T., Yamamura, I., Murata, Y., & Tokunaga, A. T. 2003, A&A, 407, 551

Wright, E. L., et al. 2010, AJ, 140, 1868

Yamagishi, M., Kaneda, H., Ishihara, D., Kondo, T., Onaka, T., Suzuki, T., & Minh, Y. C. 2012, A&A, 541, 10

Yamamura, I., Makiuti, S., Ikeda, N., Fukuda, Y., Oyabu, S., Koga, T., & White, G. J. 2010, VizieR Online Data Catalog, 2298, 0

Appendix A

Estimating Extinction from Near-Infrared Spectrum

There are several hydrogen recombination lines in the 2.5–5.0 μm spectrum. Extinction can be estimated based on the intensity ratio of these lines. The accuracy of the estimated extinction heavily depends on the signal-to-noise ratio (S/N) of the intensity ratio. This chapter describes the method to derive the extinction based on the IRC spectrum and shows that a typical uncertainty in A_V is ∼1 mag for the PNSPC samples.

A.1 Method

The observed intensity of the line emission X is given by $I_X^{obs} = I_X e^{-\tau_X}$, where I_X is the intrinsic intensity and τ_X is the extinction at the line X. The observed intensity ratio of the line X to Y is

$$\frac{I_X^{obs}}{I_Y^{obs}} = \frac{I_X}{I_Y} \exp\left(-\alpha(X,Y)A_V\right), \tag{A.1}$$

where $\alpha(X,Y)$ is defined by $(\tau_X - \tau_Y)/A_V$, which is a constant value specific to the extinction curve. Thus, the extinction is estimated by

$$A_V = \frac{\log x - \log x_o}{\alpha(X,Y)}, \tag{A.2}$$

where x is I_X/I_Y and x_o is I_X^{obs}/I_Y^{obs}. Given that the line X and Y are Brackett-α and β, respectively, the intrinsic intensity ratio is about 0.57 assuming the Case-B condition (Baker & Menzel, 1938) with the electron density of 10^4 K and the electron density of 10^4 cm^{-3}. The ratio is less sensitive to either the electron temperature or density. We adopt the extinction curve given by Mathis (1990). The value of $\alpha(\mathrm{Br}\beta, \mathrm{Br}\alpha)$ is about 0.041. The extinction estimated from the Brackett-β to α ratio is

$$A_V(\mathrm{Br}\beta, \mathrm{Br}\alpha) \simeq -24.5 \log x_o - 13.8. \tag{A.3}$$

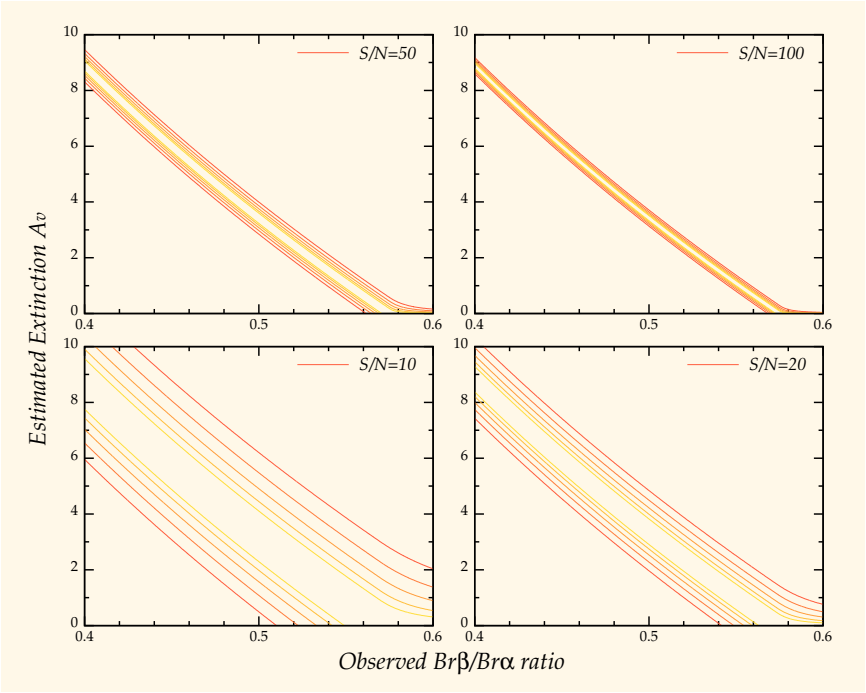

Figure A.1 – Estimated extinction and uncertainty. The contours show the confidence intervals of the 90, 80, 70, 60, and 50% of the peak value at the intensity ratio.

A.2 Uncertainty

The uncertainty in $A_V(\mathrm{Br}\beta, \mathrm{Br}\alpha)$ is investigated. The measured intensity ratio (x_o) includes a statistical error. Define the error by σ. Assuming that the variation in x_o is given by a normal distribution, the posterior probability distribution of the intensity ratio ($\bar{x}_o$) is given by

$$\mathrm{prob}(\bar{x}_o | x_o) \propto \frac{1}{\sqrt{2\pi}\sigma} \exp\left(-\frac{(x_o - \bar{x}_o)^2}{2\sigma^2}\right) \mathrm{prob}(\bar{x}_o), \tag{A.4}$$

where $\mathrm{prob}(\bar{x}_o)$ is the prior distribution of $\bar{x}_o$ given by a uniform distribution from 0 to x. From Equations (A.3) and (A.4), the posterior distribution of $A_V(\mathrm{Br}\beta, \mathrm{Br}\alpha)$ is given by

$$\mathrm{prob}(A_V | x_o) \propto \mathrm{prob}(\bar{x}_o | x_o)\mathrm{prob}(\bar{x}_o) \left|\frac{d\bar{x}_o}{dA_V}\right|. \tag{A.5}$$

The results for different S/N are shown in Figure A.1. The horizontal axis shows the observed intensity ratio (x_o), while the vertical axis is the estimated A_V value. The probability distribution is normalized so that the peak value should be unity at every x_o. The contours show the confidence intervals of the 90, 80, 70, 60, and 50% of the peak. Since a typical S/N for the PNSPC samples is ~50, the corresponding uncertainty on A_V is about 1 mag. The A_V values for the PNSPC samples are typically less than about 2 mag. Precisely estimating the extinction, based on the line intensity ratio in the IRC spectrum, is difficult.

Appendix B

Near-Infrared Spectral Fitting

The intensity of spectral features is measured by spectral fitting in Chapter 3. The fitted function is constructed by a linear-combination of template spectral features. The template spectra include continuum emission, line emissions, and the PAH features. Details of the template spectra and the fitting routine are described.

B.1 Fitted Function

As mentioned in Section 3.4.2, the fitted function is given by a linear combination of spectral features:

$$F_\lambda(\lambda) = \left[f_\lambda^{\rm cont}(\lambda) + f_\lambda^{\rm line}(\lambda) + f_\lambda^{\rm dust}(\lambda) \right] e^{-\tau(\lambda)}, \tag{B.1}$$

where $f_\lambda^{\rm cont}$, $f_\lambda^{\rm line}$, and $f_\lambda^{\rm dust}$ are respectively the components of continuum, line, and dust emission and $\tau(\lambda)$ is the optical depth at λ. The extinction curve is adopted from Mathis (1990). The extinction at the V-band and the intensities of the spectral features are taken as free parameters.

B.1.1 Spectral Templates

Continuum Emission. $f_\lambda^{\rm cont}$ is composed of a polynomial function and a step-like function. The polynomial component is defined by

$$f_\lambda^{\rm poly} = \sum_{i \leq 4} a_i \lambda^i, \tag{B.2}$$

where a_i's are the fitting parameters. The highest degree of the polynomial function is defined for each object, but it is limited below 5 since the fitting became unstable for $l \geq 5$. The step-like function is required to represent a sudden increase in the continuum at $\gtrsim 3.4$ μm (Boulanger et al., 2011). The increase is significant especially for PN G064.7+05.0 and 089.8−05.1. The step-like function is given by

$$f_\lambda^{\rm step}(\lambda) = \frac{b}{2} \left[1 + {\rm erf} \left(\frac{\lambda - 3.4}{\sigma} \right) \right], \tag{B.3}$$

Table B.1 – List of Line Emission in the Near-Infrared

Name	λ_0 (μm)	Name	λ_0 (μm)
Brakett-$\alpha^\dagger$	4.051	He II(7–6)‡	3.092
Brakett-$\beta^\dagger$	2.625	He II(9–7)‡	2.826
Pfund-$\beta^\dagger$	4.653	He II(8–7)‡	4.764
Pfund-$\gamma^\dagger$	3.740	He II(12–8)‡	2.625
Pfund-$\delta^\dagger$	3.296	He II(11–8)‡	3.096
Pfund-$\epsilon^\dagger$	3.039	He II(10–8)‡	4.051
Pfund-$\zeta^\dagger$	2.873	He II(14–9)‡	3.145
Pfund-$\eta^\dagger$	2.758	He II(13–9)‡	3.544
Humpleys-$\epsilon^\dagger$	4.671	He II(12–9)‡	4.218
Humpleys-$\zeta^\dagger$	4.376	He II(14–10)‡	4.652
He I($3P^o$–3D)	3.704	H_2(1–0)*	2.802
He I($1P^o$–1D)	4.123	H_2(1–0)*	3.003
He I(3S–$3P^o$)	4.296	H_2(1–0)*	3.234
He I($1P^o$–1S)	4.607	H_2(0–0)	3.836
He I($3P^o$–3S)	4.695	H_2(0–0)	4.181
		[Mg IV]	4.487
		[Ar VI]	4.530

Note. — †,‡: relative intensity of these lines are fixed assuming the Case B condition. *: rarely detected in the PNSPC samples. The intensities of these lines are not included in the catalog.

where b is the fitting parameter, $\mathrm{erf}(x)$ is the error function and σ is the width of the step, which is tentatively given by three times the width of line emission.

Line Emission. The profile of line emission is approximated by a Gaussian function. $f_\lambda^{\mathrm{line}}$ is given by a linear combination of Gaussian functions:

$$f_\lambda^{\mathrm{line}}(\lambda) = \sum_j \frac{c_j}{\sqrt{2\pi}\sigma} \exp\left(-\frac{(\lambda-\lambda_{j0})^2}{2\sigma^2}\right), \tag{B.4}$$

where λ_{j0} is the central wavelengths of the j-th line emission, σ is the line width and c_j's are the fitting parameters. The central wavelength is fixed in the fitting, while the line width is defined for each object since the present observations are made with the slit-less spectroscopy mode and the spectral resolution depends on the object size. The lines included in the fitting are listed in Table B.1. The name and central wavelength of line emission included in the fitting are respectively shown in the first and second columns. Some emission lines such as He II require a high excitation level. These lines do not appear when the effective temperature is low. Thus, to make the fitting stable and robust, the emission line that is apparently not detected is removed from the fitting.

Some of the H I and He II recombination lines appears at the same wavelengths. This makes it difficult to measure the line intensity accurately. To improve the fitting accuracy, the relative intensities of the H I and He II recombination lines

Table B.2 – List of PAH Features in the Near-Infrared

Band Name	λ_0 (μm)	Δ (μm)
PAH 3.25†	3.248	0.005
PAH 3.30†	3.296	0.021
PAH 3.41‡	3.410	0.030
PAH 3.46‡	3.460	0.013
PAH 3.51‡	3.512	0.013
PAH 3.56‡	3.560	0.013

Note. — †: the 3.3 μm PAH feature; ‡: the 3.4–3.5 μm PAH feature complex.

are, respectively, fixed assuming the Case B condition (Baker & Menzel, 1938). The relative intensities are adopted from Storey & Hummer (1995), assuming that the electron temperature and density are 10^4 K and 10^4 cm^{-2}, respectively. This method is also important to measure the intensity of the 3.3 μm PAH feature. The variations in the relative intensity with the electron temperature and density are almost negligible compared to the uncertainty in the observed spectrum.

Dust Emission. The spectral profile of dust emission is basically given by a Lorentzian function. The spectral resolution, however, practically changes due to the size of objects. The broadening of the spectral profile is not negligible even for dust emission. Thus, the spectral profile of dust emission is given by a convolution of a Lorentzian function and the spectral profile of line emission. $f_\lambda^{\rm dust}$ is given by:

$$f_\lambda^{\rm dust}(\lambda) = \sum_k \frac{d_k}{\pi\sqrt{2\pi}\sigma} \int d\lambda' \exp\left(-\frac{(\lambda-\lambda')^2}{2\sigma^2}\right) \frac{\Delta_k}{\Delta_k^2 + (\lambda'-\lambda_{k0})^2}, \tag{B.5}$$

where Δ_k and λ_{k0} are the width and peak wavelength of the n-th dust emission, respectively, and d_k's are the fitting parameters. The band name, central wavelength, and width of dust emission are listed in Table B.2. They are defined according to Mori et al. (2012b) and Beintema et al. (1996). The 3.3 μm PAH feature is defined by a combination of two Lorentzian functions. Four Lorentzian functions are used to represent the 3.4–3.5 μm complex features.

In the fitting, a_i's, b, c_j's, d_k's, and $A_V(\equiv \tau(V))$ are taken as free parameters. Since all the spectral features are in emission, we put a constraint on the fitting in such a way that b, c_j's, and d_k's should be non-negative.

B.2 Likelihood Function

Define the observed flux density and its uncertainty as $F_\lambda^{\rm obs}$ and $\sigma_\lambda^{\rm obs}$, respectively. We assume that the residual $\Delta_\lambda(\lambda) = [F_\lambda^{\rm obs} - F_\lambda](\lambda)$ follows a normal distribution of $\mathcal{N}(0, \sigma_\lambda^{\rm obs}(\lambda))$ when F_λ successfully fits the observed spectrum. Thus, the likeli-

hood function is given by

$$\mathcal{L} = \prod_n \frac{1}{\sqrt{2\pi}\sigma_\lambda^{obs}(\lambda)} \exp\left[-\frac{1}{2}\left(\frac{\Delta_\lambda(\lambda_n)}{\sigma_\lambda^{obs}(\lambda)}\right)^2\right], \tag{B.6}$$

where λ_n is the wavelength of the n-th bin. Though as mentioned in Appendix A, it is difficult to properly estimate A_V, based only on the near-infrared spectrum. Thus, we assume that A_V follows a normal distribution as:

$$\mathrm{prob}(A_V) \propto \exp\left[-\frac{1}{2}\left(\frac{A_V - A_V^{H\beta}}{\sigma(A_V^{H\beta})}\right)^2\right], \tag{B.7}$$

where $A_V^{H\beta}$ and $\sigma(A_V^{H\beta})$ are the V-band extinction estimated based on the Hβ to Brackett-α intensity ratio and its uncertainty, respectively. prob is used as a prior of A_V in the fitting. Therefore, the likelihood function is redefined by

$$\mathcal{L}' \propto \prod_n \frac{1}{\sqrt{2\pi}\sigma_\lambda^{obs}(\lambda)} \exp\left[-\frac{1}{2}\left(\frac{\Delta_\lambda(\lambda_n)}{\sigma_\lambda^{obs}(\lambda)}\right)^2 - \frac{1}{2}\left(\frac{A_V - A_V^{H\beta}}{\sigma(A_V^{H\beta})}\right)^2\right]. \tag{B.8}$$

The fitting parameters are defined by maximizing $\mathcal{L}'$ in such a way that b, c_j's, and d_k's should be non-negative.

The confidence interval of the fitting parameters is estimated based on a parameterized bootstrap method. We assume that the observed spectrum is derived from the normal distribution of $\mathcal{N}(F_\lambda^{obs}(\lambda), \sigma_\lambda^{obs}(\lambda))$. We obtain 1 000 sets of new spectra drawn from $\mathcal{N}(F_\lambda^{obs}(\lambda), \sigma_\lambda^{obs}(\lambda))$. The fitting parameters are defined for each spectrum. The probability distribution function of the fitting parameters is approximated by the distribution of the fitting parameter for the 1 000 samples. The lower and upper limits of the confidence interval are defined so that the confidence interval should enclose the 68% of the samples around the median.

Appendix C

Mid-Infrared Spectral Fitting

In Chapter 5, we measure the intensity of mid-infrared spectral features by spectral fitting. The fitted function is given by a linear combination of template spectral features. Details of the mid-infrared spectral components are described.

C.1 Fitted Function

The fitted function is given by a linear combination of spectral features:

$$F_\lambda(\lambda) = \left[f_\lambda^{\rm cont}(\lambda) + f_\lambda^{\rm line}(\lambda) + f_\lambda^{\rm dust}(\lambda)\right] e^{-\tau(\lambda)}, \tag{C.1}$$

where $f_\lambda^{\rm cont}$, $f_\lambda^{\rm line}$, and $f_\lambda^{\rm dust}$ are respectively the components of continuum, line, and dust emission and $\tau(\lambda)$ is the optical depth at λ. The extinction curve is adopted from Mathis (1990). Unlike the near-infrared spectral fitting, the extinction at the V-band is fixed and given by $A_V^{\rm NIR}$, which is the extinction at the V-band adopted from the results of the near-infrared spectral fitting. The intensities of the spectral features are taken as free parameters.

C.1.1 Spectral Templates

Continuum Emission. $f_\lambda^{\rm cont}$ is composed of a combination of graybody radiation and a broad plateau. The graybody component is defined as

$$f_\lambda^{\rm gray} = \sum_i \frac{a_i}{\lambda^2} \mathcal{B}_\lambda(\lambda, T_i), \tag{C.2}$$

where a_i's are the fitting parameters, $\mathcal{B}(\lambda, T_i)$ is the blackbody radiation function at λ with the dust temperature of T_i. The dust emissivity is assumed to be $\beta = -2$. The graybody component is usually given by a combination of two or three functions with different dust temperatures. The dust temperature typically ranges from 50 to 400 K. Although a large part of the continuum emission is represented by the graybody component, there is significant excess of the continuum emission

Table C.1 – List of Line Emission in the Mid-Infrared

Name	λ_0 (μm)	Name	λ_0 (μm)	Name	λ_0 (μm)
Pfund-α†	7.460	He I(1S–1P°)	7.438	[Ar II]	6.985
H(n=7–6)†	12.37	He I(1P°–1S)	7.939	[Ar III]	8.991
H(n=8–6)†	7.503	He I(1P°–1S)	8.529	[Ar V]	7.902
H(n=9–6)†	5.908	He II(10–9)	9.713	[Ar V]	13.10
H(n=10–6)†	5.129	He II(11–9)	5.583	[Na III]	7.318
H(n=9–7)†	11.31	He II(11–10)	13.13	[Ne II]	12.81
H(n=10–7)†	8.760	He II(12–10)	7.457	[Ne IV]	7.652
H(n=11–7)†	7.508	He II(13–10)	5.581	[S IV]	10.51
H(n=12–7)†	6.772	He II(13–11)	9.707	[Mg V]	5.610
H(n=11–8)†	12.39	He II(14–11)	7.205	[Mg V]	13.25
H(n=12–8)†	10.50				

Note. — †: relative intensity of these lines are fixed assuming the Case B condition.

around 6–9 μm (hereafter plateau). The plateau emission is approximated by a broad Gaussian function:

$$f_\lambda^{\rm plat} = \frac{b}{\sqrt{2\pi}\sigma} \exp\left(-\frac{(\lambda-\lambda_0)^2}{2\sigma^2}\right) \tag{C.3}$$

where λ_0 and σ are respectively the central wavelength and the width of the plateau and b is the fitting parameter. λ_0 and σ are tentatively assumed to be 7.8 and 1.1 μm, respectively.

Line Emission. The profile of line emission is approximated by a Gaussian function. $f_\lambda^{\rm line}$ is given by a linear combination of Gaussian functions:

$$f_\lambda^{\rm line}(\lambda) = \sum_j \frac{c_j}{\sqrt{2\pi}\sigma} \exp\left(-\frac{(\lambda-\lambda_{j0})^2}{2\sigma^2}\right), \tag{C.4}$$

where λ_{j0} is the central wavelength of the j-th line emission, σ is the line width and c_j's are the fitting parameters. The central wavelengths and line width are fixed in the fitting. σ is defined based on the instrumental spectral resolution (Houck et al., 2004). Table C.1 lists the emission lines included in the fitting. The name and central wavelength of line emission included in the fitting are respectively shown in the first and second column. The emission line that is apparently not detected is removed from the fitting as in the near-infrared fitting.

Some hydrogen emission lines appear at the same wavelengths as the PAH features. We assume that the relative strength of the hydrogen recombination lines is given by the Case B condition (Baker & Menzel, 1938). Assuming that the electron temperature and density are 10^4K and 10^4 cm^{-3}, respectively, the relative intensity is adopted from Storey & Hummer (1988). The variations in the relative intensity with the electron temperature and density are typically smaller than the uncertainty in the spectrum as in the near-infrared.

Table C.2 – List of PAH Features in the Mid-Infrared

Band Name	λ_0 (μm)	Δ (μm)	Band Name	λ_0 (μm)	Δ (μm)
PAH5.68	5.680	0.170	PAH11.2‡	11.23	0.135
PAH6.24	6.240	0.175	PAH11.3‡	11.30	0.249
PAH7.60†	7.600	0.334	PAH12.0	11.99	0.540
PAH7.85†	7.850	0.416	PAH12.6*	12.62	0.530
PAH7.40†	7.400	1.080	PAH12.7*	12.69	0.165
PAH8.61	8.610	0.336			

Note. — †: the 7.7 μm PAH feature complex; ‡: the 11.3μm PAH feature; *: the 12.7 μm PAH feature.

Dust Emission. The spectral profile of dust emission is given by a combination of the PAH features and a broad emission feature (SiC and silicate). The profile of the PAH features is given by a convolution of a Lorentzian function and the profile of line emission as in the near-infrared fitting. $f_\lambda^{\rm dust}$ is given by

$$f_\lambda^{\rm PAH}(\lambda) = \sum_k \frac{d_k}{\pi\sqrt{2\pi}\sigma} \int d\lambda' \exp\left(-\frac{(\lambda-\lambda')^2}{2\sigma^2}\right) \frac{\Delta_k}{\Delta_k^2 + (\lambda'-\lambda_{k0})^2}, \tag{C.5}$$

where Δ_k and λ_{k0} are the width and peak wavelength of the n-th dust emission, respectively, and d_k's are the fitting parameters. The band name, central wavelength, and width of dust emission are listed in Table C.2. They are defined based on the mid-infrared spectral fitting routine, PAHFIT, (Smith et al., 2007). The profile of the broad emission is approximated by a combination of Gaussian functions as

$$f_\lambda^{\rm broad}(\lambda) = \sum_{l=1}^{12} \frac{e_l}{\sqrt{2\pi}\sigma'} \exp\left(-\frac{(\lambda-\lambda_{l0})^2}{2\sigma'^2}\right), \tag{C.6}$$

where λ_{l0} is the central wavelength of the l-th Gaussian profile, σ' is the width of the profile, and e_l's are the fitting parameters. λ_{l0} and σ' are defined in such a way that $f_\lambda^{\rm broad}(\lambda)$ well represents the profile of the broad emission and each Gaussian component should be much larger than the PAH features. σ' is fixed and given by 1.5 μm. λ_{l0} is given by 9.5+0.25l. When the spectrum does not show any signature of the broad emission, $f_\lambda^{\rm broad}$ is removed from the fitting.

In the fitting, a_i's, b, c_j's, d_k's and e_l's are taken as free parameters. All the spectral features are in emission. In the fitting, we put a constraint in such a way that all the parameters should be non-negative.

C.2 Likelihood Function

Define the observed flux density and its uncertainty as $F_\lambda^{\rm obs}$ and $\sigma_\lambda^{\rm obs}$, respectively. We assume that the residual $\Delta_\lambda(\lambda) = [F_\lambda^{\rm obs} - F_\lambda](\lambda)$ follows a normal distribution of $\mathcal{N}(0, \sigma_\lambda^{\rm obs}(\lambda))$ when F_λ successfully fits the observed spectrum. Thus, the likeli-

hood function is given by

$$\mathcal{L} = \prod_{n} \frac{1}{\sqrt{2\pi}\sigma_{\lambda}^{\mathrm{obs}}(\lambda)} \exp\left[-\frac{1}{2}\left(\frac{\Delta_{\lambda}(\lambda_n)}{\sigma_{\lambda}^{\mathrm{obs}}(\lambda)}\right)^2\right], \tag{C.7}$$

where λ_n is the wavelength of the n-th bin. The fitting parameters are defined by maximizing $\mathcal{L}$ with the non-negative constraint mentioned above.

The confidence interval of the fitting parameters is estimated based on a parameterized bootstrap method as in the near-infrared fitting. We draw 1 000 sets of new spectra from $\mathcal{N}(F_{\lambda}^{\mathrm{obs}}(\lambda), \sigma_{\lambda}^{\mathrm{obs}}(\lambda))$, where $F_{\lambda}^{\mathrm{obs}}$ and $\sigma_{\lambda}^{\mathrm{obs}}$ are the observed flux density and its uncertainty, respectively. The fitting parameters are defined for each spectrum and the probability density function of the parameters is estimated based on the distribution of the fitting parameters. The lower and upper limits of the confidence interval are defined so that the confidence interval should enclose the 68% of the samples around the median.

Appendix D
Near-Infrared Spectral Atlas

In Chapter 3, we obtain the near-infrared spectra of Galactic PNe with the *AKARI*/IRC. The intensity and equivalent width of spectral features are measured. They are used to compile a near-infrared spectral catalog of Galactic PNe (PNSPC catalog). The tables in the PNSPC catalog are listed in this chapter.

D.1 Table Description

In Chapter 3, we compile a near-infrared spectral catalog of Galactic PNe (hereafter PNSPC catalog) based on the observations with the *AKARI*/IRC. The PNSPC catalog consists of three tables. Table D.1 shows the first one containing the basic information of the observations: the first column is PN G id, the second is the *AKARI* observation id, the third and fourth columns show the position and classification of the object, the fifth column is the total number of exposures, the seventh column shows the total integration time, the flag for saturation and contamination is shown in the eighth column, and the ninth and tenth columns show the extinction at the *V*-band toward the object estimated from the Hβ to Brα intensity ratio and the near-infrared spectral fitting with their uncertainties. The uncertainties are defined by the 68% confidence intervals. The measured intensity and equivalent width are listed in Table D.2, D.3, D.4, and D.5: the first column is the PN G id, and the following columns show the measured values with their uncertainties. The uncertainties are defined by the 68% confidence intervals. The spectral features whose intensity and equivalent width are measured are listed in Table 3.2. The intensities are shown in units of 10^{-16} W m^{-2}, while the equivalent widths are shown in units of Å. The tables show " $\cdots$ " when an emission feature is not detected. A 3-σ upper limit is shown when the signal-to-noise ratio is less than three.

Table D.1. PNSPC Catalog: Basic Information

PN G	Obs. ID	RA (J2000)	DEC (J2000)	Type	N	t_{int}	Flag	A_V(Hβ)	A_V(NIR)
		hh : mm : ss.s	dd : mm : ss.s			sec.	[sc]	mag.	mag.
(1)	(2)	(3)	(4)	(5)	(6)	(7)	(8)	(9)	(10)
002.0−13.4	3460003	18 : 45 : 50.7	−33 : 20 : 35.0	PN	16	710.56	00	$0.270^{+0.027}_{-0.022}$	$0.172^{+0.022}_{-0.005}$
003.1+02.9	3460005	17 : 41 : 52.8	−24 : 42 : 07.7	PN	9	399.69	01	$3.286^{+0.033}_{-0.032}$	$3.274^{+0.072}_{-0.077}$
011.0+05.8	3460012	17 : 48 : 19.8	−16 : 28 : 44.0	PN	18	799.38	00	$1.776^{+0.043}_{-0.042}$	$1.800^{+0.037}_{-0.002}$
027.6−09.6	3460016	19 : 16 : 28.3	−09 : 02 : 37.0	PN	9	399.69	00	$1.014^{+0.052}_{-0.045}$	$1.032^{+0.059}_{-0.007}$
037.8−06.3	3460019	19 : 22 : 56.9	+01 : 30 : 48.0	Star	17	754.97	00	$1.393^{+0.113}_{-0.110}$	$1.444^{+0.017}_{-0.071}$
038.2+12.0	3460020	18 : 17 : 34.0	+10 : 09 : 05.0	PN	9	399.69	00	$0.806^{+0.055}_{-0.062}$	$0.695^{+0.119}_{-0.047}$
046.4−04.1	3460021	19 : 31 : 16.4	+10 : 03 : 21.7	PN	9	399.69	01	$1.395^{+0.024}_{-0.023}$	$1.423^{+0.001}_{-0.001}$
051.4+09.6	3460022	18 : 49 : 47.6	+20 : 50 : 39.5	PN	17	754.97	00	$0.873^{+0.045}_{-0.044}$	$0.883^{+0.150}_{-0.012}$
058.3−10.9	3460023	20 : 20 : 08.8	+16 : 43 : 54.0	Star	18	799.38	00	$0.616^{+0.043}_{-0.041}$	$0.631^{+0.001}_{-0.003}$
060.1−07.7	3460024	20 : 12 : 42.9	+19 : 59 : 23.0	PN	14	621.74	00	$1.168^{+0.027}_{-0.023}$	$1.209^{+0.000}_{-0.000}$
060.5+01.8	3460025	19 : 38 : 08.4	+25 : 15 : 42.0	PN	18	799.38	00	$4.105^{+0.266}_{-0.195}$	$4.144^{+0.033}_{-0.038}$
064.7+05.0	3460026	19 : 34 : 45.3	+30 : 30 : 59.2	PN	17	77.86	10	$1.405^{+0.046}_{-0.043}$	$1.472^{+0.011}_{-0.016}$
071.6−02.3	3460027	20 : 21 : 03.8	+32 : 29 : 24.0	PN	18	799.38	00	$4.413^{+0.133}_{-0.115}$	$4.457^{+0.318}_{-0.013}$
074.5+02.1	3460028	20 : 10 : 52.5	+37 : 24 : 41.0	PN	18	799.38	00	$3.397^{+0.081}_{-0.077}$	$3.357^{+0.090}_{-0.053}$
082.1+07.0	3460029	20 : 10 : 23.7	+46 : 27 : 39.0	PN	18	799.38	00	$1.669^{+0.049}_{-0.044}$	$1.710^{+0.187}_{-0.004}$
082.5+11.3	3460030	19 : 49 : 46.6	+48 : 57 : 40.0	PN	9	399.69	01	$0.153^{+0.043}_{-0.042}$	$0.160^{+0.003}_{-0.005}$
089.3−02.2	3460031	21 : 19 : 07.2	+46 : 18 : 48.0	PN	18	799.38	00	$1.824^{+0.574}_{-0.378}$	$1.900^{+0.008}_{-0.005}$
089.8−05.1	3460032	21 : 32 : 31.0	+44 : 35 : 47.7	PN	18	799.38	00	$1.962^{+0.035}_{-0.036}$	$2.027^{+0.010}_{-0.006}$
095.2+00.7	3460033	21 : 31 : 50.2	+52 : 33 : 52.0	PN	18	799.38	00	$5.432^{+0.215}_{-0.199}$	$5.492^{+0.099}_{-0.128}$
100.6−05.4	3460034	22 : 23 : 55.7	+50 : 58 : 00.0	PN	18	799.38	00	$0.492^{+0.031}_{-0.030}$	$0.504^{+0.003}_{-0.001}$
111.8−02.8	3460035	23 : 26 : 14.9	+58 : 10 : 53.0	PN	8	355.28	00	$1.865^{+0.094}_{-0.102}$	$1.864^{+0.010}_{-0.004}$

Table D.1 (cont'd)

PN G	Obs. ID	RA (J2000)	DEC (J2000)	Type	N	t_{int}	Flag	$A_V(H\beta)$	A_V(NIR)
		hh : mm : ss.s	dd : mm : ss.s			sec.	[sc]	mag.	mag.
(1)	(2)	(3)	(4)	(5)	(6)	(7)	(8)	(9)	(10)
211.2−03.5	3460036	06 : 35 : 45.1	+00 : 05 : 38.0	PN	16	710.56	00	$3.449^{+0.162}_{-0.185}$	$3.493^{+0.006}_{-0.005}$
232.8−04.7	3460037	07 : 11 : 16.7	−19 : 51 : 04.0	PN	14	621.74	00	$2.893^{+0.041}_{-0.042}$	$3.006^{+0.000}_{-0.000}$
235.3−03.9	3460038	07 : 19 : 21.5	−21 : 43 : 54.3	PN	17	754.97	00	$1.561^{+0.186}_{-0.141}$	$1.619^{+0.006}_{-0.004}$
258.1−00.3	3460039	08 : 28 : 28.0	−39 : 23 : 40.0	PN	17	754.97	00	$3.993^{+0.026}_{-0.024}$	$4.061^{+0.001}_{-0.001}$
264.4−12.7	3460040	07 : 47 : 20.0	−51 : 15 : 03.4	PN	17	754.97	00	$0.680^{+0.070}_{-0.061}$	$0.690^{+0.014}_{-0.043}$
268.4+02.4	3460042	09 : 16 : 09.6	−45 : 28 : 42.8	PN	18	799.38	00	$3.771^{+0.021}_{-0.022}$	$3.901^{+0.012}_{-0.014}$
283.8+02.2	3460044	10 : 31 : 33.4	−55 : 20 : 50.5	PN	16	710.56	00	$1.535^{+0.022}_{-0.021}$	$1.559^{+0.002}_{-0.006}$
285.6−02.7	3460045	10 : 23 : 09.1	−60 : 32 : 42.3	PN	17	754.97	00	$2.080^{+0.025}_{-0.023}$	$2.122^{+0.000}_{-0.001}$
291.6−04.8	3460046	11 : 00 : 20.0	−65 : 14 : 57.8	PN	18	799.38	00	$1.770^{+0.015}_{-0.015}$	$1.797^{+0.014}_{-0.004}$
294.9−04.3	3460047	11 : 31 : 45.4	−65 : 58 : 13.7	PN	18	799.38	00	$1.777^{+0.014}_{-0.015}$	$1.794^{+0.015}_{-0.001}$
296.3−03.0	3460048	11 : 48 : 38.2	−65 : 08 : 37.3	PN	15	666.15	00	$2.303^{+0.050}_{-0.053}$	$2.334^{+0.039}_{-0.019}$
304.5−04.8	3460051	13 : 08 : 47.3	−67 : 38 : 37.6	PN	16	710.56	00	$1.313^{+0.053}_{-0.044}$	$1.359^{+0.012}_{-0.011}$
307.2−09.0	3460052	13 : 45 : 22.4	−71 : 28 : 55.7	PN	18	799.38	01	$1.131^{+0.011}_{-0.008}$	$1.159^{+0.001}_{-0.009}$
307.5−04.9	3460053	13 : 39 : 35.1	−67 : 22 : 51.7	PN	18	799.38	01	$1.541^{+0.186}_{-0.157}$	$1.629^{+0.040}_{-0.012}$
315.1−13.0	3460054	15 : 37 : 11.2	−71 : 54 : 52.9	PN	18	82.44	10	$0.772^{+0.028}_{-0.026}$	$0.782^{+0.060}_{-0.020}$
315.4+09.4	3460055	14 : 11 : 52.1	−51 : 26 : 24.1	Star	17	77.86	10	$2.064^{+0.460}_{-0.895}$	$1.958^{+0.007}_{-0.011}$
320.9+02.0	3460056	15 : 05 : 59.2	−55 : 59 : 16.5	PN	9	399.69	00	$5.014^{+0.052}_{-0.055}$	$5.113^{+0.069}_{-0.009}$
321.0+03.9	3460057	14 : 59 : 53.5	−54 : 18 : 07.5	PN	11	50.38	11	$3.091^{+0.472}_{-0.799}$	$3.019^{+5.085}_{-0.007}$
322.5−05.2	3460060	15 : 47 : 41.2	−61 : 13 : 05.6	PN	16	710.56	01	$0.768^{+0.029}_{-0.029}$	$0.824^{+0.009}_{-0.003}$
323.9+02.4	3460061	15 : 22 : 19.4	−54 : 08 : 13.1	PN	9	399.69	00	$3.015^{+0.027}_{-0.022}$	$3.086^{+0.007}_{-0.020}$
324.8−01.1	3460062	15 : 41 : 58.8	−56 : 36 : 25.6	PN	8	355.28	01	$6.272^{+0.010}_{-0.008}$	$7.003^{+0.035}_{-0.054}$

Table D.1 (cont'd)

PN G	Obs. ID	RA (J2000) hh : mm : ss.s	DEC (J2000) dd : mm : ss.s	Type	N	t_{int} sec.	Flag [sc]	A_V(Hβ) mag.	A_V(NIR) mag.
(1)	(2)	(3)	(4)	(5)	(6)	(7)	(8)	(9)	(10)
325.8−12.8	3460063	16 : 54 : 35.2	−64 : 14 : 28.4	PN	16	710.56	00	$0.482^{+0.016}_{-0.018}$	$0.494^{+0.001}_{-0.008}$
326.0−06.5	3460064	16 : 15 : 42.3	−59 : 54 : 01.0	PN	14	621.74	01	$1.198^{+0.073}_{-0.080}$	$1.214^{+0.052}_{-0.003}$
327.1−01.8	3460065	15 : 58 : 08.1	−55 : 41 : 50.3	PN	9	399.69	01	$3.791^{+0.015}_{-0.012}$	$3.976^{+0.013}_{-0.024}$
327.8−01.6	3460066	16 : 00 : 59.1	−55 : 05 : 39.7	PN	8	355.28	00	$5.079^{+0.008}_{-0.009}$	$5.392^{+0.026}_{-0.026}$
331.1−05.7	3460067	16 : 37 : 42.7	−55 : 42 : 26.5	PN	17	754.97	00	$1.316^{+0.057}_{-0.053}$	$1.363^{+0.075}_{-0.002}$
331.3+16.8	3460068	15 : 12 : 50.8	−38 : 07 : 32.0	PN	16	710.56	00	$0.094^{+0.021}_{-0.019}$	$0.101^{+0.001}_{-0.000}$
336.3−05.6	3460069	16 : 59 : 36.1	−51 : 42 : 08.4	PN	18	799.38	00	$1.297^{+0.055}_{-0.057}$	$1.343^{+0.017}_{-0.002}$
350.9+04.4	3460070	17 : 04 : 36.2	−33 : 59 : 18.0	PN	18	799.38	00	$1.803^{+0.031}_{-0.030}$	$1.809^{+0.006}_{-0.013}$
355.9+03.6	3460075	17 : 21 : 31.8	−30 : 20 : 48.0	PN	18	799.38	01	$2.757^{+0.198}_{-0.170}$	$2.699^{+0.008}_{-0.063}$
356.1+02.7	3460076	17 : 25 : 19.2	−30 : 40 : 41.0	PN	18	799.38	01	$5.828^{+1.331}_{-0.505}$	$4.444^{+0.380}_{-0.002}$
357.6+02.6	3460082	17 : 29 : 42.7	−29 : 32 : 50.0	PN	15	666.15	00	$4.453^{+1.078}_{-0.520}$	$5.718^{+0.654}_{-0.430}$
358.9−00.7	3460085	17 : 45 : 57.7	−30 : 12 : 01.0	PN	18	82.44	10	$3.010^{+0.065}_{-0.068}$	$2.983^{+0.009}_{-0.300}$
043.1+03.8	3460093	18 : 56 : 33.6	+10 : 52 : 12.0	PN	9	399.69	01	$1.910^{+0.131}_{-0.128}$	$1.957^{+0.137}_{-0.015}$
052.2−04.0	3460094	19 : 42 : 18.7	+15 : 09 : 09.0	PN	18	799.38	00	$1.651^{+0.053}_{-0.052}$	$1.689^{+0.110}_{-0.004}$
093.5+01.4	3460095	21 : 20 : 44.7	+51 : 53 : 26.1	HII	18	82.44	10	$7.396^{+0.651}_{-0.540}$	$6.977^{+0.304}_{-0.025}$
118.0−08.6	3460096	00 : 18 : 42.2	+53 : 52 : 20.0	PN	16	710.56	00	$0.366^{+0.089}_{-0.089}$	$0.340^{+0.005}_{-0.018}$
146.7+07.6	3460097	04 : 25 : 50.8	+60 : 07 : 12.7	PN	18	799.38	00	$1.505^{+0.102}_{-0.093}$	$1.552^{+0.019}_{-0.101}$
159.0−15.1	3460098	03 : 47 : 33.0	+35 : 02 : 48.9	PN	9	399.69	00	$0.409^{+0.032}_{-0.034}$	$0.416^{+0.002}_{-0.003}$
190.3−17.7	3460099	05 : 05 : 34.3	+10 : 42 : 23.8	PN	9	399.69	00	$0.318^{+0.028}_{-0.027}$	$0.321^{+0.001}_{-0.122}$
226.7+05.6	3460100	07 : 37 : 18.9	−09 : 38 : 50.0	PN	17	754.97	00	$1.601^{+0.021}_{-0.023}$	$1.644^{+0.008}_{-0.003}$
278.6−06.7	3460101	09 : 19 : 27.5	−59 : 12 : 00.3	PN	18	799.38	00	$0.712^{+0.032}_{-0.030}$	$0.725^{+0.013}_{-0.014}$

Table D.1 (cont'd)

PN G	Obs. ID	RA (J2000)	DEC (J2000)	Type	N	t_{int}	Flag	$A_V(H\beta)$	A_V(NIR)
		hh : mm : ss.s	dd : mm : ss.s			sec.	[sc]	mag.	mag.
(1)	(2)	(3)	(4)	(5)	(6)	(7)	(8)	(9)	(10)
292.8+01.1	3460102	11 : 28 : 47.4	−60 : 06 : 37.3	PN	18	799.38	00	$2.003^{+0.030}_{-0.027}$	$2.043^{+0.001}_{-0.065}$
320.1−09.6	3460103	15 : 56 : 01.7	−66 : 09 : 09.2	PN	16	710.56	00	$0.692^{+0.012}_{-0.010}$	$0.695^{+0.006}_{-0.016}$
342.1+27.5	3460104	15 : 22 : 19.3	−23 : 37 : 32.0	PN	18	799.38	00	$0.215^{+0.022}_{-0.030}$	$0.236^{+0.007}_{-0.003}$
349.8+04.4	3460105	17 : 01 : 06.2	−34 : 49 : 38.0	PN	9	399.69	00	$1.820^{+0.170}_{-0.128}$	$1.898^{+0.033}_{-0.117}$
000.3+12.2	3460107	17 : 01 : 33.6	−21 : 49 : 33.5	PN	17	754.97	00	$0.882^{+0.024}_{-0.022}$	$0.906^{+0.001}_{-0.003}$
086.5−08.8	3460114	21 : 33 : 08.3	+39 : 38 : 09.7	PN	18	799.38	01	$0.570^{+0.028}_{-0.025}$	$0.576^{+0.001}_{-0.001}$
123.6+34.5	3460115	12 : 33 : 06.8	+82 : 33 : 50.1	PN	18	799.38	01	$0.463^{+0.029}_{-0.027}$	$0.480^{+0.002}_{-0.021}$
166.1+10.4	3460116	05 : 56 : 23.9	+46 : 06 : 17.2	PN	18	799.38	00	$0.594^{+0.028}_{-0.028}$	$0.615^{+0.025}_{-0.003}$
194.2+02.5	3460117	06 : 25 : 57.2	+17 : 47 : 27.3	PN	18	799.38	00	$1.362^{+0.063}_{-0.060}$	$1.372^{+0.030}_{-0.086}$
221.3−12.3	3460118	06 : 21 : 42.7	−12 : 59 : 14.0	PN	15	666.15	00	$0.878^{+0.014}_{-0.013}$	$0.949^{+0.010}_{-0.005}$
285.4−05.3	3460120	10 : 09 : 20.8	−62 : 36 : 48.5	PN	18	799.38	00	$0.726^{+0.021}_{-0.022}$	$0.743^{+0.002}_{-0.000}$
285.7−14.9	3460121	09 : 07 : 06.3	−69 : 56 : 30.6	PN	17	754.97	00	$0.111^{+0.031}_{-0.031}$	$0.125^{+0.000}_{-0.001}$
305.1+01.4	3460122	13 : 09 : 36.4	−61 : 19 : 35.6	PN	18	82.44	10	$3.459^{+0.128}_{-0.134}$	$3.500^{+0.020}_{-0.012}$
312.6−01.8	3460123	14 : 18 : 43.3	−63 : 07 : 10.1	PN	16	710.56	00	$3.141^{+0.022}_{-0.021}$	$3.267^{+0.017}_{-0.063}$

Note. — (1) PN G ID; (2) *AKARI* observation ID; (3,4) the position of the object in the equatorial coordinates (J2000); (5) Simbad object type; (6) the number of frames; (7) the total integration time; (8) the saturation and contamination flag; 00: no saturation and no contamination, 01: contaminated, 10: saturated in the long exposures, 11: saturated and contaminated; (9) the extinction at the *V*-band based on the $I_{H\beta}/I_{Br\alpha}$ ratio; (10) the extinction at the *V*-band based on the IRC spectrum.

Table D.2. PNSPC Catalog: Extinction Corrected Intensity (1)

PN G	Bracket-α 10^{-16}W m^{-2}	He II(3.09μm) 10^{-16}W m^{-2}	He I(3.70μm) 10^{-16}W m^{-2}	He I(4.12μm) 10^{-16}W m^{-2}	He I(4.30μm) 10^{-16}W m^{-2}	He I(4.61μm) 10^{-16}W m^{-2}	He I(4.70μm) 10^{-16}W m^{-2}
(1)	(2)	(3)	(4)	(5)	(6)	(7)	(8)
002.0−13.4	$2.052^{+0.047}_{-0.033}$	...	<0.035	$0.043^{+0.018}_{-0.009}$	$0.306^{+0.026}_{-0.025}$	$0.192^{+0.013}_{-0.014}$	<0.022
003.1+02.9	$3.154^{+0.130}_{-0.072}$	<0.517	$0.203^{+0.056}_{-0.027}$	$0.195^{+0.014}_{-0.030}$	$0.427^{+0.037}_{-0.028}$	$0.725^{+0.064}_{-0.070}$	<0.292
011.0+05.8	$1.091^{+0.078}_{-0.045}$	$0.129^{+0.035}_{-0.023}$	<0.030	<0.059	<0.121	$0.223^{+0.043}_{-0.029}$	<0.065
027.6−09.6	$1.107^{+0.036}_{-0.025}$	...	$0.021^{+0.008}_{-0.005}$	$0.039^{+0.011}_{-0.011}$	$0.098^{+0.010}_{-0.010}$	$0.064^{+0.008}_{-0.006}$	<0.017
037.8−06.3	$4.670^{+0.229}_{-0.009}$	...	$0.124^{+0.099}_{-0.037}$	$0.256^{+0.081}_{-0.020}$	$1.739^{+0.144}_{-0.005}$	$0.200^{+0.110}_{-0.034}$	<0.122
038.2+12.0	$2.226^{+0.046}_{-0.054}$	...	<0.048	$0.082^{+0.016}_{-0.017}$	$0.056^{+0.033}_{-0.016}$	<0.029	<0.061
046.4−04.1	$2.433^{+0.020}_{-0.008}$	$0.110^{+0.019}_{-0.019}$	<0.040	$0.106^{+0.019}_{-0.010}$	$0.324^{+0.020}_{-0.010}$	$0.280^{+0.019}_{-0.016}$	<0.027
051.4+09.6	$3.263^{+0.090}_{-0.042}$	...	<0.068	$0.132^{+0.026}_{-0.022}$	$0.514^{+0.033}_{-0.028}$	$0.111^{+0.021}_{-0.018}$	<0.052
058.3−10.9	$4.617^{+0.063}_{-0.159}$	...	<0.116	$0.133^{+0.044}_{-0.014}$	$0.996^{+0.083}_{-0.060}$	$0.173^{+0.047}_{-0.027}$	$0.130^{+0.053}_{-0.039}$
060.1−07.7	$1.445^{+0.018}_{-0.014}$	$0.210^{+0.021}_{-0.026}$	<0.032	$0.105^{+0.013}_{-0.013}$	$0.114^{+0.016}_{-0.017}$	$0.228^{+0.020}_{-0.013}$	<0.060
060.5+01.8	$1.111^{+0.014}_{-0.005}$	...	$0.022^{+0.011}_{-0.000}$	$0.025^{+0.013}_{-0.001}$	$0.149^{+0.012}_{-0.000}$	$0.106^{+0.011}_{-0.003}$	<0.012
064.7+05.0	$34.243^{+3.819}_{-2.099}$	...	<10.845	<17.731	<11.635	<8.396	$4.072^{+2.635}_{-0.962}$
071.6−02.3	$3.467^{+0.119}_{-0.126}$	...	<0.102	$0.172^{+0.114}_{-0.049}$	$0.667^{+0.082}_{-0.070}$	<0.088	<0.146
074.5+02.1	$1.709^{+0.180}_{-0.388}$	$0.396^{+0.113}_{-0.046}$	<0.261	<0.483	<0.402	$0.274^{+0.144}_{-0.063}$	$0.169^{+0.109}_{-0.052}$
082.1+07.0	$3.854^{+0.037}_{-0.129}$	$0.447^{+0.072}_{-0.060}$	<0.000	$0.184^{+0.027}_{-0.010}$	$0.340^{+0.029}_{-0.022}$	$0.339^{+0.032}_{-0.011}$	<0.083
082.5+11.3	$0.521^{+0.017}_{-0.016}$	...	<0.019	<0.025	$0.109^{+0.020}_{-0.015}$	<0.039	<0.025
089.3−02.2	$0.767^{+0.191}_{-0.085}$	...	...	...	...	...	...
089.8−05.1	$2.994^{+0.133}_{-0.124}$	$0.258^{+0.076}_{-0.030}$	...	$0.318^{+0.086}_{-0.039}$	$0.972^{+0.090}_{-0.066}$	$0.325^{+0.082}_{-0.055}$	<0.218
095.2+00.7	$2.487^{+0.014}_{-0.071}$	...	$0.066^{+0.019}_{-0.013}$	$0.095^{+0.015}_{-0.016}$	$0.483^{+0.020}_{-0.015}$	$0.234^{+0.021}_{-0.007}$	...
100.6−05.4	$0.931^{+0.023}_{-0.025}$	$0.048^{+0.011}_{-0.013}$	<0.022	<0.020	$0.054^{+0.011}_{-0.011}$	$0.043^{+0.013}_{-0.012}$	<0.011
111.8−02.8	$5.831^{+0.206}_{-0.020}$	...	$0.520^{+0.130}_{-0.040}$	$0.831^{+0.125}_{-0.037}$	$1.866^{+0.169}_{-0.059}$	$0.614^{+0.162}_{-0.026}$	$0.451^{+0.119}_{-0.095}$

Table D.2 (cont'd)

PN G	Bracket-α 10^{-16}W m^{-2}	He II(3.09μm) 10^{-16}W m^{-2}	He I(3.70μm) 10^{-16}W m^{-2}	He I(4.12μm) 10^{-16}W m^{-2}	He I(4.30μm) 10^{-16}W m^{-2}	He I(4.61μm) 10^{-16}W m^{-2}	He I(4.70μm) 10^{-16}W m^{-2}
(1)	(2)	(3)	(4)	(5)	(6)	(7)	(8)
211.2−03.5	$1.826^{+0.072}_{-0.042}$	...	<0.132	<0.082	$0.288^{+0.052}_{-0.041}$	<0.088	<0.042
232.8−04.7	$2.785^{+0.330}_{-0.152}$	...	...	...	...	...	...
235.3−03.9	$1.121^{+0.064}_{-0.063}$	...	<0.145	<0.042	$0.166^{+0.047}_{-0.042}$	<0.098	<0.023
258.1−00.3	$3.687^{+0.405}_{-0.132}$	...	<0.149	$0.166^{+0.041}_{-0.029}$	$0.553^{+0.058}_{-0.046}$	$0.210^{+0.029}_{-0.043}$	...
264.4−12.7	$0.703^{+0.016}_{-0.020}$	...	<0.010	<0.018	$0.066^{+0.012}_{-0.007}$	$0.035^{+0.011}_{-0.009}$	<0.011
268.4+02.4	$1.590^{+0.043}_{-0.033}$	$0.229^{+0.032}_{-0.011}$	$0.049^{+0.039}_{-0.002}$	$0.211^{+0.044}_{-0.027}$	$0.303^{+0.057}_{-0.049}$	$0.161^{+0.060}_{-0.027}$	$0.103^{+0.050}_{-0.007}$
283.8+02.2	$0.720^{+0.024}_{-0.028}$	$0.326^{+0.022}_{-0.022}$	<0.004	$0.104^{+0.012}_{-0.007}$	<0.020	$0.091^{+0.018}_{-0.013}$	$0.045^{+0.012}_{-0.011}$
285.6−02.7	$4.936^{+0.185}_{-0.149}$	...	<0.000	$0.174^{+0.084}_{-0.028}$	$0.255^{+0.126}_{-0.027}$	<0.089	<0.064
291.6−04.8	$2.912^{+0.079}_{-0.067}$	$0.556^{+0.035}_{-0.030}$	$0.117^{+0.000}_{-0.022}$	$0.203^{+0.052}_{-0.008}$	$0.430^{+0.005}_{-0.036}$	$0.501^{+0.000}_{-0.054}$	$0.114^{+0.023}_{-0.013}$
294.9−04.3	$0.919^{+0.043}_{-0.039}$	...	<0.058	<0.072	$0.144^{+0.034}_{-0.030}$	<0.064	<0.060
296.3−03.0	$1.166^{+0.036}_{-0.131}$	$0.114^{+0.041}_{-0.020}$	<0.035	$0.080^{+0.063}_{-0.024}$	$0.176^{+0.065}_{-0.036}$	$0.200^{+0.032}_{-0.048}$	<0.066
304.5−04.8	$3.460^{+0.031}_{-0.049}$	$0.305^{+0.044}_{-0.035}$	...	$0.208^{+0.040}_{-0.014}$	$0.475^{+0.034}_{-0.027}$	$0.388^{+0.040}_{-0.022}$	$0.150^{+0.048}_{-0.021}$
307.2−09.0	$0.971^{+0.040}_{-0.006}$	...	<0.004	$0.048^{+0.024}_{-0.000}$	$0.191^{+0.016}_{-0.006}$	$0.063^{+0.034}_{-0.000}$	$0.068^{+0.044}_{-0.001}$
307.5−04.9	$2.659^{+0.119}_{-0.222}$	...	<0.015	$0.329^{+0.044}_{-0.042}$	$0.297^{+0.035}_{-0.030}$	$0.316^{+0.041}_{-0.031}$	$0.214^{+0.055}_{-0.031}$
315.1−13.0	$12.649^{+1.353}_{-1.450}$	...	<0.265	$0.609^{+0.209}_{-0.086}$	$0.607^{+0.246}_{-0.080}$	<0.326	$0.318^{+0.177}_{-0.074}$
315.4+09.4	<2.437	...	...	...	...	...	...
320.9+02.0	$5.982^{+0.436}_{-0.027}$	...	<0.118	$0.330^{+0.029}_{-0.036}$	$1.126^{+0.063}_{-0.038}$	$1.019^{+0.063}_{-0.013}$	$0.109^{+0.060}_{-0.000}$
321.0+03.9	...	...	...	...	...	...	...
322.5−05.2	$1.170^{+0.027}_{-0.016}$	$0.788^{+0.023}_{-0.018}$	$0.169^{+0.044}_{-0.009}$	$0.052^{+0.017}_{-0.007}$	$0.082^{+0.025}_{-0.007}$	$0.055^{+0.032}_{-0.005}$	$0.002^{+0.015}_{-0.000}$
323.9+02.4	$2.016^{+0.046}_{-0.049}$	...	<0.036	$0.157^{+0.028}_{-0.023}$	$0.248^{+0.029}_{-0.028}$	$0.207^{+0.015}_{-0.020}$	<0.035
324.8−01.1	$4.472^{+0.125}_{-0.229}$	...	$0.123^{+0.047}_{-0.036}$	$0.232^{+0.031}_{-0.042}$	$0.878^{+0.073}_{-0.084}$	$0.555^{+0.044}_{-0.065}$	<0.089

Table D.2 (cont'd)

PN G	Bracket-α 10^{-16}W m^{-2}	He II(3.09μm) 10^{-16}W m^{-2}	He I(3.70μm) 10^{-16}W m^{-2}	He I(4.12μm) 10^{-16}W m^{-2}	He I(4.30μm) 10^{-16}W m^{-2}	He I(4.61μm) 10^{-16}W m^{-2}	He I(4.70μm) 10^{-16}W m^{-2}
(1)	(2)	(3)	(4)	(5)	(6)	(7)	(8)
325.8−12.8	$1.511^{+0.032}_{-0.025}$	...	<0.020	$0.050^{+0.018}_{-0.006}$	$0.175^{+0.018}_{-0.009}$	$0.046^{+0.022}_{-0.015}$	<0.063
326.0−06.5	$0.370^{+0.011}_{-0.017}$	...	<0.022	<0.033	<0.018	<0.047	<0.015
327.1−01.8	$1.699^{+0.082}_{-0.151}$	...	$0.062^{+0.036}_{-0.013}$	<0.134	<0.293	<0.213	<0.023
327.8−01.6	$1.978^{+0.070}_{-0.027}$	$0.448^{+0.000}_{-0.008}$	$0.030^{+0.000}_{-0.000}$	$0.272^{+0.000}_{-0.005}$	$0.301^{+0.012}_{-0.003}$	$0.635^{+0.002}_{-0.008}$	$0.214^{+0.001}_{-0.002}$
331.1−05.7	$1.152^{+0.042}_{-0.064}$	...	...	$0.053^{+0.016}_{-0.008}$	$0.332^{+0.022}_{-0.024}$	<0.052	<0.086
331.3+16.8	$0.743^{+0.019}_{-0.012}$	$0.204^{+0.013}_{-0.008}$	<0.011	$0.046^{+0.018}_{-0.012}$	<0.041	$0.018^{+0.018}_{-0.005}$	$0.022^{+0.021}_{-0.006}$
336.3−05.6	$0.218^{+0.016}_{-0.012}$	$0.061^{+0.012}_{-0.009}$	<0.027	<0.010	<0.024	$0.033^{+0.019}_{-0.007}$	$0.034^{+0.017}_{-0.006}$
350.9+04.4	$2.053^{+0.088}_{-0.062}$	...	...	<0.075	$0.143^{+0.040}_{-0.011}$	$0.082^{+0.037}_{-0.026}$	<0.052
355.9+03.6	$0.758^{+0.171}_{-0.073}$	...	...	...	...	...	...
356.1+02.7	$0.709^{+0.094}_{-0.054}$	...	<0.100	...	$0.140^{+0.039}_{-0.029}$	<0.079	<0.016
357.6+02.6	$0.755^{+0.080}_{-0.098}$	...	<0.082	<0.083	$0.199^{+0.051}_{-0.043}$	$0.169^{+0.034}_{-0.026}$	<0.053
358.9−00.7	$15.057^{+0.680}_{-0.416}$	...	<0.612	$1.182^{+0.239}_{-0.348}$	<0.628	<1.040	...
043.1+03.8	$0.458^{+0.026}_{-0.013}$	...	$0.049^{+0.015}_{-0.012}$	<0.018	...	$0.058^{+0.011}_{-0.013}$	<0.043
052.2−04.0	$0.848^{+0.032}_{-0.031}$	...	<0.012	<0.017	$0.135^{+0.011}_{-0.010}$	$0.101^{+0.009}_{-0.009}$	$0.035^{+0.009}_{-0.006}$
093.5+01.4	$29.809^{+0.198}_{-0.000}$	...	$0.283^{+0.000}_{-0.000}$	$2.502^{+0.000}_{-0.000}$	$3.670^{+0.000}_{-0.000}$	$0.405^{+0.000}_{-0.000}$	$1.998^{+0.000}_{-0.000}$
118.0−08.6	$0.351^{+0.030}_{-0.019}$	...	<0.060	<0.016	<0.046	<0.044	<0.044
146.7+07.6	$0.566^{+0.039}_{-0.065}$	...	<0.043	<0.129	$0.127^{+0.040}_{-0.039}$	<0.044	<0.011
159.0−15.1	$0.477^{+0.012}_{-0.014}$	$0.107^{+0.016}_{-0.014}$	<0.038	$0.053^{+0.024}_{-0.017}$	<0.067	$0.047^{+0.023}_{-0.014}$	<0.039
190.3−17.7	$0.463^{+0.008}_{-0.007}$	...	...	$0.045^{+0.010}_{-0.010}$	$0.041^{+0.012}_{-0.007}$	$0.035^{+0.008}_{-0.009}$	<0.027
226.7+05.6	$0.468^{+0.011}_{-0.025}$	$0.050^{+0.006}_{-0.003}$	<0.007	$0.028^{+0.007}_{-0.006}$	$0.040^{+0.009}_{-0.007}$	$0.026^{+0.009}_{-0.007}$	$0.063^{+0.012}_{-0.007}$
278.6−06.7	$0.588^{+0.015}_{-0.012}$	$0.027^{+0.006}_{-0.007}$	<0.010	<0.015	$0.086^{+0.011}_{-0.007}$	$0.033^{+0.010}_{-0.008}$	<0.004

Table D.2 (cont'd)

PN G	Bracket-α 10^{-16}W m^{-2}	He II(3.09μm) 10^{-16}W m^{-2}	He I(3.70μm) 10^{-16}W m^{-2}	He I(4.12μm) 10^{-16}W m^{-2}	He I(4.30μm) 10^{-16}W m^{-2}	He I(4.61μm) 10^{-16}W m^{-2}	He I(4.70μm) 10^{-16}W m^{-2}
(1)	(2)	(3)	(4)	(5)	(6)	(7)	(8)
292.8+01.1	$0.784^{+0.069}_{-0.038}$	$0.084^{+0.015}_{-0.010}$	<0.003	$0.034^{+0.013}_{-0.010}$	$0.076^{+0.019}_{-0.012}$	$0.100^{+0.012}_{-0.010}$	<0.042
320.1−09.6	$3.249^{+0.058}_{-0.040}$	...	<0.190	$0.162^{+0.088}_{-0.029}$	<0.124	<0.021	<0.006
342.1+27.5	$0.467^{+0.014}_{-0.012}$	$0.260^{+0.019}_{-0.014}$	<0.021	<0.026	<0.042	$0.036^{+0.019}_{-0.010}$	<0.024
349.8+04.4	$0.900^{+0.034}_{-0.099}$	...	<0.018	<0.028	$0.135^{+0.015}_{-0.011}$	$0.105^{+0.015}_{-0.015}$	...
000.3+12.2	$2.768^{+0.043}_{-0.015}$	...	$0.027^{+0.030}_{-0.006}$	$0.177^{+0.025}_{-0.004}$	$0.189^{+0.022}_{-0.007}$	$0.239^{+0.035}_{-0.016}$	<0.067
086.5−08.8	$0.915^{+0.018}_{-0.020}$	$0.496^{+0.022}_{-0.017}$	<0.024	$0.086^{+0.106}_{-0.015}$	<0.133	$0.213^{+0.042}_{-0.015}$	$0.080^{+0.044}_{-0.016}$
123.6+34.5	$2.023^{+0.057}_{-0.064}$	...	<0.032	$0.148^{+0.045}_{-0.041}$	<0.160	<0.103	<0.034
166.1+10.4	$4.353^{+0.066}_{-0.077}$	...	<0.040	$0.275^{+0.051}_{-0.049}$	$0.347^{+0.056}_{-0.048}$	$0.187^{+0.055}_{-0.051}$	<0.169
194.2+02.5	$1.733^{+0.061}_{-0.050}$	$0.403^{+0.053}_{-0.051}$	<0.149	<0.178	<0.163	<0.137	<0.161
221.3−12.3	$2.767^{+0.035}_{-0.022}$	$0.732^{+0.025}_{-0.040}$	<0.037	$0.252^{+0.036}_{-0.019}$	$0.234^{+0.045}_{-0.034}$	$0.202^{+0.039}_{-0.029}$	$0.109^{+0.037}_{-0.029}$
285.4−05.3	$2.675^{+0.018}_{-0.009}$	$0.428^{+0.019}_{-0.024}$	...	$0.098^{+0.020}_{-0.004}$	$0.180^{+0.018}_{-0.012}$	$0.311^{+0.020}_{-0.011}$	<0.020
285.7−14.9	$1.286^{+0.030}_{-0.031}$	$0.225^{+0.039}_{-0.028}$	<0.045	$0.226^{+0.048}_{-0.042}$	<0.146	<0.112	<0.082
305.1+01.4	$12.462^{+1.593}_{-1.589}$	...	...	...	...	...	...
312.6−01.8	$1.396^{+0.066}_{-0.081}$	...	<0.037	$0.060^{+0.017}_{-0.016}$	$0.121^{+0.021}_{-0.017}$	$0.070^{+0.024}_{-0.023}$	<0.019

Note. — (1) PN G ID; (2) Brackett-α at 4.051 μm; (3) He II(7−6) recombination line at 3.09 μm; (4) He I($3P^o$−3D) recombination line at 3.70 μm; (5) He I($1P^o$−1D) recombination line at 4.12 μm; (6) He I(3S−$3P^o$) recombination line at 4.30 μm; (7) He I($1P^o$−1S) recombination line at 4.61 μm; (8) He I($3P^o$−3S) recombination line at 4.70 μm.

Table D.3. PNSPC Catalog: Extinction Corrected Intensity (2)

PN G	Mg IV(4.49μm) 10^{-16}W m^{-2}	Ar VI(4.53μm) 10^{-16}W m^{-2}	H_2(3.84μm) 10^{-16}W m^{-2}	H_2(4.18μm) 10^{-16}W m^{-2}	PAH(3.3μm) 10^{-16}W m^{-2}	PAH(3.4-3.5μm) 10^{-16}W m^{-2}
(1)	(2)	(3)	(4)	(5)	(6)	(7)
002.0−13.4	...	...	<0.028	$0.042^{+0.012}_{-0.009}$	$0.251^{+0.047}_{-0.036}$	$0.100^{+0.031}_{-0.027}$
003.1+02.9	$0.361^{+0.029}_{-0.050}$	...	...	...	$1.037^{+0.153}_{-0.188}$	$0.509^{+0.116}_{-0.079}$
011.0+05.8	$1.087^{+0.102}_{-0.066}$	$0.196^{+0.054}_{-0.043}$	...	...	...	...
027.6−09.6	...	...	...	...	...	...
037.8−06.3	...	...	$0.266^{+0.088}_{-0.028}$	<0.091	$5.881^{+0.197}_{-0.040}$	$1.136^{+0.162}_{-0.012}$
038.2+12.0	...	...	<0.011	<0.026	$0.443^{+0.058}_{-0.054}$	$0.120^{+0.040}_{-0.032}$
046.4−04.1	...	...	...	$0.069^{+0.021}_{-0.005}$	$0.409^{+0.042}_{-0.060}$	$0.157^{+0.079}_{-0.044}$
051.4+09.6	...	...	$0.167^{+0.026}_{-0.023}$	<0.063	$0.941^{+0.074}_{-0.094}$	$0.240^{+0.061}_{-0.046}$
058.3−10.9	...	...	$0.165^{+0.053}_{-0.030}$	<0.083	<0.572	<0.284
060.1−07.7	$5.067^{+0.039}_{-0.012}$	$2.031^{+0.027}_{-0.007}$	$0.102^{+0.017}_{-0.012}$	$0.074^{+0.017}_{-0.013}$	$2.407^{+0.042}_{-0.058}$	$1.294^{+0.033}_{-0.021}$
060.5+01.8	...	...	$0.012^{+0.012}_{-0.001}$	$0.028^{+0.010}_{-0.000}$	$0.277^{+0.019}_{-0.047}$	<0.057
064.7+05.0	...	...	<10.690	<14.352	$139.985^{+5.869}_{-6.892}$	$39.390^{+4.385}_{-1.924}$
071.6−02.3	...	...	$0.174^{+0.085}_{-0.056}$	<0.229	$6.231^{+0.399}_{-0.275}$	$1.499^{+0.208}_{-0.099}$
074.5+02.1	$4.436^{+0.343}_{-1.169}$	$6.010^{+0.695}_{-1.322}$	<0.436	...	$3.269^{+1.396}_{-0.401}$	$1.858^{+0.171}_{-0.235}$
082.1+07.0	$2.225^{+0.034}_{-0.049}$	$0.097^{+0.028}_{-0.016}$	...	...	...	...
082.5+11.3	...	...	<0.021	<0.025	...	...
089.3−02.2	...	...	...	...	$2.122^{+3.618}_{-0.358}$	$0.184^{+0.794}_{-0.000}$
089.8−05.1	$2.898^{+0.196}_{-0.166}$	$0.421^{+0.150}_{-0.045}$	<0.145	$0.292^{+0.079}_{-0.044}$	$14.222^{+0.407}_{-0.506}$	$2.111^{+0.188}_{-0.064}$
095.2+00.7	...	...	$0.110^{+0.017}_{-0.012}$	$0.046^{+0.014}_{-0.014}$	$0.682^{+0.029}_{-0.060}$	$0.273^{+0.033}_{-0.025}$
100.6−05.4	$0.058^{+0.012}_{-0.012}$	...	...	...	...	...
111.8−02.8	...	...	$0.518^{+0.147}_{-0.035}$	$0.315^{+0.140}_{-0.047}$	$2.359^{+0.290}_{-0.378}$	$1.065^{+0.345}_{-0.172}$

Table D.3 (cont'd)

PN G	Mg IV(4.49μm) 10^{-16}W m^{-2}	Ar VI(4.53μm) 10^{-16}W m^{-2}	H_2(3.84μm) 10^{-16}W m^{-2}	H_2(4.18μm) 10^{-16}W m^{-2}	PAH(3.3μm) 10^{-16}W m^{-2}	PAH(3.4-3.5μm) 10^{-16}W m^{-2}
(1)	(2)	(3)	(4)	(5)	(6)	(7)
211.2−03.5	...	...	$0.113^{+0.052}_{-0.037}$	...	$0.376^{+0.571}_{-0.040}$	$0.035^{+0.114}_{-0.000}$
232.8−04.7	...	...	<1.093	<0.371	$9.634^{+1.588}_{-0.500}$	$2.458^{+1.094}_{-0.240}$
235.3−03.9	...	...	<0.140	...	$0.599^{+0.090}_{-0.079}$	<0.220
258.1−00.3	...	...	$0.244^{+0.054}_{-0.037}$	<0.041	$0.327^{+0.168}_{-0.070}$	<0.105
264.4−12.7	...	...	<0.003	<0.020	<0.065	<0.043
268.4+02.4	$5.328^{+0.198}_{-0.139}$	$3.658^{+0.196}_{-0.115}$	$0.154^{+0.038}_{-0.024}$	$0.206^{+0.036}_{-0.036}$	$10.239^{+0.243}_{-0.098}$	$4.371^{+0.124}_{-0.086}$
283.8+02.2	$5.446^{+0.116}_{-0.164}$	$0.944^{+0.023}_{-0.048}$	<0.006	<0.031	<0.176	...
285.6−02.7	...	...	$0.084^{+0.107}_{-0.023}$	$0.094^{+0.122}_{-0.025}$	$1.491^{+0.202}_{-0.085}$	$0.279^{+0.306}_{-0.055}$
291.6−04.8	$10.204^{+0.302}_{-0.178}$	$8.162^{+0.023}_{-0.535}$	$0.152^{+0.031}_{-0.012}$	$0.255^{+0.052}_{-0.016}$	$7.261^{+0.167}_{-0.301}$	$3.730^{+0.143}_{-0.120}$
294.9−04.3	...	...	<0.062	<0.037	<0.226	<0.026
296.3−03.0	$0.908^{+0.059}_{-0.102}$	$0.409^{+0.036}_{-0.054}$	<0.111	<0.113	$0.499^{+0.410}_{-0.080}$	$0.206^{+0.123}_{-0.034}$
304.5−04.8	$4.450^{+0.057}_{-0.050}$	$0.847^{+0.049}_{-0.016}$	$0.149^{+0.035}_{-0.023}$	$0.143^{+0.031}_{-0.028}$	$1.299^{+0.123}_{-0.248}$	$0.467^{+0.106}_{-0.075}$
307.2−09.0	...	...	$0.059^{+0.017}_{-0.000}$	$0.024^{+0.017}_{-0.003}$	$0.193^{+0.051}_{-0.056}$	$0.033^{+0.047}_{-0.008}$
307.5−04.9	...	...	<0.173	<0.154	$2.396^{+0.209}_{-0.227}$	$0.280^{+0.137}_{-0.084}$
315.1−13.0	...	...	$0.464^{+0.280}_{-0.104}$	$0.294^{+0.304}_{-0.086}$	$3.979^{+0.540}_{-0.454}$	$0.962^{+0.411}_{-0.193}$
315.4+09.4	...	...	...	...	<10.811	$15.831^{+3.777}_{-3.209}$
320.9+02.0	...	...	$0.160^{+0.046}_{-0.035}$	$0.175^{+0.037}_{-0.041}$	$3.198^{+0.126}_{-0.193}$	$1.239^{+0.092}_{-0.066}$
321.0+03.9	...	...	...	...	$83.596^{+8.544}_{-4.265}$	$54.316^{+16.881}_{-3.788}$
322.5−05.2	$13.040^{+0.095}_{-0.203}$	$0.207^{+0.128}_{-0.015}$	$0.134^{+0.029}_{-0.011}$	$0.005^{+0.014}_{-0.001}$	...	...
323.9+02.4	...	...	<0.090	<0.109	$2.130^{+0.054}_{-0.112}$	$0.917^{+0.036}_{-0.036}$
324.8−01.1	...	...	$0.094^{+0.045}_{-0.024}$	$0.199^{+0.046}_{-0.036}$	$0.784^{+0.110}_{-0.148}$	$0.252^{+0.121}_{-0.042}$

Table D.3 (cont'd)

PN G	Mg IV(4.49μm) 10^{-16}W m^{-2}	Ar VI(4.53μm) 10^{-16}W m^{-2}	H_2(3.84μm) 10^{-16}W m^{-2}	H_2(4.18μm) 10^{-16}W m^{-2}	PAH(3.3μm) 10^{-16}W m^{-2}	PAH(3.4-3.5μm) 10^{-16}W m^{-2}
(1)	(2)	(3)	(4)	(5)	(6)	(7)
325.8−12.8	...	...	$0.039^{+0.015}_{-0.008}$	$0.022^{+0.015}_{-0.004}$	...	...
326.0−06.5	...	...	<0.034	<0.024	$0.086^{+0.171}_{-0.016}$	<0.068
327.1−01.8	...	...	<0.049	<0.076	<1.376	<0.745
327.8−01.6	$3.453^{+0.012}_{-0.029}$	$4.000^{+0.185}_{-0.034}$	...	...	$2.550^{+0.116}_{-0.109}$	$1.455^{+0.004}_{-0.020}$
331.1−05.7	...	...	$0.033^{+0.013}_{-0.006}$	<0.042	...	...
331.3+16.8	$1.183^{+0.020}_{-0.032}$	...	<0.037	<0.023	$0.141^{+0.052}_{-0.018}$	$0.062^{+0.032}_{-0.014}$
336.3−05.6	$0.382^{+0.022}_{-0.014}$	$0.412^{+0.026}_{-0.024}$	...	...	$0.456^{+0.091}_{-0.052}$	$0.239^{+0.032}_{-0.025}$
350.9+04.4	...	...	...	...	...	...
355.9+03.6	...	...	...	...	...	...
356.1+02.7	...	...	...	...	$0.525^{+0.178}_{-0.132}$	<0.038
357.6+02.6	...	...	...	...	$0.664^{+0.125}_{-0.126}$	<0.137
358.9−00.7	...	...	...	...	...	...
043.1+03.8	...	...	<0.022	<0.020	<0.062	<0.007
052.2−04.0	...	...	<0.017	$0.033^{+0.010}_{-0.008}$	$0.054^{+0.050}_{-0.016}$	<0.055
093.5+01.4	...	...	$3.287^{+0.000}_{-0.000}$	$2.139^{+0.000}_{-0.000}$	$40.668^{+0.633}_{-0.358}$	$19.463^{+0.235}_{-0.000}$
118.0−08.6	...	...	...	...	...	...
146.7+07.6	...	...	<0.121	<0.108	$5.166^{+0.517}_{-0.993}$	$1.127^{+0.016}_{-0.228}$
159.0−15.1	$0.855^{+0.029}_{-0.033}$	...	<0.036	...	...	...
190.3−17.7	...	...	$0.047^{+0.010}_{-0.010}$	<0.030	<0.050	...
226.7+05.6	$0.397^{+0.013}_{-0.015}$	$0.173^{+0.013}_{-0.012}$	$0.018^{+0.008}_{-0.004}$	$0.040^{+0.008}_{-0.005}$	$0.832^{+0.055}_{-0.060}$	$0.503^{+0.026}_{-0.023}$
278.6−06.7	$0.101^{+0.013}_{-0.009}$	...	<0.012	<0.020	$0.097^{+0.030}_{-0.016}$	<0.040

Table D.3 (cont'd)

PN G	Mg IV(4.49μm) 10^{-16}W m^{-2}	Ar VI(4.53μm) 10^{-16}W m^{-2}	H_2(3.84μm) 10^{-16}W m^{-2}	H_2(4.18μm) 10^{-16}W m^{-2}	PAH(3.3μm) 10^{-16}W m^{-2}	PAH(3.4-3.5μm) 10^{-16}W m^{-2}
(1)	(2)	(3)	(4)	(5)	(6)	(7)
292.8+01.1	$0.062^{+0.018}_{-0.014}$	···	<0.020	<0.035	$0.456^{+0.045}_{-0.041}$	$0.244^{+0.049}_{-0.030}$
320.1−09.6	···	···	$0.183^{+0.110}_{-0.032}$	$0.095^{+0.083}_{-0.022}$	$3.468^{+0.125}_{-0.090}$	$0.791^{+0.190}_{-0.065}$
342.1+27.5	$2.906^{+0.047}_{-0.054}$	$0.437^{+0.030}_{-0.019}$	<0.020	$0.029^{+0.020}_{-0.009}$	<0.142	<0.013
349.8+04.4	···	···	···	···	$0.479^{+0.036}_{-0.054}$	$0.152^{+0.025}_{-0.027}$
000.3+12.2	···	···	$0.107^{+0.032}_{-0.010}$	$0.061^{+0.028}_{-0.006}$	<0.169	···
086.5−08.8	$1.395^{+0.047}_{-0.035}$	$2.735^{+0.079}_{-0.089}$	···	···	<0.099	<0.046
123.6+34.5	···	···	<0.117	<0.094	<0.172	<0.026
166.1+10.4	···	···	$0.145^{+0.073}_{-0.041}$	<0.081	$0.232^{+0.269}_{-0.065}$	<0.180
194.2+02.5	$2.476^{+0.091}_{-0.103}$	$0.318^{+0.090}_{-0.089}$	<0.208	<0.085	$3.839^{+0.233}_{-0.164}$	$1.050^{+0.130}_{-0.115}$
221.3−12.3	$6.744^{+0.056}_{-0.077}$	$2.090^{+0.055}_{-0.026}$	$0.176^{+0.043}_{-0.035}$	$0.104^{+0.039}_{-0.026}$	$0.617^{+0.081}_{-0.127}$	<0.319
285.4−05.3	$2.841^{+0.016}_{-0.027}$	$0.291^{+0.019}_{-0.007}$	<0.023	$0.061^{+0.022}_{-0.007}$	$0.223^{+0.053}_{-0.055}$	<0.062
285.7−14.9	$0.660^{+0.052}_{-0.057}$	<0.080	<0.107	<0.023	<0.325	<0.117
305.1+01.4	···	···	···	···	$7.362^{+2.383}_{-1.750}$	$10.911^{+2.813}_{-2.017}$
312.6−01.8	···	···	<0.073	<0.067	<0.156	<0.042

Note. — (1) PN G ID; (2) [Mg IV] fine-structure line at 4.49 μm; (3) [Ar VI] fine-structure line at 4.53 μm; (4) H_2(0−0) at 3.84 μm; (5) H_2(0−0) recombination line at 4.18 μm; (6) PAH emission at 3.30 μm; (7) PAH emission around 3.4–3.5 μm.

Table D.4. PNSPC Catalog: Extinction Corrected Equivalent Width (1)

PN G	Bracket-α Å	He II(3.09μm) Å	He I(3.70μm) Å	He I(4.12μm) Å	He I(4.30μm) Å	He I(4.61μm) Å	He I(4.70μm) Å
(1)	(2)	(3)	(4)	(5)	(6)	(7)	(8)
002.0−13.4	$2957.95^{+67.95}_{-47.67}$	...	<44.12	$63.83^{+26.17}_{-12.62}$	$481.78^{+41.01}_{-38.75}$	$345.09^{+24.26}_{-25.87}$	<42.26
003.1+02.9	$2051.08^{+84.79}_{-47.00}$	<226.49	$106.18^{+29.41}_{-13.88}$	$133.75^{+9.66}_{-20.56}$	$334.87^{+28.74}_{-22.30}$	$778.00^{+68.78}_{-75.16}$	<351.55
011.0+05.8	$2055.23^{+146.45}_{-85.71}$	$143.20^{+39.36}_{-25.95}$	...	<116.89	<269.93	$593.46^{+115.03}_{-76.74}$	<180.10
027.6−09.6	$3292.42^{+106.27}_{-75.82}$	...	$51.09^{+19.55}_{-12.53}$	$120.68^{+34.28}_{-32.75}$	$329.61^{+32.37}_{-34.37}$	$250.27^{+32.92}_{-23.53}$	<68.11
037.8−06.3	$497.58^{+24.41}_{-0.93}$	...	$13.92^{+11.10}_{-4.18}$	$26.89^{+8.51}_{-2.07}$	$176.72^{+14.61}_{-0.47}$	$18.95^{+10.35}_{-3.23}$	...
038.2+12.0	$3020.96^{+62.45}_{-72.83}$	...	<56.11	$113.83^{+22.51}_{-23.27}$	$83.00^{+49.54}_{-24.17}$	<49.47	<109.29
046.4−04.1	$3221.70^{+26.47}_{-10.85}$	$104.15^{+17.83}_{-18.06}$	<44.19	$145.72^{+26.17}_{-13.36}$	$483.08^{+29.17}_{-14.26}$	$480.25^{+31.76}_{-27.81}$	<48.59
051.4+09.6	$1891.64^{+52.11}_{-24.21}$	...	<36.56	$77.43^{+15.18}_{-13.21}$	$314.11^{+20.20}_{-16.88}$	$74.80^{+13.95}_{-12.04}$	<36.59
058.3−10.9	$1560.02^{+21.29}_{-53.79}$	...	<36.24	$45.35^{+14.97}_{-4.86}$	$350.81^{+29.38}_{-21.24}$	$64.53^{+17.60}_{-10.04}$	$49.20^{+20.01}_{-14.76}$
060.1−07.7	$1703.38^{+20.74}_{-16.31}$	$180.64^{+17.84}_{-22.24}$	<31.65	$127.86^{+16.27}_{-15.90}$	$151.00^{+20.55}_{-22.55}$	$341.78^{+30.54}_{-20.07}$	<92.87
060.5+01.8	$2259.56^{+27.99}_{-9.55}$	...	$38.53^{+18.79}_{-0.79}$	$51.86^{+27.22}_{-1.22}$	$338.74^{+27.06}_{-0.10}$	$274.24^{+28.84}_{-7.29}$	<32.95
064.7+05.0	$508.65^{+56.73}_{-31.18}$	...	<180.39	<260.43	<170.09	<132.87	$67.26^{+43.52}_{-15.89}$
071.6−02.3	$643.47^{+21.99}_{-23.46}$	...	<18.22	$32.23^{+21.41}_{-9.18}$	$128.22^{+15.79}_{-13.37}$	<18.44	<31.71
074.5+02.1	$1315.48^{+138.47}_{-298.94}$	$298.65^{+85.32}_{-34.49}$	<210.79	<367.35	<299.47	$209.52^{+110.56}_{-48.04}$	$133.61^{+86.31}_{-41.48}$
082.1+07.0	$2964.25^{+28.50}_{-98.92}$	$232.37^{+37.26}_{-31.41}$	<0.04	$147.81^{+21.66}_{-8.26}$	$305.12^{+25.89}_{-19.33}$	$372.60^{+35.61}_{-12.26}$	<96.76
082.5+11.3	$1864.57^{+61.94}_{-57.15}$	...	...	<92.48	$436.70^{+79.00}_{-58.64}$	<178.86	...
089.3−02.2	$61.60^{+15.32}_{-6.86}$	...	...	...	...	...	...
089.8−05.1	$299.97^{+13.29}_{-12.40}$	$35.45^{+10.48}_{-4.09}$	...	$31.77^{+8.54}_{-3.93}$	$95.95^{+8.88}_{-6.49}$	$30.94^{+7.81}_{-5.21}$	<20.49
095.2+00.7	$1457.63^{+8.14}_{-41.60}$	...	$36.76^{+10.46}_{-7.34}$	$56.42^{+8.90}_{-9.29}$	$293.67^{+12.25}_{-9.04}$	$150.28^{+13.20}_{-4.46}$	...
100.6−05.4	$2680.88^{+66.62}_{-72.17}$	$93.18^{+21.91}_{-25.39}$	<52.02	<61.14	$174.56^{+34.49}_{-34.19}$	$156.57^{+48.52}_{-45.32}$	...
111.8−02.8	$396.93^{+13.99}_{-1.37}$	...	$35.07^{+8.78}_{-2.67}$	$56.50^{+8.53}_{-2.52}$	$126.03^{+11.42}_{-4.01}$	$40.31^{+10.66}_{-1.71}$	$29.32^{+7.73}_{-6.15}$

Table D.4 (cont'd)

PN G	Bracket-α	He II(3.09μm)	He I(3.70μm)	He I(4.12μm)	He I(4.30μm)	He I(4.61μm)	He I(4.70μm)
	Å	Å	Å	Å	Å	Å	Å
(1)	(2)	(3)	(4)	(5)	(6)	(7)	(8)
211.2−03.5	$544.44^{+21.43}_{-12.62}$	...	<36.54	<24.87	$90.09^{+16.40}_{-12.68}$	<29.04	...
232.8−04.7	$176.14^{+20.89}_{-9.62}$	...	...	...	...	...	...
235.3−03.9	$331.88^{+18.92}_{-18.70}$	...	<40.30	...	$51.01^{+14.60}_{-13.04}$	<31.82	...
258.1−00.3	$1613.54^{+177.35}_{-57.80}$	...	<61.68	$73.19^{+18.29}_{-12.80}$	$249.92^{+26.03}_{-20.89}$	$102.34^{+13.96}_{-21.00}$	...
264.4−12.7	$2807.38^{+64.22}_{-78.18}$	...	<37.17	<74.39	$277.45^{+50.87}_{-28.65}$	$144.82^{+45.64}_{-39.71}$	...
268.4+02.4	$379.06^{+10.30}_{-7.77}$	$65.10^{+9.03}_{-3.06}$	$11.79^{+9.44}_{-0.53}$	$50.24^{+10.55}_{-6.38}$	$72.10^{+13.54}_{-11.65}$	$38.38^{+14.29}_{-6.38}$	$24.55^{+11.99}_{-1.56}$
283.8+02.2	$1666.53^{+55.29}_{-64.44}$	$565.73^{+37.80}_{-37.75}$	...	$248.71^{+29.32}_{-17.38}$	<50.88	$264.43^{+51.04}_{-37.06}$	$136.13^{+37.26}_{-33.85}$
285.6−02.7	$2336.20^{+87.79}_{-70.65}$	...	...	$84.59^{+40.97}_{-13.57}$	$131.51^{+65.04}_{-13.92}$	<51.94	<39.06
291.6−04.8	$1166.71^{+31.85}_{-27.00}$	$220.59^{+13.79}_{-11.90}$	$45.22^{+0.17}_{-8.39}$	$81.68^{+21.02}_{-3.35}$	$174.90^{+1.95}_{-14.53}$	$203.49^{+0.16}_{-21.91}$	$46.29^{+9.45}_{-5.30}$
294.9−04.3	$1128.27^{+52.38}_{-47.83}$	...	<62.60	<90.45	$189.75^{+45.08}_{-39.37}$	<89.20	<83.75
296.3−03.0	$2253.28^{+69.66}_{-252.63}$	$130.67^{+47.10}_{-22.73}$	<53.46	$161.09^{+127.38}_{-48.28}$	$393.86^{+145.99}_{-79.66}$	$510.19^{+82.46}_{-123.24}$	<171.70
304.5−04.8	$2595.24^{+23.18}_{-37.11}$	$154.60^{+22.30}_{-17.82}$	...	$163.54^{+31.22}_{-11.33}$	$418.36^{+30.14}_{-23.82}$	$425.16^{+43.61}_{-24.16}$	$175.96^{+56.12}_{-24.77}$
307.2−09.0	$2523.10^{+102.96}_{-16.85}$	...	...	$127.65^{+64.87}_{-1.06}$	$538.39^{+46.36}_{-17.62}$	$199.57^{+105.79}_{-0.91}$	$220.94^{+142.00}_{-1.85}$
307.5−04.9	$2612.83^{+116.86}_{-218.21}$	...	...	$333.10^{+44.29}_{-42.98}$	$325.85^{+38.47}_{-32.67}$	$422.83^{+54.71}_{-41.40}$	$306.55^{+78.68}_{-43.79}$
315.1−13.0	$2905.53^{+310.72}_{-333.03}$	...	...	$144.87^{+49.57}_{-20.48}$	$158.77^{+64.32}_{-20.94}$	<107.34	$113.49^{+63.27}_{-26.53}$
315.4+09.4	<14.18	...	...	...	...	...	...
320.9+02.0	$2753.26^{+200.78}_{-12.52}$	...	<48.05	$155.90^{+13.85}_{-16.81}$	$572.17^{+32.12}_{-19.18}$	$625.23^{+38.66}_{-8.22}$	$72.48^{+39.63}_{-0.12}$
321.0+03.9	...	...	...	...	...	...	...
322.5−05.2	$3996.05^{+91.02}_{-55.74}$	$3126.12^{+93.09}_{-70.36}$	$576.76^{+150.65}_{-29.65}$	$176.64^{+58.88}_{-23.40}$	$281.78^{+84.16}_{-22.66}$	$188.36^{+108.90}_{-18.61}$	$6.65^{+52.65}_{-0.89}$
323.9+02.4	$2365.00^{+54.16}_{-58.04}$	...	<39.98	$186.72^{+32.96}_{-27.75}$	$303.73^{+35.47}_{-34.03}$	$278.47^{+20.37}_{-26.36}$	...
324.8−01.1	$3959.36^{+110.68}_{-202.96}$	...	$105.79^{+40.57}_{-31.23}$	$207.31^{+27.47}_{-37.30}$	$811.34^{+67.64}_{-77.33}$	$559.57^{+44.68}_{-65.58}$	<93.12

Table D.4 (cont'd)

PN G	Bracket-α Å	He II(3.09μm) Å	He I(3.70μm) Å	He I(4.12μm) Å	He I(4.30μm) Å	He I(4.61μm) Å	He I(4.70μm) Å
(1)	(2)	(3)	(4)	(5)	(6)	(7)	(8)
325.8−12.8	$1836.98^{+38.95}_{-30.00}$	...	<20.70	$62.25^{+22.84}_{-7.84}$	$234.05^{+24.26}_{-11.61}$	$69.59^{+32.77}_{-23.14}$	<99.83
326.0−06.5	$1374.87^{+42.43}_{-63.77}$	...	<64.20	<127.92	<75.15	<205.92	...
327.1−01.8	$2100.09^{+101.64}_{-186.48}$	...	$60.73^{+35.14}_{-12.21}$	<172.17	<405.50	<306.15	<32.57
327.8−01.6	$1356.38^{+48.35}_{-18.46}$	$216.75^{+0.07}_{-3.94}$	$17.54^{+0.01}_{-0.21}$	$191.49^{+0.07}_{-3.48}$	$224.11^{+8.96}_{-1.94}$	$499.17^{+1.18}_{-5.99}$	$168.76^{+0.86}_{-1.43}$
331.1−05.7	$876.65^{+32.21}_{-48.40}$	...	...	$41.18^{+12.31}_{-6.01}$	$272.04^{+18.13}_{-19.59}$	<44.49	<74.34
331.3+16.8	$1788.98^{+46.92}_{-28.46}$	$435.95^{+26.94}_{-16.37}$	...	$112.92^{+43.25}_{-29.69}$	<104.76	$49.10^{+50.79}_{-13.51}$	$62.81^{+59.76}_{-17.67}$
336.3−05.6	$974.16^{+70.43}_{-55.28}$	$179.94^{+34.96}_{-27.08}$	<103.08	...	<119.23	$179.19^{+103.36}_{-37.26}$	$195.95^{+98.52}_{-36.59}$
350.9+04.4	$751.29^{+32.14}_{-22.79}$	...	...	<27.97	$55.74^{+15.68}_{-4.09}$	$34.64^{+15.67}_{-10.89}$	<22.50
355.9+03.6	$448.77^{+101.12}_{-43.17}$	...	...	...	...	...	...
356.1+02.7	$760.04^{+100.98}_{-57.69}$	...	<90.03	...	$172.68^{+47.95}_{-35.92}$	<120.99	...
357.6+02.6	$1390.93^{+148.13}_{-180.03}$	...	<108.97	<162.74	$450.92^{+116.79}_{-96.96}$	$465.29^{+92.38}_{-71.71}$	<150.32
358.9−00.7	$761.15^{+34.39}_{-21.03}$	...	<24.81	$62.51^{+12.65}_{-18.39}$	<36.83	<72.25	...
043.1+03.8	$1220.99^{+68.23}_{-35.26}$	...	$125.15^{+38.19}_{-31.40}$	<48.10	...	$150.58^{+30.01}_{-34.52}$	<112.99
052.2−04.0	$2820.42^{+107.00}_{-102.44}$	...	<36.79	<58.22	$485.28^{+39.64}_{-34.60}$	$417.14^{+37.20}_{-35.25}$	$152.15^{+40.99}_{-24.05}$
093.5+01.4	$1561.04^{+10.35}_{-0.00}$	...	$14.30^{+0.00}_{-0.00}$	$131.81^{+0.00}_{-0.00}$	$195.79^{+0.00}_{-0.00}$	$21.89^{+0.00}_{-0.00}$	$108.16^{+0.00}_{-0.00}$
118.0−08.6	$869.72^{+73.98}_{-48.24}$	...	<132.56	...	<121.16	<125.70	<126.77
146.7+07.6	$301.44^{+20.65}_{-34.73}$	...	<21.32	<69.53	$70.38^{+22.19}_{-21.96}$	...	...
159.0−15.1	$1668.24^{+43.29}_{-47.42}$	$269.42^{+39.31}_{-35.01}$	<111.39	$189.65^{+86.40}_{-61.34}$	<260.21	$199.51^{+100.18}_{-59.22}$	<168.35
190.3−17.7	$2128.23^{+36.71}_{-32.73}$	...	...	$214.47^{+49.26}_{-45.28}$	$211.20^{+59.94}_{-36.26}$	$200.37^{+48.96}_{-49.53}$	<159.13
226.7+05.6	$1602.50^{+36.91}_{-87.23}$	$142.56^{+16.36}_{-9.12}$	...	$99.32^{+24.72}_{-20.11}$	$145.55^{+32.85}_{-26.33}$	$101.20^{+36.40}_{-26.81}$	$248.33^{+46.43}_{-28.45}$
278.6−06.7	$2060.51^{+53.33}_{-40.41}$	$75.83^{+17.90}_{-19.08}$	...	<52.85	$331.54^{+40.59}_{-27.79}$	$142.99^{+44.45}_{-33.73}$	...

Table D.4 (cont'd)

PN G	Bracket-α Å	He II(3.09μm) Å	He I(3.70μm) Å	He I(4.12μm) Å	He I(4.30μm) Å	He I(4.61μm) Å	He I(4.70μm) Å
(1)	(2)	(3)	(4)	(5)	(6)	(7)	(8)
292.8+01.1	$2679.66^{+234.61}_{-130.23}$	$203.83^{+36.48}_{-22.95}$	...	$120.72^{+44.92}_{-33.88}$	$295.72^{+74.83}_{-46.17}$	$450.29^{+54.95}_{-46.06}$	<196.76
320.1−09.6	$1674.42^{+29.70}_{-20.58}$	...	<90.48	$84.74^{+45.92}_{-14.93}$	<67.89	...	...
342.1+27.5	$2080.62^{+64.35}_{-54.64}$	$754.98^{+56.66}_{-40.05}$	<75.92	<121.87	<218.71	$224.51^{+121.87}_{-64.06}$	<156.61
349.8+04.4	$2261.68^{+86.23}_{-249.61}$	...	<37.74	<74.02	$374.58^{+42.57}_{-31.79}$	$315.92^{+45.13}_{-44.42}$	...
000.3+12.2	$2981.39^{+46.41}_{-15.75}$	...	$24.80^{+27.51}_{-5.23}$	$197.58^{+27.75}_{-4.86}$	$227.93^{+26.34}_{-8.28}$	$329.98^{+47.88}_{-22.44}$	<95.42
086.5−08.8	$1243.81^{+23.92}_{-27.11}$	$530.62^{+23.35}_{-18.71}$	...	$119.70^{+146.36}_{-21.43}$	...	$315.01^{+62.71}_{-22.14}$	$120.36^{+66.55}_{-24.13}$
123.6+34.5	$3172.43^{+88.92}_{-100.72}$	...	...	$241.31^{+72.73}_{-66.00}$	<283.51	<212.05	...
166.1+10.4	$1725.64^{+26.07}_{-30.61}$	...	...	$112.16^{+20.93}_{-20.13}$	$152.05^{+24.61}_{-20.99}$	$93.96^{+27.47}_{-25.54}$	<88.10
194.2+02.5	$360.98^{+12.64}_{-10.49}$	$79.25^{+10.45}_{-10.06}$	<29.36	<37.60	<35.68	<32.94	<40.50
221.3−12.3	$2095.31^{+26.68}_{-16.95}$	$385.54^{+13.11}_{-20.87}$	...	$198.10^{+28.03}_{-14.66}$	$201.45^{+38.49}_{-29.56}$	$202.24^{+39.05}_{-28.53}$	$112.93^{+38.23}_{-30.10}$
285.4−05.3	$3832.85^{+25.98}_{-12.30}$	$419.35^{+19.07}_{-23.35}$	...	$147.96^{+30.69}_{-5.90}$	$305.97^{+31.27}_{-20.32}$	$674.76^{+43.28}_{-23.74}$	...
285.7−14.9	$1259.65^{+28.97}_{-30.31}$	$185.51^{+32.28}_{-23.25}$	<39.37	$225.31^{+47.77}_{-42.00}$	<152.71	<124.60	<92.04
305.1+01.4	$60.09^{+7.68}_{-7.66}$	...	...	...	...	...	...
312.6−01.8	$3537.66^{+166.63}_{-204.65}$	...	<74.22	$158.10^{+45.24}_{-40.94}$	$345.23^{+58.89}_{-48.56}$	$218.51^{+74.29}_{-71.69}$	<58.98

Note. — (1) PN G ID; (2) Brackett-α at 4.051 μm; (3) He II(7−6) recombination line at 3.09 μm; (4) He I($3P^o$−3D) recombination line at 3.70 μm; (5) He I($1P^o$−1D) recombination line at 4.12 μm; (6) He I(3S−$3P^o$) recombination line at 4.30 μm; (7) He I($1P^o$−1S) recombination line at 4.61 μm; (8) He I($3P^o$−3S) recombination line at 4.70 μm.

Table D.5. PNSPC Catalog: Extinction Corrected Equivalent Width (2)

PN G	Mg IV(4.49μm) Å	Ar VI(4.53μm) Å	H_2(3.84μm) Å	H_2(4.18μm) Å	PAH(3.3μm) Å	PAH(3.4-3.5μm) Å
(1)	(2)	(3)	(4)	(5)	(6)	(7)
002.0−13.4	...	...	<37.37	$63.40^{+18.07}_{-14.03}$	$437.37^{+82.20}_{-61.78}$	$188.12^{+58.27}_{-50.43}$
003.1+02.9	$338.08^{+26.90}_{-47.00}$	...	...	...	$719.66^{+106.15}_{-130.68}$	$375.10^{+85.14}_{-58.05}$
011.0+05.8	$2713.30^{+253.66}_{-164.00}$	$501.10^{+138.35}_{-109.99}$	...	...	...	...
027.6−09.6	...	...	...	...	...	...
037.8−06.3	...	...	$29.35^{+9.68}_{-3.06}$	...	$1113.24^{+37.21}_{-7.62}$	$213.52^{+30.39}_{-2.25}$
038.2+12.0	...	...	...	<36.31	$687.71^{+90.01}_{-84.66}$	$201.56^{+66.95}_{-53.00}$
046.4−04.1	...	...	...	$96.84^{+29.85}_{-6.66}$	$610.56^{+62.88}_{-89.15}$	$250.13^{+126.23}_{-69.81}$
051.4+09.6	...	...	$92.35^{+14.48}_{-12.58}$	<37.28	$718.98^{+56.41}_{-71.53}$	$193.30^{+48.99}_{-37.38}$
058.3−10.9	...	...	$53.28^{+17.21}_{-9.85}$	<28.80	<258.67	<134.75
060.1−07.7	$7248.06^{+55.40}_{-17.53}$	$2955.31^{+38.80}_{-10.01}$	$108.89^{+17.93}_{-12.71}$	$92.42^{+21.76}_{-15.74}$	$3246.69^{+57.16}_{-78.00}$	$1873.07^{+47.41}_{-30.13}$
060.5+01.8	...	...	$22.90^{+22.22}_{-2.09}$	$59.53^{+21.67}_{-0.16}$	$649.19^{+44.70}_{-109.79}$	<140.75
064.7+05.0	...	...	<168.74	<209.70	$5665.52^{+237.53}_{-278.93}$	$1296.12^{+144.28}_{-63.29}$
071.6−02.3	...	...	$31.55^{+15.38}_{-10.26}$	<43.21	$1740.48^{+111.48}_{-76.72}$	$430.83^{+59.79}_{-28.34}$
074.5+02.1	$3313.02^{+255.84}_{-873.21}$	$4516.93^{+522.71}_{-993.37}$	<348.04	...	$3972.33^{+1697.06}_{-487.75}$	$2389.52^{+219.57}_{-301.90}$
082.1+07.0	$2258.60^{+34.01}_{-49.89}$	$100.93^{+28.96}_{-17.17}$	...	...	...	...
082.5+11.3	...	...	<68.69	<93.37	...	...
089.3−02.2	...	...	...	...	$206.92^{+352.78}_{-34.95}$	$19.41^{+83.71}_{-0.00}$
089.8−05.1	$280.40^{+19.00}_{-16.05}$	$40.50^{+14.41}_{-4.34}$	<14.56	$29.05^{+7.88}_{-4.38}$	$2682.02^{+76.80}_{-95.48}$	$357.31^{+31.86}_{-10.80}$
095.2+00.7	...	...	$62.38^{+9.55}_{-6.85}$	$27.45^{+8.66}_{-8.51}$	$561.78^{+23.51}_{-49.22}$	$235.96^{+28.73}_{-21.18}$
100.6−05.4	$205.01^{+43.74}_{-43.97}$	...	...	...	...	...
111.8−02.8	...	...	$35.12^{+9.99}_{-2.36}$	$21.38^{+9.53}_{-3.22}$	$250.88^{+30.86}_{-40.15}$	$115.44^{+37.45}_{-18.68}$

Table D.5 (cont'd)

PN G	Mg IV(4.49μm) Å	Ar VI(4.53μm) Å	H_2(3.84μm) Å	H_2(4.18μm) Å	PAH(3.3μm) Å	PAH(3.4-3.5μm) Å
(1)	(2)	(3)	(4)	(5)	(6)	(7)
211.2−03.5	...	...	$32.03^{+14.90}_{-10.47}$	...	$154.63^{+234.47}_{-16.53}$	$15.27^{+49.33}_{-0.00}$
232.8−04.7	...	...	<66.04	...	$892.50^{+147.12}_{-46.28}$	$233.12^{+103.78}_{-22.73}$
235.3−03.9	...	...	<39.78	...	$246.59^{+36.89}_{-32.53}$	<93.23
258.1−00.3	...	...	$103.52^{+22.75}_{-15.74}$	...	$193.06^{+99.28}_{-41.31}$	...
264.4−12.7	...	...	...	<81.77	<311.39	<225.67
268.4+02.4	$1266.70^{+47.03}_{-32.93}$	$869.53^{+46.55}_{-27.24}$	$36.87^{+9.13}_{-5.81}$	$49.06^{+8.57}_{-8.52}$	$4094.64^{+97.34}_{-39.11}$	$1738.99^{+49.46}_{-34.17}$
283.8+02.2	$15152.15^{+322.15}_{-454.94}$	$2669.94^{+65.01}_{-135.18}$	...	<75.32	<473.82	...
285.6−02.7	...	...	$36.87^{+47.00}_{-10.26}$	$46.39^{+60.50}_{-12.25}$	$842.65^{+114.16}_{-48.23}$	$171.11^{+187.73}_{-34.00}$
291.6−04.8	$4155.90^{+123.04}_{-72.70}$	$3322.59^{+9.52}_{-217.88}$	$59.37^{+12.14}_{-4.52}$	$103.03^{+21.16}_{-6.65}$	$4273.65^{+98.01}_{-177.45}$	$2261.18^{+86.49}_{-72.83}$
294.9−04.3	...	...	<70.35	<46.89	<338.33	...
296.3−03.0	$2221.49^{+144.78}_{-248.36}$	$1017.22^{+89.53}_{-133.76}$	<186.32	<236.64	$943.01^{+774.28}_{-150.79}$	$430.35^{+256.25}_{-71.71}$
304.5−04.8	$4472.40^{+56.88}_{-50.66}$	$877.55^{+50.73}_{-16.12}$	$97.93^{+23.29}_{-15.33}$	$116.35^{+25.42}_{-22.68}$	$1044.46^{+98.69}_{-199.08}$	$403.20^{+91.68}_{-65.07}$
307.2−09.0	...	...	$142.03^{+42.41}_{-1.12}$	$66.36^{+46.25}_{-7.22}$	$656.82^{+173.10}_{-191.24}$	$119.06^{+167.96}_{-28.31}$
307.5−04.9	...	...	<158.04	<160.01	$3235.08^{+281.71}_{-306.56}$	$386.17^{+188.08}_{-116.38}$
315.1−13.0	...	...	$97.53^{+58.85}_{-21.95}$	$72.06^{+74.54}_{-21.11}$	$1103.79^{+149.65}_{-125.96}$	$283.61^{+121.21}_{-56.92}$
315.4+09.4	...	...	...	...	<96.73	$143.42^{+34.22}_{-29.07}$
320.9+02.0	...	...	$68.28^{+19.40}_{-14.75}$	$84.82^{+17.87}_{-19.63}$	$1781.39^{+70.09}_{-107.55}$	$744.06^{+55.39}_{-39.70}$
321.0+03.9	...	...	...	...	$888.95^{+90.86}_{-45.35}$	$526.46^{+163.62}_{-36.72}$
322.5−05.2	$44552.26^{+325.72}_{-693.23}$	$708.81^{+435.82}_{-51.65}$	$456.22^{+99.50}_{-36.22}$	$17.88^{+47.80}_{-2.03}$	...	...
323.9+02.4	...	...	<101.65	<130.51	$3457.82^{+87.51}_{-182.12}$	$1559.88^{+61.56}_{-61.89}$
324.8−01.1	...	...	$81.52^{+38.99}_{-20.72}$	$179.36^{+41.40}_{-32.52}$	$1130.78^{+159.02}_{-214.12}$	$359.76^{+172.14}_{-59.97}$

Table D.5 (cont'd)

PN G	Mg IV(4.49μm) Å	Ar VI(4.53μm) Å	H_2(3.84μm) Å	H_2(4.18μm) Å	PAH(3.3μm) Å	PAH(3.4-3.5μm) Å
(1)	(2)	(3)	(4)	(5)	(6)	(7)
325.8−12.8	...	...	$43.70^{+16.78}_{-8.49}$	$27.95^{+19.26}_{-4.65}$	...	...
326.0−06.5	...	...	<111.58	<95.38	$313.94^{+628.18}_{-57.71}$	<271.69
327.1−01.8	...	...	<52.16	<100.68	<1593.60	<964.93
327.8−01.6	$2676.76^{+9.46}_{-22.72}$	$3119.37^{+144.19}_{-26.38}$	...	...	$1973.97^{+90.08}_{-84.68}$	$1214.68^{+3.17}_{-16.39}$
331.1−05.7	...	...	$22.92^{+9.45}_{-4.33}$	<33.44	...	...
331.3+16.8	$3181.03^{+53.56}_{-85.30}$	...	<84.43	<57.44	$461.24^{+171.36}_{-58.03}$	$213.81^{+110.59}_{-47.77}$
336.3−05.6	$1990.09^{+114.70}_{-74.38}$	$2184.41^{+137.20}_{-128.21}$	...	...	$2210.52^{+439.58}_{-250.22}$	$1290.84^{+173.75}_{-133.66}$
350.9+04.4	...	...	...	...	...	...
355.9+03.6	...	...	...	...	...	...
356.1+02.7	...	...	...	...	$659.80^{+223.21}_{-166.06}$	...
357.6+02.6	...	...	...	...	$1022.94^{+193.22}_{-193.30}$	<243.50
358.9−00.7	...	...	...	...	...	...
043.1+03.8	...	...	<56.57	<54.37	<209.36	...
052.2−04.0	...	...	<53.49	$114.73^{+33.41}_{-28.54}$	$211.38^{+198.07}_{-63.15}$	<232.90
093.5+01.4	...	...	$168.45^{+0.00}_{-0.00}$	$113.23^{+0.00}_{-0.00}$	$3184.90^{+49.59}_{-28.00}$	$1556.49^{+18.77}_{-0.01}$
118.0−08.6	...	...	...	...	...	...
146.7+07.6	...	...	<62.17	<59.06	$3956.08^{+396.14}_{-760.47}$	$889.28^{+12.46}_{-179.53}$
159.0−15.1	$3536.40^{+119.33}_{-136.10}$	...	<115.54	...	...	...
190.3−17.7	...	...	$194.72^{+41.85}_{-40.03}$	<147.66	<252.55	...
226.7+05.6	$1512.83^{+47.94}_{-56.70}$	$663.53^{+51.14}_{-47.92}$	$56.73^{+25.16}_{-13.28}$	$140.32^{+28.46}_{-19.20}$	$3611.54^{+236.97}_{-258.41}$	$2308.75^{+118.71}_{-106.18}$
278.6−06.7	$418.37^{+52.38}_{-36.87}$	...	<38.87	<73.56	$424.56^{+130.24}_{-69.15}$	<184.51

Table D.5 (cont'd)

PN G	Mg IV(4.49μm) Å	Ar VI(4.53μm) Å	H_2(3.84μm) Å	H_2(4.18μm) Å	PAH(3.3μm) Å	PAH(3.4-3.5μm) Å
(1)	(2)	(3)	(4)	(5)	(6)	(7)
292.8+01.1	$262.43^{+74.96}_{-60.70}$	···	<60.78	<127.87	$1740.43^{+170.98}_{-154.46}$	$1009.03^{+200.85}_{-122.14}$
320.1−09.6	···	···	$89.75^{+53.98}_{-15.55}$	$50.46^{+44.30}_{-11.70}$	$2339.82^{+84.63}_{-60.60}$	$572.73^{+137.46}_{-47.16}$
342.1+27.5	$16973.24^{+274.41}_{-313.00}$	$2618.28^{+178.01}_{-111.58}$	···	$139.88^{+94.99}_{-45.15}$	<659.49	···
349.8+04.4	···	···	···	···	$1259.21^{+93.68}_{-142.28}$	$444.56^{+73.91}_{-77.76}$
000.3+12.2	···	···	$103.95^{+30.84}_{-9.58}$	$69.34^{+31.82}_{-7.01}$	<208.59	···
086.5−08.8	$2033.72^{+69.03}_{-51.70}$	$4002.78^{+115.63}_{-130.30}$	···	···	<166.85	<80.75
123.6+34.5	···	···	<163.60	<156.94	<304.33	···
166.1+10.4	···	···	$53.29^{+26.74}_{-15.08}$	<33.96	$113.62^{+131.34}_{-31.62}$	<92.22
194.2+02.5	$570.58^{+21.03}_{-23.83}$	$74.38^{+21.07}_{-20.90}$	<41.92	<18.13	$1139.59^{+69.08}_{-48.76}$	$324.57^{+40.21}_{-35.59}$
221.3−12.3	$6375.74^{+53.39}_{-72.60}$	$2016.41^{+52.75}_{-24.93}$	$118.66^{+28.68}_{-23.67}$	$84.13^{+31.99}_{-20.82}$	$514.95^{+67.93}_{-106.30}$	<285.89
285.4−05.3	$5582.26^{+30.84}_{-52.55}$	$591.83^{+38.12}_{-14.17}$	<28.28	$95.29^{+33.75}_{-10.92}$	$344.03^{+81.52}_{-84.26}$	···
285.7−14.9	$718.53^{+56.11}_{-61.79}$	<87.70	<97.92	···	<410.20	<152.69
305.1+01.4	···	···	···	···	$76.30^{+24.70}_{-18.14}$	$105.90^{+27.31}_{-19.58}$
312.6−01.8	···	···	<163.06	<181.74	<394.47	<118.43

Note. — (1) PN G ID; (2) [Mg IV] fine-structure line at 4.49 μm; (3) [Ar VI] fine-structure line at 4.53 μm; (4) H_2(0−0) at 3.84 μm; (5) H_2(0−0) recombination line at 4.18 μm; (6) PAH emission at 3.30 μm; (7) PAH emission around 3.4–3.5 μm.